Investigation of Flow Boiling Phenomena in Small-Scale Complex Geometries

Amir Hooshang Raeisi Dehkordi

Submitted for the degree of Doctor of Philosophy

Heriot-Watt University

School of Engineering and Physical Sciences

May 2012

ABSTRACT

This study concerns measurement and prediction of single-phase and flow boiling heat transfer coefficients and pressure drops in mini multi-channel geometries with and without interconnecting passages, including plate channel; parallel channel; in-line pin-fin and in-line off-set pin-fin surfaces. Experiments were performed with refrigerant R113 and deionised water at atmospheric pressure. Single-phase and flow boiling heat transfer coefficients and pressure drops were obtained over a range of effective heat fluxes and mass fluxes. For the plate and parallel channel surfaces, the results obtained have been compared with several published macro- and micro-channels correlations. For the in-line and in-line off-set pin fin surfaces, as the geometries have some similarities with tube bundles, the results obtained have been predicted using the standard correlations for tube bundles. The results also have been compared with several existing correlations developed based on macro-scale tube bundles and micro-pin-fin surfaces data.

The saturated flow boiling heat transfer coefficients for the parallel channel and pin-fin surfaces were similar to within the experimental uncertainty, and considerably higher than the plate channel values, all dependent on heat flux and reasonably independent of mass flux and vapour mass fraction. This indicated that the dominant heat-transfer mechanism in the saturated boiling flow regime was nucleate boiling for all surfaces. The parallel channel, in-line and off-set pin-fin surfaces improved heat transfer by increasing the surface area and the heat transfer coefficient in comparison with the plate channel surface. The two-phase pressure drops in the parallel channel and pin-fin surfaces were considerably larger than that for the plate channel surface. Thus, the reduction in wall temperature is achieved by a significant pressure drop penalty. For the pin-fin surfaces, at low vapour qualities the heat transfer coefficients were in reasonable agreement with the conventional scale tube bundles correlations however as the vapour quality increases, the correlations were not able to predict the heat transfer coefficient as unlike the conventionally-sized tube bundles, the convective enhancement does not happen in the mini-pin-fin surfaces tested. The nucleate pool boiling correlation of Cooper (1984) provided a good agreement with the data for all surfaces tests with R113 and deionised water. The measured two-phase pressure drops for both pin-fin surfaces tests with R113 and deionised water were in a good agreement with the predicted values obtained from standard correlations for tube bundles, indicating pressure drop methods maybe transferable.

DEDICATION

I would like to dedicate my thesis to my beloved mum and dad for opening my eyes to the world and instilling the importance of hard work and higher education, and my sister, Gita, who has encouraged and supported me all the way since the beginning of my studies, and also my brother-in-law, Morteza, for his enormous support during my PhD.

Finally, I would like to dedicate my thesis to all those who believe in the richness of learning.

ACKNOWLEDGEMENTS

It would not have been possible to write this doctoral thesis without the help and support of the kind people around me, to only some of whom it is possible to give particular mention here.

Above all, I would like to thank my supervisors, Dr. Peter A. Kew, and Dr David A. McNeil, who were enormously generous and supportive throughout my PhD studies. They brought a vision of the larger picture and a sense of direction at times when my research had stalled. Their patience, enthusiasm, strong work ethics, extensive knowledge and experience will undoubtedly help me throughout my future career. The good advice, support and friendship of my second supervisor, Dr David A. McNeil, have been invaluable on both an academic and a personal level, for which I am extremely grateful.

I would like to recognize and thank the following Mechanical Workshop Technicians; Richard Kinsella (technician/team leader), Kenneth Carruthers (technician), and Alistair Blyth (technician), for their support and assistance since the start of my PhD.

I also would like to thank my parents for providing me with an endless supply of love and encouragement, my sister, Gita, and my brother-in-law, Morteza, for their enormous and unequivocal support throughout, as always, for which my mere expression of thanks likewise does not suffice.

Finally, I would like to extend my gratitude to the Heriot-Watt University, School of Engineering and Physical Sciences (EPS) for their financial, academic and technical support for my graduate work.

ACADEMIC REGISTRY
Research Thesis Submission

Name*:*	Amir Hooshang Raeisi Dehkordi		
School/PGI:	Engineering and Physical Sciences (EPS)		
Version: *(i.e. First, Resubmission, Final)*	Final	Degree Sought (Award **and** Subject area)	PhD, Mechanical Engineering

Declaration

In accordance with the appropriate regulations I hereby submit my thesis and I declare that:

1) the thesis embodies the results of my own work and has been composed by myself
2) where appropriate, I have made acknowledgement of the work of others and have made reference to work carried out in collaboration with other persons
3) the thesis is the correct version of the thesis for submission and is the same version as any electronic versions submitted*.
4) my thesis for the award referred to, deposited in the Heriot-Watt University Library, should be made available for loan or photocopying and be available via the Institutional Repository, subject to such conditions as the Librarian may require
5) I understand that as a student of the University I am required to abide by the Regulations of the University and to conform to its discipline.

* *Please note that it is the responsibility of the candidate to ensure that the correct version of the thesis is submitted.*

Signature of Candidate*:*	Amir Hooshang Raeisi Dehkordi	Date:	

Submission

Submitted By *(name in capitals):*	AMIR HOOSHANG RAEISI DEHKORDI
Signature of Individual Submitting:	
Date Submitted:	

For Completion in the Student Service Centre (SSC)

Received in the SSC by *(name in capitals):*			
Method of Submission *(Handed in to SSC; posted through internal/external mail):*			
E-thesis Submitted ***(mandatory for final theses)***			
Signature:		Date:	

TABLE OF CONTENTS

LIST OF FIGURES

LIST OF TABLES

NOMENCLATURE

Bo	Boiling number
C	Martinelli-Chisholm constant
c_p	specific heat at constant pressure (kJ/kgK)
Co	Convection number
D	diameter (mm)
D_v	modified volumetric diameter (mm)
E	convective enhancement factor
$Eö$	Eotvös number
f	friction factor
Fr	Froude number
g	gravitational acceleration (m/s^2)
G	mass flux (kg/m^2s)
h	heat-transfer coefficient (W/m^2)
h_{fg}	enthalpy of evaporation (kJ/kg)
H	test-piece heights (mm)
k	thermal conductivity (W/mK)
L	test-piece lengths (mm) / Laplace constant (Chapter 2)
L_p	length of vapour and liquid bubble pair (mm)
m	fin parameter
M	mass flow rate (kg/s)
M_W	molecular weight (g/mol)
N_{Conf}	Confinement number
Nu	Nusselt number
Nu_r	average Nusselt number
P	pressure (bar)
P_r	reduced pressure
Pr	Prandtl number
q	heat flux (kW/m^2)
Re	Reynolds number
R_p	surface roughness
S	nucleate boiling suppression factor / pin fins pitch (mm)
T	temperature (K)

U	Velocity (m/s)
v	specific volume (m^3/kg)
W	test-piece widths (mm)
We	Weber number
x	thermodynamic equilibrium quality
X	Martinelli parameter / pitch to diameter ratio
X_o	bubble growth parameter
z	distance from test-piece inlet (mm)

Greek Characters

α	thermal diffusivity / void fraction
β	ratio of channel depth to width
δ	film thickness
ε	error
ϵ	surface roughness
λ	vapour-phase parameters
ψ	liquid-phase parameters
η	fin efficiency
θ	angle
μ	dynamic viscosity
ρ	mass density
σ	surface tension
ϕ_f^2	two-phase multiplier
Δp	pressure drop
ΔT	temperature difference

Subscripts

3	three walls heating
4	four walls heating
A	acceleration
act	actual
b	bulk fluid value
$cell$	cell
ch	channel
cor	correlation
$crit$	critical
cv	convective
D	diagonal
eff	effective value
eq	equivalent
f	fluid value
F	friction
fg	difference of saturated liquid and vapour values
fo	liquid only value
g	gas/vapour value
h	at the heater / hydraulic
in	inlet value
l	liquid value
L	longitudinal
lam	laminar
m	mean value
nb	nucleate boiling
out	outlet value
sat	saturated value
sp	single-phase value
sub	sub-cooled value
T	transverse
tc	at thermocouple location
tot	total value

tp	two-phase value
tt	turbulent liquid - turbulent vapour
tur	turbulent
tv	turbulent liquid - viscous vapour
v	vapour
vt	viscous liquid - turbulent vapour
vv	viscous liquid - viscous vapour
w	wall value

LIST OF PUBLICATIONS BY THE CANDIDATE

1. P.R. Bobbili, **A.H. Raeisi**, P.A. Kew, D.A. McNeil, An experimental investigation of flow boiling in a mini pin fin heat sink, 11th UK National Heat Transfer Conference, UKHTC, London, September 2009.

2. D.A. McNeil, **A.H. Raeisi**, P.A. Kew, P.R. Bobbili, 2010, A comparison of flow boiling heat-transfer in in-line mini pin fin and plane channel flows, Journal of Applied Thermal Engineering, 30, pp. 2412-2425.

3. **A.H. Raeisi**, D.A. McNeil, P.A. Kew, R.S. Hamed, Boiling heat-transfer in mini-pin-fin channel flows, 12th UK National Heat Transfer Conference, UKHTC, Leeds, August 2011.

4. **A.H. Raeisi**, D.A. McNeil, P.A. Kew, A comparison of water and R113 flow boiling heat transfer and pressure drop in an in-line mini-pin-fin channel flow [In-press].

5. D.A. McNeil, **A.H. Raeisi**, P.A. Kew, Flow Boiling Heat Transfer in Micro to Macro Transition Flows [In-press].

CHAPTER 1

INTRODUCTION

1.1. Introduction to Boiling Heat Transfer

Boiling heat transfer is an effective mode of heat transfer that occurs with a change in phase from liquid to vapour. Pool boiling and flow boiling are two basic types of boiling. Pool boiling is boiling on a heating surface submerged in a pool of quiescent liquid. Flow boiling is boiling in a flowing stream of fluid. In flow boiling the heating surface can be the channel wall confining the flow (Tong and Tang, 1997).

Boiling heat transfer plays a key role in several applications in chemical, petrochemical, food, refrigeration and other allied industries. Examples of such applications are in reboilers, heat exchangers and heat exchanger reactors (HEX). Boiling heat transfer is a widely studied area in engineering due to its ability to transfer heat at very low superheat. This process is used in many thermal components and energy systems, as it provides important advantages in comparison with its single phase counterparts; much higher heat transfer coefficients, much smaller coolant flow rates and better temperature uniformity.

In this study, flow boiling heat transfer characteristics and pressure drops in mini-multi-channel geometries with and without interconnecting passages are investigated. It is worth noting that what happens in flow boiling process in mini- and micro-scale flow passages can be quite different from macro-scale flow passages. Many of the controlling phenomena and mechanisms change from macro- to mini- and micro-scale. For example, the role of surface tension (capillary) forces becomes much stronger in small-scale flow passages, while gravitational forces are weakened. Therefore, two-phase flow pattern maps, flow boiling heat transfer methods and two-phase pressure drop models developed for macro-scale flow passages cannot be extrapolated to mini- and micro-scale flow passages, except for specific documented cases (Thome, 2004a).

An overall review of two-phase flow patterns, flow boiling heat transfer characteristics and two-phase pressure drop in mini- and micro-scale flow passages is presented in Chapter 2, Literature Survey. But, as this study has been focused on flow boiling in

horizontal flow passages, a general introduction on flow boiling and two-phase flow patterns in conventional flow passages is presented in this chapter. An introduction to flow boiling phenomena and flow boiling in horizontal conventional tubes is presented in the following sections. Because of some similarities between pin-fin surfaces geometry investigated in this study and tube bundles, boiling on tube bundles is introduced afterwards. Subsequently, to better understanding the flow boiling mechanism, two-phase flow patterns and flow pattern maps in conventional horizontal channels are described. Finally, the present study is introduced and an introduction to flow boiling in mini- and micro-flow passages and their applications is presented.

1.2. Introduction to Flow Boiling

Flow boiling is the boiling of the fluid under forced-flow conditions. It is also referred to as *forced convective boiling*. The process of flow boiling is most commonly used inside vertical and horizontal tubes and channels, in annuli, and on the outside of horizontal tube bundles. Flow boiling heat transfer contains both convective and nucleate boiling heat transfer contributions. The major flow boiling heat transfer regimes are:

- Single-phase convective heat transfer to liquid
- Subcooled nucleate boiling
- Saturated nucleate boiling
- Two-phase forced convection region
- Single-phase convective heat transfer to vapour

The local flow boiling heat transfer coefficient is mainly a function of heat flux, vapour quality, mass velocity, flow channel geometry and orientation, flow patterns and fluid properties (Thome, 2003). A boiling curve similar to pool boiling curve is obtained for flow boiling inside a heated tube or over the tube bundles, as is shown in Figure 1.1. The curve is drawn for a constant total flow rate and a system pressure. The boiling curve is described in details for a flow boiling process in a uniform heated horizontal tube in section 1.2.1.

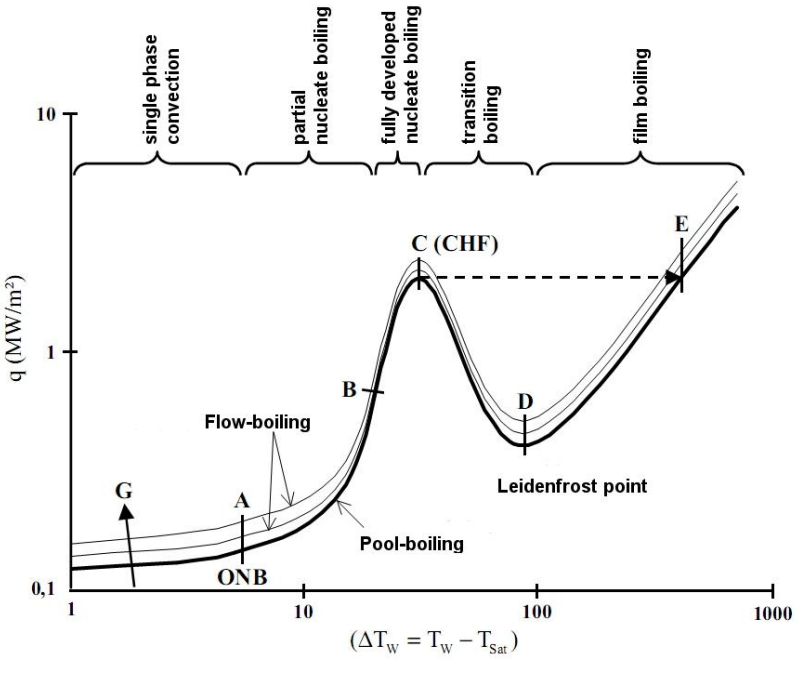

Figure 1.1 Flow and pool Boiling curves for light water, according to Nukiyama's boiling curve (Sattelmayer, 2011)

1.2.1 Flow Boiling in Horizontal Conventional Tubes

Figure 1.2 illustrates schematically forced convective boiling in a horizontal conventional tube, heated by a uniform heat flux. Widely used definitions of two-phase flow patterns are included in the figure. As is shown, the liquid enters the tube in the sub-cooled condition, therefore the first mode of heat transfer is single-phase forced convection. The heat transfer coefficient depends strongly on the mass flux and very weakly on the wall superheat in single-phase forced convection. Thus the heat flux varies linearly with the wall superheat, the difference between the wall temperature and the saturation temperature, as is shown in Figure 1.1. With increasing the wall superheat, sub-cooled flow boiling regime occurs, where the bulk fluid is still in a sub-cooled state and the wall temperature is above the local saturation temperature, until Point A, onset of nucleate boiling (ONB). After nucleate boiling initiation, point A and thereafter, an improvement in heat transfer coefficient occurs as the wall superheat is increased until point C. The region AB is called the partial nucleate boiling region. In this region, both single-phase forced convection and nucleate boiling heat transfer contribute to the total heat transfer rate. Nucleate boiling curves with different mass fluxes overlap each other at point B. The region BC is called the fully developed

nucleate boiling region. In this region bubbles merge and form different flow regimes. Possible flow regimes are bubbly, plug, slug and annular, Figure 1.2. The critical heat flux (CHF) occurs when the thin liquid film in annular flow dries out, point C. The magnitude of the critical heat flux depends on the local vapour quality, mass flux and system pressure. After the occurrence of the critical heat flux, the wall temperature increases rapidly, and transition and film boiling occur thereafter.

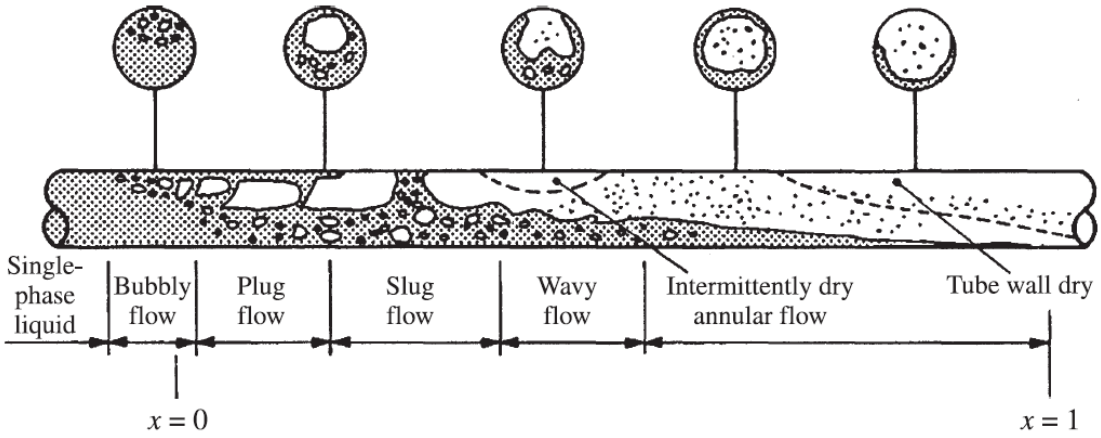

Figure 1.2 Flow boiling process and flow patterns during evaporation in a horizontal conventional-size tube with a uniform heat flux (Collier and Thome, 1994)

Flow patterns for a horizontal conventional heated tube were mentioned briefly in this section, but general flow patterns in horizontal conventional channels (typically $D > 10\,mm$) are described in more details in section 1.3.1. As flow patterns are influenced by the size of the channels, a review of two-phase flow patterns in horizontal mini- and micro-channels is presented in Chapter 2, literature survey.

1.2.2 Flow Boiling on Tube Bundles

Boiling on the shell-side of horizontal tube bundles is another important flow boiling process. George Stephenson (1829) first boiled water on the outside of a tube bundle in his "Rocket" locomotive. Afterwards, boiling on the shell-side of bundles has been a common process in the power and process industries. Majority of boiler and evaporators

produced nowadays are based on shell and tube design such as; Fire-tube boilers, kettle reboilers, full-bundle evaporators, waste heat boilers, Figure 1.3.

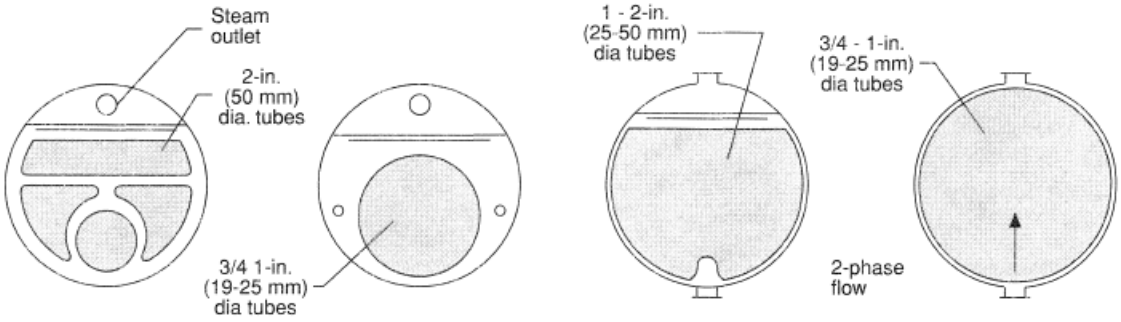

Figure 1.3 Sections through shell and tube boilers; from left, fire-tube boiler, kettle reboiler, full-bundle evaporator, waste heat boiler (Cornwell, 2011)

Figure 1.4 shows a schematic of a simplified tube bundle. Two-phase flow patterns and heat transfer regimes are also included in the figure. Sub-cooled liquid enters the bundle from below and flows upward past the tubes. Single-phase forced convective heat transfer is the first mode of heat transfer as the inlet flow is in sub-cooled state. Once the wall temperature passes the local saturation temperature, T_{sat}, and the bulk fluid is still in a sub-cooled state, sub-cooled boiling occurs and the bubbly flow regime begins.

As the fluid moves upwards, the bulk fluid temperature reaches the local saturation temperature and the saturated nucleate boiling regime begins. In this regime, the speed of bubbles departure from the top of the tubes increases. This leads to form the bubble jets flow pattern. Farther up the bubbles coalesce into larger sizes and form the sliding bubbles, as they move up between the tubes. As the vapour quality increases, the flow becomes chaotic and unstable. This led to form the chugging flow regime. At higher vapour quality at the top of the tube bundle, the liquid becomes entrained in the vapour. This is the spray flow regime. Convection heat transfer through liquid film on the tubes is the heat transfer mode for this regime.

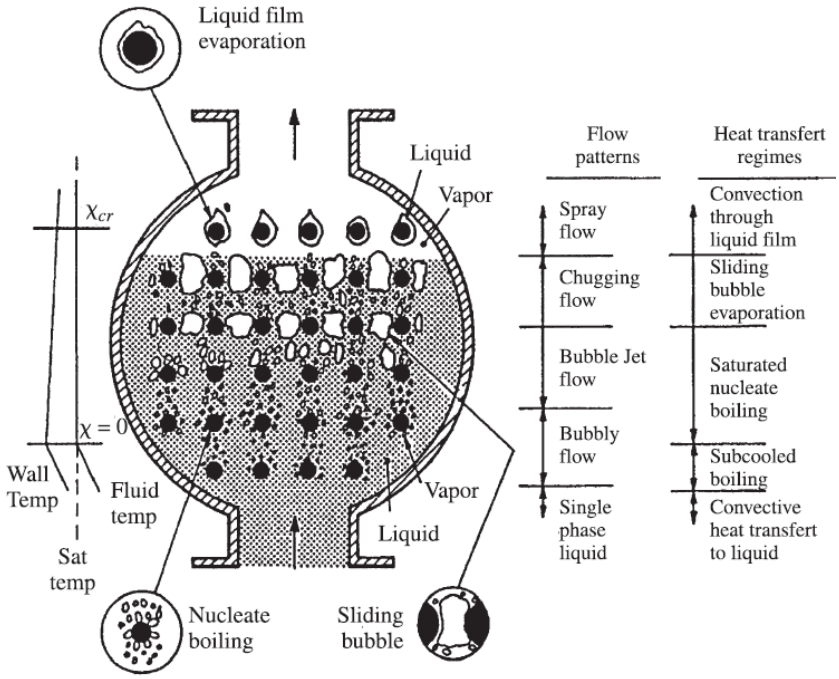

Figure 1.4 Boiling on a horizontal tube bundle (Collier and Thome, 1994)

1.3. Two-Phase Flow Patterns

Two-phase flow patterns are the variety of the liquid and the generated vapour configurations during fluid evaporation. Since a specific flow pattern depends on the conditions of flow, heat flux, pressure and the geometry of the flow passages, there are several regimes and flow patterns in pool and flow boiling processes. Because of the difference in dominant conditions, flow patterns are also different from pool boiling to flow boiling. For example, the buoyancy effect is significant in a pool boiling system while the flow forced convection effect is significant in flow boiling inside a channel (Collier and Thome, 1994).

Pool boiling consists of several regimes such as natural convection, nucleate boiling, partial film boiling and stable film boiling. Nucleate boiling is characterized by a very high heat transfer rate for only a small temperature difference and consists of two sub regimes; local boiling which is nucleate boiling in a sub-cooled liquid and bulk boiling which is nucleate boiling in a saturated liquid. At high population of the bubbles, vapour forms an insulating blanket covering the heating surface and raises the surface temperature. The critical heat flux occurs in this condition and immediately after that boiling becomes unstable and the mechanism is called partial film boiling or transition

boiling. After that a stable vapour film is formed on the heating surface and the heat transfer rate reaches a minimum, this is called stable film boiling. In this regime by increasing the wall temperature, heat transfer rate also is increased by thermal radiation (Tong and Tang, 1997).

The pool boiling regimes which were mentioned above, also exist in the flow boiling process. Flow patterns in flow boiling process are influenced by the effect of surface tension and gravity for horizontal flows, which acts to stratify the liquid to the bottom and the vapour to the top of the channel. Flow boiling flow patterns are also different from large diameter tubes to smaller diameter tubes and channels. The role of surface tension becomes more important in smaller diameter channels and affects the flow patterns in flow boiling process in narrow channels. Bubble formation, coalescence, and local dry out conditions are also influenced by the size of the channels. Therefore, because of the more complicated mechanisms in flow boiling process in smaller channels, various research groups use different categories or names to describe the same thing, or use additional subcategories that other do not (Thome, 2004a). A summary of flow patterns studies in channels with small hydraulic diameters and in small-scale complex geometries such as pin-fin surfaces are presented in Chapter 2, Literature Survey.

Collier and Thome (1994) in a general categorization listed flow patterns which are clearly distinguishable and generally recognized in both conventional horizontal and vertical channels. Several major flow regimes in both types of channels are often separated from each other by regime transition regions in flow regime maps. Since this study has focused on the flow boiling process in horizontal flow passages, the following sections present general two-phase flow patterns and flow pattern map for horizontal flows.

1.3.1. Two-Phase Flow Patterns in Horizontal Channels

Flow patterns in horizontal two-phase flows are complicated by asymmetry of the phases. This complication results from the influence of gravity. Horizontal two-phase flows have been observed to represent at least six major two-phase flow patterns. The transition from one pattern to the next is mainly dependent on the hydrodynamic parameters of the channel flow as well as heat transfer patterns. The commonly

identifiable flow patterns in a horizontal channel are as follows; Bubbly flow, Plug flow, Stratified flow, Wavy flow, Slug flow and annular flow. Figure 1.5 shows the morphological shapes of these general flow patterns in a horizontal conventional circular channel, given by Alves (1954).

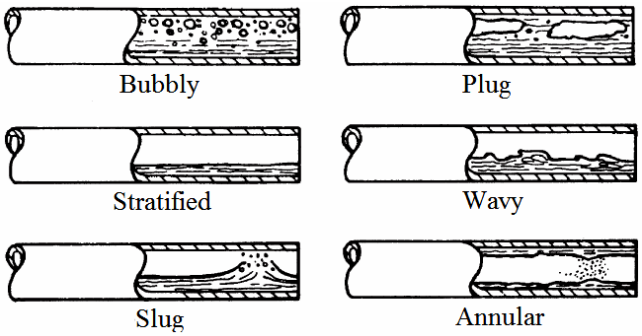

Figure 1.5 Flow patterns in horizontal flow (Alvez, 1954)

1.3.2. Two-Phase Flow Pattern Map for Horizontal Channels

Flow pattern maps are used to predict the transition from one type of two-phase flow pattern to another and hence to identify a particular pattern for a given set of local flow parameters (Thome, 2003). Baker (1954) developed the first two-phase flow pattern map for the petrochemical industry for flow of oil and gas in horizontal large diameter pipes. Afterwards, Taitel and Dukler (1976) developed one of the most widely used two-phase flow pattern maps for horizontal flows. Researchers widely studied flow patterns for gas-liquid flows in conventional channels and channels with smaller hydraulic diameters. A comprehensive review of flow patterns in rectangular channels has been reported by Hosler (1967). Fukano et al. (1989) presented a summary of two-phase flow patterns studies in horizontal flows.

In the past three decades, a number of flow pattern maps have been developed for horizontal small diameter pipes and narrow rectangular channels. For example, Wambsganss et al. (1991) investigated two-phase flow patterns and transitions in a small, horizontal rectangular channel and developed a flow pattern map. They reported that, the existing flow pattern maps for circular tubes and large rectangular channels are not commonly applicable to the small rectangular channels. The map of Baker (1954)

which is known as a reliable flow pattern map for horizontal flows is presented here. Figure 1.6 shows the Baker flow pattern map.

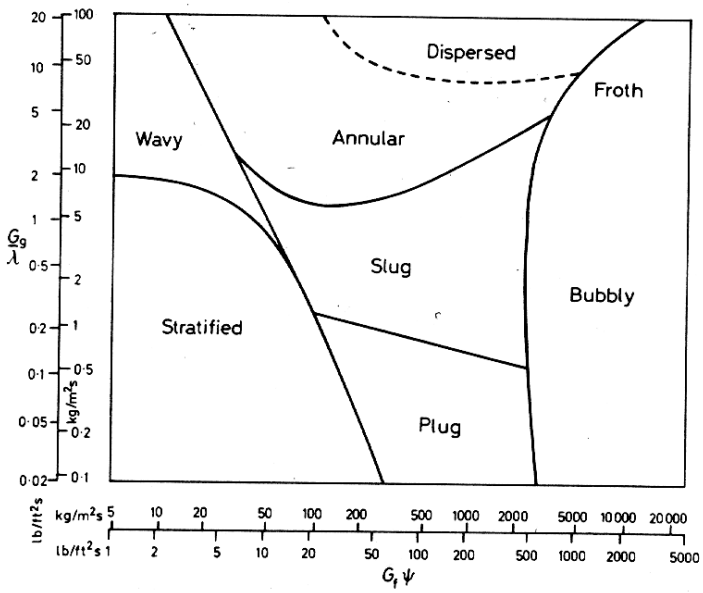

Figure 1.6 Flow pattern map for horizontal flow (Baker, 1954)

G_f, G_g, ψ, and λ in Figure 1.6 are the liquid and vapour mass fluxes, and liquid and vapour-phase parameters, respectively. Liquid and vapour-phase parameters evaluated from

$$\psi = \left(\frac{\sigma_{water}}{\sigma}\right)\left[\left(\frac{\mu_f}{\mu_{water}}\right)\left(\frac{\rho_{water}}{\rho_f}\right)^2\right]^{1/3} \tag{1.1}$$

$$\lambda = \left(\frac{\rho_g}{\rho_{air}}\frac{\rho_f}{\rho_{water}}\right)^{1/2} \tag{1.2}$$

where ρ_f, ρ_g, μ_f, and σ are the liquid density, vapour density, fluid viscosity and liquid surface tension. Air and water reference values obtained at 20℃.

1.4. Present Study

Recent advances in electronic technology and mini- and micro-fabrication techniques have led to an increasing intensity in heat generation in compact electronic equipments. The heat flux from such components can be significantly in excess of the capabilities of

conventional-size heat sinks. Most conventional-size electronic equipments heat sinks use air-cooling, but with the invention of compact electronic components with high heat fluxes it has been recognised that significant amount of the heat can be removed by direct or indirect liquid-cooling. As it was shown in Figure 1.1, the single-phase convection region, from the origin to A, offers the lowest heat flux or cooling capability for a given wall superheat. A new method that can be applied is to use flow boiling in mini- and micro-heat sinks to dissipate high heat fluxes from these compact electronic equipments. This would transfer significantly more heat than its single-phase equivalent. Technical advantages of these heat sinks in comparison with the macro-scale evaporators include smaller dimensions, smaller coolant flow rate, better temperature uniformity and lower thermal resistance.

Flow boiling in mini- and micro-flow passages can be used for cooling many high power density devices such as compact heat exchangers, Micro Electro Mechanical Systems (MEMS), microprocessors, laser diode arrays, automotive and stationary fuel cells, micro-chemical reactors, radar and aerospace avionics components and Light Emitting Diodes (LEDs). This has led to an abundance of research into flow boiling in small-scale flow passages.

Many researchers have spent a great deal of effort understanding flow boiling heat transfer phenomena and the development of reliable modelling procedures for mini and micro-flow passages. There are a number of fundamental issues for mini- and micro-scale flow passages. The methods derived for macro-scale evaporators are no longer appropriate for mini- and micro-scale components. Research has concentrated on macro- and micro-scale features; less has been reported for passages with hydraulic diameter of the order of 1 millimetre. This study was initiated to fill this gap. Therefore a fundamental experimental and numerical study was undertaken to investigate the measurement and prediction of averaged local flow boiling heat transfer coefficients and pressure drops in mini-multi-channel geometries with and without interconnecting passages.

CHAPTER 2

LITERATURE SURVEY

2.1 Introduction

Research in convective boiling and two-phase flows has been significantly stimulated since the Second World War (1939-1945) by the advent of the nuclear and rocket technologies. A wide range of investigations was carried out thereafter because of the high significance of this field. Gouse (1964) showed a significant rise in the number of published papers and reports on boiling and two-phase flow. The graph indicated an exponential rise in the number of publications available with time.

With the emergence of compact heat exchangers, many researchers have spent a great deal of effort aimed at understanding flow boiling and two-phase flow characteristics in these compact heat exchangers which containing mini- and micro-scale flow passages. This was mainly due to the compact heat exchangers multi-stream capabilities, high thermal efficiencies, small size, low weight, design flexibility and energy savings. The compact heat exchangers also have wide applications in transportation industries, chemical process industries and highly efficient heating or cooling processes, where they are used as evaporators and condensers for refrigeration and air conditioning. Reviews on flow boiling and two-phase flow in small-scale flow passages reported by many researchers including Thome (2004a), Cheng (2006), and Kandlikar (2010), show a growing number of studies on flow boiling and two-phase flow in mini- and micro-channels.

Two-phase flow transport and flow boiling is a fundamental phenomena including flow boiling heat transfer, pressure drop and flow patterns in mini- and micro-scale flow passages are quite different from that in macro-scale flow passages. The methods derived for macro-scale evaporators are no longer appropriate for mini- and micro-scale components. This resulted from changing in controlling phenomena and mechanisms from macro- to mini- and micro-scale. Therefore in the following section, transition from macro to mini- and micro-scale flow passages is presented and various definitions of mini- and micro-channels are described. Subsequently the literature survey that is

available and essential with regards to two-phase flow and flow boiling in mini- and micro-scale flow passages is presented. The literature survey is subdivided into the following main sections:

- ❖ Flow boiling and two-phase flows in single tubes and multiple parallel channels
- ❖ Flow boiling and two-phase flows in complex geometries

2.2 Macro- to Mini- and Micro-Scale Transition in Flow Boiling

Transition from macro- to mini- and micro-scale channels in flow boiling and two-phase flows can be quite different from single-phase flows. Although decreasing the channels size cause significant effects on friction factors and heat transfer coefficients in small channels in single-phase flows, studies and experiments with very smooth internal channels have shown that macro-scale methods for single-phase flows can still be considered to channels with minimum hydraulic diameters of $5-10\,\mu m$ (Thome, 2004b). Therefore, for single-phase flows, channels with hydraulic diameters larger than this size can still be considered as macro-channels.

The distinction between macro-scale and mini- and micro-scale channels for flow boiling and two-phase flows is quite different from single-phase flows. Unfortunately, for flow boiling and two-phase flows a recognized categorisation criterion from macro-scale to mini- and micro-scale is not clearly established yet in the literature. Instead, there are various definitions on this issue. Many researchers classified macro- and micro-scale channels based on the hydraulic diameter. In some cases, some researchers proposed a meso-scale range between macro- and micro-scale (Thome, 2004a).

For the first time, Shah (1986) distinct macro-scale channels from small-scale channels by defining a heat exchanger containing channels with hydraulic diameter of $6\,mm$ (surface area density ratio of $700\,m^2/m^3$) as a compact heat exchanger. Brauner and Moalem-Maron (1992) defined the Eotvös number, Eö, criterion for the dominance of surface tension for small diameter channels, as

$$E\ddot{o} = \frac{g(\rho_f - \rho_g)D_h^2}{\sigma} < 1.0 \qquad (2.1)$$

where g is the acceleration due to gravity, σ is the surface tension, D_h is the hydraulic diameter, and ρ_f and ρ_g are the liquid and vapour densities, respectively. Eotvös number is also known as the Bond number. The parallel channel and pin-fin surfaces which were examined in present study, contained flow passages with hydraulic diameter of the order of $1\,mm$. The tests were carried out with R113 and deionised water as working fluids at atmospheric pressure. The Bond number value for the present study geometries was equal to 1 and 0.15 for R113 and water test series respectively. Therefore for the tests with R113, tests were carried out at the transition boundary from macro- to micro-scale based on Bond number.

For a two-phase mixture flowing in a channel with a hydraulic diameter of D_h, Cornwell and Kew (1993) defined the Confinement number, N_{Conf}, which is based on the definition of Laplace constant, i.e.

$$N_{Conf} = \left[\frac{\sigma}{\mathrm{g}(\rho_f - \rho_g)D_h^2}\right]^{1/2} \tag{2.2}$$

They showed that when $N_{Conf} > 0.5$, micro-scale methods could be applied, otherwise macro-scale methods had to be used. Triplett et al. (1999a) defined small channels as channels with hydraulic diameter of the order, or smaller than Laplace constant (capillary length) , L, as follows:

$$L = \left[\frac{\sigma}{\mathrm{g}(\rho_f - \rho_g)}\right]^{1/2} \tag{2.3}$$

Capillary length is a characteristic length scale for fluid subject to a body force from gravity and a surface force due to surface tension. For the present study the capillary length was obtained as $1\,mm$ and $2.5\,mm$ for tests with R113 and deionised water respectively.

Serizawa et al. (2002) classified micro-channels based on the proposed criterion by Suo and Griffith (1964) as follows:

$$\frac{L}{D} \geq 3.3 \tag{2.4}$$

where L is the Laplace constant (capillary length) defined by Equation (2.3), and D is the channel diameter. Other researchers have claimed that three length scales are

needed, macro, mini and micro. Mehendale et al. (2000) classified the channels through the hydraulic diameter. Micro-channels occurred in the range $1-100\,\mu m$, mini-channels in the range $100\,\mu m-1\,mm$, macro-channels in the range $1-6\,mm$ and conventional channels at values greater than $6\,mm$.

Kandlikar (2001) took a similar approach, classifying micro-channels in the range $50-600\,\mu m$, mini-channels in the range $600\,\mu m-3\,mm$ and macro-channels at values greater than $3\,mm$. Kandlikar (2002) in another study recommended the following classification and size ranges: micro-channels ($10-200\,\mu m$), mini-channels ($200\,\mu m-3\,mm$) and conventional channels at values greater than $3\,mm$.

The macro- mini- and micro-scale channels classifications based on the hydraulic diameter are summarized in table 2.1.

Table 2.1 Macro-, mini-, and micro-scale classification based on the hydraulic diameter

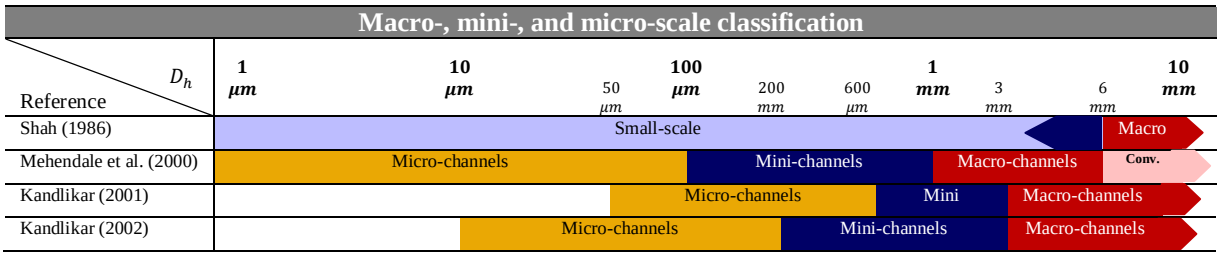

It seems that there is no unified definition of transition criterion from macro- to mini- and micro-scale channels until now. Therefore, researchers use different criteria of mini- and micro-channels. For example, some researchers such as Wolk et al. (2000) considered a hydraulic diameter of $6\,mm$ while, some other researchers such as Wongwises et al. (2000) took a hydraulic diameter of $7.5\,mm$ as the criterion of transition from conventional channels to mini-channels. Although a number of classifications are based on the hydraulic diameter, in fact these classifications cannot relate the two-phase flow mechanisms and controlling forces to the channel diameter. The change from methods valid at the macro-scale to those valid at the micro-scale results from a change in the controlling forces, for example, gravity forces becoming less important than surface tension forces. It thus seems unlikely that hydraulic diameter ranges will prove to be universal. An approach similar to that taken by Kew and Cornwell (1997) seems more likely to lead to a universal classification. Kew et al.

(2006) have shown that the Confinement number is also applicable to more complex geometries.

2.3 Flow Boiling and Two-Phase Flows in Single Tubes and Multiple Parallel Channels

Before beginning, it is worth noting that while circular tubes are the norm of macro-scale evaporators, non-circular channels are more common in mini- and micro-scale evaporators and compact heat exchangers. A pioneering study in single-phase micro-channel heat sinks was undertaken by Tuckerman and Pease (1981). Afterwards micro-channel heat sinks have received considerable attention by researchers. Single-phase flows in micro-channel heat sinks have been widely studied (Celata et al., 2004; Kandlikar and Grande, 2004; Li et al., 2004; Lee and Garimella, 2005).

With rapid development of mini- and micro-scale electronic devices used in several engineering applications and industries including lasers, supercomputers, automotive, aerospace, air-separation and cryogenic industries, the use of high heat flux compact heat exchangers and cooling systems to remove high heat fluxes from these small devices became quite necessary. Therefore, researches have shifted to two-phase mini- and micro-heat sinks, as this would transfer significantly more heat than its single-phase equivalent. Among a wide range of researches in flow boiling heat transfer in mini- and micro-scale structures in the past three decades, flow boiling in single and parallel mini- and micro-channels has been studied quite extensively. A review of some of the most related and most important investigations on flow patterns, heat transfer and pressure drop in single tubes and channels and multiple parallel small, mini- and micro-channels is presented in the following sections.

2.3.1 Flow Patterns

Two-phase flow patterns in quite small-scale channels have been studied since 1950s. A primarily study was undertaken by Richardson (1958). He investigated the behaviour of air/water mixtures in horizontal rectangular channels. The experiments were performed for three different channels with cross sections of 6.35×50.8, 12.7×50.8 and

$25.4 \times 50.8\, mm^2$, and hydraulic diameters, D_h, of 11.3, 20.3 and $33.9\, mm$, respectively. He presented a flow pattern map for each of the three channels tested. In general, bubbly, plug and slug flow regimes were observed. He stated that because of the small heights of the channels, liquid reaches the top surface of the channels and minimized the occurrence of stratified and wavy flows.

Hosler (1968) investigated the two-phase flow patterns in a vertical rectangular channel, with a cross section of $25.4 \times 3.14\, mm^2$ and a hydraulic diameter, D_h, of $5.68\, mm$, at high pressure of $2 - 14\, MPa$. He identified three flow regimes: bubbly flow, slug flow and annular flow. He concluded that "*flow patterns observed in boiling flow appear similar to flow patterns observed in adiabatic flow*". He stated that by increasing the pressure, the bubble size decreases and the transition from each regime to another one occur at higher local qualities.

Barnea et al. (1983) studied flow pattern transition of air-water mixture in 5 circular tubes in both vertical and horizontal directions. Two of tested tubes had inner diameters of 4 and $6\, mm$. They developed a flow pattern map for small parameter tubes by using the superficial velocities of air and water. For the $4\, mm$ diameter tube, dispersed bubble, intermittent and annular flow regimes were observed.

Wambsganss et al. (1991) studied two-phase flow patterns and transitions of air/water mixtures in a small, horizontal, rectangular channel, with a cross section of $19.05 \times 3.18\, mm$ ($D_h = 5.45\, mm$) and in two aspect ratios of 6 and $1/6$. Adiabatic flow patterns were investigated over a large mass flux range of $50 - 2000\, kg/m^2 s$. For aspect ratio of $1/6$, bubbly, plug, slug and annular flow regimes were observed while for aspect ratio of 6 in addition to these observations, stratified and wavy flows were observed as well. The authors developed flow pattern maps and compared with existing flow pattern maps of circular pipes, capillary tubes and generalized rectangular two-phase flow pattern maps of Troniewski and Ulbrich (1984), which were based on larger rectangular channels. They concluded that "*while qualitative agreement existed, these maps are not generally applicable to the subject small rectangular channel on the quantitative basis*".

In a smaller size, Damianides and Westwater (1988) studied two-phase flow patterns of air-water mixture in a horizontal rectangular channel with hydraulic diameter of

1.74 mm and 5 circular tubes with inner diameter of 1 to 5 mm. They observed bubble, plug, slug, wavy, and annular flow regimes.

Cornwell and Kew (1993) investigated flow boiling of R-113 in small rectangular parallel channels. Two different test pieces were examined. Test pieces were composed of 75 and 36 parallel channels with cross sections of $1.2 \times 0.9\ mm^2$ ($D_h = 1.03\ mm$) and $3.25 \times 1.1\ mm^2$ ($D_h = 1.64\ mm$), respectively. The mass fluxes used were within the range $117 - 627\ kg/m^2s$ and the heat fluxes within the range $3 - 20\ kW/m^2$. Three flow patterns were observed; isolated bubbles, confined bubbles and annular-slug flows. The isolated bubbles sizes were small in compare with the channel size. This regime was found in a very low quality region. In the confined bubbles regime, the bubbles were as large as the channels size and were restricted by the channel walls. In this case authors proposed the Confinement number as presented by Equation (2.2). The annular-slug flow pattern was observed at the quality more than 0.2. In their subsequent studies the authors, Cornwell and Kew (1995) and Kew and Cornwell (1997), confirmed these flow regime visualizations. Their confined bubbles flow regime is equivalent to the elongated bubble or slug flow regime, used by others.

Wilmarth and Ishii (1994) investigated the characterization of two-phase flow regimes of air-water mixture in narrow rectangular vertical and horizontal channels. Two test pieces were examined with channels heights of 1 and 2 mm and widths of 20 and 15 mm, respectively ($D_h = 1.9$ and 3.53 mm, respectively). For horizontal flows, they observed five flow regimes as; stratified smooth flow, plug flow, slug flow, dispersed bubbly flow and wavy annular flow.

Tran et al. (1996) studied flow boiling heat transfer and flow patterns of liquid R-12 in a small circular channel ($D = 2.46\ mm$) and a small rectangular channel ($D_h = 2.40\ mm$). They reported that, for mini- and micro-channels, the transition from slug to annular flow happened at much higher vapour qualities ($x \approx 0.6 - 0.7$) in compare with macro-channels ($x \approx 0.25 - 0.35$).

Kasza et al. (1997) studied micro-scale flow visualization of nucleate boiling of water in a small rectangular channel with a cross section of $2.5 \times 6\ mm^2$ ($D_h = 3.53\ mm$). They observed bubbly, slug and annular flow regimes. They reported an interesting observation on individual bubbles and their coalescence with vapour slugs and other bubbles. The bubbles growing in the thin film surrounding vapour slugs, with a

0.67 mm average thickness, did not easily coalesce with the vapour in the slug regime. They reported the occurrence of nucleate boiling in thin liquid films in both slug and annular flow regimes.

Lin et al. (1998) investigated flow regimes of air-water mixture in a small circular tube with internal diameter of 2.1 mm. They observed three distinct flow regimes; slug, wavy and annular flow regimes. The observed flow regimes were compared with predicted flow regimes from the previous studies by Barnea et al. (1983), Damianides and Westwater (1988), Wambsganss et al. (1991) and Mishima and Hibiki (1996). The comparisons showed that no general flow map was available for large range of hydraulic diameters and flow rate of small tubes and channels.

Kuwahara et al. (2000) investigated flow boiling of R-134a in a 1.2 mm horizontal capillary tube. The mass fluxes used were within the range $80 - 1260\ kg/m^2s$ and the vapour qualities within $0.008 - 0.975$. Five flow regimes were observed; bubbly flow, plug flow, slug flow, wavy-annular flow, and annular flow. Their observation was in a quite poor agreement with macro-scale flow pattern maps of Baker (1954) and Taitel and Dukler (1976).

Feng and Serizawa (2000) observed flow regimes of air-water mixture in a 50 μm diameter tube. They categorized their observations as follows: bubble flow, elongated bubble (slug) flow, annular flow, liquid ring flow, liquid lump flow and mist flow. Liquid ring flow is quite likely to be some type of intermediate transition regime. Liquid ring flow and liquid lump flow are called slug-annular flow transitions by some other researchers such as Triplett et al. (1999a).

Yang and Shieh (2001) studied flow boiling of R-134a in small circular horizontal tubes with hydraulic diameter of $1,2$ and 3 mm. They compared their flow regimes observations with adiabatic air-water mixture and categorized their observations as follows: bubbly flow, plug flow, wavy flow, slug flow, annular flow and dispersed flow. They also developed a flow pattern map based on liquid velocity versus gas velocity.

Steinke and Kandlikar (2003) and Kandlikar and Steinke (2004) investigated two-phase flow patterns of water in six parallel trapezoidal micro-channels with hydraulic diameter of 0.207 mm (0.214 mm wide by 0.200 mm deep) and length of 57.15 mm. Tests were performed over a mass flux range of $157 - 1782\ kg/m^2s$ and heat flux

range of $55 - 898\ kW/m^2$. They observed bubbly flow, slug flow (constrained bubble), annular flow, annular flow with nucleation in the thin film, churn flow, and dry out. They stated that, the conventional and mini-channels flow boiling regimes also occur in micro-channels. All observed flow-boiling regimes agreed with those found by Kew and Cornwell (1997) and many other researchers. The bubble flow or isolated bubble flow was very intermittent. The most commonly observed flow-boiling regime was annular-slug flow. The slug flow regime was the second most common observed flow regime.

Revellin and Thome (2007) studied flow patterns of two refrigerants, R-134a and R-245fa, in two small tubes with diameters of 0.509 and $0.790\ mm$ and varied length of 20 to $70\ mm$. The mass fluxes were within $200 - 2000\ \mathrm{kg/m^2s}$ and heat fluxes up to $597\ \mathrm{kW/m^2}$.They developed a new type of diabatic flow pattern map for evaporating flows in micro-channels. They classified their flow regimes observations into three flow regimes: the isolated bubble regime includes both bubbly and slug flows, the coalescing bubble regime, and the annular regime.

Felcar et al. (2007) studied flow patterns in a tube with hydraulic diameter of $2.32\ mm$. They modified the Taitel and Dukler (1976) method in the transition from intermittent to annular flow regime. They presented their flow patterns classifications as follows: dispersed flow, annular flow, intermittent flow, and smoothly and wavy stratified flow. In their classifications, churn, slug, elongated bubbles, plug and pseudo-slug flows were characterized as intermittent flows, annular and slug-annular were considered as annular flows. Figure 2.1 illustrates their flow pattern visualizations and nomenclature.

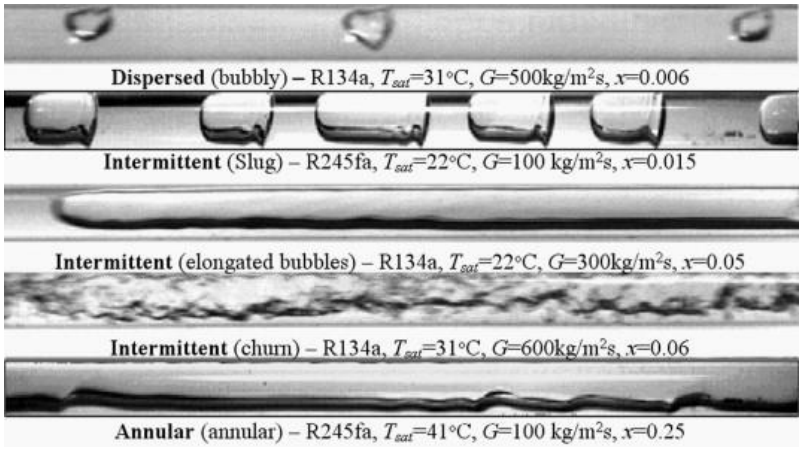

Figure 2.1 Flow pattern visualizations and their nomenclature (Felcar et al., 2007)

Ong and Thome (2009) studied flow boiling heat transfer and two-phase flow patterns of three refrigerants, R-134a, R-236fa and R-245fa in a $1.03\ mm$ channel. Tests were performed for mass fluxes from 200 to $1600\ kg/m^2s$ and heat fluxes from $2.3\ kW/m^2$ to $250\ kW/m^2$. They observed three flow regimes; isolated bubble regime, coalescing bubble regime, and annular regime for all three fluids.

Arcanjo et al. (2010) studied quasi-diabatic two-phase flow patterns of R-134a and R-245fa in a stainless steel tube with diameter of $2.32\ mm$. The mass fluxes used were within the range $50 - 600\ kg/m^2s$. A transparent tube just downstream the heated section was used for flow patterns observations. Four flow patterns were observed: bubbly, elongated bubbles, churn, and annular flows. They compared the observed flow patterns with previous researches predictions provided by Barnea et al. (1983), Felcar et al. (2007), Revellin and Thome (2007) and Ong and Thome (2009). They presented that, methods suggested by Felcar et al. (2007) and Ong and Thome (2009) predicted quite reasonably the present observed flow patterns.

Wang et al. (2011) studied flow boiling visualization of FC-72 and ethanol in three high-aspect ratio micro-channels with hydraulic diameters of $571\ \mu m$, $762\ \mu m$, and $1454\ \mu m$. Tests were performed for mass fluxes of 11.2, 22.4, and $44.8\ kg/m^2s$, a wide range of heat fluxes and constant inlet temperature of 25 ℃. FC-72 and ethanol showed similar vapour dynamics and flow boiling behaviour. Bubble nucleation, confined bubbly flow, slug-annular flow, annular flow and wispy-annular flow with evaporating film regimes were observed. Besides, periodic recoiling and re-wetting were observed for both FC-72 and ethanol.

As was mentioned above, various flow pattern observations and flow pattern maps were reported and still are reported in literature. It was concluded that flow pattern maps for macro-channels are not generally applicable to mini- and micro-channels. The hydraulic diameter of the channel significantly affects the two-phase flow pattern. This is a result of the dominant controlling force changing from gravity to surface tension. Some flow patterns observed in macro-channels, such as stratified and wavy flow did not occur in some of the mini- and micro-channels studied. Although several studies have been reported but there is still a great deal of research required to develop a general and reliable flow pattern map for mini- and micro-channels.

2.3.2 Heat Transfer Characteristics

A preliminary study in small-scale channels was undertaken by Lazarek and Black (1982). They measured the local flow boiling heat transfer coefficient and critical heat flux for saturated flow boiling of liquid R-113 in a small vertical circular tube. The tube had an internal diameter of $3.15\,mm$ and heated lengths of 123 and $246\,mm$. They presented the local flow boiling heat transfer coefficients as a function of heat flux as follows.

$$h_{tp} = \left(30 Re_{fo}^{0.857} Bo^{0.714} \frac{k_f}{D_h}\right) \tag{2.5}$$

where liquid only Reynolds number, Re_{fo}, and Boiling number, Bo, evaluated from

$$Re_{fo} = \frac{GD_h}{\mu_f} \tag{2.6}$$

$$Bo = \frac{q''}{Gh_{fg}} \tag{2.7}$$

where G, μ_f, and h_{fg} are mass flux, dynamic viscosity of liquid and enthalpy of evaporation, respectively. They also developed a critical heat flux correlation to predict the vapour quality at dry out conditions.

Kandlikar (1983) developed a correlation to predict the saturated flow boiling heat transfer coefficients in horizontal and vertical tubes. He refined this preliminary correlation in another study (Kandlikar, 1990) from 24 experimental investigations with 10 fluids. Finally, he proposed a general correlation for saturated flow boiling heat transfer inside horizontal and vertical tubes with water, R-11, R13-B1, R-22, R-113, R-114, R-152a, nitrogen, and neon as the working fluids, which best predicted the boiling heat transfer coefficients for the Reynolds number ranges of $Re_f \geq 200$. The Kandlikar correlation, developed for the saturated flow boiling inside vertical and horizontal tubes is given by

$$h_{tp} = h_f\left[C_1 Co^{C_2} (25 Fr_{fo})^{C_5} + C_3 Bo^{C_4} F_{fl}\right] \tag{2.8}$$

where the single-phase liquid-only heat transfer coefficient, h_f, is given by

$$h_f = 0.023 Re_f^{0.8} Pr_f^{0.4} \left(\frac{k_f}{D}\right) \tag{2.9}$$

and Convection number, Co, and liquid only Froude number, Fr_{fo}, are given by

$$Co = \left(\frac{1-x}{x}\right)^{0.8} \left(\frac{\rho_g}{\rho_f}\right)^{0.5} \tag{2.10}$$

$$Fr_{fo} = \frac{G^2}{\rho_f^2 g D} \tag{2.11}$$

F_{fl} in Equation (2.8) is the fluid dependent parameter, which is varied from 1.0 to 4.7 for these 10 working fluids. For water and R-113, F_{fl} is 1.0 and 1.3, respectively. Constants in Equation (2.8) are given in Table 2.2. Prandtle number, Pr_f, in Equation (2.9) is evaluated from

$$Pr_f = \frac{\mu_f C_p}{k_f} \tag{2.12}$$

ρ_f, ρ_g and x in Equations (2.10) and (2.11) are liquid density, vapor density, and thermodynamic equilibrium quality, respectively.

Table 2.2 Constants in the proposed correlation, Equation (2.8)

Constant	Convective region	Nuclear region
C_1	1.136	0.6683
C_2	-0.9	-0.2
C_3	667.2	1058
C_4	0.7	0.7
C_5	0.3	0.3

Cornwell and Kew (1993) and Kew and Cornwell (1995) carried out a series of tests in order to investigate the two-phase flow patterns and heat transfer coefficients dependency in small rectangular vertical channels. Two different test pieces composed of 75 and 36 parallel channels with cross sections of $1.2 \times 0.9\ mm^2$ ($D_h = 1.03\ mm$) and $3.25 \times 1.1\ mm^2$ ($D_h = 1.64\ mm$) respectively, were examined. The mass fluxes

used were within the range $117 - 627\ kg/m^2s$ and the heat fluxes within the range $3 - 20\ kW/m^2$. Three flow patterns were observed; isolated bubbles, confined bubbles and annular-slug flows. They observed a strong link between the flow pattern and the heat transfer coefficient. They proposed the heat transfer coefficient correlations for each region as follows:

Isolated bubbles region: $h_{tp} = C_1 Re_{fo}^{0.8} Bo^{0.7} \frac{k_f}{D_h}$ (2.13a)

Confined bubbles region: $h_{tp} = C_2 Re_{fo}^{0.8} Bo^{0.3} N_{Conf}^{0.5} Pr_f^{0.4} \frac{k_f}{D_h}$ (2.13b)

Annular-slug flow region: $h_{tp} = C_3 ENu_{fo} \frac{k_f}{D_h}$ (2.13c)

where C_1, C_2 and C_3 are the experimental constants, and E is the enhancement factor. As is shown, they stated that, heat transfer coefficient is a function of heat flux ($h_{tp} \propto q"^{0.7}$) in the isolated bubbles regime, indicating the dominance of nucleate boiling. By transition from isolated bubble region to confined bubble region as the bubbles occupy the channel cross section, dependency of heat transfer coefficient on heat flux decreases, as in the annular-slug region convective boiling is dominant.

Tran et al. (1993) studied flow boiling heat transfer of R-12 in a small horizontal rectangular channel with cross-section of $4.06 \times 1.7\ mm^2$ ($D_h = 2\ mm$) and overall length of $0.9\ m$. Tests were performed over a quality range of 0.15 to 0.8, mass fluxes in the range of $50 - 400\ kg/m^2s$ and heat fluxes in the range of $4 - 34\ kW/m^2$. They stated that, nucleation mechanism is dominant in flow boiling in channels with small cross- sectional area. They reported that, the heat transfer coefficients obtained over the tested large range of heat and mass fluxes, were strongly a function of heat flux and weakly dependent on mass flux.

Tran et al. (1996) studied flow boiling heat transfer characteristics and two-phase flow patterns of liquid R-12 in a small circular channel ($D_h = 2.46\ mm$) and a small rectangular channel ($D_h = 2.40\ mm$). The mass fluxes used were within the range $44 - 832\ kg/m^2s$, heat fluxes within the range $3.6 - 19\ kW/m^2$ and the vapour qualities up to 0.94. Local heat transfer coefficients were obtained as a function of quality along the channels. Similar to previous studies by Tran et al. (1993) in a small rectangular channel with R-12 and Lazarek and Black (1982) and Wambsganss et al.

(1993) in a small circular channel with R-113, nucleate boiling heat transfer mechanism was found to be dominant over the full range of qualities, while in conventional channels the convective heat transfer mechanism is dominant at qualities typically above 0.2. A comparison was made between the circular and rectangular channel data with quite the same hydraulic diameter and same working fluid. They stated that heat transfer coefficients were different in very small amounts, which according to the experimental uncertainty is negligible.

Kew and Cornwell (1997) investigated flow boiling of R-141b flowing through four circular tubes $500\,mm$ long with diameters of 1.39, 2.05, 2.87 and $3.69\,mm$ and a square section channel with the same length and hydraulic diameter of $2.10\,mm$. Tests were performed for mass fluxes within the range $188 - 1480\,kg/m^2s$ and heat fluxes within the range $9.7 - 90\,kW/m^2$. The experimental flow boiling heat transfer coefficients were compared with existing correlations of Lazarek and Black (1982), Liu and Winterton (1988) and Tran et al. (1995) and nucleate pool boiling correlation of Cooper (1984). They reported that, existing flow boiling heat transfer correlations do not perform well when applied to the small-scale channels having a confinement number of the order of 0.5 and above. The nucleate pool boiling correlation of Cooper (1984) best predicted the experimental data.

Peng and his co-workers (1993, 1994 and 1996) carried out a series of experimental investigations on flow boiling through rectangular micro-channels, with cross section sizes range from $0.1 \times 0.3\,mm^2$ to $0.6 \times 0.7\,mm^2$. They stated that, flow boiling heat transfer coefficients significantly affected by sub-cooling, mass flux, channel geometry and liquid species. They reported that boiling was initiated at very low wall superheat and immediately shifted to fully nucleate boiling regime. In another study, Peng et al. (1998) investigated flow boiling characteristics in micro-channels by analyzing the thermodynamics of the liquid phase transition. They theoretically derived a non-dimensional parameter, N_{mb}, and related criteria, that determine the phase transition in micro-channels. Dimensionless parameter N_{mb} was defined as

$$N_{mb} = \frac{h_{fg}\alpha_v}{c\pi(v_g - v_f)q"D_h} \tag{2.14}$$

where h_{fg} is enthalpy of evaporation, α_v is thermal diffusivity, and v_g and v_f are vapour and liquid specific volume at saturation temperature, respectively. Equation

(2.14) implies that nucleation is related to the applied heat flux, $q"$, the thermal fluid properties and the micro-channel hydraulic diameter, D_h. They stated that, the nucleation condition in micro-channels expresses as

$$N_{mb} \leq 1.0 \tag{2.15}$$

The predictions (Peng et al., 1998) were compared with experimental observations of various researchers such as Lin et al. (1994), Peng and co-workers (1993, 1994 and 1996) and Ding et al. (1996). The predictions were in a very good agreement with the experimental observations, and provided a very good theoretical basis for their observations.

Bao et al. (2000) experimentally investigated Flow boiling heat transfer coefficients of Freon R11 and HCFC123 in a copper mini-tube with an inner diameter of $1.95\ mm$, the total length of $870\ mm$ and the heated length of $270\ mm$. Tests were performed for heat fluxes in the range of $5-200\ kW/m^2$, mass fluxes in the range of $50-1800\ kg/m^2s$, vapour quality of up to 0.9, and system pressures in the range of $200-500\ kPa$. With respect to the applied operating conditions, the experimental heat transfer coefficients were obtained within the range of $1-18\ kW/m^2K$. They stated that, in the range examined, the heat transfer coefficients were strongly dependent on heat flux and the system pressure, and quite independent of mass flux and vapour quality. This indicated that, the dominant heat transfer mechanism over a wide range of flow conditions was mainly nucleate boiling. The experimental data were compared with some existing correlations such as Chen (1966); Lazarek and Black (1982); Klimenko (1982); Gungor and Winterton (1986); Liu and Winterton (1991); and Steiner and Taborek (1992). None of the correlations could predict the experimental data over the whole range examined. The nucleate pool boiling correlation of Cooper (Cooper, 1984) reasonably predicted the experimental data.

Jacobi and Thome (2002) proposed a new heat transfer model for evaporation of elongated bubble flows in micro-channels based on the assumption of dominant thin-film evaporation heat transfer mechanism in elongated bubble flows. The model predicted all trends in micro-channel heat transfer coefficient both quantitatively and qualitatively also predicted flow-boiling heat transfer coefficients quantitatively for experimental data of Bao et al. (2000) with several

fluids, Freon, R-11, and HCFC123. The local heat transfer coefficient based on the proposed heat transfer model was expressed as follows

$$h_{tp} = k_f \left(\delta_o - \frac{qL_p(t)}{4h_{fg}\rho_f U(t)} \right)^{-1} \tag{2.16}$$

where δ_o, L_p, ρ_f, U , k_f and h_{fg} are the film thickness, length of the vapour and liquid bubble (pair length), mass density of the liquid, liquid-slug/vapour-bubble pair velocity, thermal conductivity of the liquid and latent heat of evaporation, respectively. This new model supported the idea that thin-film evaporation into elongated bubbles is the important heat transfer mechanism in micro-channel evaporation.

Qu and Mudawar (2002) investigated prediction and measurement of incipient boiling heat flux in a micro-channel heat sink. The heat sink was made from a piece of copper and contained 21 rectangular cross section micro-channels. The micro-channels were $0.231\ mm$ wide and $0.713\ mm$ deep with $44.8\ mm$ length. The deionised water with inlet liquid velocities within the range of $0.13 - 1.44\ m/s$ and inlet temperatures of 30, 60 and 90℃ was supplied into the heat sink. The outlet pressure was 1.2 bar. Boiling incipience was identified with existing and growing the first bubbles on the micro-channels wall near the outlet, not at the hottest corners because of the effect of bubble size and surrounding temperature on the bubble departure. Normally in conventional channels the first bubbles grow and collapse but in micro-channels they grow and depart into the liquid flow. They reported that bubble departure size decreased with increasing velocity. At incipient boiling a small number of nucleation sites appeared simultaneously, near the outlet of micro-channels. A comprehensive mechanistic model was constructed to predict the incipient boiling heat flux based on the bubble departure criteria. The model combined both mechanical and thermal considerations and was capable of predicting the size of bubbles departing from micro-channel surfaces, the temperature on bubble interface, and the location of the first bubble to depart. The model predictions showed good agreement with the experimental data. The incipient boiling heat flux increased with increasing the inlet velocity and decreasing the inlet temperature.

Qu and Mudawar (2003a) investigated flow boiling heat transfer of water in the same micro-channel heat sink as the one used in their previous study (Qu and Mudawar,

2002). Tests were performed over a mass flux range of $135 - 402\ kg/m^2s$, inlet temperatures of 30, 60℃, and an outlet pressure of $1.17\ bar$. They stated that, the saturated flow boiling heat transfer coefficients in the micro-channel heat sink decreased with increasing thermodynamic equilibrium quality and were strongly dependent on mass flux, and weakly dependent on heat flux. This indicated that annular flow was the dominant two-phase flow pattern in micro-channels at moderate to high heat fluxes and the dominant heat transfer mechanism in the micro-channel heat sink was forced convective boiling and not nucleate boiling. The experimental saturated flow boiling heat transfer coefficients were also compared with six popular macro-channels heat transfer correlations, Chen (1966); Shah (1976, 1982); Gungor and Winterton (1986); Kandlikar (1990); Liu and Winterton (1991) and Steiner and Taborek (1992), and five mini- and micro-channels correlations, Lazarek and Black (1982); Wambsganss et al. (1993); Tran et al. (1996); Lee and Lee (2001); Yu et al. (2002); Warrier et al. (2002). None of the eleven heat transfer coefficient correlations was able to predict the correct trend of the experimental data accurately.

Wu and Cheng (2003) carried out an experimental investigation to study flow boiling heat transfer of water in horizontal silicon micro-channels at high heat fluxes. The test section was consisted of Eight parallel micro-channels, with similar trapezoidal cross-section, $0.427\ mm$ top wide, $0.208\ mm$ bottom wide, and $0.146\ mm$ depth, with the hydraulic diameter of $0.186\ mm$ and the length of $30\ mm$. Tests were performed for different wall heat fluxes within the range $135 - 226\ kW/m^2$ and time average mass fluxes within the range $112 - 146\ kg/m^2s$. At sufficiently high heat flux and low mass flux, an unsteady Liquid Two-phase Vapour Alternating Flow (LTVAF) appeared in the micro-channels. Based on the amounts of heat fluxes and mass fluxes beyond the incipient boiling point, large-amplitude oscillations of temperature and pressures were observed. At highest heat flux and lowest mass flux, the oscillation amplitudes of inlet, outlet and wall temperatures were as large as $80°C$, $176°C$, and $229°C$, respectively. During the two-phase period, for first time a peculiar and violent two-phase flow pattern also was observed, Figure 2.2.

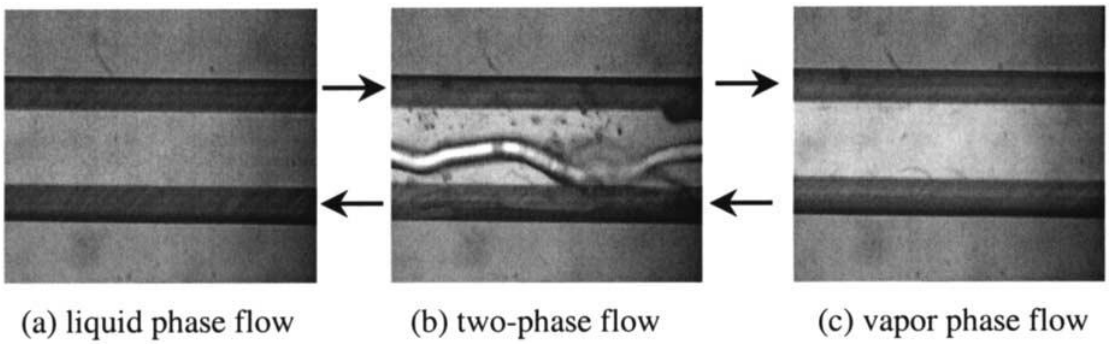

Figure 2.2 Liquid/Two-Phase/Vapor Alternating Flow (LTVAF): $q = 226\ kW/m^2$ and $G = 112\ kg/m^2s$

Steinke and Kandlikar (2003) investigated flow boiling heat transfer of water in six parallel micro-channels. The channels had a slightly trapezoidal cross section, with the top and bottom widths differencing by about $15\ \mu m$, with the average width of $0.214\ mm$, depth of $0.200\ mm$ (hydraulic diameter of $0.207\ mm$) and length of $57.15\ mm$. Tests were performed over a mass flux range of $157 - 1782\ kg/m^2s$, heat flux range of $55 - 898\ kW/m^2$, inlet temperature of $22°C$, mass quality from sub-cooled state to 1.0, and atmospheric pressure at the channels exit. The achieved experimental Nusselt numbers were in a reasonable agreement with predictions using conventional theories. The dominance of nucleate boiling flow was reported. They also reported that, the heat transfer coefficients in micro-channels were improved over conventional channels.

Kandlikar and Steinke (2004) continued their investigations in the same micro-channels and with similar operating conditions as their previous study (Steinke and Kandlikar, 2003). Their results showed that the local flow boiling heat transfer coefficients decrease with increasing quality. This trend was consistent with the nucleate boiling dominant flow. A flow reversal due to bubble nucleation followed by its rapid growth observed under certain conditions in parallel flow channels. This flow pattern was also observed by Kandlikar et al. (2001) in mini-channels. Kandlikar and Steinke (2003) and Kandlikar and Balasubramanian (2003) proved that the general Kandlikar flow-boiling correlation (Kandlikar, 1990), Equation (2.8), can be modified to use with micro-channel flow. The modified Kandlikar correlation for heat transfer coefficient prediction was expressed as follows

$$h_{tp} = h_f\left[0.6683Co^{-0.2}(1-x)^{0.8}(Fr_{fo}) + 1058Bo^{0.7}(1-x)^{0.8}F_{fl}\right] \qquad (2.17)$$

where Co, Bo, Fr_{fo}, h_f and x are Convection number, Equation (2.10), Boiling number, Equation (2.7), Froude number with all liquid only flow, Equation (2.11), heat transfer coefficient with all liquid flow, Equation (2.9) and quality, respectively. The F_{fl} number is equal to 1.0. This correlation was applied to the Steinke and Kandlikar (2004) work and showed a good agreement with the experimental data between qualities of 0.2 to 0.80.

Lee and Mudawar (2005b) experimentally studied flow boiling heat transfer characteristics of R-134a in a micro-channel heat sink. The heat sink was made from a piece of copper. The rectangular cross section micro-channels were formed by cutting 53 micro-slots into the top surface of the copper block. The micro-channels were $0.231\ mm$ wide and $0.713\ mm$ deep with $25.3\ mm$ length. Tests were performed over heat fluxes in the range $159 - 938\ kW/m^2$, mass fluxes in the range $127 - 654\ kg/m^2s$, inlet quality of $0.001 - 0.25$, outlet quality of $0.49 -$*superheat*, and inlet pressure of $1.44 - 6.60\ bar$. While prior studies by Mudawar (Qu and Mudawar, 2003a) and some other researchers reported either nucleate flow boiling or convective flow boiling (annular film boiling) as dominant heat transfer mechanisms in mini- and micro-channels, in this study Lee and Mudawar (2005b) stated that the flow boiling heat transfer was linked with different mechanisms for low, medium and high qualities. Three quality ranges provided: low quality range, $x_e = 0 - 0.05$, medium quality range, $x_e = 0.05 - 55$ and high quality range $x_e = 0.55 - 1.0$. They reported that, nucleate boiling occurs only at low quality range with very low heat fluxes. Higher heat fluxes produce medium or high quality flows dominated by convective flow boiling. A new heat transfer coefficient correlation was developed based on the different quality ranges as follows

$$h_{tp} = 3.856 X^{0.267} h_{sp,f} \quad \text{for} \quad 0.0 \le x_e < 0.05 \tag{2.18a}$$

$$h_{tp} = 436.48\, Bo^{0.522} We_{fo}^{0.351} X^{0.665} h_{sp,f} \quad \text{for} \quad 0.05 \le x_e < 0.55 \tag{2.18b}$$

$$h_{tp} = max\left\{\left(108.6\, X^{1.665} h_{sp,g}\right), h_{sp,g}\right\} \quad \text{for} \quad 0.55 \le x_e \le 1.0 \tag{2.18c}$$

where $h_{sp,f}$ and $h_{sp,g}$ are liquid and vapour single-phase heat transfer coefficients, respectively. X is the Martinelli (Lockhart and Martinelli, 1949) parameter and is evaluated from

$$X = \left[(dp/dz)_f/(dp/dz)_g\right]^{0.5} \quad (2.19)$$

We_{fo} in Equation (2.18b) is liquid only Weber number and is evaluated from

$$We_{fo} = \frac{v_f G^2 D_h}{\sigma} \quad (2.20)$$

The correlation predictions showed an excellent agreement with the experimental data.

Hetsroni et al. (2005) investigated explosive boiling of water in parallel micro-channels. Two-phase flow patterns and flow boiling heat transfer coefficients of water in 21 parallel micro-channels with isosceles triangle cross section with $250\ \mu m$ base were investigated. The parameter ranges examined were: inlet Reynolds number from 25 to 60; mass fluxes from 95 to 340 kg/m^2s; and heat fluxes from 80 to 330 kW/m^2. They presented that, the flow boiling heat transfer coefficients were strongly dependent on the vapour quality. Dryout occurred immediately after venting of elongated bubbles. It was proved that under certain flow and heat transfer conditions explosive boiling occurs in micro-channels.

Qi et al. (2007b) investigated flow boiling heat transfer characteristics and critical heat flux of liquid nitrogen in several micro-tubes with the diameters of 0.531, 0.834, 1.042 and 1.931 mm. Tests were run for mass fluxes within the range $897 - 4740\ kg/m^2s$ and heat fluxes within the range $13.17 - 119.0\ kW/m^2$. The effects of the heat flux, mass flux, pressure and tube diameter on the flow boiling heat transfer coefficients were investigated. Two heat transfer mechanisms were observed; a nucleate boiling dominated region for low mass quality, where the heat transfer coefficient was dependent on heat flux but insensitive to mass flux, and the convection evaporation dominated region for high mass quality, where the heat transfer coefficient was dominated by mass flux and insensitive to heat flux. The obtained heat transfer coefficients were compared with existing correlations of Klimenko (1982), Shah (1984), Chen (Edelstein et al., 1984) and Tran et al. (1996). None of the correlations could predict the heat transfer coefficients for 0.531, 0.834 and 1.042 mm tubes, while for 1.931 mm tube Chen (Edelstein et al., 1984) correlation reasonably predicted the heat transfer coefficients, indication heat transfer characteristics of 1.931 mm tube were similar to those of conventional channels. A new correlation was proposed to predict the experimental heat transfer coefficients as follows;

$$h_{tp} = 1059.83Bo^{0.454}We^{0.045}K_p^{0.106}X^{0.107}N_{conf}{}^{-1.825}\frac{k_f}{D_h} \text{ for } x < 0.3 \quad (2.21a)$$

$$h_{tp} = 0.0042Bo^{-0.872}We^{-0.059}K_p^{0.293}X^{0.065}N_{conf}{}^{-1.704}\frac{k_f}{D_h} \text{ for } x \geq 0.3 \quad (2.21b)$$

where Bo, N_{conf} and X are Boiling number, Confinement number, and Martinelli parameter, respectively, and are evaluated from Equation (2.7), (2.2) and (2.19), respectively. Fluid Weber number, We, and Dimensionless parameter K_p are given by

$$We = \frac{DG^2(1-x)^2}{\sigma\rho_f} \quad (2.22)$$

$$K_p = \frac{P}{[\sigma g(\rho_f - \rho_g)]^{0.1}} \quad (2.23)$$

Ong and Thome (2009) studied flow boiling heat transfer and two-phase flow patterns of three refrigerants, R-134a, R-236fa and R-245fa in a 1.03 mm channel. Tests were performed for mass fluxes from 200 to 1600 kg/m^2s and heat fluxes from 2.3 kW/m^2 to 250 kW/m^2. They presented that, the local saturated flow boiling heat transfer coefficients are dependent on heat flux and mass flux, indicating the presence of nucleate and convective boiling, respectively. The stated that, changes in heat transfer trends correspond well with flow regime transitions.

Basu et al. (2011) investigated flow boiling heat transfer characteristics of R-134a in three horizontal circular mini- and micro-tubes with length of 120, 127 and 128 mm and inner diameter of 0.50, 0.96, and 1.60 mm, respectively. Tests were performed for mass fluxes in the range of $300 - 1500\ kg/m^2s$, heat fluxes in the range of $0 - 350\ kW/m^2$, saturation pressures in the range of $490 - 1160\ kPa$ and exit qualities in the range of $0.0 - 1.0$. They measured the local heat transfer coefficients at 10 axial locations along the tubes. It was reported that, the heat transfer coefficients were dependent on heat flux and saturation pressure and independent of mass flux, presenting nucleate boiling domination. They also compared heat transfer data with seven existing flow boiling correlations and developed a new correlation. Data were not in a good agreement with the previous correlations predictions, but showed a quite good agreement with the new developed correlation within the 30% error limit.

Balasubramanian et al. (2011) experimentally investigated flow boiling heat transfer of deionised water in straight and expanding micro-channels, with similar dimensions and operating conditions for both surfaces. The test pieces were made from a piece of copper $25 \times 25\, mm^2$, containing micro-channels having widths of 0.3, 0.9 and $2.1\, mm$. Tests were performed on both micro-channels over a range of mass fluxes, $100 - 133\, kg/m^2 s$ and heat fluxes up to $1400\, kW/m^2$. They stated that under similar operating conditions, although the expanding micro-channel heat sink having a lower convective heat transfer area but had a better heat transfer performance, lower pressure drop and temperature oscillations than the straight micro-channel counterpart.

Hu et al. (2011) Investigated flow boiling of FC-72 in parallel mini-channels under sub-atmospheric pressure. The test piece was made from a piece of oxygen-free copper. 14 parallel rectangular channels were drilled into the copper test piece. Channels had $0.8\, mm$ width, $2\, mm$ depth ($D_h = 1.14\, mm$) and $20\, mm$ length. Tests were run for mass fluxes within the range $71 - 250\, kg/m^2 s$, heat fluxes within the range $250 - 1400\, kW/m^2$, outlet quality of up to 0.9 and initial pressure of 73 and $110\, kpa$. They reported that, the average heat transfer coefficients were strongly dependent on both mass flux and heat flux. The maximum heat transfer coefficient was found to shift to a lower exit quality with the increase of mass flux rate. The heat transfer coefficient data obtained at atmospheric pressure had the same trend as that of sub-atmospheric pressure but at higher values. The heat transfer coefficients were also compared with several existing correlations. Experimental heat transfer coefficients were predicted reasonably well by conventional and narrow channels correlations. Kandlikar (1990) correlation showed best agreement with the experimental data.

Wang et al. (2011) studied flow boiling of FC-72 and ethanol in high-aspect ratio micro-channels. The test section was a rectangular borosilicate glass channel. Three high-aspect ratio micro-channels were tested, with hydraulic diameters of $571\, \mu m$ ($6\, mm$ wide and $0.3\, mm$ high), $762\, \mu m$ ($8\, mm$ wide and $0.4\, mm$ high), and $1454\, \mu m$ ($8\, mm$ wide and $0.8\, mm$ high), and with aspect ratios of 20, 20 and 10, respectively. The $1454\, \mu m$ channel was also considered as micro-channel, because of the narrow channel depth. Tests with FC-72 were conducted in all the three channels, while ethanol was only tested in the channel with hydraulic diameter of $1454\, \mu m$. Tests were performed for mass fluxes of 11.2, 22.4, and $44.8\, kg/m^2 s$, a wide range of heat fluxes and constant inlet temperature of 25 ℃. As surface tension of FC-72 is much lower than

ethanol, for tests with FC-72, the wall temperature fluctuated with low amplitudes and with the existence of temperature gradient in the channel axial direction. While for tests with ethanol, wall temperature fluctuated with higher amplitudes and lower gradient in the channel axial direction. With increasing the mass flux, ONB and CHF increased. The CHF for ethanol was higher than that for FC-72. It was reported that, the local flow boiling heat transfer coefficients were decreased with vapour quality and increased with heat flux before reaching the dry out point. Ten existing correlations for macro-, mini- and micro-channels were assessed. Predictions of three micro-channel correlations of Lee and Lee (2001), Warrier et al. (2002) and Bertsch et al. (2009) showed very good agreement with measurements for ethanol, while all the ten correlations poorly predicted the FC-72 measurements, indicating the liquid properties effects is crucial in developing a more accurate correlation. A modified correlation was proposed for FC-72 and ethanol with a mean average error (MAE) of 23.6%.

As has been discussed above, the majority of previous experimental investigations of flow boiling in mini- and micro-channels have shown that local flow-boiling heat transfer coefficients are almost independent of vapour quality, weakly dependent on mass flux, fairly dependent on pressure, and strongly dependent on heat flux. Such trends in conventional, mini- and micro-channels propose the nucleate boiling as the dominant heat transfer mechanism. But still there are some inconsistencies, indicating more research with different fluids and channels dimensions and geometries is required.

2.3.3 Pressure Drop

Lazarek and Black (1982) in a preliminary study in small-scale channels, measured saturated flow boiling pressure drop of R-113 in a vertical circular tube with an internal diameter of 3.15 mm. Frictional and acceleration pressure drops were correlated based on the accepted two-phase techniques reported in literature. The frictional pressure drop data were correlated by using the Martinelli (Lockhart and Martinelli, 1949) parameter, Equation (2.19), for turbulent-turbulent liquid and vapour flow, X_{tt}, i.e.,

$$\Delta P_{tp.f} = \left(1 + \frac{20}{X_{tt}} + \frac{1}{X_{tt}^2}\right) \Delta P_{sp.f} \tag{2.24}$$

where $\Delta P_{sp.f}$ is the liquid single-phase pressure drop, obtained from

$$\Delta P_{sp.f} = f\frac{LG^2(1-x)^2}{2D\rho_f} \tag{2.25}$$

Friction factor, f, in Equation (2.25) was obtained from Blasius friction factor expression for turbulent liquid flow as follows

$$f = 0.316\left[\frac{G(1-x)D}{\mu_f}\right]^{-0.25} \tag{2.26}$$

Predictions showed a quite good agreement with the measurements.

Tong et al. (1997) experimentally investigated the effects of important parameters including mass flux, inlet temperature, exit pressure, tube internal diameter, and length-to-diameter ratio on two-phase pressure drop across small-diameter tubes in highly sub-cooled flow boiling. Four tubes with different inner diameters of 1.05, 1.38, 1.80 and $2.44\,mm$ and two length to diameter ratios of 25 and 50 were tested. Tests were performed for heat fluxes up to $80\,MW/m^2$, mass fluxes within the range $25{,}000 - 45{,}000\,kg/m^2\,s$, exit pressures within the range $4 - 16\,bar$, and inlet temperatures within the range $22 - 66°C$. They stated that, mass flux, tube diameter, and length-to-diameter ratio are the major parameters that strongly affect the pressure-drop curves. Two-phase pressure drops increase with increasing mass flux and length-to-diameter ratio and decrease with increasing internal diameter. They also reported that, unlike single-phase flows, inlet temperature and exit pressure have quite significant effects on two-phase pressure drops.

Triplett et al. (1999b) studied two-phase frictional pressure drop of air-water mixture in horizontal circular mini-channels with hydraulic diameters of 1.1 and $1.45\,mm$ and semi-triangular mini-channels with hydraulic diameters of 1.09 and $1.49\,mm$. The experiments were performed for the condition of gas and liquid superficial velocities from 0.02 to $80\,m/s$ and 0.02 to $8\,m/s$, respectively. A one-dimensional model based on the numerical solution of mass and momentum conservation equations was developed in order to calculate the channels two-phase pressure drops, using various two-phase friction models. They reported that, for bubbly and slug flow patterns, the two-phase friction factor based on homogeneous mixture assumption provided the best agreement with experimental data, while for annular flow the homogeneous mixture model significantly over predicted the frictional pressure drop.

Warrier et al. (2002) studied sub-cooled and saturated nucleate boiling of FC-84 in horizontal parallel mini-channels. The test section was made of aluminium and consisted of five parallel rectangular mini-channels, each having a hydraulic diameter of $0.75\,mm$, total length-to-diameter ratio of 433.5 and effective heated length-to-diameter ratio of 409.8. Experiments were performed for mass fluxes in the range of $557-1600\,kg/m^2s$, inlet liquid temperatures of 26, 40, and 60℃ , and heat fluxes of up to $59.9\,kW/m^2$. The two-phase pressure drops across the channels were measured and compared with the correlation of Tran et al. (2000). Experimental data showed a quite reasonable agreement with the Tran et al. (2000) correlation predictions. A new correlation was developed for two-phase flow pressure drop under sub-cooled and saturated nucleate boiling conditions. An excellent agreement between the new correlation predictions and tests measurements was achieved.

Qu and Mudawar (2003c) investigated flow boiling pressure drop of water in a micro-channel heat sink containing 21 parallel micro-channels. The micro-channel heat sink employed in this study was used in their previous studies, Qu and Mudawar (2002) and Qu and Mudawar (2003a). The micro-channels were $0.231\,mm$ wide and $0.713\,mm$ deep with $44.8\,mm$ length. Tests were performed for mass fluxes of $134.9-400.1\,kg/m^2s$, inlet temperatures of 30 and 60℃, and outlet pressure of 1.17 bar. The widely used Homogeneous model (Collier and Thome, 1994), four generalized macro-channels two-phase pressure drop correlations of Lockhart-Martinelli (Lockhart and Martinelli, 1949; Chisholm, 1983), Martinelli-Nelson (Martinelli and Nelson, 1948), Chisholm (1973), and Friedel (1979), and four correlations of Mishima and Hibiki (1996), Tran et al. (2000), Lee and Lee (2001), and Yu et al. (2002), which are based on the separated flow model and were specifically developed for mini- and micro-channels, were examined. It was reported that, correlations based on turbulent flow over predict the data while those including the combination of laminar liquid and laminar vapour flow showed quite reasonable agreement with the data. Correlations developed based on mini- and micro-channels data showed a better agreement with the experimental data. They proposed a new correlation to predict the micro-channels two-phase pressure drop, as follows

$$\Delta P_{tp,f} = \frac{L_{sat}}{x_{e,out}} \int_{x_{e,0}}^{x_{e,out}} \frac{2 f_f G^2 (1-x_e)^2 v_f}{D_h} \phi_f^2 \, dx_e \tag{2.27}$$

where ϕ_f^2 is the two-phase multiplier and evaluated from

$$\phi_f^2 = \left(1 + \frac{C}{X} + \frac{1}{X^2}\right) \tag{2.28}$$

where constant C is evaluated from

$$C = 21[1 - \exp(-0.319 \times 10^3 D_h)](0.00418G + 0.0613) \tag{2.29}$$

Wen and Kenning (2004) experimentally investigated two-phase pressure drop during flow boiling of water in a vertical mini-channel. The mini-channel had a rectangular cross section of $2 \times 1\ mm^2$. The experiments were performed for heat fluxes within the range $25 - 105\ kW/m^2$, mass fluxes within the range $57 - 211\ kg/m^2s$ and exit quality from 0.09 to 0.30. The measured pressure drops were compared with Homogeneous equilibrium model and three correlations of Lockhart-Martinelli (1949), Chisholm (1973), and Tran et al. (2000). They reported that, although Lockhart-Martinelli correlation has been developed based on conventional channels but with modified C value, predicted the experimental data with an uncertainty of 35%, while the mini-channel correlation of Tran et al. (2000) over-estimated the experimental data by 100%. The homogeneous model had an uncertainty of 50% and Chisholm method also over-predicted the experimental data by 300%.

Lee and Mudawar (2005a) in the first part of a two-part study investigated two-phase pressure drop of R-134a in a micro-channel heat sink, containing 53 rectangular micro-channels, $0.231\ mm$ wide, $0.713\ mm$ deep and $25.3\ mm$ long. The micro-channel heat sink used in this part was the same as the one used in the second part (Lee and Mudawar, 2005b) which reviewed in previous section, section 2.3.2. Experimental operating conditions spanned the following ranges: heat fluxes of $316–938\ kW/m^2$, mass fluxes of $127 - 654\ kg/m^2s$, inlet quality of $0.001 - 0.25$, outlet quality of $0.49 -$*superheat*, and inlet pressure of $1.44 - 6.60\ bar$. The total pressure drop increased with increasing mass flux and/or heat flux. The measured pressure drops were compared with Homogeneous equilibrium model with several popular models of two-phase mixture viscosity. Experimental pressure drops were also compared with several macro- and mini-channel correlations based on the separated flow model. Popular macro-channel separated flow model correlations showed better predictions than some mini-channel correlations. Since slug and annular flow regimes were dominant at high heat fluxes in this study, a new correlation based on the separated flow model was developed. Excellent agreement was achieved between the new correlation predictions

and present R-134a data and a previous study data carried out with water as working fluid (Qu and Mudawar, 2003c).

Qi et al. (2007a) investigated flow boiling instabilities and pressure drop of liquid nitrogen in micro-tubes. Experiments were performed with four different micro tubes with the diameters of 0.531, 0.834, 1.042 and 1.931 mm. The adiabatic and diabatic two-phase flow pressure drop characteristics were investigated and four different models including Homogeneous model and three classical separated flow models, L-M model; Chisholm B coefficient model and Friedel model, were used to predict the experimental two-phase flow pressure drops in the micro-tubes. Since the density ratio of liquid to vapor for nitrogen was small enough, allowed the liquid and vapor phase mix well at high mass fluxes, therefore the homogeneous model predicted the experimental data better than those three classical separated flow models. Stable oscillations of pressure drop, mass flux and wall temperatures were observed at ONB for the micro-tubes with the diameter of 1.042 and 1.931 mm. The pressure drop and mass flux oscillations had a phase difference about $180°$ and the wall temperature oscillations were in the same phase with the pressure drop.

Agostini et al. (2008) investigated two-phase pressure drop of R-236fa flowing in a silicon multi-micro-channel heat sink containing 67 parallel micro-channels, 0.223 mm wide, 0.680 mm high and 20 mm long. Tests were performed at saturated flow boiling conditions for critical heat fluxes within the range $219 - 522\ kW/m^2$ and mass fluxes within the range $276 - 992\ kg/m^2s$. The inlet saturation temperatures of $20.31 \leqslant T_{sat,in} \leqslant 34.27\ °C$ and the inlet sub-coolings of $0.4 \leqslant \Delta T_{sub} \leqslant 15.3\ K$ were found to have a negligible effect on the saturated critical heat flux. Pressure drop measurements were measured and analysed, showing that the homogeneous equilibrium model could precisely predict the observed trends.

Balasubramanian et al. (2011) experimentally investigated flow boiling pressure drop of deionised water in straight and expanding micro-channels. The test pieces were made from a piece of copper, $25 \times 25\ mm^2$, containing micro-channels having widths of 0.3, 0.9 and 2.1 mm. Tests were performed on both micro-channels over a range of mass fluxes, $100 - 133\ kg/m^2s$ and heat fluxes up to $140\ W/cm^2$. They reported that, the two-phase pressure drop across the expanding micro-channel heat sink reduced in

compare with the straight one, and the pressure drop and wall temperature fluctuations were significantly lower than its straight counterpart.

Hu et al. (2011) studied flow boiling of FC-72 in 14 parallel rectangular mini-channels with hydraulic diameter of $1.14\ mm$ under sub-atmospheric pressure. Tests operating conditions were as follows: mass fluxes within the range $71 - 250\ kg/m^2s$, heat fluxes within the range $250 - 1400\ kW/m^2$, outlet quality of up to 0.9 and initial pressure of 73 and $110\ kpa$. It was reported that, the two-phase pressure drop through the mini-channel heat sink increased with the increase of heat flux.

As discussed in some of the above literature reviews, two-phase pressure drops in channels generally increased with increasing mass flux and/or heat flux. While two-phase pressure drop in conventional channels can be predicted reasonably using established methods in channels, in mini- and micro-channels greater divergence exists and back flows and dry out conditions make it more complicated. Therefore, still more researches in mini- and micro-channels need to be done.

A summary of the most related literatures on flow boiling and two-phase flows in single tubes and multiple parallel channels which were discussed in previous sections is presented in Table 2.3.

Table 2.3 Summarised literatures on flow boiling and two-phase flows in single tubes and multiple parallel channels

Author	Year	Channel type	Fluid	D_h (mm)	G (kg/m^2s)	q (kW/m^2)
Lazarek and Black	1982	Circular	R-113	3.15	125 – 750	14 – 380
Wambsganss et al.	1991	Rectangular	Air-water	5.45	50 – 2000	–
Cornwell and Kew	1993	Rectangular	R-113	1.03, 1.64	117 – 627	3 – 20
Tran et al.	1993	Rectangular	R-12	2	50 – 400	4 – 34
Peng et al.	1994	Rectangular	Water	0.133 – 0.343	500 – 1626	–
Tran et al.	1996	Rectangular, Circular	R-12	2.4 2.46	44 – 832	3.6 – 19
Kew and Cornwell	1997	Circular	R141b	1.39 – 3.69	188 – 1480	9.7 – 90
Tong et al.	1997	Circular	Water	1.05 – 2.44	25000 – 45000	0 – 80,000
Kuwahara et al.	2000	Circular	R-134a	1.2	80 – 1260	–
Bao et al.	2000	Circular	R-11/R-123	1.95	50 – 1800	5 – 200
Warrier et al.	2002	Rectangular	FC-84	0.75	557 – 1600	1.0 – 59.9
Qu and Mudawar	2002	Rectangular	Water	0.698	135 – 402	1 – 1750
Qu and Mudawar	2003a	Rectangular	Water	0.349	135 – 402	10 – 1300
Qu and Mudawar	2003c	Rectangular	Water	0.349	134.9 – 400.1	10 – 1300
Steinke and Kandlikar	2003	Trapezoidal	Water	0.207	157 – 1782	55 – 898
Wu and Cheng	2003	Trapezoidal	Water	0.186	112 – 146	135 – 226
Kandlikar and Steinke	2004	Trapezoidal	Water	0.207	157 – 1782	55 – 898
Wen and Kenning	2004	Rectangular	Water	1.3	57 – 211	25 – 105
Lee and Mudawar	2005a	Rectangular	R-134a	0.35	127 – 654	316 – 938
Lee and Mudawar	2005b	Rectangular	R-134a	0.35	127 – 654	159 – 938
Hetsroni et al.	2005	Triangle	Water	0.25	95 – 340	80 – 330
Revellin and Thome	2007	Circular	R-134a/R-245fa	0.509, 0.790	200 – 2000	0 – 597
Qi et al.	2007b	Circular	Nitrogen	0.531 – 1.931	897 – 4740	13 – 119
Agostini et al.	2008	Rectangular	R-236fa	0.33	276 – 992	219 – 522
Ong and Thome	2009	Circular	R-134a/R-236fa/R-245fa	1.03	200 – 1600	2.3 – 250
Arcanjo et al.	2010	Circular	R-134a/R-245fa	2.32	50 – 600	–
Basu et al.	2011	Circular	R-134a	0.5 – 1.6	300 – 1500	0 – 350
Balasubramanian et al.	2011	Rectangular	Water	0.3 – 2.1	100 – 133	0 – 1400
Hu et al.	2011	Rectangular	FC-72	1.14	71 – 250	250 – 1400
Wang et al.	2011	Rectangular	FC-72/Ethanol	0.571 – 1.454	11.2 – 44.8	2.9 – 7.5

2.4 Flow Boiling and Two-Phase Flows in Complex Geometries

For boiling in complex geometries, many studies have been undertaken at the macro-scale. Several researches have studied various flow patterns, heat transfer, pressure drop, and void fraction characteristics for flow across a bank of conventional size tube bundles that are several millimetres or larger in diameter. For example, Schrage et al. (1988), Dowlati et al. (1990, 1992) and Feenstra et al. (2000) have investigated void fraction distributions, Hwang and Yao (1986), Jensen and Hsu (1988), Cornwell (1990), Houston and Cornwell (1996), Dowlati et al. (1996), and Burnside and Shire (2005), have investigated flow boiling heat transfer, while Ishihara et al. (1980), proposed a method for the frictional two-phase multiplier. A state-of-the-art review of researches on two-phase flow and flow boiling across horizontal conventional and small tube bundles have been reported by Ribatski and Thome (2007). Studies of two-phase flow on staggered and in-line tube bundles for upward, downward, and side-to-side flows were covered.

Recent development in micro-fabrication techniques allows small scale complex geometries such as mini- and micro-pin fin surfaces, drilled cavities, re-entrant cavities and alumina sprayed particles to be fabricated and explored. Fewer studies have been undertaken in these complex mini- and micro-scale flow passages. A review of some of the important flow boiling and two-phase flow investigations on flow patterns, heat transfer and pressure drop characteristics in complex mini- and micro-scale flow passages is presented in the following sections.

2.4.1 Flow Patterns

Flow boiling heat transfer coefficients and pressure drops in mini- and micro-scale flow passages are strongly dependent on two-phase flow patterns (Kandlikar et al., 2006). Therefore, the first step in understanding flow boiling in mini- and micro-scale flow passages is the characterization of how the fluid flows through the flow passages. The progression of flow patterns in mini- and micro-scale flow passages is different from those in conventional channels and tube bundles. This difference results from differences in relative magnitudes of shear, viscous, and surface tension forces. A number of studies have been undertaken to study two-phase flow patterns in complex

mini- and micro-scale flow passages. Some of the important studies are presented in this section.

Kosar and Peles (2007) investigated two-phase flow patterns in micro-pin fins, manufactured as NACA $66-021$ hydrofoils. The fins were in a staggered arrangement with 12 or 13 fins lateral to the flow on a lateral pitch of $150\ \mu m$ and 20 fins in the flow direction with a longitudinal pitch of $500\ \mu m$. Each fin had a chord length of $100\ \mu m$, a length of $500\ \mu m$, a wetted perimeter of $1.03\ mm$ and a height of $243\ \mu m$. The working fluid was R-123 at pressures between 486 and $539\ kpa$. The experiments were conducted by setting the mass flow rate and increasing the voltage to the heater in steps of $1\ V$ until critical heat flux occurred. From their visual observations bubbly, wavy intermittent and spray-annular flow patterns were identified depending on the heat flux and mass velocity. They also constructed a flow map to specify the transition boundaries between each flow pattern.

Krishnamurthy and Peles (2007) studied adiabatic nitrogen-water two-phase flow patterns across a staggered array of circular micro-pin fins. The test piece was $1.5\ mm$ wide and $10\ mm$ long and contained 68 rows of fins in either 9 or 10 columns. The fins were $100\ \mu m$ in diameter and $100\ \mu m$ high and were configured in a staggered array with a longitudinal and transverse pitch of $150\ \mu m$. Two-phase flows were supplied to the test piece for Reynolds number ranging from 5 to 50. Four different flow patterns of bubbly slug, gas-slug, bridge, and annular flows were observed. They defined bubbles as dispersed gas in the liquid with the size of less than or equal to the spacing between the pin-fins, i.e., $50\ \mu m$. The gas-slug was defined as a continuous gas phase which covered four or more pin-fins. At higher gas velocities, the gas-slug flow merged and the liquid crossed along the channel and shaped a bridge, which named as bridge flow pattern. Flow patterns were mapped and compared with conventional scale and micro-channel flow maps. It was found that, the trend observed in the flow patterns transitions were better predicted by the micro-channel flow patterns map.

Krishnamurthy and Peles (2008) investigated two-phase flow patterns and heat transfer mechanisms of water across a bank of circular pin fins at atmospheric pressure. The fins had a diameter of $100\ \mu m$ and a height of $250\ \mu m$ and were placed in a staggered configuration with a pitch of $150\ \mu m$. There were 11 or 12 columns and 68 rows. Orifice plates were placed upstream of the test piece to suppress thermo-hydraulic

instabilities. Tests were carried out by setting a constant mass flux between 346 and 794 kg/m^2s and increasing the voltage to the heater in steps of 0.5 V until critical heat flux occurred. Flow patterns were observed through flow visualization and classified as vapour slug and annular flow. They also mapped the observed flow patterns as a function of superficial gas and liquid Reynolds numbers.

Krishnamurthy and Peles (2010a) reported flow patterns of 1-methoxy-hepta-fluoro-propane (HFE 7000) in 5 micro-channels, 200 μm wide and 243 μm deep ($D_h = 222\ \mu m$). Each micro-channel contained a single row of 24 in-line 100 μm circular pin-fins. Tests were performed for mass fluxes in the range of $350 - 827\ kg/m^2s$ and wall heat fluxes in range of $10 - 110\ W/cm^2$. They manually classified their observations into three major flow patterns: bubbly flow, which categorized into two regions: isolated bubbles and bubbles interacting, multiple flow, and annular flow along the channel length. They mapped their flow patterns as a function of the boiling number and the normalized axial distance.

Krishnamurthy and Peles (2010b) studied flow patterns, bubble departure diameter and bubble departure frequency, on the same test facility as Krishnamurthy and Peles (2010a) and with the same operating conditions. Bubbly flow, multiple flows, and wavy-annular flow regimes were observed. Nucleation sites were mostly observed at $\theta = 0°$ and $\theta = 180°$. It was found that for $\theta = 0°$, the bubble departure frequency quickly increased with wall heat flux, while for $\theta = 180°$, the bubble departure frequency first increased and then decreased with wall heat flux. For both nucleation sites bubble departure diameter decreased with increasing wall heat flux.

As it has been discussed above, various flow pattern observations were reported and still are reported in literature. There is still a great deal of efforts and additional researches required to develop a general and reliable flow pattern map and flow patterns transition boundaries in mini- and micro-scale flow passages.

2.4.2 Heat Transfer Characteristics

With transition from flow boiling on conventional tube bundles to smaller diameter tube bundles and mini- and micro-pin-fins, reduction of the tube diameter decreases the

bubbles size and the sliding bubbles effects. Although for small tube bundles and mini- and micro-pin fins, heat transfer coefficient decreases due to absence of sliding bubbles at low qualities, but the effect of turbulence due to rising bubbles will still lead to an enhancement in heat transfer coefficient. At higher vapour qualities higher values of heat transfer coefficient are achieved (Adom et al. 2010).

A review of various surface enhancement methods has been reported by Honda and Wei (2004) for nucleate boiling heat transfer. The key issues identified were the temperature overshoot required to initiate boiling, the effect of liquid sub-cooling and the critical heat flux. The overshoot temperature is shown to decrease with increased roughness of the microstructure. However, the most effective method of reducing temperature overshoot was gasification of the liquid. This could allow boiling below the saturation temperature and had little effect on the performance at high, or near critical, heat flux. Honda and Wei (2004) also reported that the heat transfer and critical heat flux were found to improve with enhanced area, but not in direct proportion. Critical heat flux was found to increase with increasing sub-cooling. The most effective enhancement method was found to be pin fins. This gave enhanced heat transfer because vapour trapped between the fins provided additional nucleation sites. Additionally, these spaces retained vapour for longer, giving enhanced heat transfer. The optimum spacing of the fins depended on liquid sub-cooling.

Honda et al. (2002) undertook nucleate boiling studies, from free convection up to critical heat flux, on a pin-fin array using FC-72 at atmospheric pressure as the working fluid. The pin fins were $50\ \mu m$ square, $60\ \mu m$ high and were ordered in an in-line square pitch configuration with a $100\ \mu m$ pitch. The test piece was $10\ mm$ square. Heat fluxes of up to $620\ kW/m^2$ were used with liquid sub-coolings of up to 45℃. The additional fin area was not included in the calculation of the heat-transfer coefficient. In the free convection region, for the same wall-to-fluid temperature difference, the pin fins had a lower heat flux than a flat surface, despite having an area enhancement of 2.2. This was because the pin fins lay below the thermal boundary layer. At higher temperature differences, the pin fins produced heat fluxes up to 1.8 times larger and a greater critical heat flux. The rapid growth in heat flux was caused by vapour trapped between the pin fins. The bubbles grew to many times the volume of a pin fin, so at critical heat flux, the surface was covered with very large bubbles. When dissolved gas

was included, boiling was observed at negative saturation-to-wall temperature differences.

Kosar et al. (2005a) investigated flow boiling of water in parallel rectangular micro-channels with reentrant cavities. The test piece was $10\,mm$ long and $1.8\,mm$ wide, consisting of 5 parallel rectangular micro-channels with a hydraulic diameter of $227\,\mu m$ ($200\,\mu m$ wide and $246\,\mu m$ deep), which spaced $200\,\mu m$ apart. Micro-channels sidewalls possessed an array of interconnected reentrant cavities, $7.5\,\mu m$ wide and $100\,\mu m$ apart. Tests were performed over a range of effective heat fluxes, $280-4450\,kW/m^2$, and mass fluxes, $41-302\,kg/m^2s$. Both nucleate and convective dominant boiling mechanisms were observed. The transition between nucleate and convective boiling was identified based on the Reynolds and the Boiling number. Nucleate boiling was dominant for low Reynolds and Boiling numbers, while High Reynolds and Boiling numbers promoted convective boiling. Two correlations were developed to predict the experimental heat transfer coefficients for both nucleate and convective boiling mechanisms as follows

$$h_{tp} = 1.068 q''^{0.64} \qquad \text{(Nucleate boiling)} \tag{2.30a}$$

$$h_{tp} = 4.068 \times 10^4 Re_{fo}^{0.12} \times (1 - x_e)^{0.8} \left(\frac{1-x_e}{x_e}\right)^{0.02} \qquad \text{(Convective boiling)} \tag{2.30b}$$

Experimental data were also compared with number of existing correlations. Among the tested correlations, Kandlikar (Kandlikar, 1990) correlation provided the best prediction.

Kosar et al. (2005b) investigated flow boiling of deionised water at a reduced exit pressure of $47\,kPa$, using the same test piece and at the same operating conditions as their previous study, Kosar et al. (2005a). Similar to the previous study, two nucleate and convective dominant boiling heat transfer mechanisms were observed. Average two-phase heat transfer coefficients were measured and compared to the results obtained from previous tests at atmospheric exit pressure. They reported that, similar to conventional and mini-channels, measured heat transfer coefficients increased with exit pressure at the same exit quality. Similar to atmospheric pressure data, nucleate boiling was dominant for low Reynolds and Boiling numbers. Transition from nucleate to convective dominant boiling heat transfer mechanism occurred at lower Reynolds and

Boiling numbers than that at atmospheric pressure. A general heat transfer mechanism map was also developed.

Lie et al. (2007) investigated flow boiling of FC-72 on plain and pin finned surfaces at atmospheric pressure. Two pin-fin surfaces were tested, one with fins $200\ \mu m$ square and $70\ \mu m$ high on a square in-line arrangement with a $400\ \mu m$ pitch, and one with fins $100\ \mu m$ square and $70\ \mu m$ high on a square in-line arrangement with a $200\ \mu m$ pitch. The mass fluxes used were within the range $287 - 431\ kg/m^2s$ and the heat fluxes within $1 - 100\ kW/m^2$. Single-phase and flow boiling heat-transfer coefficients were reported. The single-phase heat-transfer coefficients were based on the mean-wall to fluid-inlet temperature difference and the base area of the heat-transfer surface. The boiling coefficients used the mean-wall to fluid-saturation temperature difference. The mass flux was found to have only a slight effect on the boiling heat-transfer coefficient. The temperature at the onset of nucleate boiling was found to increase with increasing mass flux and, for the same temperature difference, the largest heat transfer occurred with the $100\ \mu m$ fins. Cross-flow between channels was evident. The degree of wall superheat required for the onset of boiling was lower for the finned surfaces, with increased nucleation sites being evident in the corners of the fins. Bubbles grew to many times the size of the fins and became elongated and distorted. The bubble departure diameter reduced with increasing mass flux and with the addition of fins. The departure frequency increased with mass flux and the addition of fins. Correlations of the heat-transfer coefficients were produced by assuming that a convective and boiling component of heat flux existed.

Kosar and Peles (2007) investigated flow boiling heat transfer of R-123 in a staggered array of hydrofoil-based micro-pin fins, manufactured as NACA $66 - 021$ hydrofoils. The pin-fins specifications and tests operating conditions were explained in details in previous section. The fluid entered the test section in a sub-cooled state. The test section was split into single- and two-phase lengths from the video record. The exit quality was obtained from a heat balance. Single-phase, partial boiling and fully-developed boiling ranges were identified. Average heat-transfer coefficients were deduced using the fin-efficiency concept. The single-phase heat-transfer coefficient was found to vary from 4.8 to $15.5\ kW/m^2K$ in the mass flux range $972 - 2349\ kg/m^2s$ via a power law relationship with an exponent of 0.75. The boiling heat-transfer coefficient was found to increase in the assumed nucleate boiling region and decrease in the assumed

convective boiling region to critical heat flux. Critical heat flux was therefore due to the dryout mechanism. The bubbly, wavy intermittent and spray-annular flow patterns were identified. Nucleate boiling heat transfer was associated with the bubbly and wavy intermittent flow patterns while convective boiling was associated with the spray-annular flow pattern. The measured boiling data were not well predicted by macro-channel methods. The critical heat flux increased with mass flux, decreased with exit quality and was reasonably well predicted from micro-channel methods.

Krishnamurthy and Peles (2008) reported flow boiling of water across staggered circular pin fins with diameter of $100\,\mu m$ and a height of $250\,\mu m$. The test piece specifications and tests operating conditions were mentioned in previous section in more details. The average wall temperature was derived from the heater resistance. Local thermistors allowed the local heat-transfer coefficient to be deduced using the fin efficiency approach and assuming no heat transfer from the fin tips. At all but the highest mass flux, single-phase heat transfer progressed to fully developed boiling. At the highest heat flux these regimes were separated by a partial boiling regime. The partial boiling regime was caused by large vapour slugs on the test piece preceding annular flow. The single-phase heat-transfer coefficient was found to be proportional to the mass flux. The two-phase heat-transfer coefficient was found to vary moderately with mass flux and to be independent of heat flux, suggesting convective boiling domination. A Chen type correlation was deduced by neglecting the nucleate boiling component and applying a Reynolds analogy, for which a single-phase coefficient proportional to a one third power law with mass flux was used.

Ma et al. (2009) investigated flow boiling of FC-72 at atmospheric pressure on square pin finned arrays. The fins were $30\,\mu m$ wide and arranged on a square in-line configuration with a pitch of $60\,\mu m$. Two fin heights of $60\,\mu m$ and $120\,\mu m$ were tested. Both were compared to an open channel, or smooth, flow. The test pieces were $10\,mm$ square and $0.5\,mm$ high and were placed in a flow channel $30\,mm$ wide and $5\,mm$ high. The test piece location was $300\,mm$ from the flow inlet. The downstream flow length was longer. The channel flow characteristics were therefore not affected by the thermo-hydraulics of the test piece. The FC-72 liquid was saturated with air to prevent overshot at the onset of boiling. Channel liquid velocities of 0.5, 1 and $2\,m/s$ were tested at inlet sub-coolings of 15, 25 and $35\,K$. Tests were carried out by increasing the Joule heating in steps until critical heat flux occurred. The smooth test

piece showed the critical heat flux to increase with both liquid velocity and subcooling. The fin area was not corrected in the heat transfer analysis. For the same wall-fluid temperature difference, the single and two-phase heat fluxes were significantly enhanced by the addition of fins and an increase in fin height. Boiling heat-transfer was enhanced by increased nucleation in the gaps between the fins. At liquid velocities of 0.5 and $1\ m/s$, the two-phase heat flux varied as a power law of the temperature difference, while at $2\ m/s$, it varied linearly. This suggested that nucleate boiling and forced convective heat transfer were important. Critical heat flux increased with liquid velocity, sub-cooling and the addition of fins. Yuan et al. (2009) reported very similar work with a fin width of $50\ \mu m$ on a $100\ \mu m$ pitch, as follows. The conclusions were very similar.

Yuan et al. (2009) investigated sub-cooled flow boiling heat transfer of FC-72 over two silicon chips contained micro-pin-fins and a smooth silicon chip. Two different micro-pin fin surfaces were studied, both contained squared micro-pin-fins, $50\ \mu m$ wide, $60\ \mu m$ and $120\ \mu m$ high, respectively, and with $100\ \mu m$ pitches. The tests were performed at the fluid velocities of 0.5, 1 and $2\ m/s$ and liquid sub-coolings of 15, 25 and $35\ K$. It was found that, for the same mass fluxes and liquid sub-coolings, both micro-pin-fin surfaces had significant heat transfer enhancement in compare with the smooth silicon chip. The critical heat fluxes for both pin-fin surfaces were increased with mass flux and sub-cooling. A higher critical heat flux was achieved for both pin-fin surfaces in compare with the smooth chip. They reported that, with increasing liquid sub-cooling and mass flux, the effect of single-phase forced convection was increased, therefore the rate of critical heat flux enhancement was increased at low liquid sub-cooling of 15℃, while at larger liquid sub-cooling of 35℃, the rate of critical heat flux enhancement was decreased.

Qu and Siu-Ho (2009a) investigated water boiling at atmospheric pressure in a square pin-fin array. The test piece was $33.8\ mm$ long and $10\ mm$ wide and contained 1950 fins $200\ \mu m$ wide and $670\ \mu m$ high on a staggered configuration with a lateral and transverse pitch of $400\ \mu m$. The ratio of the total to the base area was 3.9. Fin efficiency was used to include the pin-fin areas in the heat-transfer analysis. Water with mass fluxes of $183 - 420\ kg/m^2 s$ and with subcoolings of 10, 40 and $70\ K$ were supplied to the test piece. Heat fluxes ranged from 237 to $2485\ kW/m^2$. Three in wall thermocouples allowed local heat-transfer coefficients to be deduced. Partitioning the

test piece into sub-cooled and saturated liquid portions from a heat balance allowed single and two-phase heat transfer to be identified. Only the saturated heat-transfer coefficients obtained at exit gas-mass fractions greater than 0.01 were reported. The saturated boiling values had unusual characteristics, being insensitive to mass flux and heat flux, but not exit quality. The observed flow pattern was said to be annular which suggested that the boiling heat-transfer mechanism was convective. The lack of mass flux dependency was explained in terms of a constant liquid film induced by the pin fins, and sub-cooled entrained liquid. The data were correlated in terms of an 'equilibrium' heat-transfer coefficient and the exit gas-mass fraction.

Krishnamurthy and Peles (2010a) studied flow boiling of 1-methoxy-hepta-fluoro-propane (HFE 7000) in a test piece containing 5 micro-channels with hydraulic diameter of $222\ \mu m$. Each micro-channel contained a single row of 24 in-line $100\ \mu m$ circular pin-fins, with pitch to diameter ratio of 4. Tests were performed for mass fluxes in the range of $350 - 827\ kg/m^2s$ and wall heat fluxes in range of $100 - 1100\ kW/m^2$. The measured local flow boiling heat transfer coefficients were compared with corresponding single-phase heat transfer coefficients. The sub-cooled flow boiling heat transfer coefficient was considerably higher than the corresponding single-phase flow. The flow boiling heat transfer data for micro-channel surface equipped with pin-fins were also compared with a plain micro-channel surface data. It was shown that, the presence of pin fins considerably enhanced the heat transfer coefficient.

Chang et al. (2010) investigated Sub-cooled flow boiling heat transfer and associated bubble characteristics of FC-72 on a heated micro-pin-finned silicon chip. The same test sections and operating conditions were used as Lie et al. (2007). The test piece was a rectangular channel, $20\ mm$ wide, $5\ mm$ high and $150\ mm$ long, equipped with a $10\ mm$ square silicon chip, located at the central bottom surface of the channel. Three different geometries of micro-structures on the silicon chips were examined; a smooth silicon chips and two surface micro-structures in the form of square micro-pin fins on the silicon chips. The silicon chips micro-structures named as smooth, pin-finned 100 and pin-finned 200 surfaces. Two pin-finned 100 and 200 surfaces contained micro-pin fins, 100 and $200\ \mu m$ square, respectively, and $70 \mu m$ high, with a fins distance of equal to the width of the fins for both surfaces. The mass flux used were within the range $287 - 431\ kg/m^2s$, the heat fluxes within the range $1 - 100\ kW/m^2$ and the

inlet sub-cooling from 2.3 to 4.3 ℃. Single-phase and sub-cooled flow boiling heat transfer coefficients were reported. The sub-cooled flow boiling heat transfer coefficient was reduced at increasing inlet liquid sub-cooling. The mass fluxes were found to have only a slight effect on the sub-cooled flow boiling heat transfer coefficient. The single-phase convection and flow boiling heat transfer coefficients were significantly higher in pin-fin surfaces in compare with the smooth one. The mean bubble departure diameter and active nucleation site density reduced with increasing mass flux and inlet liquid sub-cooling. They proposed empirical correlations for the heat transfer and bubble characteristics in the FC-72 sub-cooled flow boiling.

Xue et al. (2011) studied heat transfer performance of FC-72 over a silicon chip with micro-pin-fins in three different test systems including pool boiling, natural circulation flow boiling, and forced flow boiling. The test piece was a square P-doped N-type silicon chip, $10\,mm$ wide, $10\,mm$ long and $0.5\,mm$ high. Two surfaces were tested, one a smooth chip without pin-fins (chip S), and one with micro-pin-fins $30\,\mu m$ square and $60\,\mu m$ high (chip PF30-60). For the forced flow boiling system, FC-72 were supplied to the test section with two fluid velocities of 0.5 and $1\,m/s$ and liquid sub-coolings of 25 and $35\,K$. It was reported that, in all three test systems, the micro-pin-fin surface significantly increased the heat transfer in compare to the smooth surface. Wall superheat for forced flow boiling tests was smaller than pool boiling and natural circulation flow boiling tests. At the fluid velocity of $1\,m/s$, the forced flow boiling critical heat flux was the highest one.

Morshed et al. (2012) investigated convective heat transfer in a micro-channel with integration of copper nanowires (CuNWs) coatings. The test piece was a single micro-channel, $360\,\mu m$ high, $5\,mm$ wide, and $26\,mm$ long ($D_h = 672\,\mu m$), contained nanowires, $200\,nm$ in diameter and $30\,\mu m$ high, on the bottom surface of the micro-channel. Nanowires were directly grown using electrochemical deposition technique. Deionised water as coolant with mass fluxes of 45.95, 95.67, and 143.79 kg/m^2s and inlet temperatures in the range of $40-80$ ℃ were supplied to the micro-channel. Single-phase and two-phase convective heat transfer coefficients were reported. The CuNWs coated surface results were also compared with the bare Cu surface. They reported that, bare Cu and CuNWs coated surfaces show similar flow boiling behaviour. Surface superheat was significantly reduced for the ONB by using CuNWs coated

surface. CuNWs coatings have been found to enhance single-phase heat transfer rate by up to ~25%, whereas in the flow boiling regime, the enhancement was up to ~56%.

As was reviewed above, the majority of previous experimental investigations of flow boiling in mini- and micro-pin-fin surfaces and other complex geometries showe that the presence of pin fins considerably enhance the heat transfer coefficient. It was found that, with increasing liquid sub-cooling and mass flux the rate of critical heat flux enhancement is increased, while increasing in exit quality decreases the critical heat flux. Both nucleate boiling and convective boiling heat transfer mechanisms were reported. The majority of previous researchers reported that, nucleate boiling heat transfer is associated with the bubbly and intermittent flow patterns while convective boiling is associated with the annular flow pattern. Despite the fact that some of the discussed flow boiling heat transfer characteristics in mini- and micro-pin-fin surfaces are common with conventional tube bundles characteristics, but in most of the previous studies the measured flow boiling data were not well predicted by macro-scale methods. Researches indicate that there are still some inconsistencies, and more researches with different fluids, geometries, and wider range of heat and mass fluxes is required.

2.4.3 Pressure Drop

Krishnamurthy and Peles (2007) studied adiabatic nitrogen-water two-phase flow pressure drop across a staggered array of circular micro-pin fins, containing 68 rows of fins, 100 μm in diameter and 100 μm high with a longitudinal and transverse pitch of 150 μm, in either 9 or 10 columns. Two-phase flows were supplied to the test piece for Reynolds number ranging from 5 to 50. Pressure drops were obtained and compared to conventional tube bundles and micro-channels data. A modified two-phase frictional multiplier based on the Chisholm (Grant and Chisholm, 1979) model was developed in terms of the Martinelli parameter, X_{vv}, i.e.,

$$(\phi_f)^2 = 1 + \frac{BRe_f}{X_{vv}} + \frac{1}{{X_{vv}}^2} \tag{2.31}$$

where B is an empirically defined constant. Unlike previous some conventional scale and micro-channel studies, the two-phase frictional multiplier was found to be strongly dependent on mass-flux and weakly dependent on flow pattern.

Kosar (2008), working on the same test facility as Kosar and Peles (2007), reported single and two-phase pressure drops for the hydrofoil test piece. For a set mass flux, the pressure drop reduced at low heat fluxes due to the reduced viscosity of the fluid, while at higher heat fluxes, after the onset of significant vapour generation, the pressure drop increased. Pressure drop increased with mass flux and with gas-mass fraction for the same mass flux. Thus, for the same heat flux, a lower mass flux could have a larger pressure drop than a larger one because of the larger exit gas-mass fraction. A Chisholm type fit was attempted to the two-phase friction multiplier, deduced from the pressure-drop measurements using the laminar-laminar flow combination Martinelli parameter, X_{vv}. The correlation was poor. The flow map transition from bubbly to wavy intermittent flow was found to occur when X_{vv} was 1.8 and the transition from wavy intermittent to spray-annular occurred when X_{vv} was 3.

Krishnamurthy and Peles (2009) investigated surface tension effects on an adiabatic study of nitrogen-ethanol flow across a staggered array of circular pin fins. The fins were $100\ \mu m$ in diameter and $100\ \mu m$ high and were configured in a staggered array with a longitudinal and transverse pitch of $150\ \mu m$. Flow patterns, void fraction and pressure drop were studied. It was found the flow patterns affected the pressure drop characteristics. The nitrogen-ethanol pressure drops were also compared with the pressure drop results for water from a previous study, Krishnamurthy and Peles (2007). The two-phase pressure drop for water was found to be higher than for ethanol, indicating the effect of flow pattern transition on the pressure drop. A modified Chisholm type correlation was produced for the two-phase multiplier. An interfacial friction factor was deduced using methods similar to Rahman et al. (1996). The interfacial friction factor was found to be a function of surface tension ratio of the water and ethanol (σ_w/σ).

Qu and Siu-Ho (2009b) investigated flow boiling pressure drop of water in a micro-pin-fin heat sink. The square micro-pin fins were in a staggered arrangement having a $200 \times 200\ \mu m^2$ cross-section and $670\ \mu m$ high. Water with mass fluxes of $183 - 420\ kg/m^2 s$ and with sub-coolings of 10, 40 and 70 K were supplied to the test piece. Heat fluxes ranged from 237 to $2485\ kW/m^2$. They reported that, the total two-phase pressure drop in the micro-pin fin surface was affected strongly by the rate of vapour generation, as with commencing of the saturated boiling regime, the two-phase pressure drop significantly increased. The two-phase pressure drops were dominated by frictional

pressure drop component. They examined ten existing two-phase pressure drop models and correlations to predict the flow boiling pressure drop across the micro-pin fins. The Lockhart–Martinelli correlation for laminar liquid–laminar vapor combination in conjunction with a previous single-phase friction factor correlation provided the best agreement with the data.

Kosar et al. (2010) studied flow boiling pressure drop of water and R-123 across three different micro-pin fin heat sinks under unstable boiling conditions. Three different pin fin arrangements were examined; (a) circular pin fins having a diameter of $100\ \mu m$ and a height of $243\ \mu m$, were placed in a staggered configuration with a pitch of $150\ \mu m$, using R-123 as working fluid, (b) similar circular pin fins were placed in a staggered configuration with longitudinal and transverse pitches of $350\ \mu m$ and $150\ \mu m$ respectively, using water as working fluid, and finally (c) Hydrofoil pin fins having a chord thickness of $100\ \mu m$, length of $500\ \mu m$ and a height of $243\ \mu m$, were placed in a staggered configuration with longitudinal and transverse pitches of $500\ \mu m$ and $300\ \mu m$ respectively, using water as working fluid. They used flow images and Fast-Fourier Transform (FFT) of pressure signals during flow boiling to clarify experimental results. They reported that, flow instabilities during flow boiling in micro-pin fin surfaces are of concern similar to parallel micro-channel surfaces. The magnitude of the pressure drop fluctuations for water tests was lower than that for R-123 tests. Unlike the R-123 tests, for the tests operated with water no significant change was observed in the fast-Fourier transform (FFT) profiles with unstable boiling. According to the flow patterns visualisations they stated that, the high frequency of oscillations for the tests operated with R-123 was in agreement with the frequency of the rapid bubble growth instabilities.

Morshed et al. (2012) reported flow boiling pressure drop of deionised water in a single micro-channel of $672\ \mu m$ hydraulic diameter with integration of copper nanowires (CuNWs) coatings, $200\ nm$ in diameter and $30\ \mu m$ high, on the bottom surface of the micro-channel. Tests were performed for mass fluxes of 45.95, 95.67, and 143.79 kg/m^2s and inlet temperatures in the range of $40 - 80$ ℃. The CuNWs coated surface results were compared with the bare Cu surface. It was reported that, with increasing the heat flux, pressure fluctuations increase for both surfaces and CuNWs coating does not show any significant effect on managing the two-phase flow instabilities in the micro-channel. CuNWs coating was found to enhance single-phase regime pressure drop by

$\sim 20\%$, while no obvious change of pressure drop in the fully developed boiling regime was observed.

As discussed above, similar to single and multiple parallel channels, two-phase pressure drop in pin-fin surfaces increases with increasing mass flux, and gas mass fraction. Thus, for a set heat flux, a lower mass flux could have a larger pressure drop than a larger one because of the larger exit gas-mass fraction. For a set mass flux, the pressure drop is reduced at low heat fluxes due to the reduced viscosity of the fluid. It was found the flow patterns also strongly affect the pressure drop characteristics.

A summary of the most related literatures on flow boiling and two-phase flows in complex geometries which were discussed in previous sections is presented in Table 2.4.

Macro sized heat exchangers typically have tubes $20\ mm$ in diameter on an in-line or staggered arrangement with a pitch to diameter ratio of about 1.5. Micro pin fins in the range $30 - 200\ \mu m$ in diameter on in-line and staggered arrangements have been investigated. Less has been reported in between. The objective of this study is to investigate the flow boiling characteristics, heat transfer coefficient, and pressure drop in different mini flow passages, single and multiple parallel channels, and in-line and off-set pin-fin surfaces at an intermediate size, flow passages with hydraulic diameter of the order of $1\ mm$, using R-113 and deionised water at atmospheric pressure as the working fluids. A combination of flow passages with hydraulic diameter of the order of $1\ mm$ and R-113 as the working fluid was chosen to cover the two-phase flows transition zone from macro- to micro-scale flow passages based on the Bond number ($Bo = 1$). Deionised water has a much higher surface tension than R-113. The Bond number for water data is much less than R-113 data. Thus deionised water was selected to make comparisons with R-113 data. Therefore Five test series were carried out as follows,

- Plate channel test piece with R113 as working fluid
- Parallel channel test piece with R113 as working fluid
- In-line pin-fin test piece with R113 as working fluid
- Off-set pin-fin test piece with R113 as working fluid
- In-line pin-fin test piece with water as working fluid

Tests procedures and experimental operating conditions are fully described in Chapter 5.

Table 2.4 Summarised literatures on flow boiling and two-phase flows in complex geometries

Author	**Year**	**Shape and geometry of pin-fins**	**Fluid**	D_{eq} * (mm)	S_L (mm)	S_T (mm)	G (kg/m^2s)	q (kW/m^2)
Honda et al.	2002	Square, In-line	FC-72	0.06	0.1	0.1	$25-200$	$0-620$
Kosar et al.	2005a 2005b	Micro-channels with reentrant cavities	Water	0.227	–	–	$41-302$	$280-4450$
Lin et al.	2007	Square, In-line Square, In-line	FC-72	0.255 0.127	0.4 0.2	0.4 0.2	$287-431$	$1-100$
Kosar and Peles	2007	Hydrofoil, staggered	R-123	0.1	0.5	0.15	$976-2349$	$190-3120$
Kosar	2008	Hydrofoil, staggered	R-123	0.1	0.5	0.15	$976-2349$	$190-3120$
Krishnamurthy and Peles	2007	Circular, staggered	Nitrogen-water	0.1	0.15	0.15	$0-200$	–
Krishnamurthy and Peles	2008	Circular, staggered	Water	0.1	0.15	0.15	$346-794$	$200-3500$
Krishnamurthy and Peles	2009	Circular, staggered	Nitrogen-ethanol	0.1	0.15	0.15	$0-218$	–
Ma et al.	2009	Squared, in-line	FC-72	0.04	0.06	0.06	–	–
Yuan et al.	2009	Squared, in-line	FC-72	0.063	0.1	0.1	–	–
Qu and Siu-Ho	2009a	Squared, staggered	Water	0.255	0.4	0.4	$183-420$	$237-2485$
Qu and Siu-Ho	2009b	Squared, staggered	Water	0.255	0.4	0.4	$183-420$	$237-2485$
Kosar et al.	2010	Circular, staggered Circular, staggered Hydrofoil, staggered	R-123 Water Water	0.1 0.1 0.1	0.15 0.35 0.5	0.15 0.15 0.3	$576-1351$	$250-3000$
Krishnamurthy and Peles	2010a	5 Micro-channels containing in-line circular pin fins	HFE 7000	0.1	0.4	0.4	$350-827$	$100-1100$
Chang et al.	2010	Square, In-line Square, In-line	FC-72	0.255 0.127	0.4 0.2	0.4 0.2	$287-431$	$1-100$
Xue et al.	2011	Square, in-line	FC-72	0.04	0.06	0.06	$200-400$	$0-700$
Morshed et al.	2012	Micro-channel containing nano-wires	Water	0.0002	–	–	$46-143.8$	$0-600$

*D_{eq}: Equivalent diameter $((4 \times W_{fin})/\pi)$

2.5 Key Conclusions

- What best defines transition from macro to mini and micro-scale flow passages is not yet clear but the threshold to confined bubble flow is a good transition criterion. Therefore an approach similar to that taken by Kew and Cornwell (1997) seems more likely to lead to a universal classification.
- Flow pattern maps for macro-channels are not generally applicable to mini- and micro-channels. Many of the controlling phenomena and mechanisms change from macro to mini and micro-scale. This is resulted from change in dominant

controlling forces such as surface tension (capillary) and gravity forces from macro to mini and micro-scale flow passages.

- The most dominant flow regimes observed in small scale flow passages were elongated bubble flow (including slug flow or confined bubble flow) and annular flow. Some researchers also reported observing isolated bubble flow (bubbly flow) and several other regimes, such as liquid ring flow and liquid lump flow, which were probably transition regimes.
- Two-phase flows in mini and micro-channels are affected by surface tension force. Therefore both surface roughness and wettability between the flow passages surfaces and the fluid affect the two-phase flow patterns. The general trends of the flow pattern transitions are not so significantly affected by the surface contamination (wettability), except for the fact that the rivulet/multi-rivulet flows are sensitive to the wettability effect (Barajas and Panton, 1993).
- Surface roughness is effective in enhancing nucleate boiling. However, the enhancement is not directly related to the surface roughness parameter.
- The majority of previous experimental investigations of flow boiling in mini- and micro-channels have shown that local flow-boiling heat transfer coefficients are almost independent of vapour quality, weakly dependent on mass flux, fairly dependent on pressure, and strongly dependent on heat flux. Such trends in conventional, mini- and micro-channels propose the nucleate boiling as the dominant heat transfer mechanism.
- Two-phase pressure drops in single and multiple parallel channels and also in pin fin surfaces generally increase with increasing mass flux and/or heat flux. Pressure drop increases with increasing mass flux and vapour content. For the same heat flux, as the mass flux increases, the vapour content decreases, leading to a trend dependent on both mass flux and vapour quality. Two-phase pressure drops are also affected by the flow passages surface roughness.
- In conclusion, the state-of-the-art of two-phase flow and heat transfer in mini and micro-scale flow passages is still in its infancy and much fundamental experimental and analytical work remains to be done.

CHAPTER 3

EXPERIMENTAL RIG

In order to carry out an experimental investigation of flow boiling characteristics, heat transfer coefficients and two-phase pressure drops in small flow passages on a range of fluids including deionised water and refrigerant R113, an experimental rig was designed. The preliminary rig was built before. In this study a series of rig development work including pump and flow meter replacement, relocation of the condenser and secondary cooler, and test section design modification, were carried out. Tests were only carried out at atmospheric pressure but the rig was designed to give a wider range of pressure up to 10 bar. The experimental rig used in obtaining data and the associated uncertainties in measurement are described in this chapter.

3.1. Experimental Rig

Figure 3.1 illustrates the experimental rig. The rig is composed of four major systems, several sub-systems and various components. Four major systems are as follow:

- Liquid flow loop containing the test section
- Condensate cooling system
- High-speed imaging system
- Data acquisition system

The working fluids which were used in the liquid flow loop for each test series were Trichlorotrifluoroethane (R113) and deionised water. R113 is a colour-less and transparent liquid at room temperature without toxicity, corrosion and flammability, but with high stability. It has a very low freezing point of $-35℃$ and a moderate boiling point of $47.57℃$ at normal atmospheric pressure. It has got good dielectric properties like FC-72 and much smaller surface tension than that of water. At $20℃$ R113 has a surface tension of $0.03\ N/m$ compared to $0.073\ N/m$ for water. Table 3.1 presents delegate values for thermo-physical properties of R-113

and water. Bond number (Bo), Capillary length (L), and Confinement number (N_{conf}) values obtained based on the present study flow passages hydraulic diameter, channels with hydraulic diameter of the order of $1\,mm$, for R113 and water at the saturation temperatures and atmospheric pressure are also included in Table 3.1.

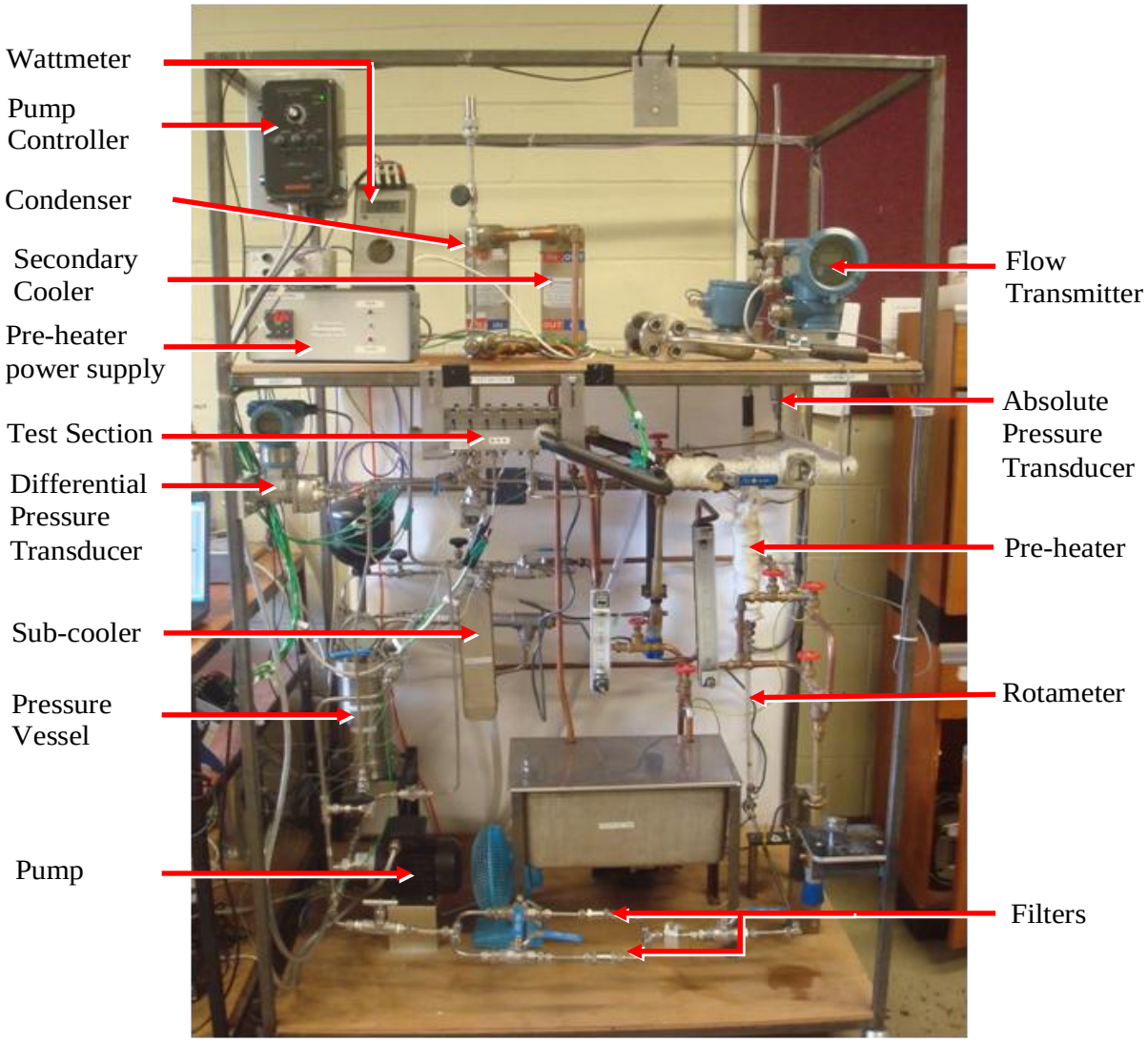

Figure 3.1 Experimental rig

Table 3.1 Thermo-physical properties of R-113 and water at selected conditions (Incropera and Dewitt, 2007; Sonntag et al., 2008)

R113

Molecular Mass $[g/mol]$	Critical Temperature $T_{critical}\ [K]$	Critical Pressure $P_{critical}\ [MPa]$
187.37	487.54	3.411

Bond number (Bo)	Capillary length (L)	Confinement number (N_{conf})
1	1 mm	1

P [bar]	T_{sat} [K]	h_f $[kJ/kg]$	h_g $[kJ/kg]$	ρ_f $[kg/m^3]$
1.0	320.37	242.7	387.36	1510.1
10.0	412.38	335.62	442.31	1240.8

T_{sat} [K]	P [bar]	ρ_f $[kg/m^3]$	k_f $[W/mK]$	μ_f $[Pa.s]$	$C_{P,f}$ $[kJ/kgK]$	σ $[N/m]$
290	0.32391	1580.1	0.0768	0.000763	0.946	0.030
320.7	1.01325	1507.3	0.0705	0.000516	0.984	0.015

Water

Molecular Mass $[g/mol]$	Critical Temperature $T_{critical}\ [K]$	Critical Pressure $P_{critical}\ [MPa]$
18.015	647.3	22.12

Bond number (Bo)	Capillary length (L)	Confinement number (N_{conf})
0.15	2.51 mm	2.51

P [bar]	T_{sat} [K]	h_f $[kJ/kg]$	h_g $[kJ/kg]$	ρ_f $[kg/m^3]$
1.0	372.77	417.44	2675.46	958.77
10.0	179.91	762.79	2778.08	887.31

T_{sat} [K]	P [bar]	ρ_f $[kg/m^3]$	k_f $[W/mK]$	μ_f $[Pa.s]$	$C_{P,f}$ $[kJ/kgK]$	σ $[N/m]$
290	0.0194	998.6	0.598	0.001080	4.184	0.073
373.15	1.01325	957.85	0.680	0.000279	4.217	0.060

The experimental rig major systems, sub systems and components are described as follows.

3.1.1. Flow Loop

Figure 3.2 illustrates the schematic of flow loop that supplies the liquid coolant to the heat sink at desired operation conditions. Liquid coolant was pumped from the pressure vessel and circulated through the flow loop. The accumulator, which connected to the pressure vessel, provided precise pressure for the coolant fluid. The pressure vessel was completely filled with liquid to reduce the mass flow rate fluctuations. The Pump supplied the motive force for the coolant fluid to circulate through the loop. Upon exiting the fluid from the pump a portion of the flow returned to the pressure vessel through a by-pass loop. Valves in the by-pass and main lines allowed the desired mass flow rate to be set. The remaining portion of the liquid entered the test loop containing the test section and was passed through the filter. The coarse filter ($250\ \mu m$) was used initially to remove large debris. The finer ($50\ \mu m$) filter was used during testing, to prevent any particles from blocking the test piece mini-size flow passages. Liquid was then passed from the filter to the flow meter for mass flow rate measurements. From the flow-meter, the liquid was passed through a pre-heater, where the liquid temperature was set to obtain a subcooling of between 2 and 12℃ before it passed through a sight glass, where visual observation confirmed liquid only at entry into the test section. At the top of the pre-heater another sight glass with a valve was designed, which was connected to outside for fine degassed fluid flow control. The liquid then was entered the test section, where boiling occurred. The test section and the related components are fully described in section 3.1.3. Fluid from the test section was passed to a T-piece, where the liquid and vapour were separated. The vapour moved vertically upwards and was condensed in the condenser before being re-united with the separated liquid that flowed vertically downwards. Another valve was installed at the top of the condenser which allowed the non-condensable gases to be removed. The condensate and liquid flow then passed through a sub-cooler before returning to the pressure vessel. The condenser and sub-cooler were connected to the laboratory tap water supply, with separate circuits and control. The condensate cooling system is described in Section 3.1.5.

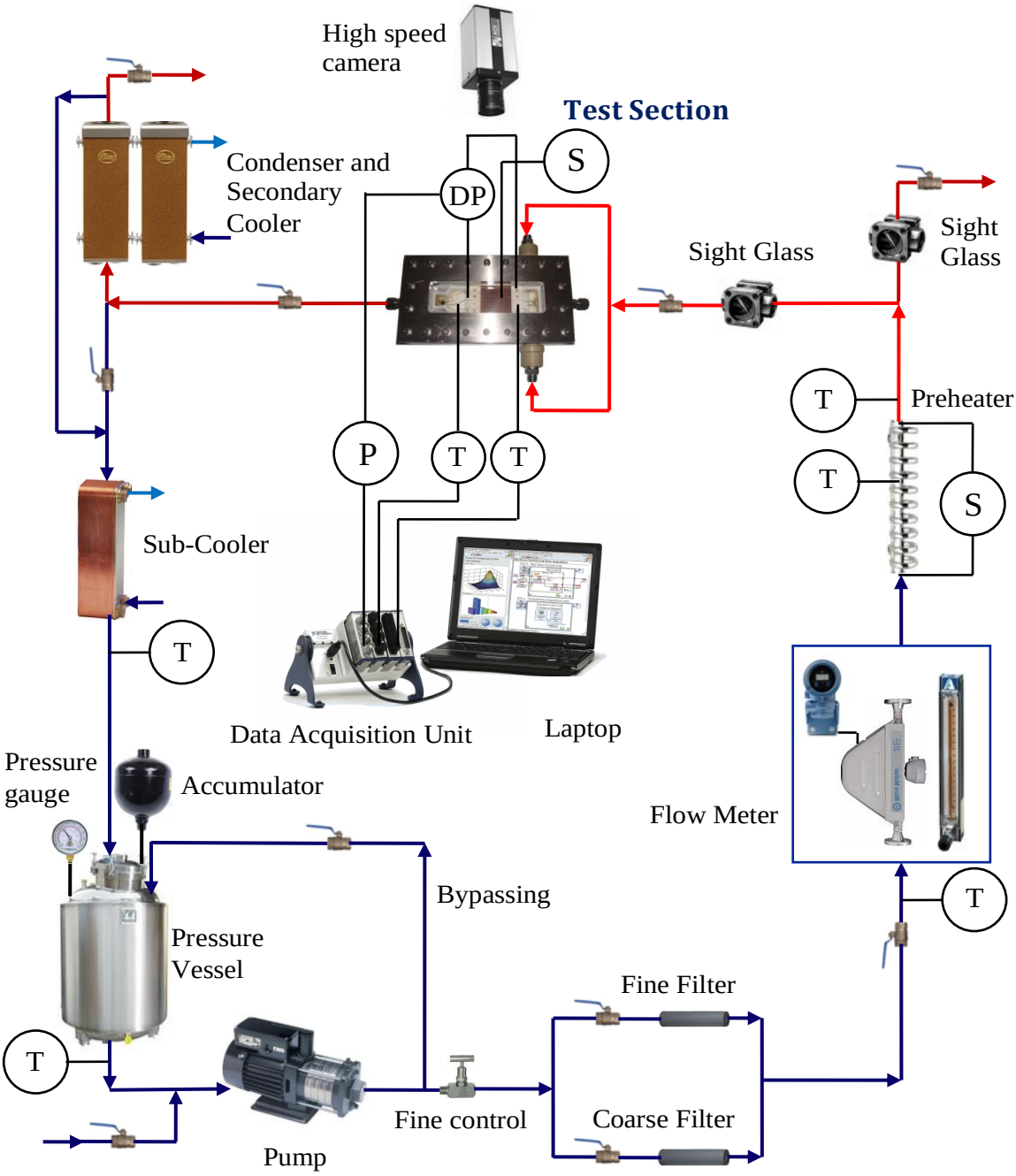

Figure 3.2 Schematic of flow loop

3.1.2. Flow Loop Components Specifications

The specifications of the flow loop's key components; such as pump, filters, flow meter, pre-heater, condenser and sub-cooler are described in this section. The test section is fully described in section 3.1.3.

❖ ***Pump***

As it was mentioned in chapter two, five test series were carried out for different geometries and different working fluids. For the first two test series, in-line pin-fin and plate channel test pieces with R113 as working fluid, a multi-chamber diaphragm pump was used, Figure 3.3a. The diaphragm pump was replaced with a micro motion gear pump for next series of tests, off-set pin-fin and parallel channel test pieces with R113 as working fluid and in-line pin-fin test piece with water as working fluid. The micro motion magnetic drive gear pump, magnetically coupled to a TEFC inverter rated motor. Figure 3.3b illustrates the Micro motion Pump with TEFC motor. The pumps specifications are shown in Table 3.2.

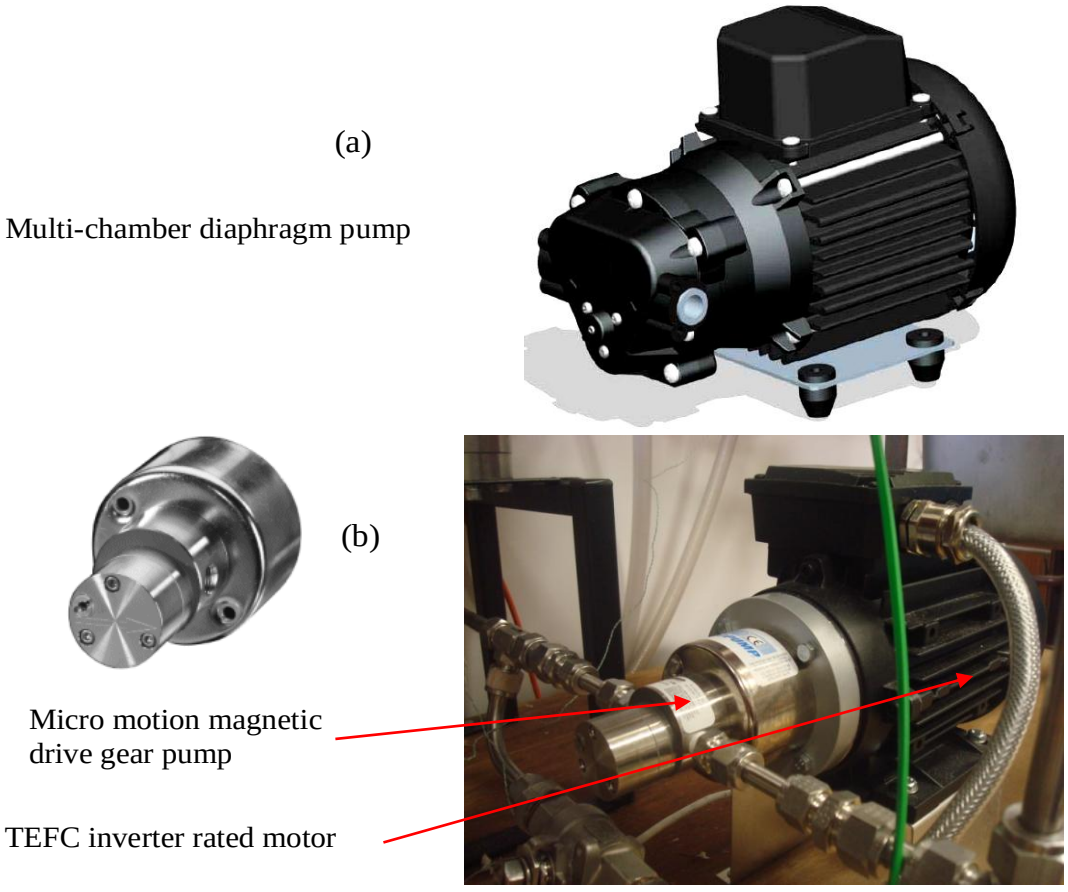

Figure 3.3 (a) Multi-chamber diaphragm pump, (b) Micro motion gear pump

Table 3.2 Pumps specifications

Multi-chamber Diaphragm Pump				
Model	Overall height	Overall length	Overall width	Weight
AD 4/90	149 mm	210 mm	98 mm	3.8 kg
Max body pressure	Max flow rate	Closed valve head	Temp range	Motor output
20 bar	3000 ml/min	89 m	$0 - 77$ ℃	55 W
Micro Motion Magnetic Gear Pump				
Model	Gear material	Static seals	Pump body material	Max speed
GJ-N23	PTFE	PTFE	316 stainless steel	10,000 rpm
Max system pressure	Max differential pressure	Max flow rate	Viscosity range	Max Temp
21 bar	1 bar	1500 ml/min	$0.2 - 1500$ cp	200 ℃

❖ *Filters*

Two Parker F6 Series filters were used in the flow loop to remove debris in order to prevent any particles from blocking the test piece mini-size flow passages. Figure 3.4 illustrates a typical shape of the filters. The filters specifications are shown in table 3.3.

Figure 3.4 Filters

Table 3.3 Filters specifications

50 μm F6 Series Parker Filter			
Model	Configuration	Body material	Seal material
M10A-F6L-50-T-SS	In-line	Stainless steel	PTFE
Internal diameter	Micron rating	Pressure rating	Temperature rating
10 mm	50	276 bar	-54 to 204 ℃
250 μm F6 Series Parker Filter			
Model	Configuration	Body material	Seal material
M10A-F6L-250-T-SS	In-line	Stainless steel	PTFE
Internal diameter	Micron rating	Pressure rating	Temperature rating
10 mm	250	276 bar	-54 to 204 ℃

- ***Flow Meter***

In order to measure the mass flow rate for first two test series; in-line pin-fin and plate channel test pieces with R113, a micro motion coriolis mass flow-meter was used. The setup was consisted of two parts; a Micro Motion Coriolis ELITE Mass Flow-meter with accuracy of $\pm 0.1\%$ of reading, Figure 3.5a, and a Micro Motion Coriolis MVD flow transmitter, Figure 3.5b. The micro motion coriolis flow-meter was replaced with a size-7 rotameter, Figure 3.5c, for next series of tests; off-set pin-fin and parallel channel test pieces with R113 and in-line pin-fin test piece with water as working fluid. The liquid flow rate was measured to $\pm 1.5\%$ of reading in the rotameter. The rotameter was calibrated on working fluid using the 'Calibrating Data for Metric Series Rotameters' handbook (Rotameter manufacturing company limited). The rotameter calibration calculations are shown in Appendix A. The micro motion mass flow-meter and rotameter specifications according to the calculations and calibration are shown in Tables 3.4 and 3.5 respectively.

Table 3.4 Micro motion mass flow meter specifications

Micro Motion Coriolis ELITE Mass Flow-meter				
Model	Mass flow accuracy at Max flow	Density accuracy at all rates	Pressure drop at Max flow	Velocity at Max flow
CMF010M	$\pm 0.1\%$	± 0.5 kg/m^3	0.311 bar	2.37 m/s
Flow rate range	Max Pressure	Temperature range	Viscosity range for water	Density range for water
0.1-15.0 g/sec	10.0 bar	15-100 ℃	958-999 kg/m^3	0.28-0.89 cp
Micro Motion Coriolis MVD flow transmitter				
Model	Power	Display option		
1700	$18-30$ V DC $85-265$ V AC	Dual line display for process variables and totalizer reset		

Table 3.5 Rotameter specifications

Size 7 Rotameter with R113 as working fluid				
Type	Length	Metering head diameter	Float material	Float weight
Size 7	30 cm	7.6 mm	Stainless Steel	2.48 g
Flow rate range	Scale reading range	Mass flow accuracy	Working temperature	Working pressure
4.01-20.04 g/s	$3.1-26.8$ cm	$\pm 1.5\%$	18 ℃	1 bar
Size 7 Rotameter with deionised water as working fluid				
Type	Length	Metering head diameter	Float material	Float weight
Size 7	30 cm	7.6 mm	Korannite	0.775 g
Flow rate range	Scale reading range	Mass flow accuracy	Working temperature	Working pressure
0.995-8.95 g/s	$1.6-27.2$ cm	$\pm 1.5\%$	18 ℃	1 bar

(a) (b) (c)

Figure 3.5 (a) Micro Motion Coriolis ELITE Mass Flow-meter, (b) Micro Motion Coriolis MVD flow transmitter, and (c) Size-7 rotameter

❖ ***Pre-heater***

Two Watlow Watrod tubular heaters were used before the test section to set the fluid temperature to desired value before entering the test section, Figure 3.6. The heaters were wrapped around a copper tube through which the test fluid flowed. The tube and heaters were insulated with mineral wool. The tubular heaters were 3 cm in diameter and 3 and 23 cm in length, in order to generate to different range of 200 and 2000 W heat, respectively. Table 3.6 shows the Watlow Watrod tubular pre-heater specifications.

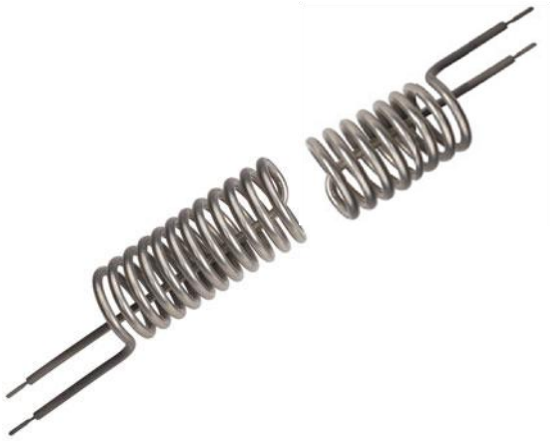

Figure 3.6 Watlow Watrod tubular heaters

Table 3.6 Watlow Watrod tubular heater specifications

Heater 1						
Model	Material	Diameter	Length	Max. Operating temperature	Max. Watt densities	Max. Heat
Watrod tubular	Stainless steel	3 cm	3 cm	650 ℃	9.3	200 W
Heater 2						
Model	Material	Diameter	Length	Max. Operating temperature	Max. Watt densities	Max. Heat
Watrod tubular	Stainless steel	3 cm	23 cm	650 ℃	9.3	2000 W

Pre-heater was insulated with a PTFE band, in order to decrease the heat loss from heater to the ambient.

- ***Condenser and Secondary Cooler***

Two Brazed Plate Heat Exchangers were used in condensate cooling system, one as the condenser, in order to condense the vapour leaving the test section, and another one as the secondary cooler, allowing the temperature of the coolant to be controlled. Figure 3.7 illustrates the condenser and secondary cooler set up. Table 3.7 shows the Brazed Plate Heat Exchanger specifications, which used as condenser.

Figure 3.7 Condenser and secondary cooler

Table 3.7 Specifications of the Brazed Plate Heat Exchangers, used as condenser and secondary cooler

Brazed Plate Heat Exchanger				
Model	Number of plates	Heat transfer area	Plate material	Gasket material
SL32-BR25-OB-40-TL-COND	40	1.28 m^2	0.4 mm AISI 316	Copper brazed
Max. working Temperature	Max. working Pressure	Liquid hold up volume	Weight empty	Frame type
100.0 ℃	20.0 bar	2 dm^3	6 kg	BR

❖ ***Sub-cooler***

A Brazed Plate Heat Exchanger was used in condensate cooling system, as the sub-cooler, in order to decrease the condensate liquid temperature to an ideal temperature, before returning to the pressure vessel, Figure 3.8. The sub-cooler specifications are shown in Table 3.8.

Figure 3.8 Sub-cooler

Table 3.8 Specifications of the Brazed Plate Heat Exchanger, used as sub-cooler

Sub-cooler				
Model	Number of plates	Heat transfer area	Plate material	Gasket material
SL23-BR25-AA-10-TL	10	0.19 m^2	0.4 mm AISI 316	Copper brazed
Max. working Temperature	Max. working Pressure	Liquid hold up volume	Weight empty	Frame type
185.0 ℃	12.0 bar	0.5 dm^3	2 kg	BR

3.1.3. Test Section

Figure 3.9 illustrates the construction of the test section which is composed of a stainless steel clamping plate, a transparent glass cover plate, a copper test piece which includes mini flow passages, an aluminum housing, Internal PTFE Insulation, a ceramic heater, a PTFE block with securing plate, and thermocouples.

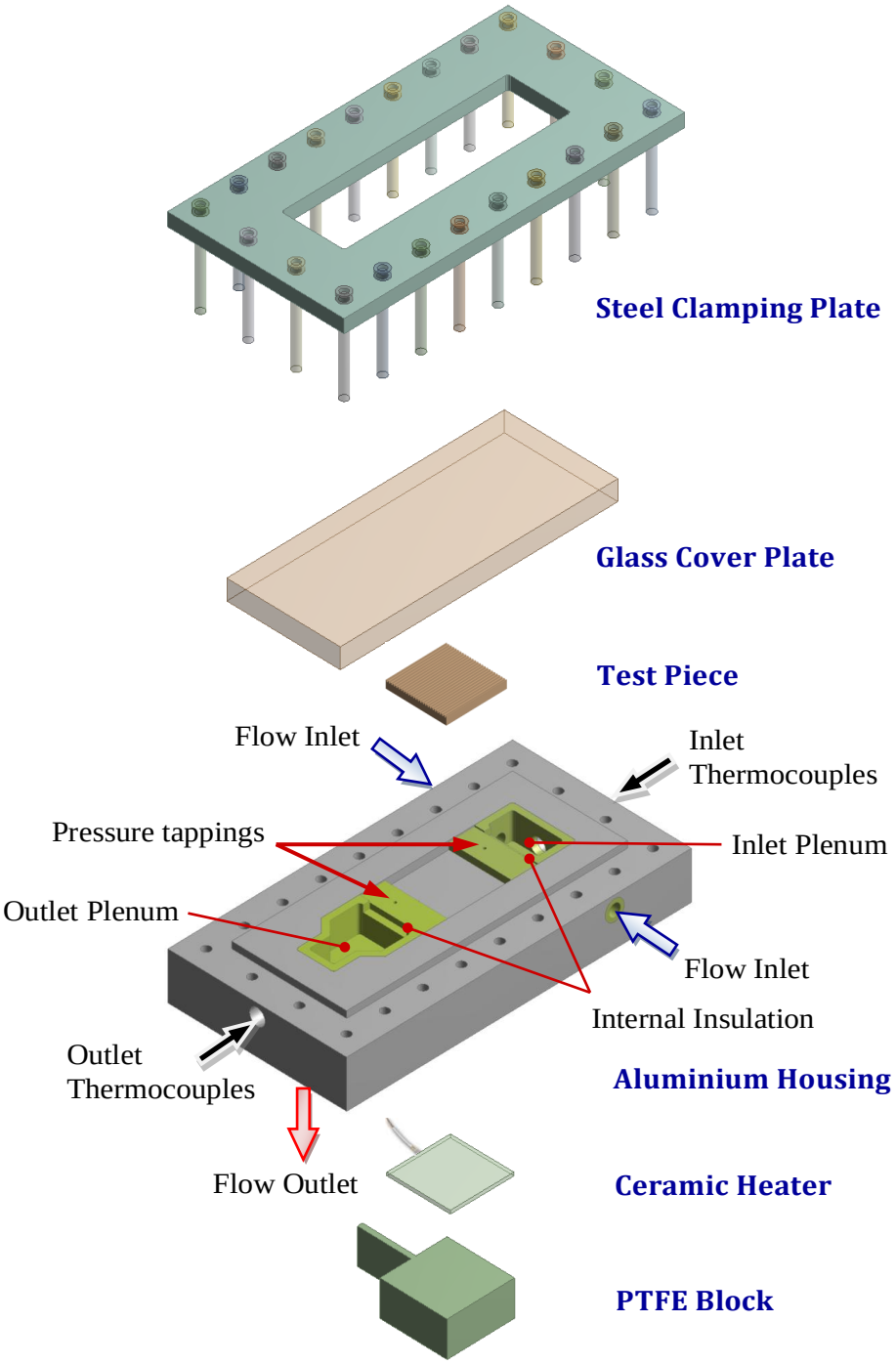

Figure 3.9 Test section construction

The longitudinal cross-section of the test section assembly without internal PTFE insulation is illustrated in Figure 3.10a. A numerical simulation was carried out to predict the conducted heat distribution in the aluminum housing in order to optimize the applied heat flux from heater to the test piece, which is fully described in Chapter 4. This led to a layer of PTFE insulation being placed on all internal fluid-aluminum interfaces. Figure 3.10b illustrates the longitudinal cross-section of the test section assembly with internal PTFE insulation.

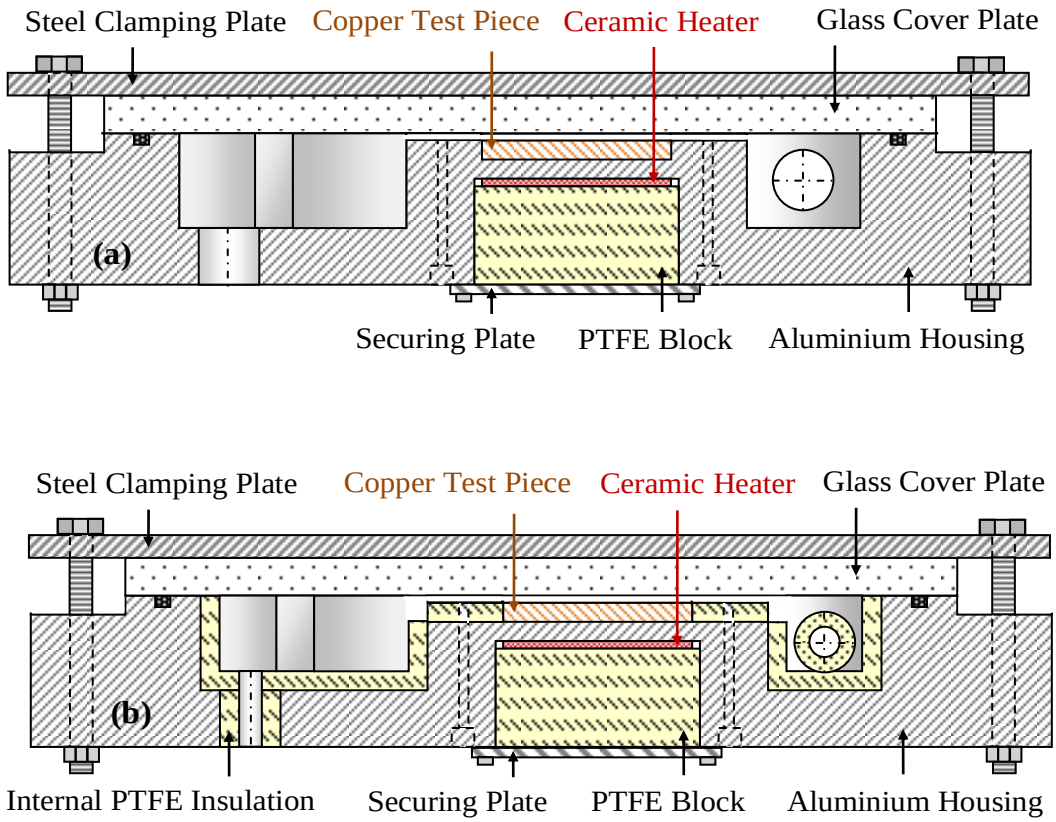

Figure 3.10 Longitudinal cross-section of the test section assembly, (a) without internal insulation, (b) with internal insulation

The housing contains inlet and outlet plenums, inlet and outlet ports, pressure tappings, temperature instrumentation ports and O-ring groove. Recesses were machined in the top central part of the housing, where the copper test piece was inserted, and the bottom central part to accommodate the heater and PTFE block.

A groove was machined into the housing top surface, around the test piece and inlet and outlet plenums. A rubber O-ring filled the groove to maintain leak-proof assembly. Liquid entered the inlet plenum of the test-section through the two inlet

ports, set at 90° to the direction of flow in the test piece to ensure even flow distribution. Video recording and flow visualization confirmed the even flow distribution during all test series. The inlet plenum dimensions were set to reduce the liquid velocity to close to zero before it accelerated into the settling length upstream of the test piece, Figure 3.11.

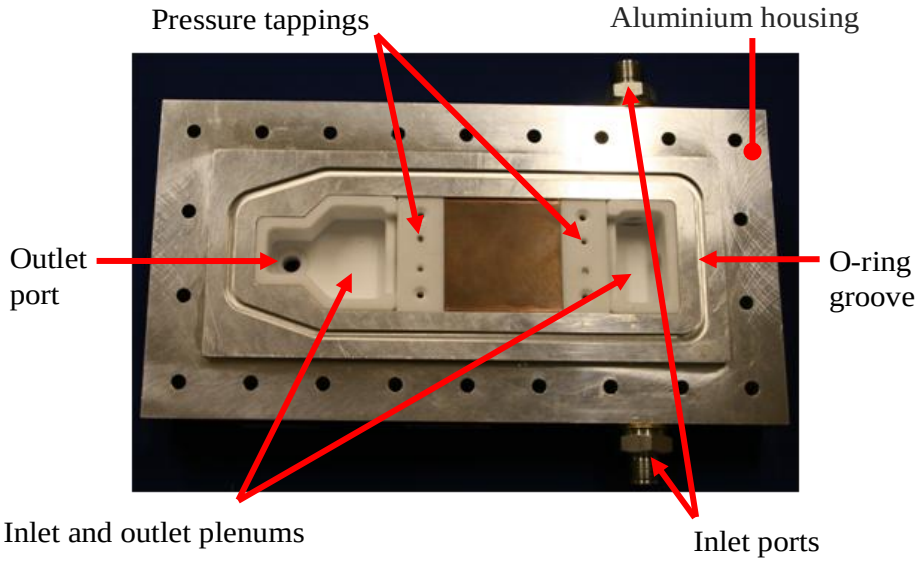

Figure 3.11 Test section open view with internal insulation

Two sheathed type-K thermocouples were located in the inlet and outlet plenums, upstream and downstream of the test piece, to measure the inlet and outlet temperatures, Figure 3.12. Thermocouples were calibrated in a water bath. Calibration of the thermocouples is described in Appendix B. The thermocouples specifications are shown in Table 3.9.

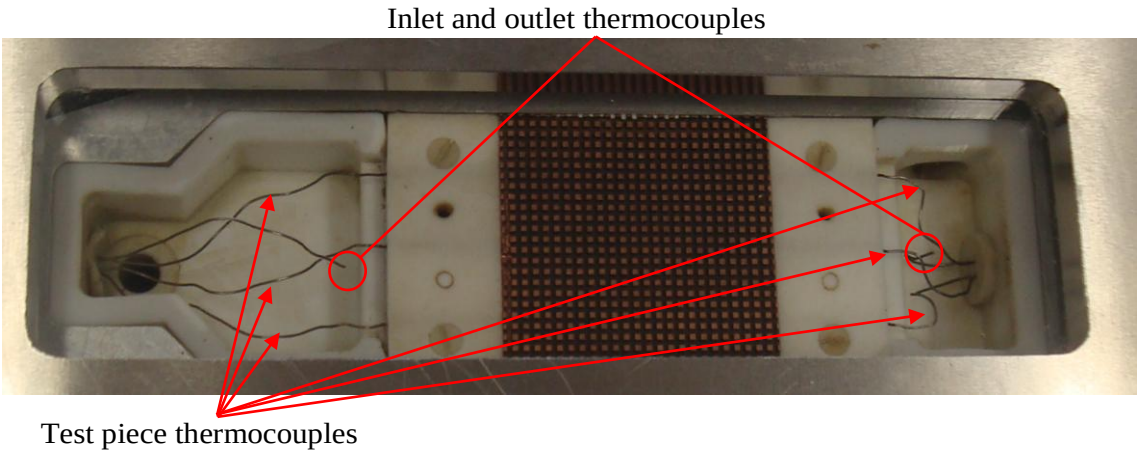

Figure 3.12 Test section top view, showing the thermocouples

Table 3.9 Test piece and, inlet and outlet plenums thermocouples specifications

Mineral insulated thermocouples					
Type	Plug type	Length	Diameter	Sheath material	Accuracy
K	Miniature flat pin plug	$200\ mm$	$0.5\ mm$	310 Stainless steel	$\pm 0.1\ K$

Pressure tappings were located just upstream and downstream of the test piece. The liquid inlet pressure was measured at the upstream tapping with an SENSIT OEM absolute pressure transducer accurate to $\pm 0.2\%$ of reading, Figure 3.13. The absolute pressure transducer specifications are shown in Table 3.10.

Figure 3.13 Absolute pressure transducer

Table 3.10 Absolute pressure transducer specifications

SENSIT OEM pressure transmitter				
Model	Pressure range	Excitation	Output-span	Output-zero
M6420-50	$0 - 12\ bar$	$10 - 32\ Vdc$	$16mA \pm 1\%$ of span at zero Pressure	$4mA \pm 1\%$ span
Output	Operating Temp. range	Thermal zero shift	Thermal span shift	Output resistance
$4 - 20\ mA$	$-25\ to\ 80$ ℃	$< \pm 0.08\%$ of span/℃	$< -0.04\%$ of reading/℃	$> 10M\Omega$

The pressure difference across the tappings was measured with a Rosemount differential pressure transducer, model $3051C$. Figure 3.14 illustrates the differential pressure transducer. This was a smart transducer that allowed the pressure drop range to be set prior to testing. The transducer was accurate to $\pm 0.25\%$ of reading. The pressure transducer's specifications are shown in Table 3.11.

Figure 3.14 Rosemount differential pressure transducer

Table 3.11 Differential pressure transducer specifications

Rosemount differential pressure transducer		
Model	Measurement type	Output
$3051C$	Differential	$4-20\ mA$ Hart
Reference accuracy	Total performance	Long term stability
$\pm 0.065\%$ of span with 0.04% optional	$\pm 0.15\%$ of span	$\pm 0.125\%$ of URL for 5 years

The fluid boiled as it passed across the test piece. Heat was supplied to the test section from a Watlow Ultramic ceramic heater. Table 3.12 illustrates the heater specifications. The heater was $50\ mm$ square and was placed at the bottom central

part of the housing, below the test piece. Its heat generation range was up to 2 kW. One type-K thermocouple was integrated into the heater assembly by the manufacturer to measure the heater temperature and improve the accuracy with optimised temperature sensing, Figure 3.15.

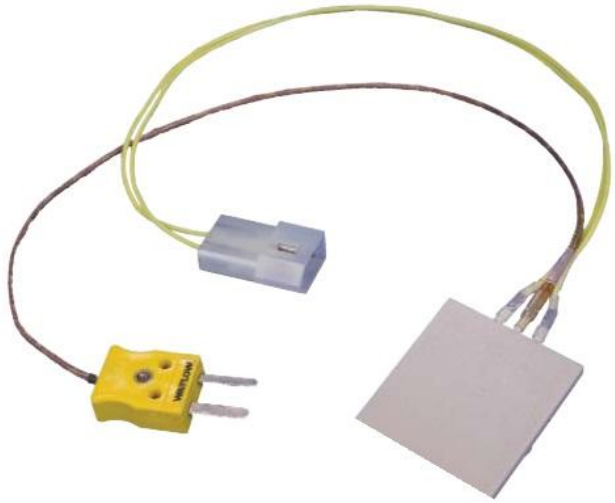

Figure 3.15 Heater with integral thermocouple and power supply cable

Table 3.12 Watlow Ultramic ceramic heater specifications

Watlow Ultramic Ceramic Heater				
Model	Size	Watts	W/cm^2	Voltage
Ultramic 600	$50\ mm \times 50mm \times 2.5mm$	1938	77.52	240
Thermal conductivity	Surface temperature	Terminal temperature	Max. Ramp rate	Surface finish
140 W/mK	600 ℃	400 ℃	150 ℃/s	$< 0.8\ \mu m$

The heater was fixed to the test section by a PTFE block and a securing plate, Figure 3.16. The PTFE block was located between the securing plate and the heater to minimize heat transfer from the lower surface of the heater, Figure 3.10. Power to the heater was adjusted to give the required heat flux. The heat load was measured with a RS wattmeter to $\pm 1\%$ of reading.

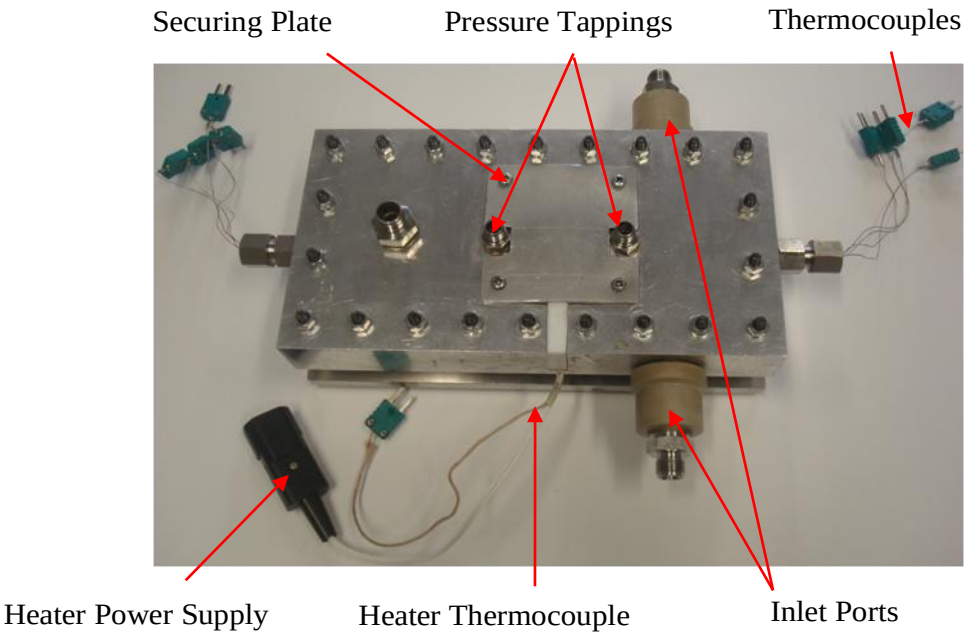

Figure 3.16 Test section bottom view

Closed channels and the inlet and outlet plenums were formed by clamping a glass cover plate from the top. The transparent cover plate allowed visualization to the boiling phenomena occurring inside the channels.

3.1.4. Description of the Test Pieces

With the aim of investigation and comparison of flow boiling characteristics, heat transfer coefficient, and pressure drop in diverse mini multi-channel geometries, with and without interconnecting passages, four different test pieces were fabricated, each containing different mini flow passages features. Each test piece was constructed from a piece of oxygen-free copper, $50\ mm$ wide by $50\ mm$ long and $6\ mm$ high. Channels and pin fins geometries were formed by micro-slotting the top surface of the copper block. All test pieces geometries are described as follow.

❖ *Plate Channel Test Piece*

The plate channel test piece is shown in Figure 3.17. A single channel was formed by cutting the top surface of the copper block, $49mm$ wide and $1mm$ deep in the longitudinal direction. Therefore a single channel, $49mm$ wide and $50mm$ long, with a fluid hydraulic diameter ($D_{h,fluid}$) of $1.96\,mm$ and a heat hydraulic diameter ($D_{h,heat}$) of $3.84\,mm$ obtained. Fluid and heat hydraulic diameters were evaluated from

$$D_{h,fluid} = \frac{4A}{P_{wetted}} \tag{3.1}$$

$$D_{h,heat} = \frac{4A}{P_{heated}} \tag{3.2}$$

where A and P are the channel cross sectional area and cross section perimeter.

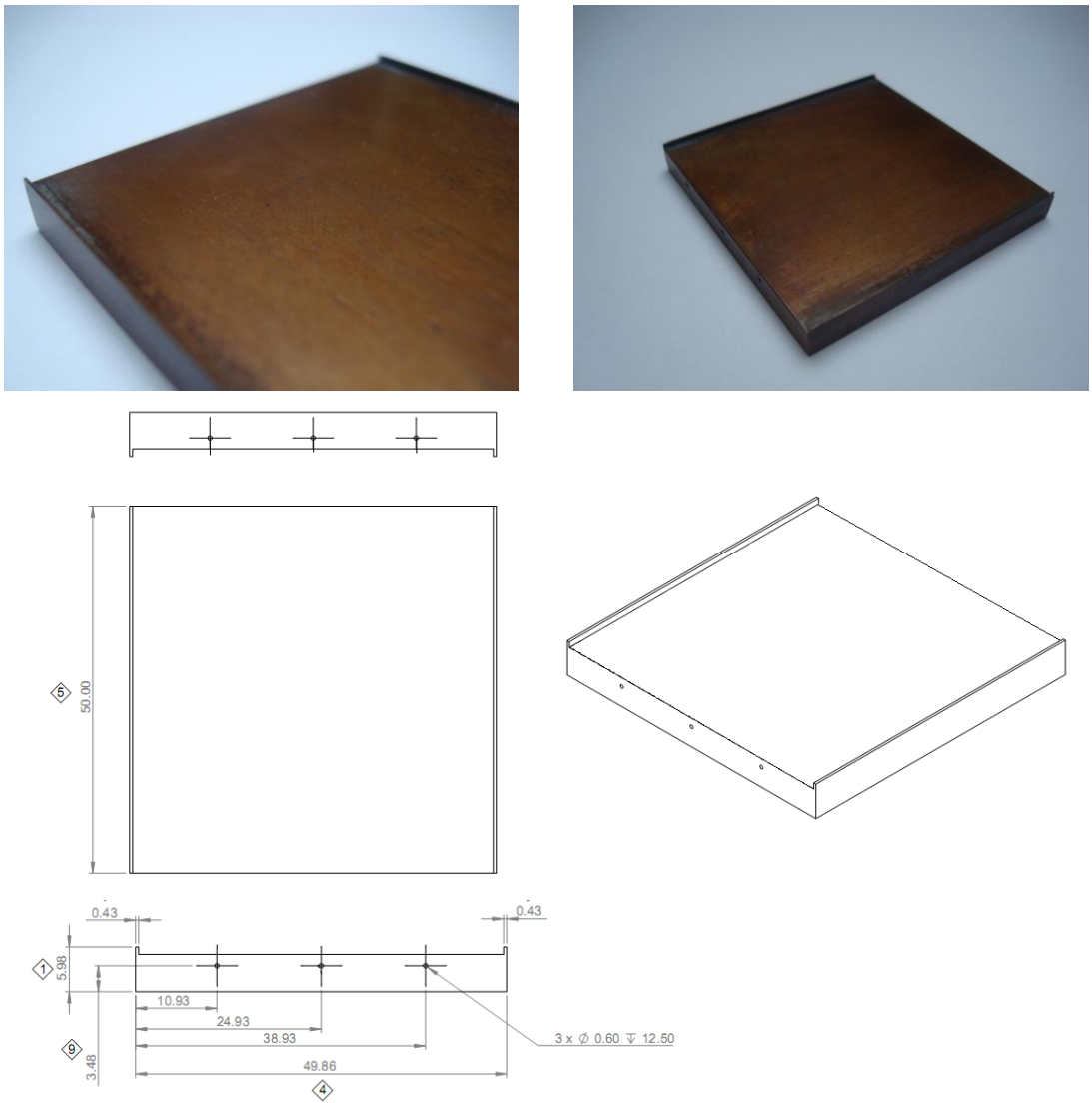

Figure 3.17 Plate channel test piece

❖ *Parallel Channel Test Piece*

The parallel channel test piece is shown in Figure 3.18. The geometry was formed by cutting slots $1mm$ wide and $1mm$ deep in the longitudinal direction. The slots are $1mm$ apart, therefore 25 parallel channels with $1mm$ square cross-sectional area, a length of $50\,mm$, and a fluid hydraulic diameter of $1\,mm$ and a heat hydraulic diameter of 1.33 mm obtained.

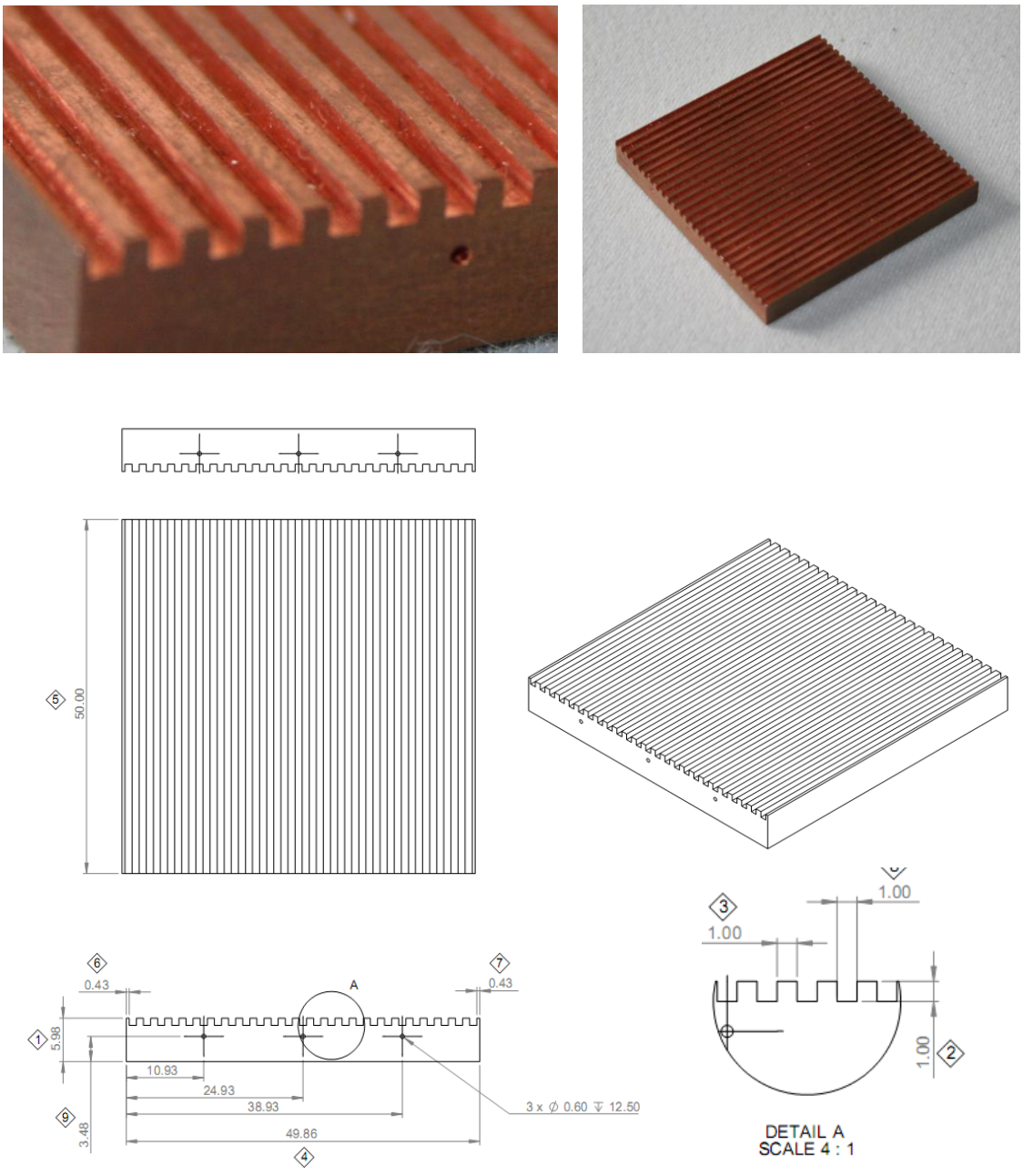

Figure 3.18 Parallel channel test piece

❖ *In-Line Pin-Fin Test Piece*

The in-line pin-fin test piece is shown in Figure 3.19. The complex geometry was formed by cutting slots $1mm$ wide and $1mm$ deep in the longitudinal and transverse directions. The slots are $1mm$ apart, therefore a surface containing square pin-fins 1 mm wide and 1 mm high placed in an in-line arrangement with a 2 mm pitch obtained.

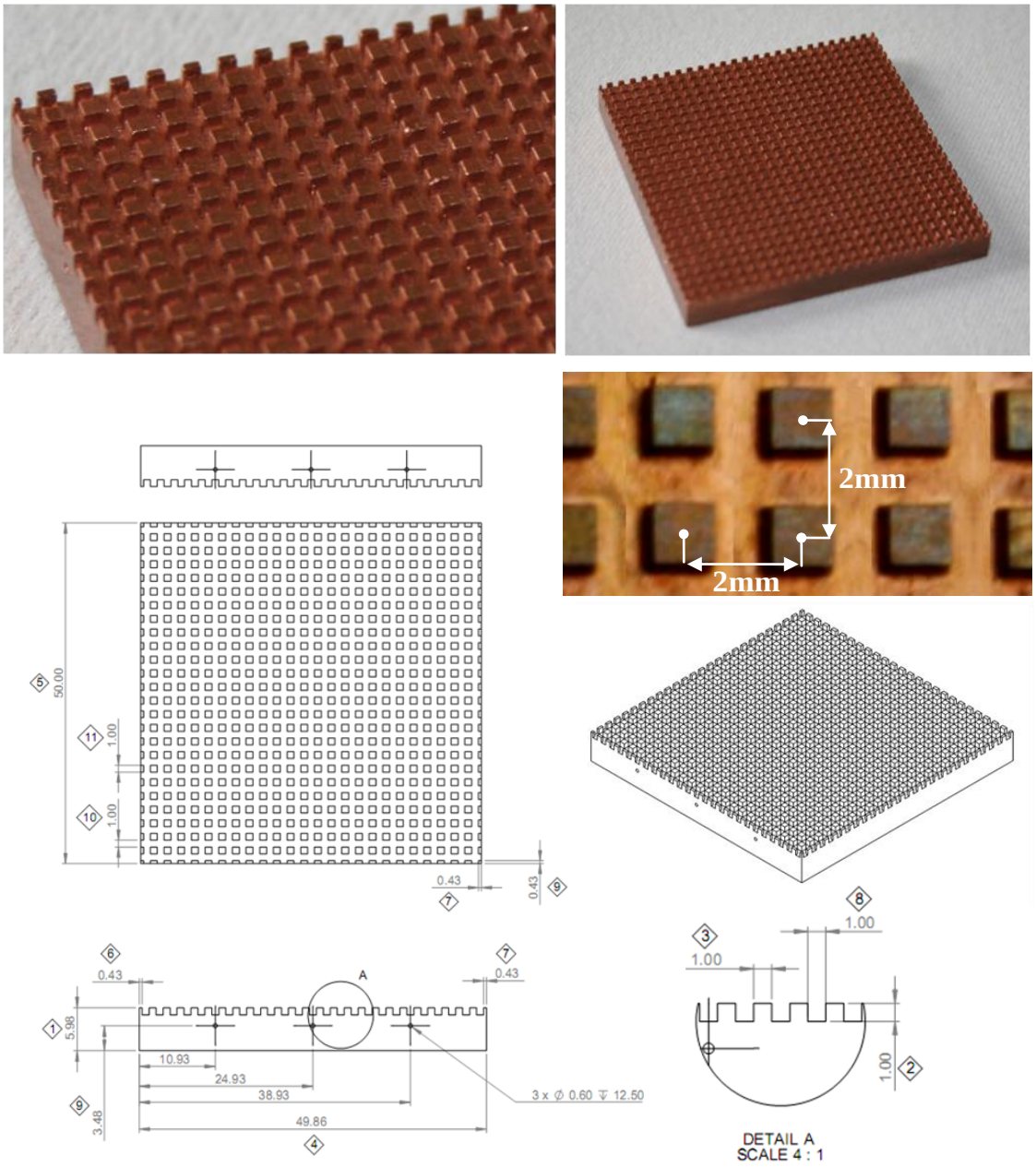

Figure 3.19 In-line pin-fin test piece

❖ *In-Line Off-set Pin-Fin Test Piece*

The in-line off-set pin-fin test piece is shown in Figure 3.20. The complex geometry was formed by cutting slots $1mm$ wide and $1mm$ deep in longitudinal direction. Remained material removed from fins with a $4mm$ pitch in transverse direction to produce off-set arrangement. Therefore a surface containing square pin fins $1\ mm$ wide and $1\ mm$ high placed in a rotated isosceles triangle arrangement with a $4\ mm$ transverse pitch and a $1mm$ longitudinal pitch is obtained.

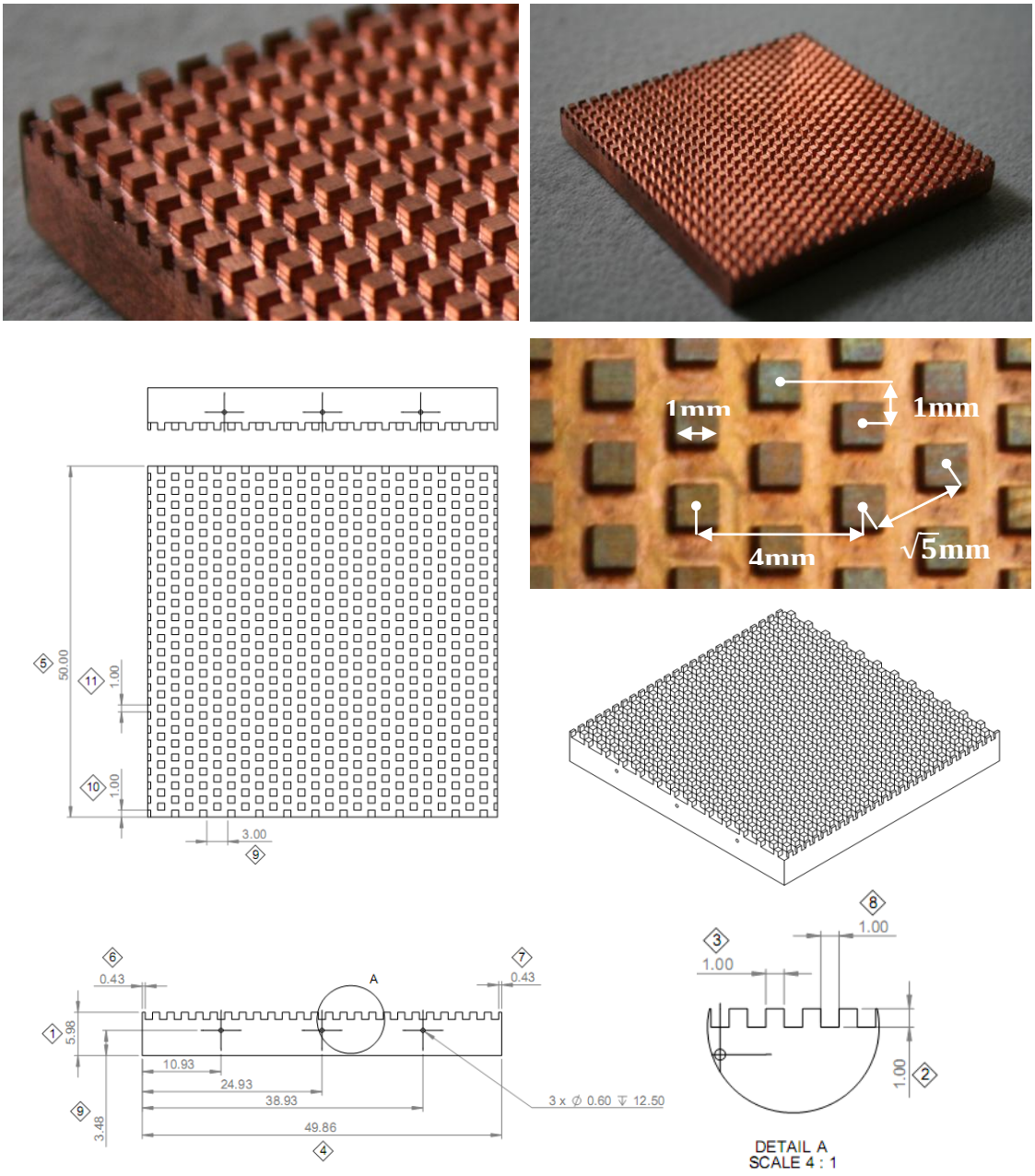

Figure 3.20 In-line off-set pin-fin test piece

As copper metal is oxidised to black copper oxide by air after a while, each test piece was used once for each series of tests after manufacture.

Six holes, $0.6\ mm$ in diameter by $12.5\ mm$ long, were drilled into the each test piece, three at the inlet and three at the outlet ends. The holes were located $2.5\ mm$ from the top of the boiling surface and 11, 25 and $39\ mm$ from an edge, as were shown in Figure 3.17 to 3.20. These holes accommodate six sheathed type-K thermocouples, $0.5\ mm$ in diameter, below the boiling surface to measure the temperature distribution inside the test piece. All thermocouples were calibrated in a water bath, Appendix B, and were accurate to $\pm 0.1\ K$. The transverse locations of these thermocouples are shown in Figure 3.21. A thermal paste was used inside the holes to ensure good contact between the thermocouples and the copper test piece. The thermal paste also was used between the heater and aluminium housing and, copper test piece and aluminium housing to ensure a better thermal conductivity.

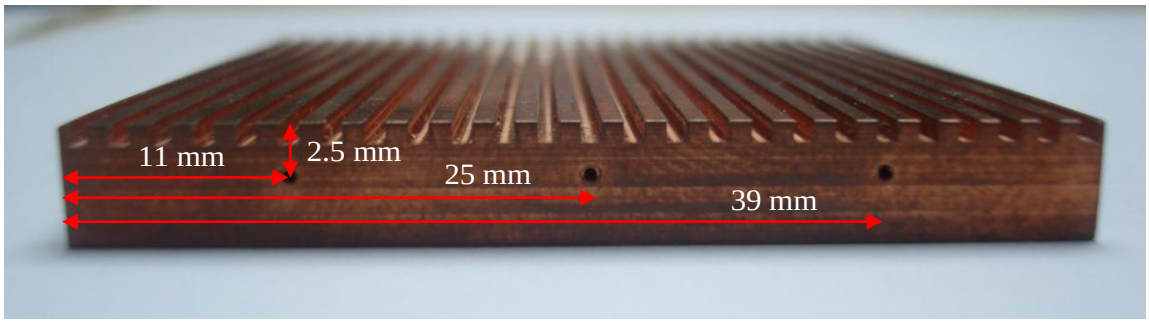

Figure 3.21 The longitudinal locations of the test pieces thermocouples

3.1.5. Condensate Cooling System

The Condensate cooling system was completely isolated from the liquid flow loop containing the test section, and was connected to the laboratory tap water supply. It supplies water to the condenser and sub-cooler to condense the exited vapour from the test section and decrease the condensate liquid temperature before returning to the pressure vessel. Figure 3.22 illustrates the schematic of condensate cooling system. As it is shown, the condensate cooling system was composed of two separated circuits.

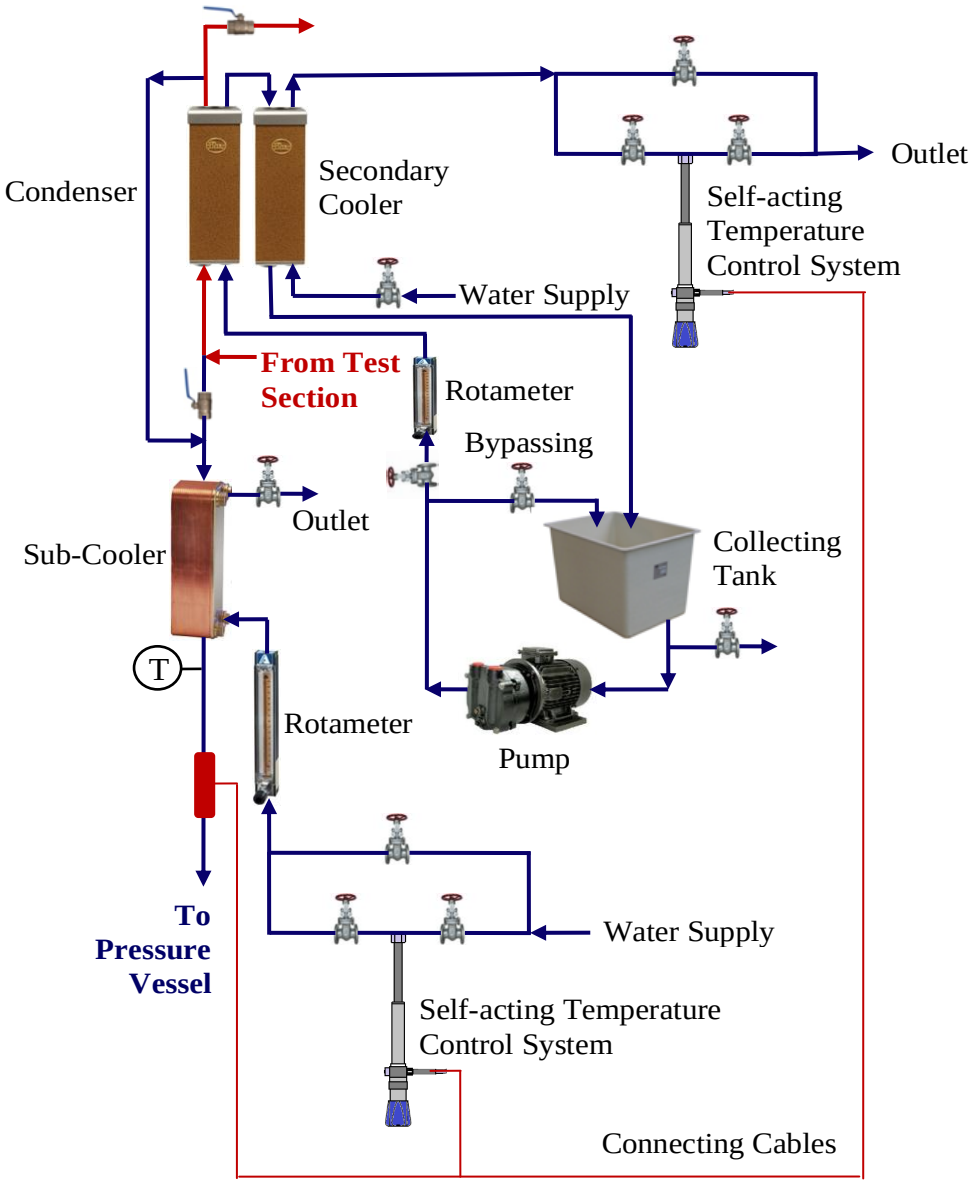

Figure 3.22 Schematic of condensate cooling system

3.1.6. Data Acquisition System

A data acquisition system was used to convert the resulting samples into digital numeric values that can be manipulated by a PC. The pressure transducers were connected to an NI 9205 unit, while the thermocouples were connected to four NI 9211 thermocouple differential units. All units were connected to a NI cDAQ-9172, Legacy NI CompactDAQ Chassis. Table 3.13 illustrates the NI units' specifications. NI CompactDAQ Chassis and connected units are shown in Figure 3.23.

Table 3.13 NI units' specifications

NI 9205				
Product name	Form factor	Operating system	Measurement type	Channels
NI 9205	CompactDAQ	Windows	Voltage	32
Resolution	Voltage range	Operating temperature	Isolation type	Ch-to-COM
16 $bits$	$-10\ to\ 10\ mV$	$-40\ to\ 70$ ℃	Ch-Earth isolation	$\pm 1.5\ V$
NI 9211				
Product name	Form factor	Operating system	Measurement type	Channels
NI 9211	CompactDAQ	Windows	Temperature, thermocouple, voltage	4
Resolution	Voltage range	Operating temperature	Isolation type	Ch-to-COM
24 $bits$	$-80\ to\ 80\ mV$	$-40\ to\ 70$ ℃	Ch-Earth isolation	$\pm 1.5\ V$

(a) **(b)** **(c)**

Figure 3.23 (a) NI cDAQ-9172 Chassis, (b) NI 9211 unit, (c) NI 9205 unit

The readings of thermocouples and pressure transducers were recorded using a PC, and controlled with LabVIEW software. The LabVIEW programme front panel and block diagram figures are shown in Appendix C. The temperature, pressure, and pressure drop readings were obtained over a 40 s period, during which 2000 readings of each were obtained. This gave reproducible average values for all.

3.1.7. High-Speed Imaging System

A high speed imaging system was used for the visualization study, to investigate the two-phase flow behaviour in the small flow passages. A Kodak micro-motion 1000 camera was located above the test section, immediately above the test piece, to take high speed videos of the boiling occurring on the test piece. The camera is shown in Figure 3.24a.

(a) **(b)**

Figure 3.24 (a) The Kodak high-speed camera with a Cosmicar lens, (b) The lighting system

High shutter speed and high magnification are two important necessities for capturing the complicated interfacial features in the small-scales. The Kodak camera system which was used in the present study has frame speeds up to 400 frames/s. During the experiments, camera was set to 240 frames/s at a resolution of 720×480 pixels. However, practical shutter speeds depends on the lighting system. Lighting was provided by two flash sources as illustrated in Figure 3.24b. Flashes were connected by cable to the motion-corder analyzer and were fitted with a flexible hanger on the top of the test section and focused the light on the region of the test piece. To achieve high magnifications, a Cosmicar lens was used. It provided 1.8 to 22 magnifications and a 12.5 to 75 mm field of view. To have a higher quality of capturing two different Hoya $49mm$ eyepieces were used.

3.2. Measurements Uncertainty

The heat loss in the test section and determination of accurate value of the supplied heat flux to the test piece was the major concern in this study. A numerical simulation was carried out to investigate the heat loss in the test section and optimize the design of the test section to avoid heat dissipation in the test section, which is described in Chapter 4.

Apart from this major uncertainty, other minor uncertainties were including the uncertainties in the temperature measurements which were $\pm 0.1\,K$ for thermocouples readings, and accuracies of other measurement instruments; $\pm 0.1\%$ for the micro-motion, coriollis, mass-flow meter, $\pm 1.5\%$ for the size-7 rotameter readings, $\pm 0.2\%$ and $\pm 0.25\%$ for the absolute pressure transducer and the differential pressure transducer readings respectively. The accuracy of RS wattmeter, which was used for measuring the heat load, was $\pm 1\%$ of reading. A summary of the measurement instruments accuracies based on the measured parameters are shown in Table 3.14.

Table 3.14 Measurement instruments accuracies base on the measured parameters

Temperature	
Measurement Instrument	Accuracy
Type K Thermocouples	$\pm 0.1\,K$
Pressure	
Measurement Instrument	Accuracy
SENSIT OEM Absolute Pressure Transducer	$\pm 0.2\%$
Rosemount Differential Pressure Transducer	$\pm 0.25\%$
Flow rate	
Measurement Instrument	Accuracy
Micro Motion Coriollis Mass Flow-meter	$\pm 0.1\%$
Size-7 Rotameter	$\pm 1.5\%$
Heat	
Measurement Instrument	Accuracy
RS Wattmeter	$\pm 1.0\ \%$

It is worth noting that, the data acquisition system has minor uncertainties, including temperature and pressure measurement units' uncertainties. This resulted from converting the data from binary values to engineering units. Unit NI 9211 has an accuracy of 0.05%, while unit NI 9205 for selected range of $0 - 10\ V$, has an accuracy of $\pm 6.23 mV$. It is also based on the selected range of pressure measurements. Therefore the total measurements uncertainties were a combination of measurement instruments and data acquisition system uncertainties.

The experimental rig major systems, sub-systems, and their components and also the design of the test section were described in this chapter. There is an important issue for the test section. Due to significant thickness of the aluminium housing in the test section, the applied heat flux from the heater was distributed in the aluminium housing. In order to optimize the applied heat flux from the heater to the test piece, a numerical simulation was carried out to simulate the conduction heat distribution in the aluminium housing, which is described in the following Chapter.

CHAPTER 4

ANALYSIS OF THE TEST SECTION

The design of the test section is described in the previous Chapter. In this Chapter a numerical analysis of the heat flow through the test section is described. This analysis is used to determine and optimize the effective heat flux through the test specimen.

The test section was designed to operate at pressures of up to 10 bar. Thus, the aluminium housing had significant thickness that allows several heat paths to exist from the heater to the fluid. Figure 4.1 illustrates the possible longitudinal and transverse heat paths through the aluminium housing.

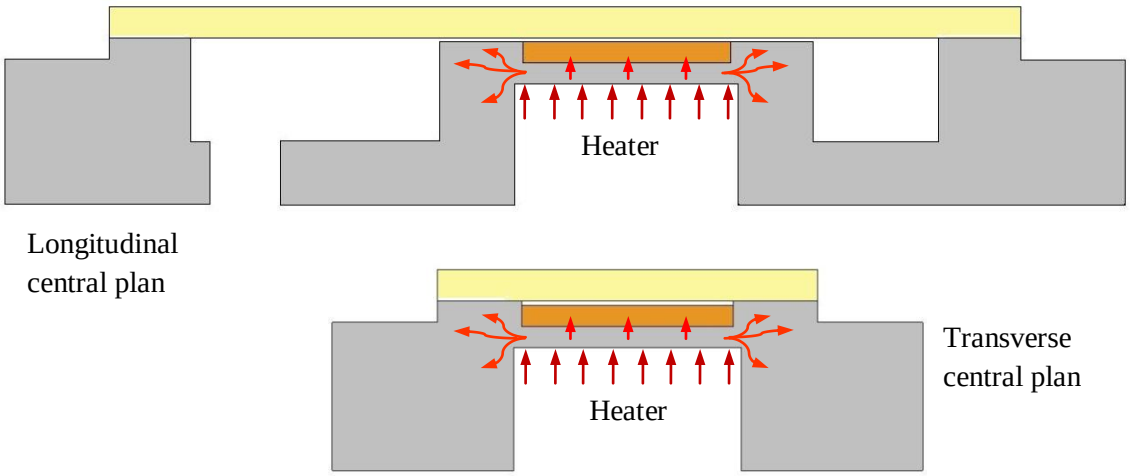

Figure 4.1 Aluminium housing heat paths

Before starting the experimental study, a numerical simulation was carried out to predict the conducted heat distribution in the aluminium housing, in order to optimize the applied heat flux from heater to the test piece.

The conduction heat distribution was simulated using numerical modeling based on the finite volume method. Ansys CFX 11 software was used as the Computational Fluid Dynamics Solver for the computer simulations. A three-dimensional numerical model was developed. Numerical simulation consisted of geometry creation, region

specification, mesh generation, domains creation, boundary conditions assignment and Energy Equation solution.

4.1 Geometry Creation

A multi-body geometry was created using Ansys Workbench 1.0. Figure 4.2a illustrates the actual test section. The steel clamping plate, glass cover plate, ceramic heater and the PTFE Block below it were not numerically modelled. The graphical representation of the modelled test section was composed of the aluminium housing and the test piece, and is shown in Figure 4.2b.

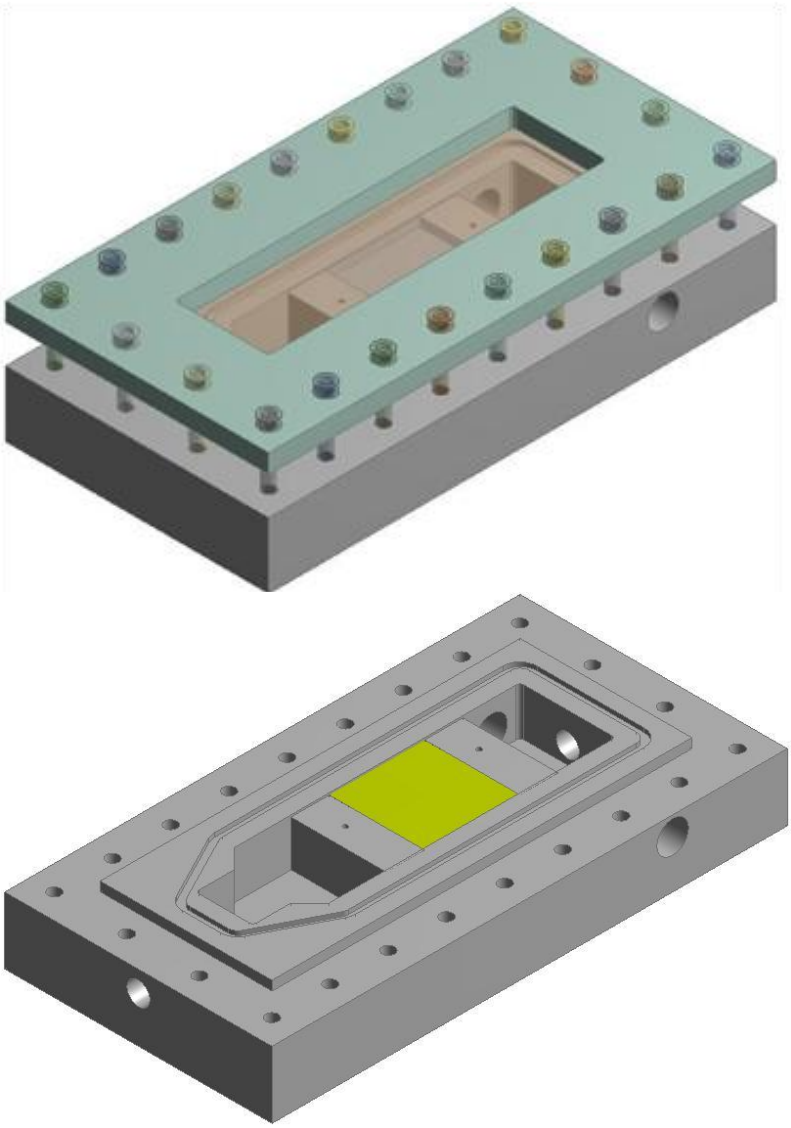

(a)

(b)

Figure 4.2 (a) test section actual 3D model, (b) Simulated test section

4.2 Mesh Generation

A part of the modelled test section shown in Figure 4.2b, was used in the numerical simulation. In order to set up the mesh, the model geometry created in Design Modeler was moved into CFX-Mesh. Firstly, Composite 2D Regions were created from the solid faces of the geometry to allow boundary conditions to be assigned in CFX-Pre afterwards. The 'Standard meshing with CFX-Mesh' option was used for meshing the test section. The Delaunay Surface Mesher for surface meshing and Advancing Front Volume Mesher for volume meshing were used. Since the test piece and settling length were composed of small walls $1mm$ in size, the distribution of the mesh elements were poor in these locations. To avoid this problem and refine the mesh to a higher quality, surface proximity was used in these regions. The test section was meshed as a multi-domain body, allowing the appropriate thermal conductivity to be entered for each material in the test section. Tetrahedral mesh elements were used by the software for the volume mesh generation.

An initial short study was undertaken to investigate the mesh quality and the mesh independency on the computational simulation. Mesh densities were varied from an initial number of 302,800 elements up to 1,380,100 elements in order to optimise the mesh density, achieve high mesh quality and obtain reasonable convergence. Information about the meshes specifications are shown in Table 4.1.

Table 4.1 Meshes specifications for the test section without insulation

MESHSE SPECIFICATIONS						
SPACING	Default Body Spacing	Maximum Spacing [mm]	20	20	10	10
	Default Face Spacing	Face Spacing Type	*Angular Resolution*			
		Angular Resolution [deg]	30	30	30	30
		Min Edge length [mm]	1	0.5	0.2	0.1
		Max Edge length [mm]	20	20	10	10
		Radius of influence [mm]	0	0	0	0
		Expansion Factor	1.2	1.2	1.2	1.2
	Face Spacing	Face Spacing Type	*Angular Resolution*			
		Angular Resolution [deg]	18	18	18	18
		Min Edge Length [mm]	1	0.5	0.2	0.1
		Max Edge Length [mm]	20	20	10	10
		Radius of Influence [mm]	0	0	0	0
		Expansion Factor	1.2	1.2	1.2	1.2
		Location	*PTFE-Fluid interfaces* *Test piece-Fluid interface*			
CONTROLS	-					
PERIODICITY	-					
INFLATION	-					
STRETCH	-					
PROXIMITY	Edge Proximity		*yes*	*yes*	*yes*	*yes*
	Surface Proximity		*yes*	*yes*	*yes*	*yes*
	Elements Across Gap		4	4	4	4
	Maximum number of Passes		5	5	5	5
Elements			302, 826	501, 992	800, 886	1,380, 153

Trial runs were performed on the meshed geometry to check the size and quality of the meshes and also to investigate the mesh independency on a specific parameter of the computational domain. The heat flux at the solid-fluid interface was used to investigate the heat movement from the heater to the fluid. Because of conservation of energy in computational solution this was found to be independent of the mesh density, therefore

temperature distribution at a central longitudinal line at the solid-fluid interfaces along the test section was chosen as the convergence parameter. Figure 4.3 illustrates the location of the line.

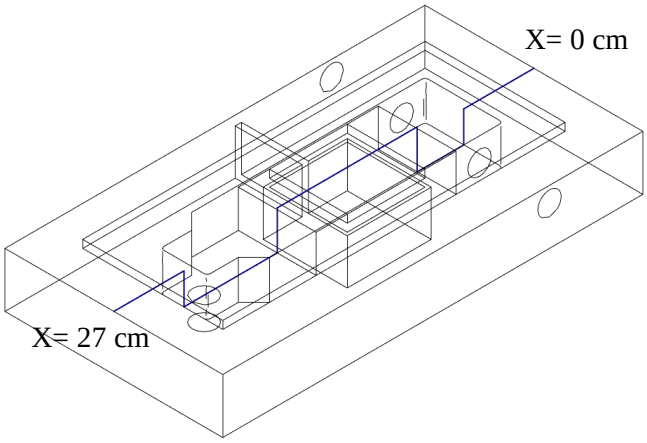

Figure 4.3 Location of the central longitudinal line

The variation of solid-fluid interface temperature along the line with the number of elements for two mesh densities of 502,000 and 801,000 is shown in Figure 4.4. Additional simulations are not shown.

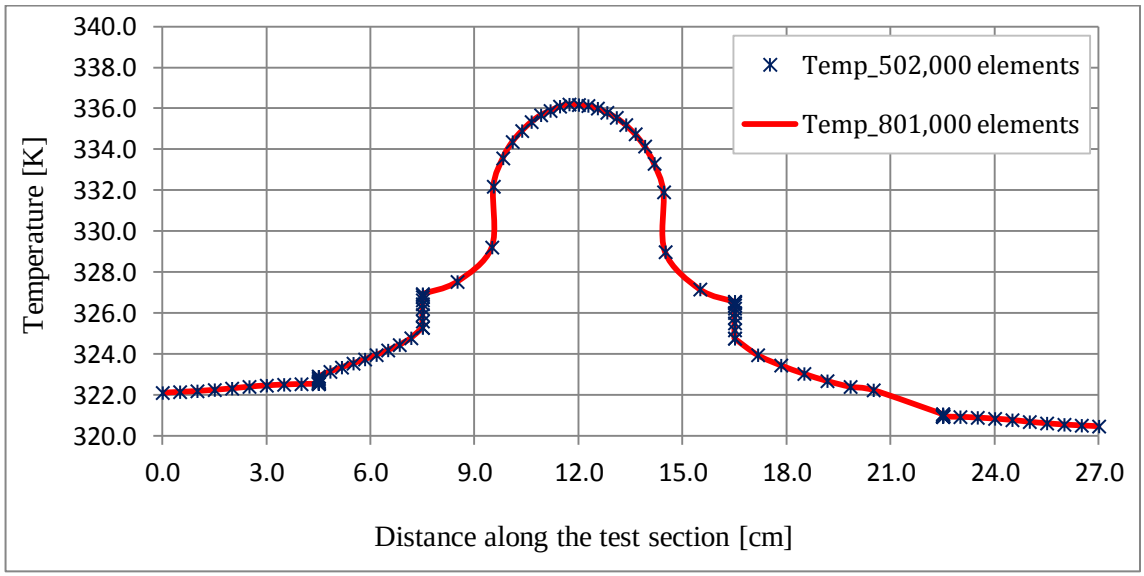

Figure 4.4 Mesh independence study; variation of central line temperature at the solid-fluid interface with number of elements

No change is observed in the obtained temperature distribution along the central line for these mesh densities. This demonstrates that the number of elements is sufficient for mesh independency in the computational simulation to be achieved. Therefore according to the high mesh quality and reasonable convergence time, 801,000 Finite volumes were chosen as the optimal mesh density. Figure 4.5 illustrates the meshed geometry for the chosen number of elements.

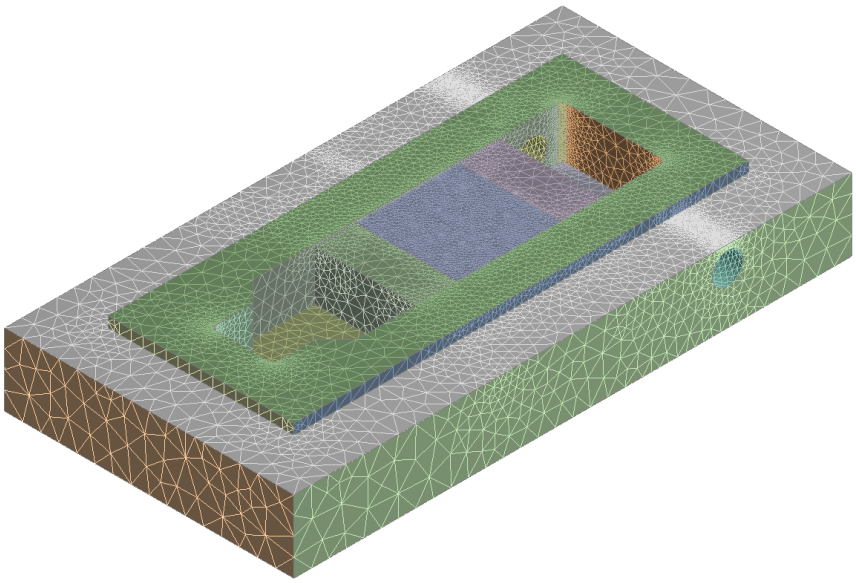

Figure 4.5 Schematic of the meshed test section without insulation

4.3 Assignment of Boundary Conditions

After mesh generation, the meshed geometry was moved into the CFX-Pre. Before Boundary Conditions assignment, two solid-domains were specified, one for the aluminium housing and one for the copper test piece. Properties of aluminium and copper at room temperature were specified for the housing and the test piece respectively. The physical properties neglected temperature dependency. Subsequently the boundary conditions were assigned for the specified domains. R113 was assumed as the liquid interface boundary in the numerical simulation. Since the unit cell is a 3D representation of the model, the boundary conditions were specified for the faces of the model. Each face needs to be given a boundary condition. Boundary conditions for

numerical modelling were close to the experimental operating conditions. The locations of the boundary conditions are shown in Figure 4.6.

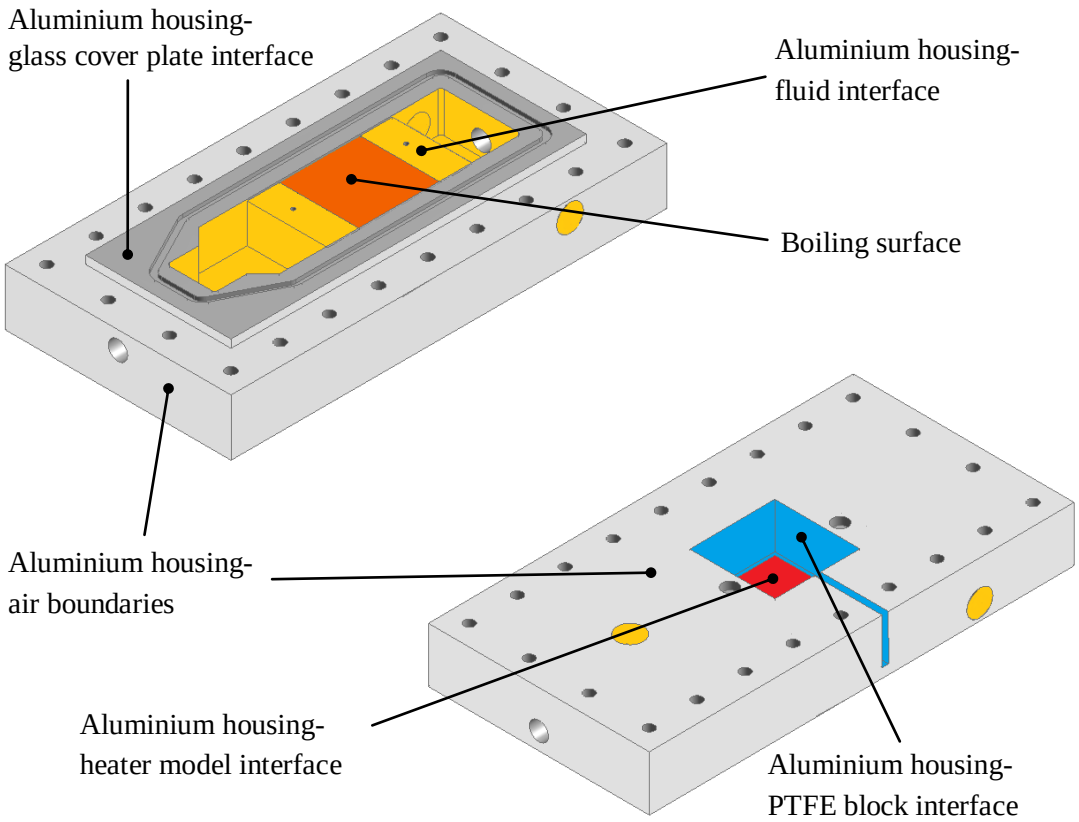

Figure 4.6 Location of the boundary conditions for simulated model without insulation

Heat-transfer coefficient with temperature boundary conditions were assumed at all fluid-solid boundaries. For the aluminium housing-liquid boundaries, the heat-transfer coefficient was set to $100\ W/m^2K$ and the liquid temperature to $318\ K$. At all outer surfaces, aluminium housing-air boundaries, the heat-transfer coefficient was set to $50\ W/m^2K$ and the air temperature to $290\ K$. On the boiling surface, according to the applied heat flux, the heat transfer coefficient was set to 3, 4 or 5 kW/m^2K and the fluid temperature to $320\ K$. Calculations of the assigned boundary conditions are presented in Appendix D.

The ceramic heater, glass cover plate and the PTFE block below it were not explicitly modelled. A constant heat flux boundary condition was assumed at the heater model interface. A heat-transfer coefficient with temperature boundary was assumed at the aluminium housing-glass cover plate interface. This was based on glass heat conductivity calculations. The heat-transfer coefficient was set to $10\ W/m^2K$ and the temperature to $290\ K$. The approximation of constant heat transfer coefficient is reasonable due to the minor amount of the heat loss from this face. An adiabatic boundary was assumed for the aluminium housing-PTFE block interface.

The assigned boundary conditions are illustrated in Figure 4.7. In order to increase the thermal conductivity of the copper test piece and aluminium housing thermal interfaces, a very thin layer of thermal paste was used to fill microscopic interfaces air-gaps. Therefore zero thermal resistance was assumed between the copper test piece and the aluminium housing with continuous temperature and heat flux. The continuity of the temperature and heat flux was automatically used in the CFX for the computational domain. Table 4.2 shows the assigned boundary conditions for the simulated model.

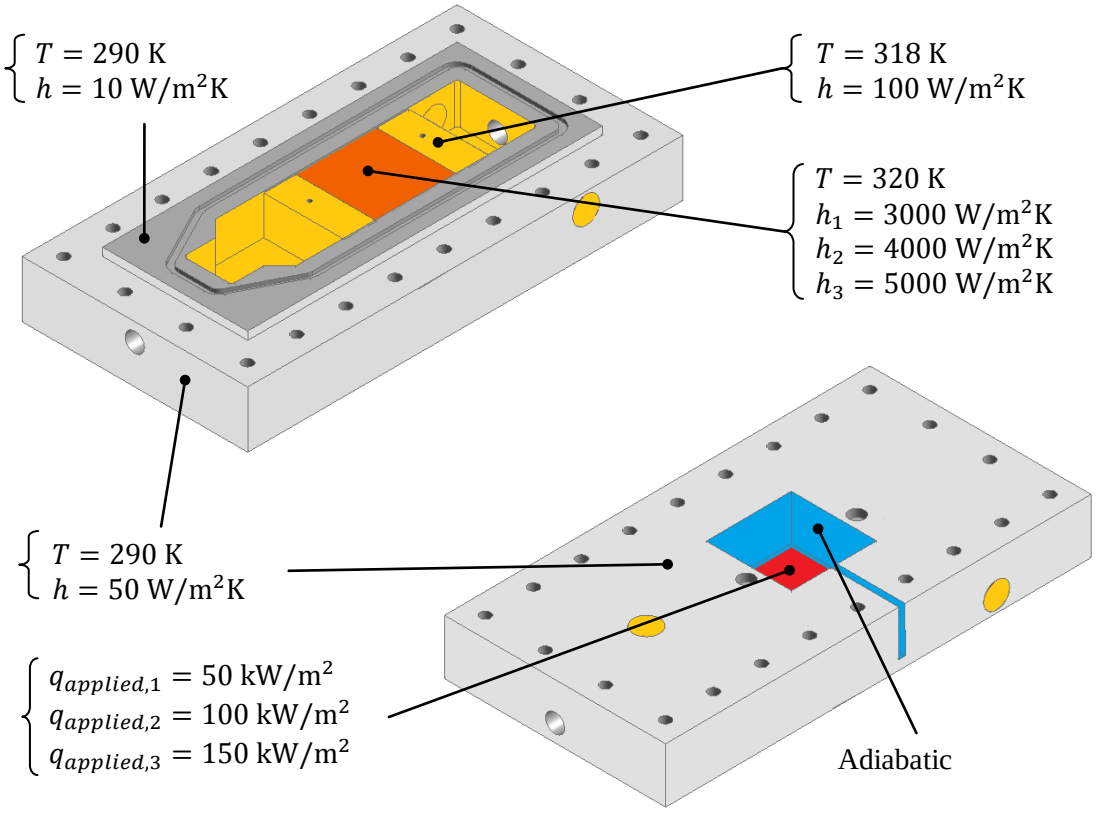

Figure 4.7 Boundary conditions for simulated model without insulation

Table 4.2 Boundary conditions for simulated model without insulation

Aluminum housing		
Region	*Boundary Condition*	*Values*
Aluminum housing-fluid interface	Heat-transfer coefficient with temperature	$T = 318$ K $h = 100$ W/m^{2}K
Aluminum housing-Ambient interface	Heat-transfer coefficient with temperature	$T = 290$ K $h = 50$ W/m^{2}K
Aluminum housing-Cover plate interface	Heat-transfer coefficient with temperature	$T = 290$ K $h = 10$ W/m^{2}K
Aluminium housing-Heater interface	Constant Heat Flux	$q_{applied,1} = 50$ kW/m^2 $q_{applied,2} = 100$ kW/m^2 $q_{applied,3} = 150$ kW/m^2
Aluminium housing-Test piece interface	Automatic Solid-Solid Domain Interface Side 1	
Aluminum housing-PTFE block interface	Adiabatic	
Copper test piece		
Region	*Boundary Condition*	*Values*
Copper test piece - fluid interface	Heat-transfer coefficient with temperature	$T = 320$ K $h_{1,\ q1} = 3000$ W/m^{2}K $h_{2,\ q2} = 4000$ W/m^{2}K $h_{3,\ q3} = 5000$ W/m^{2}K
Copper test piece - housing interface	Automatic Solid-Solid Domain Interface Side 2	

After setting up the simulation and boundary conditions assignment, the simulation was run as steady state in the CFX-Solver. Simulations were run using High Resolution methods and the Physical Timescale option was used for convergence control. The Energy equation in three-dimensions was solved for the volume mesh. Under the stated assumptions, the energy equation is as follow;

$$\nabla^2 \mathrm{T} = 0 \tag{4.1}$$

The results are described in the next session.

4.4 Results and Discussion

To obtain the effective heat flux at the boiling surface, simulations were run for applied heat fluxes of 50, 100 and 150 kW/m^2 with corresponding heat transfer coefficients of 3, 4, and 5 kW/m^2K respectively, at the boiling surface. Table 4.3 shows the achieved heat fluxes on the solid boundaries for different applied heat fluxes.

Table 4.3 Achieved heat fluxes on the solid boundaries for the test section without insulation

Boundaries	*Test 1*	*Test 2*	*Test 3*
Heat flux at heater [W/m^2]	50,000	100,000	150,000
Two-phase heat transfer coefficient [W/m^2]	3000	4000	5000
Heat flux_Housing-ambient [W/m^2]	1,285.27	1,602.05	1,834.14
Heat flux_Housing- test piece [W/m^2]	6,460.83	30,591.8	57,442.9
Heat flux_Housing-cover plate [W/m^2]	316.125	415.631	488.457
Heat flux_Housing-fluid [W/m^2]	75.823	579.9	1,060.04
Heat flux_Housing-PTFE block [W/m^2]	386.816	841.369	1,301.99
Heat flux_Test piece-housing [W/m^2]	6,357.29	29,147.6	54,479
Heat flux_Test piece-fluid [W/m^2]	5581.21	39,289.1	77,355

Typical temperature distributions from the simulations are shown in Figure 4.8. The same temperature scale was used for all figures. These simulations were undertaken with the aluminium body exposed to the atmosphere and in direct contact with the flowing fluid. As has been shown in Table 4.3, these simulations indicated that applied heat fluxes of 50, 100, and 150 kW/m^2 at the heater surface would produce 5.6, 39.3, and 77.4 kW/m^2 heat fluxes at the boiling surface, respectively. With only liquid flowing in the test loop, Figure 3.2, temperature rises were measured across the test piece, allowing the heat gain to be estimated from the mass flow rate of liquid and the inlet and outlet temperatures. The gain in sensible heat confirmed the simulation results.

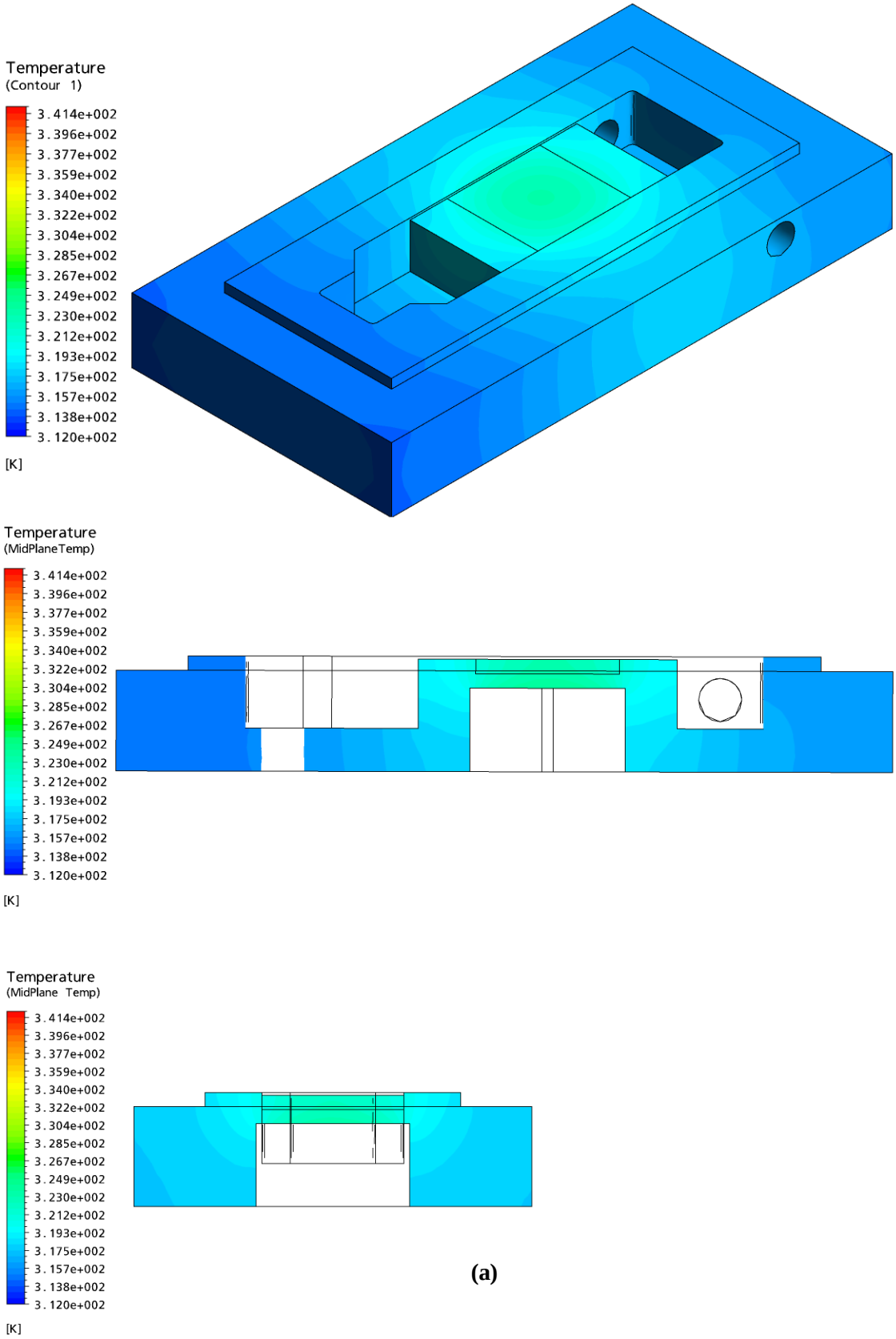

Figure 4.8 Predicted temperature distributions at the test section without insulation, for applied heat flux of (a) 50 kW/m^2, (b) 100 kW/m^2, and (c) 150 kW/m^2

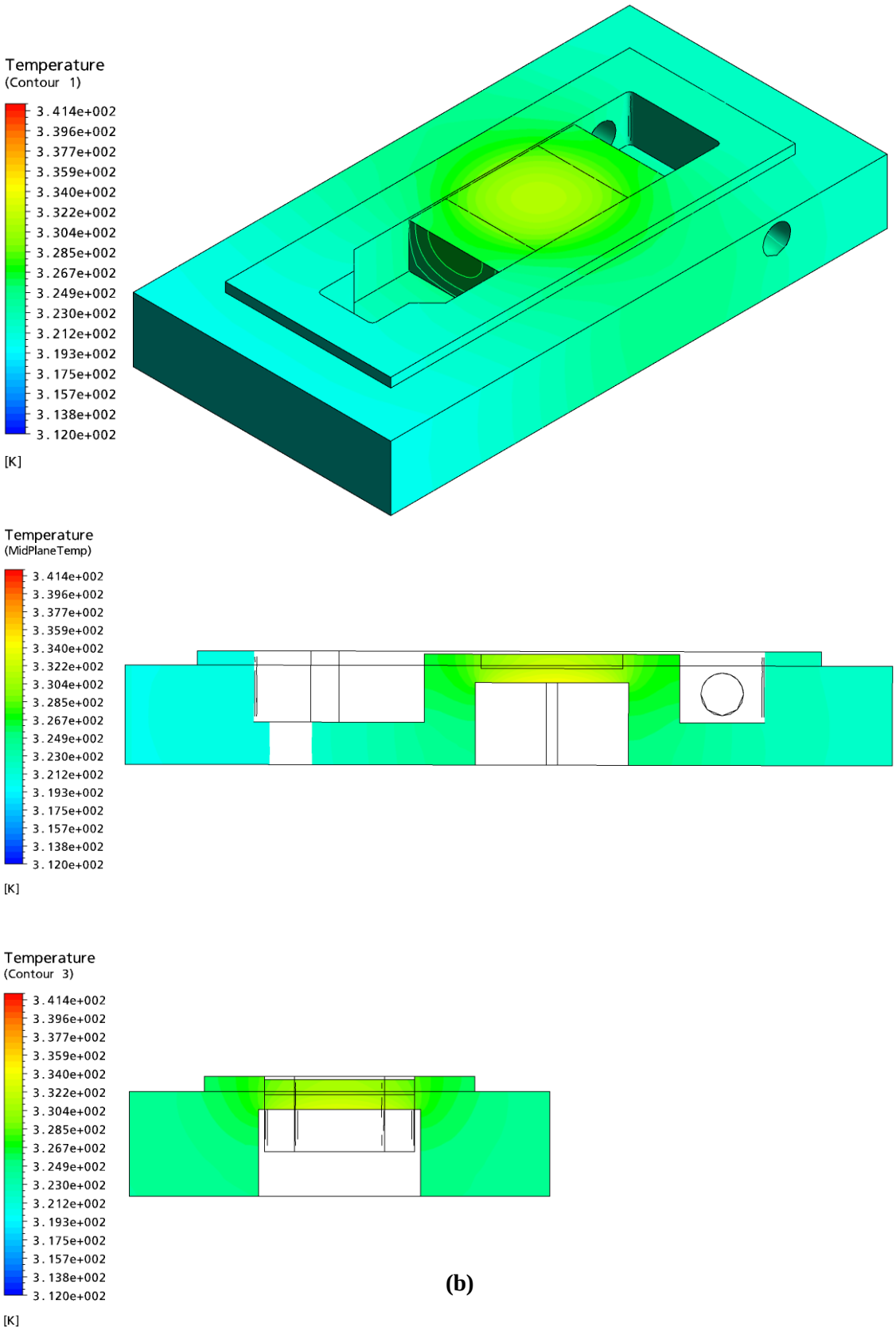

Figure 4.8 (continued) Predicted temperature distributions at the test section without insulation, for applied heat flux of (a) 50 kW/m^2, (b) 100 kW/m^2, and (c) 150 kW/m^2

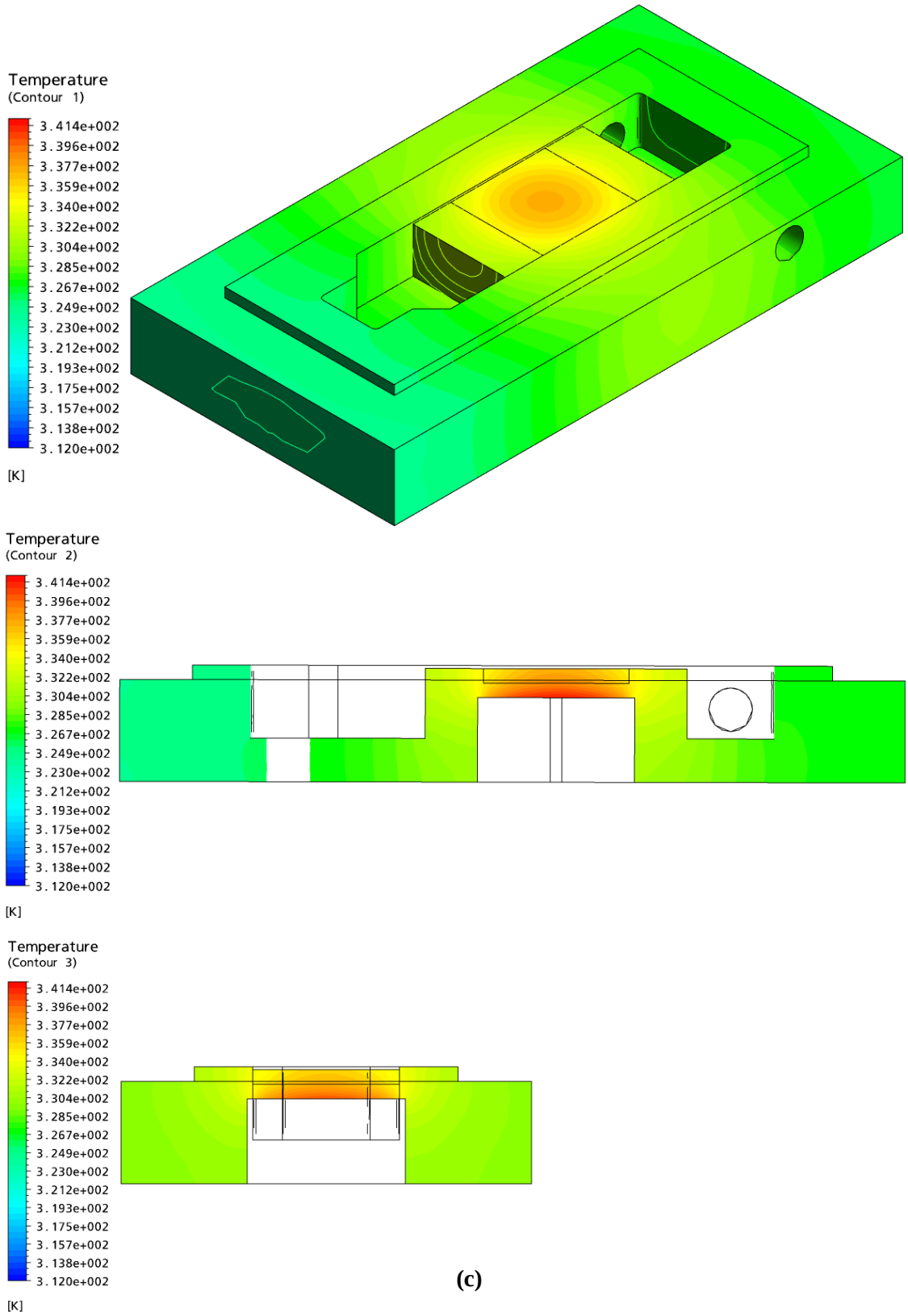

Figure 4.8 (continued) Predicted temperature distributions at the test section without insulation, for applied heat flux of (a) 50 kW/m^2, (b) 100 kW/m^2, and (c) 150 kW/m^2

Further simulations were undertaken to aid the design of the test section's insulation. A layer of PTFE with the thickness of t was designed for the all internal fluid-aluminium interfaces and added to the existing geometry. Figure 4.9 illustrates the geometry with the internal PTFE insulation.

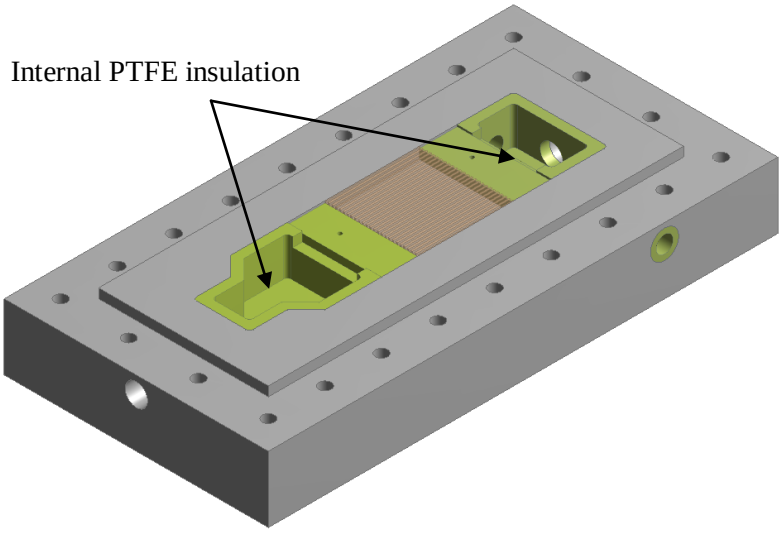

Figure 4.9 Simulated test section with internal insulation

The new design of the test section was meshed. Information about the new mesh specifications is shown in Table 4.4. High mesh quality and reasonable convergence time, required 1,244,300 Finite volumes to be used. Figure 4.10 illustrates a schematic view of the meshed geometry.

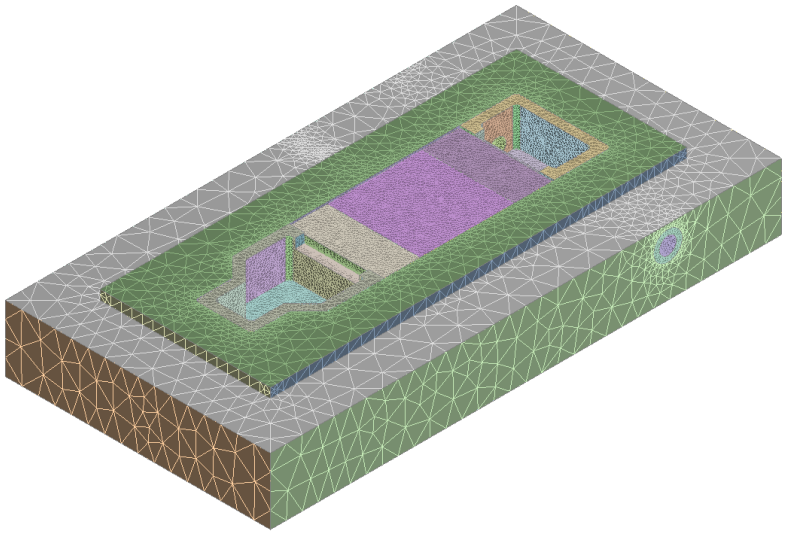

Figure 4.10 Schematic of the meshed test section with internal insulation

Table 4.4 Mesh specifications for the test section with insulation

MESH			
SPACING	Default Body Spacing	Maximum Spacing	10 *mm*
	Default Face Spacing	Face Spacing Type	*Angular Resolution*
		Angular Resolution	30°
		Minimum Edge Length	0.2 *mm*
		Maximum Edge Length	10 *mm*
		Radius of Influence	0 *mm*
		Expansion Factor	1.2
	Face Spacing	Face Spacing Type	*Angular Resolution*
		Angular Resolution	18°
		Min Edge Length	0.1 *mm*
		Max Edge Length	10 *mm*
		Radius of Influence	0 *mm*
		Expansion Factor	1.2
		Location	*PTFE-Fluid interfaces* *Test piece-Fluid interface*
CONTROLS	-		
PERIODICITY	-		
INFLATION	-		
STRETCH	-		
PROXIMITY	Edge Proximity		*yes*
	Surface Proximity		*yes*
	Elements Across Gap		4
	Maximum number of Passes		5
Elements	1,244,300		

After mesh generation in CFX-Mesh, Internal insulation domains were added to the existing domains in CFX-Pre. Properties of PTFE at room temperature were specified for the internal insulation domains. Automatically zero thermal resistance was assumed between all solid domains with continuous temperature and heat flux. Again, boundary conditions close to the experimental operation conditions were used. Figure 4.11 shows the location of the boundary conditions. An assumed layer of wool insulation on the external surfaces was made. The assigned boundary conditions for the new model are illustrated in Figure 4.12 and described in Table 4.5.

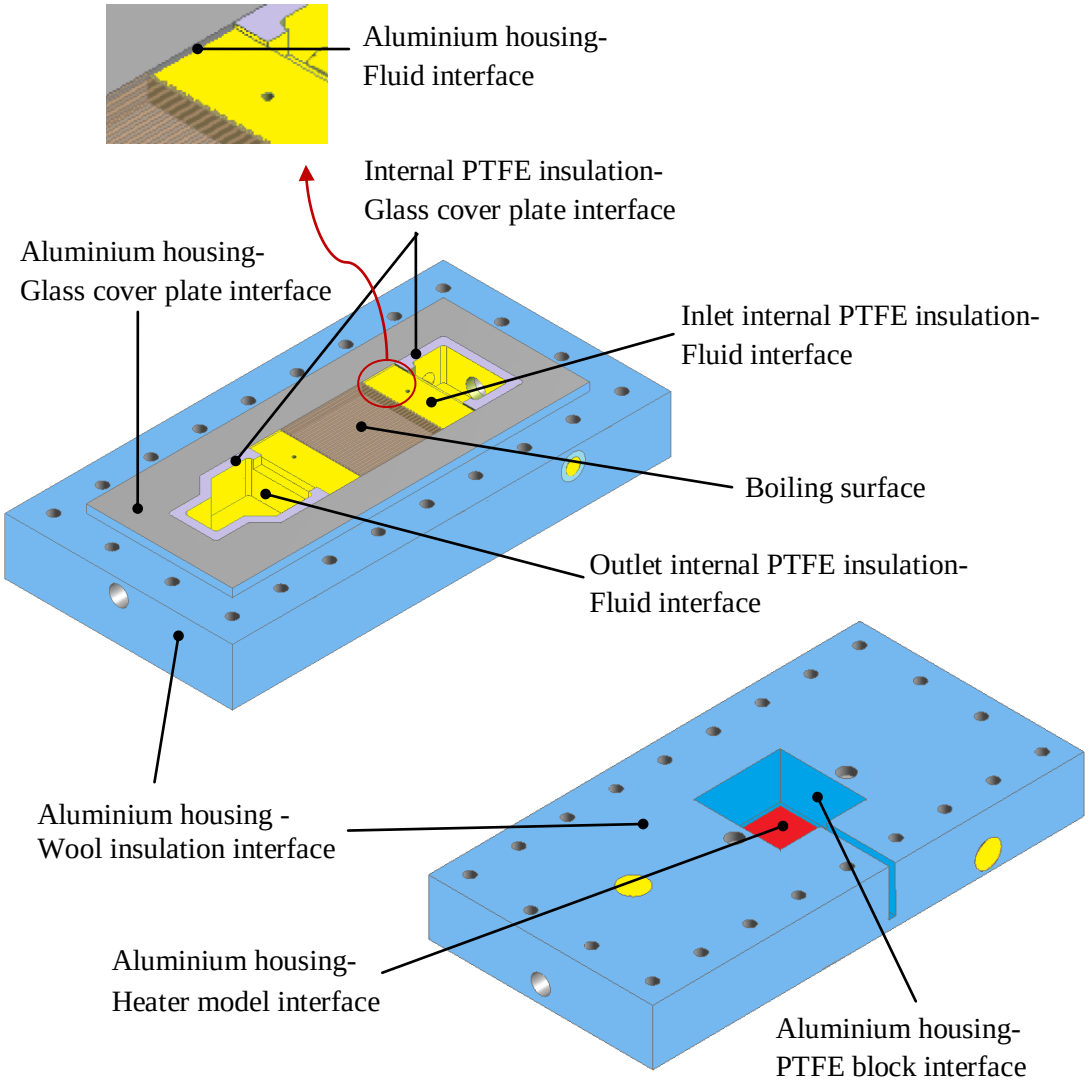

Figure 4.11 Location of boundary conditions for simulated model with internal and external insulation

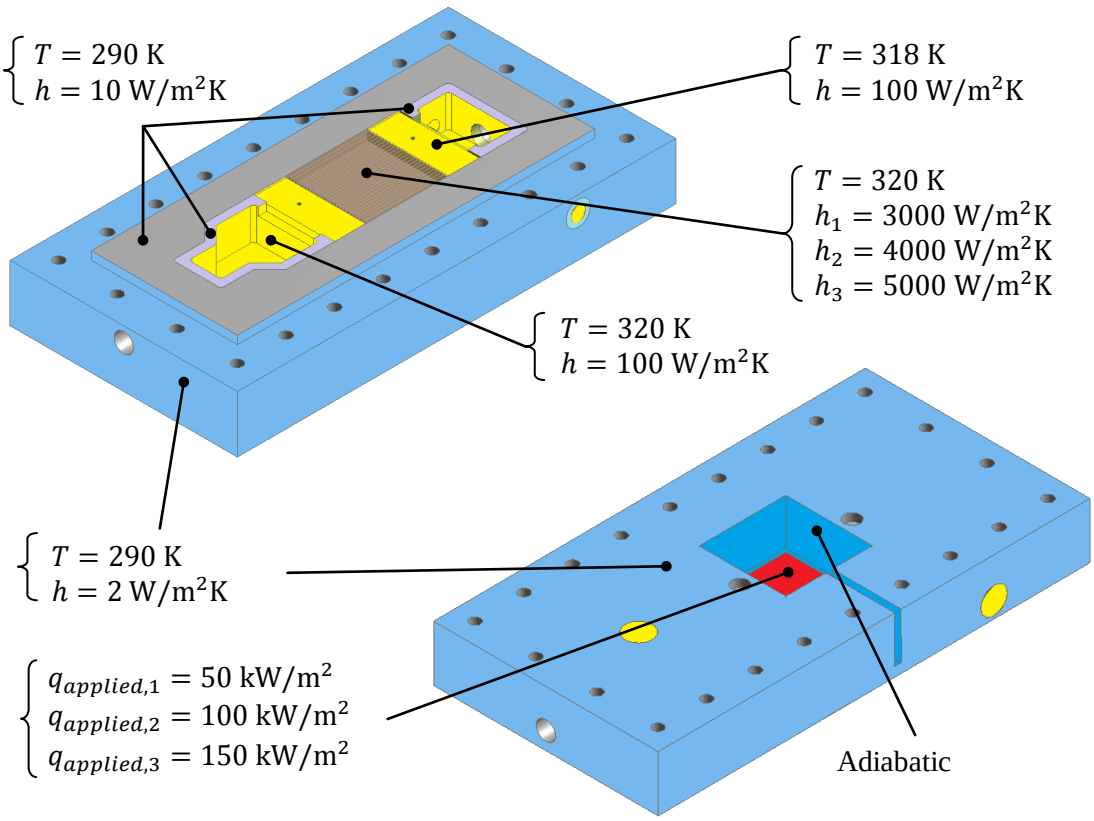

Figure 4.12 Boundary conditions for simulated model with internal and external insulation

Table 4.5 Boundary conditions for simulated model with internal and external insulation

Aluminum housing		
Region	*Boundary Condition*	*Values*
Aluminum housing-Fluid interface	Heat-transfer coefficient with temperature	$T = 320$ K $h = 100$ W/m^{2}K
Aluminum housing-Wool insulation interface	Heat-transfer coefficient with temperature	$T = 290$ K $h = 2$ W/m^{2}K
Aluminum housing-Glass cover plate interface	Heat-transfer coefficient with temperature	$T = 290$ K $h = 10$ W/m^{2}K
Aluminium housing-Heater model interface	Constant Heat Flux	$q_{applied,1} = 50$ kW/m^2 $q_{applied,2} = 100$ kW/m^2 $q_{applied,3} = 150$ kW/m^2
Aluminium housing-Test piece interface	Automatic Solid-Solid Domain Interface Side 1	

Aluminum housing- PTFE block interface	Adiabatic	
Aluminum housing- Inner PTFE interface	Automatic Solid-Solid Domain Interface Side 1	
Copper test piece		
Region	*Boundary Condition*	*Values*
Copper test piece - Fluid interface	Heat-transfer coefficient with temperature	$T = 320$ K $h_1 = 3000$ W/m^{2}K $h_2 = 4000$ W/m^{2}K $h_3 = 5000$ W/m^{2}K
Copper test piece - Housing interface	Automatic Solid-Solid Domain Interface Side 2	
Copper test piece - Inner PTFE interface	Automatic Solid-Solid Domain Interface Side 2	
Internal PTFE insulation		
Region	*Boundary Condition*	*Values*
Inlet internal PTFE insulation- Fluid interface	Heat-transfer coefficient with temperature	$T = 318$ K $h = 100$
Outlet internal PTFE insulation- Fluid interface	Heat-transfer coefficient with temperature	$T = 320$ K $h = 100$
Internal PTFE insulation- Copper test piece	Automatic Solid-Solid Domain Interface Side 2	
Internal PTFE insulation - Housing interface	Automatic Solid-Solid Domain Interface Side 2	
Internal PTFE insulation - Cover plate interface	Heat-transfer coefficient with temperature	$T = 290$ K $h = 10$ W/m^{2}K
Internal PTFE insulation - Wool insulation interface	Heat-transfer coefficient with temperature	$T = 290$ K $h = 2$ W/m^{2}K

Simulations were run for the same applied heat fluxes and corresponding heat transfer coefficients at the boiling surface as previously. Several thicknesses of internal PTFE insulation and external wool insulation were investigated. This led to a $25\ mm$ layer of insulating wool being placed on all external surfaces, with the exception of the viewing

window required for visual observations, Figure 4.13a. Additionally, all internal fluid-aluminium surfaces were insulated with a 6 mm layer of PTFE, Figure 4.13b. Table 4.6 shows the achieved heat fluxes on the solid boundaries for different applied heat fluxes, at the new test section design with internal and external insulation.

Table 4.6 Achieved heat fluxes on the solid boundaries for test section with internal and external insulation

Boundaries	***Test 1***	***Test 2***	***Test 3***
Heat flux at heater $[W/m^2]$	50,000	100,000	150,000
Two-phase heat transfer coefficient $[W/m^2]$	3000	4000	5000
Heat flux_Housing-wool insulator $[W/m^2]$	89.7886	107.708	119.485
Heat flux_Housing- test piece $[W/m^2]$	34,238.3	72,261.9	110,979
Heat flux_Housing-cover plate $[W/m^2]$	430.128	519.685	578.412
Heat flux_Housing-fluid $[W/m^2]$	1,176.71	1,868.65	2,316.74
Heat flux_Housing-PTFE block $[W/m^2]$	526.149	1,054.37	1,582.76
Heat flux_Housing-inner PTFE $[W/m^2]$	927.559	1,648.516	2,238.64
Heat flux_Inner PTFE-housing $[W/m^2]$	744.329	1,209.09	1,531.748
Heat flux_Inner PTFE-test piece $[W/m^2]$	1627.81	2,562.544	3,367.86.28
Heat flux_Inner PTFE-cover plate $[W/m^2]$	714.34	866.27	966.143
Heat flux_Inner PTFE-fluid $[W/m^2]$	1,132.347	1,810.903	2,256.56
Heat flux_Inner PTFE-wool $[W/m^2]$	254.982	346.776	407.112
Heat flux_Test piece-housing $[W/m^2]$	33,192.1	69,998	107,461
Heat flux_Test piece-inner PTFE $[W/m^2]$	4,387.98	5,767.703	6,832.737
Heat flux_Test piece-fluid $[W/m^2]$	**41,720**	**88,795.1**	**136,875**

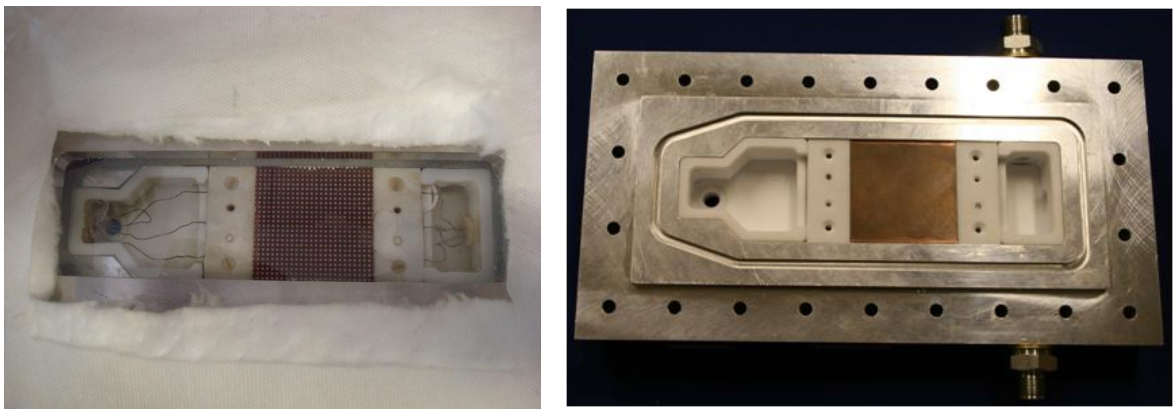

(a) (b)

Figure 4.13 Final design of the test section, (a) with wool insulation, (b) open section

As is shown in Table 4.6, the simulations indicated that these changes would give a heat flux of 41.7, 88.8, and 136.9 kW/m^2 at the boiling surface when a heat flux of 50, 100, and 150 kW/m^2 was applied by the heater, respectively. Typical temperature distributions from the simulations are shown in Figure 4.14.

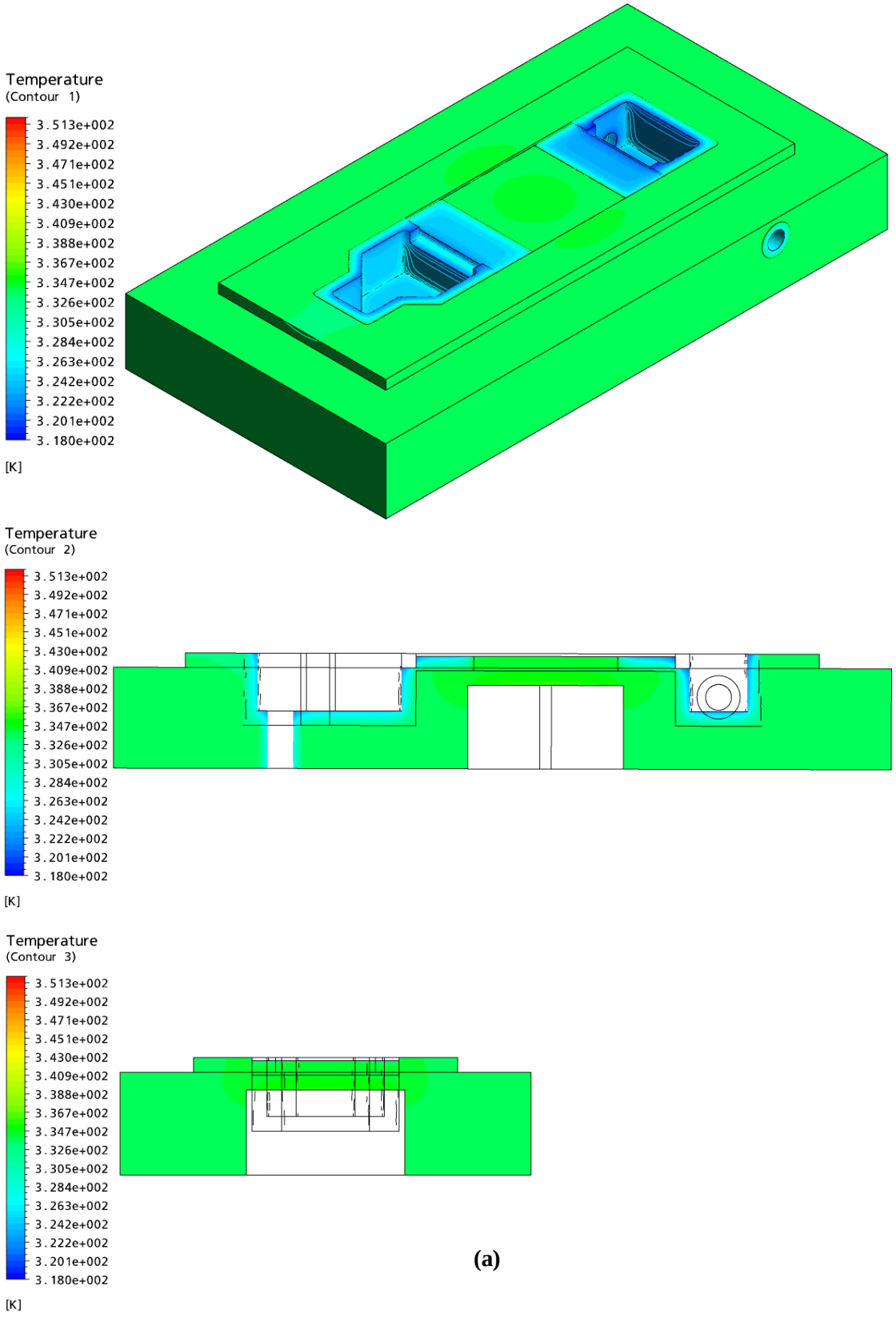

Figure 4.14 Predicted temperature distributions at the test section with internal and external insulation, for applied heat flux of (a) 50 kW/m^2, (b) 100 kW/m^2, and (c) 150 kW/m^2

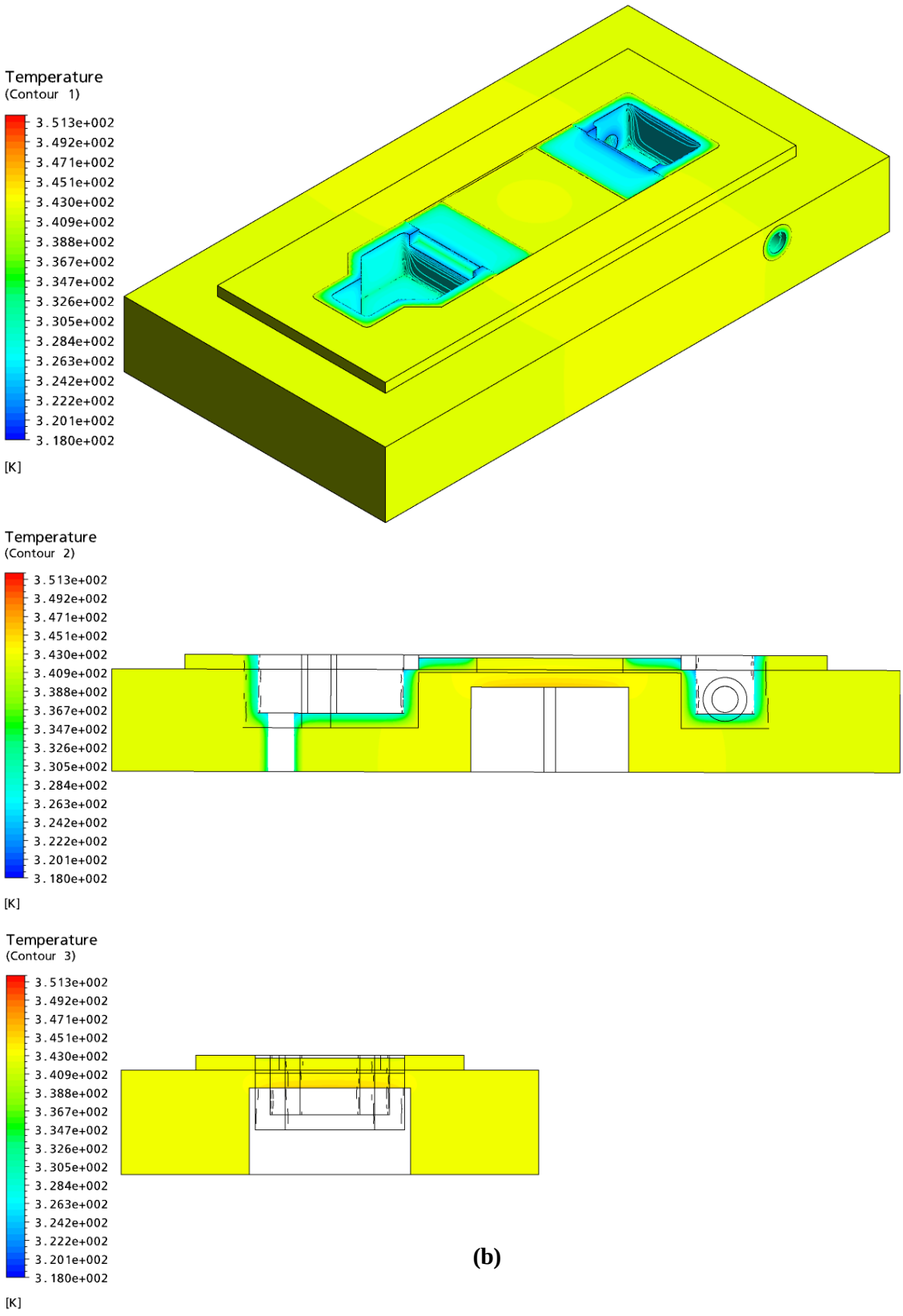

Figure 4.14 (continued) Predicted temperature distributions at the test section with internal and external insulation, for applied heat flux of (a) 50 kW/m^2, (b) 100 kW/m^2, and (c) 150 kW/m^2

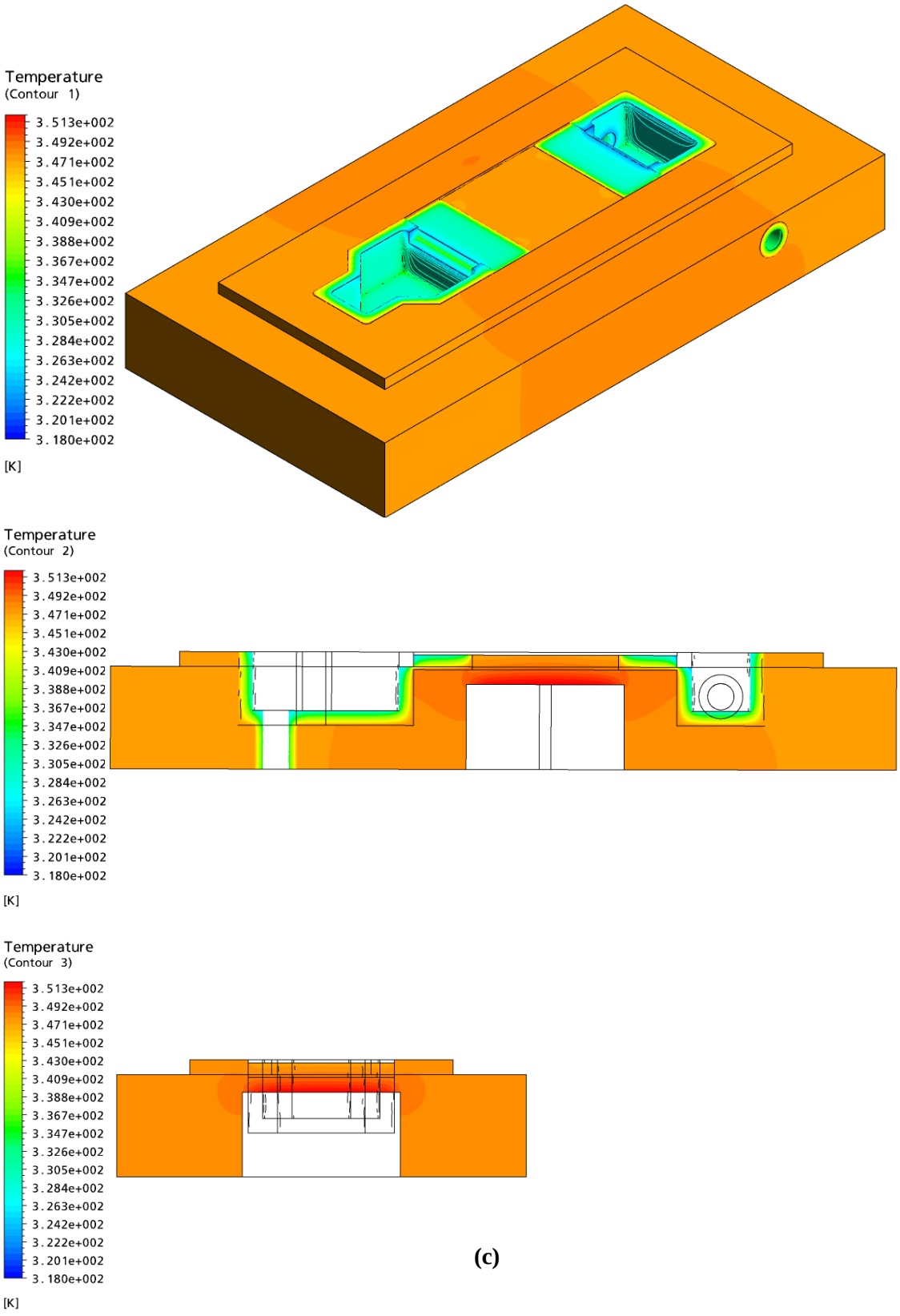

Figure 4.14 (continued) Predicted temperature distributions at the test section with internal and external insulation, for applied heat flux of (a) 50 kW/m^2, (b) 100 kW/m^2, and (c) 150 kW/m^2

The heat flow from the heater to the test piece is proportional to the difference between the heater temperature, T_h, and the test piece surface temperature, T_w. Data taken when the liquid outlet temperature was below the saturation temperature, deduced from the outlet fluid pressure, were used to establish this relationship. The effective heat flux, q_{eff}, was determined from the ratio of increase in sensible heat of the liquid to the base area of the test piece, and was correlated by

$$q_{eff} = B\,(T_h - T_w) - C \tag{4.2}$$

where the heat flux is in kW/m^2 and the temperatures are in Kelvin. The constant terms B and C, were obtained from a series of single-phase tests for each test piece. Table 4.7 gives values of B and C for all test series. Values of B were obtained from the trend-line's equation which go through the experimental data for all series of tests. Figure 4.15 illustrates the trend-lines equations for all test series.

Table 4.7 Values of B and C in Equation (4.2)

	Test piece	Working Fluid	B	C
1	Plate channel	R113	2.8910	1.452
2	Parallel channel	R113	2.2615	1.452
3	In-line pin fin	R113	2.8910	1.452
4	Staggered pin fin	R113	5.1634	1.452
5	In-line pin fin	Water	7.9974	3.872

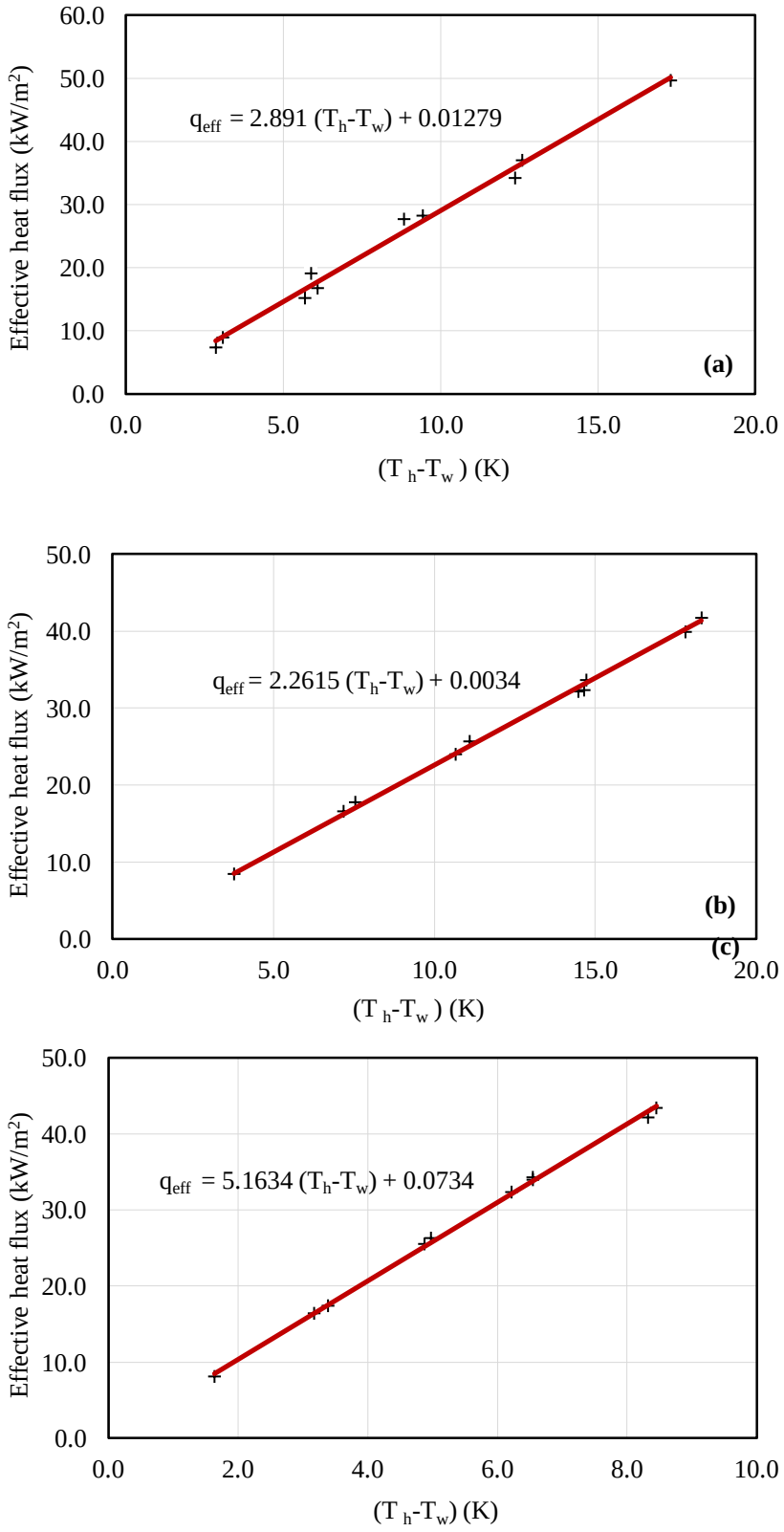

Figure 4.15 Variation of effective heat flux with $(T_h - T_w)$ for (a) Plate channel and In-line pin-fin with R113, (b) Parallel channel with R113, and (c) Off-set pin-fin with R113

As it is shown, the constant values in the trend-lines are too small and are negligible. The constant term C estimates the heat loss through the glass window. This corresponds to $3.63\,W$ for tests with R113 and $9.68\,W$ for tests with water as working fluid. A constant value is reasonable because the fluid temperature, and therefore the bulk of the test section temperatures, were close to the saturation temperature of working fluid at atmospheric pressure. If the transmission efficiency is taken as the ratio of the effective heat flux to the heat flux applied by the heater, Equation (4.2) led to transmission efficiencies of $58-90\%$, depending on the mass flux, with 85% being typical, which is very close to the numerical simulation.

CHAPTER 5

EXPERIMENTAL PROGRAMME

This chapter presents the experimental programme, and is divided into three sections. Section 5.1 specifies the operating conditions, section 5.2 describes the experimental procedure and finally section 5.3 presents the data reduction methods.

5.1. Operating Conditions

Five test series were carried out to investigate flow boiling characteristics; heat transfer coefficient and pressure drop in different mini flow passages with different working fluids as follows:

- Plate channel test piece with R113 as working fluid
- Parallel channel test piece with R113 as working fluid
- In-line pin-fin test piece with R113 as working fluid
- In-line off-set pin-fin test piece with R113 as working fluid
- In-line pin-fin test piece with water as working fluid

The flow boiling tests were performed by supplying working fluid near atmospheric pressure to the test section with $2-12\,K$ sub-cooling. Prior to performing each flow boiling tests, a series of single-phase tests was conducted within the same flow rate range as the flow boiling tests.

The single-phase tests were performed by supplying fluid flow near atmospheric pressure and temperature to the test section. Two single-phase tests were carried out prior to each flow boiling test; one for investigating the single-phase heat transfer coefficients and one for investigating the single-phase pressure drops under isothermal conditions. Five equally spaced mass flow rates, similar to those for flow boiling tests, were used for each test series. The operating conditions for single-phase and flow boiling tests are described based on the test series as follows.

5.1.1. Plate Channel Surface Tests with R113

For the plate surface, single-phase heat transfer coefficients were obtained for heat loads in the range of $25 - 75\ W$. This provided apparent heat fluxes in the range of $10 - 30\ kW/m^2$. As the plate surface had a smaller heat transfer area than the other surfaces, for the same heat flux, the wall temperature was higher. Lower heat fluxes were therefore applied during the plate tests to prevent excessive temperatures in the heater. Five equally spaced mass flow rates between $2.45\ g/s$ and $12.25\ g/s$ were used. This provided mass fluxes in the range of $50 - 250\ kg/m^2s$, Table 5.1. The plate single-phase pressure drops were too small to be measured by the pressure transducer.

For flow boiling tests, liquid R113 was supplied near atmospheric pressure to the test section with $3 - 8\ K$ sub-cooling. Heat transfer and pressure drop data were obtained for heat loads in the range of $25 - 404\ W$. These were applied to each mass flow rate in steps of $25\ W$, with the $375\ W$ load avoided. This gave apparent heat fluxes in the range of $10 - 161.6\ kW/m^2$, Table 5.1. The five mass flow rates used in the single-phase tests were used for each heat flux. For the plate surface at the lower mass fluxes, some of the larger heat fluxes were not possible, as damage to the electrical heater would have resulted from the excessive temperatures generated by the reduced heat-transfer area available relative to the other enhanced area test pieces.

5.1.2. Parallel Channel Surface Tests with R113

For the parallel channel test piece, single-phase heat transfer coefficients were obtained for heat loads in the range of $25 - 126\ W$, this gave apparent heat fluxes of $10 - 50.4\ kW/m^2$, based on the base area of the test piece. Five equally spaced mass flow rates between $5.0\ g/s$ and $15.0\ g/s$ were used. This provided mass fluxes in the range of $200 - 600\ kg/m^2s$, based on the restricted flow area in the test piece channels. Single-phase pressure drops were obtained under isothermal conditions for the same mass fluxes, Table 5.1.

For flow boiling tests, liquid R113 was supplied near atmospheric pressure to the test section with $4 - 7\ K$ sub-cooling. Heat transfer and pressure drop data were obtained for heat loads in the range of $25 - 405\ W$, in steps of $25\ W$, with the $375\ W$ load

avoided. This gave apparent heat fluxes in the range of $10 - 162\ kW/m^2$. The five mass flow rates used in the single-phase tests were used for each heat flux, Table 5.1.

5.1.3. In-Line Pin-Fin Surface Tests with R113

For the in-line pin-fin surface with R113 as working fluid, single-phase heat transfer coefficients were acquired over the following range of parameters. Heat loads of $25 - 140\ W$. This gave apparent heat fluxes of $10 - 56\ kW/m^2$, based on the base area of the test piece. Five equally spaced mass flow rates between $2.5\ g/s$ and $12.5\ g/s$ were used. This provided mass fluxes in the range of $100 - 500\ kg/m^2s$, based on the restricted flow area in the test piece flow passages. Single-phase pressure drops were obtained under isothermal conditions for the same mass fluxes, Table 5.1.

For flow boiling tests, liquid R113 was supplied near atmospheric pressure to the test section with $2 - 5\ K$ of sub-cooling. Heat transfer and pressure drop data were obtained for heat loads in the range of $25 - 403\ W$, in steps of $25\ W$, with the $375\ W$ load avoided. This gave apparent heat fluxes in the range of $10 - 161.2\ kW/m^2$. The five mass flow rates used in the single-phase tests were used for each heat flux, Table 5.1.

5.1.4. In-Line Off-Set Pin-Fin Surface Tests with R113

For the in-line off-set pin-fin surface, single-phase heat transfer coefficients and pressure drops were obtained for the same conditions as parallel channel single-phase tests, Table 5.1.

For flow boiling tests, heat transfer and pressure drop data were obtained for heat loads in the range of $25 - 404\ W$, in steps of $25\ W$, with the $375\ W$ load avoided. This gave apparent heat fluxes in the range of $10 - 161.6\ kW/m^2$. The five mass flow rates used in the single-phase tests were used for each heat flux, Table 5.1.

5.1.5. In-Line Pin-Fin Surface Tests with Deionised Water

These series of tests were carried out to compare water flow boiling heat transfer coefficient and pressure drop with R113 data for the in-line pin-fin test piece. As liquid specific heat capacity and enthalpy of evaporation for water are much higher than that for R113, these series of tests with water were carried out in lower mass flow rates and higher heat fluxes, to obtain quite similar conditions as R113 tests at the exit of the in-line pin-fin test piece.

Single-phase heat transfer coefficients were acquired for heat loads in the range of $25 - 723\ W$. This gave apparent heat fluxes of $10 - 289.2\ kW/m^2$, based on the base area of the test piece. Five equally spaced mass flow rates between $1\ g/s$ and $5\ g/s$ were used. This provided mass fluxes in the range of $40 - 200\ kg/m^2s$, based on the restricted flow area in the test piece flow passages. Single-phase pressure drops were obtained under isothermal conditions for the same mass fluxes, Table 5.1.

For flow boiling tests, water was supplied near atmospheric pressure to the test section with $4 - 12\ K$ sub-cooling. Heat transfer and pressure drop data were obtained for heat loads in the range of $100 - 1210\ W$. These were applied to each mass flow rate in steps of $100\ W$. This gave apparent heat fluxes in the range of $40 - 484\ kW/m^2$. The five mass flow rates used in the single-phase tests were used for each heat flux, Table 5.1.

Operating conditions in more details for all test series are presented in Appendix E. Table 5.1 illustrates a summary of operating conditions for single-phase and flow boiling tests. As the ratio of the heat flux (q) to the mass flux (G) is an important combination factor, values of $q_{applied}/G$ for single-phase heat transfer tests and flow boiling tests are included in Table 5.1.

Table 5.1 Operating conditions for single-phase and flow boiling tests

Single-phase Heat Transfer Tests								
Test piece	**Fluid**	$T_{f,in}$ [°C]	M [g/s]	G_{max} [kg/m^{2}s]	Re	$Q_{applied}$ [W]	$q_{applied}$ [kW/m^2]	$\frac{q_{applied}}{G}$ [kJ/kg]
Plate channel	R113	18.5-21.7	2.45-12.25	50-250	256-1346	25-75	10-30	0.08-0.15
Parallel channel	R113	13.9-20.7	5.0-15.0	200-600	349-1104	25-126	10-50.4	0.05-0.1
In-line Pin-fin	R113	18.7-23.2	2.5-12.5	100-500	171-905	25-140	10-56	0.08-0.15
Off-set Pin-fin	R113	17.6-20.6	5.0-15.0	200-600	334-1056	25-126	10-50.4	0.05-0.1
In-line Pin-fin	Water	19.6-23.9	1.0-5.0	40-200	51-306	25-723	10-289.2	0.2-2.0
Single-phase Pressure Drop Tests (Isothermal)								
Test piece	**Fluid**	$T_{f,in}$ [°C]	M [g/s]	G_{max} [kg/m^{2}s]	Re	$Q_{applied}$ [W]	$q_{applied}$ [kW/m^2]	
Plate channel	R113	19.8-21.1	2.45-12.25	50-250	134-680	0	0	
Parallel channel	R113	20.7-21.3	5.0-15.0	200-600	277-841	0	0	
In-line Pin-fin	R113	20.3-21.6	2.5-12.5	100-500	174-893	0	0	
Off-set Pin-fin	R113	18.0-20.2	5.0-15.0	200-600	338-1042	0	0	
In-line Pin-fin	Water	19.6-21.2	1.0-5.0	40-200	51-255	0	0	
Flow Boiling Tests								
Test piece	**Fluid**	$T_{f,in}$ [°C]	M [g/s]	G_{max} [kg/m^{2}s]	Re	$Q_{applied}$ [W]	$q_{applied}$ [kW/m^2]	$\frac{q_{applied}}{G}$ [kJ/kg]
Plate channel	R113	38.1-42.1	2.45-12.25	50-250	331-1736	25-404	10-161.6	0.04-2.0
Parallel channel	R113	38.7-41.8	5.0-15.0	200-600	465-1443	25-405	10-162.0	0.02-0.81
In-line Pin-fin	R113	39.8-43.3	2.5-12.5	100-500	225-1164	25-403	10-161.2	0.02-1.6
Off-set Pin-fin	R113	38.0-41.9	5.0-15.0	200-600	440-1382	25-404	10-161.6	0.02-0.81
In-line Pin-fin	Water	85.4-94.1	1.0-5.0	40-200	152-849	100-1210	40-484	0.2-12.1

5.2. Experimental Procedure

Prior to running each flow boiling test series, the working fluid was degassed by vigorous boiling for nearly 2 hours to force any dissolved gases to run away from the system to the ambient. During this period the vent valve above the condenser was periodically opened to allow dissolved gases to escape to the atmosphere. This also set the test pressure to near atmospheric. After degassing the liquid, as it was observed that no gas/air bubble coming out of the liquid inside the test piece prior to boiling, flow boiling tests were carried out.

Tests were conducted by setting the required liquid mass flow rate and inlet temperature. Mass flow rate was set by the by-pass valve and adjusted by the throttling valve located before the filters. The pre-heater was connected to a controller. With respect to the test's mass flow rate, the controller was set to the required applied heat to the fluid flow which was passing the pre-heater, to provide the desired inlet temperature. Simultaneously the test section heater was set to the desired heat flux to the test piece. The liquid was circulated through the flow loop until the required entry temperature was achieved. This took approximately $1.5 - 2$ hours. Steady state conditions were achieved when the fluid outlet, heater and the aluminium housing temperatures were shown to be stable. This took approximately $35 - 40$ minutes. All of the required readings and video recordings were obtained before the heat flux was re-set to the next desired value and the process repeated. During the tests to maintain the system pressure near the atmospheric pressure, the vent valve above the condenser was periodically open and a balloon was attached to it to prevent the vapour to escape from the system.

5.3. Data Reduction

For single-phase tests the working fluid which had a liquid specific heat capacity of c_p, was delivered into the test piece with a temperature close to the room temperature ($T_{f,in} \ll T_{sat,in}$), without any pre-heating. A range of heat loads was chosen to give a rise in fluid temperature across the test piece of at least $5\ K$, and up to a temperature less than saturation temperature at the test piece exit,

corresponding to the local exit pressure. Therefore a single-phase liquid region was achieved across the test piece, Figure 5.1a.

For flow boiling tests, the working fluid was supplied into the test piece in a sub-cooled state ($T_{f,in} < T_{sat,in}$), while inlet temperature was close to the local saturation temperature. The heat flux was applied to the test piece, therefore the test piece was segregated into two regions, based on the value of liquid thermodynamic equilibrium quality, x_{e}: an upstream subcooled region ($x_{\mathrm{e}} < 0$) with the length of L_{sub} and a downstream boiling region ($x_{\mathrm{e}} \geq 0$) with the length of L_{sat}, as shown in Figure 5.1b. Regions separating point was determined by the location of zero thermodynamic equilibrium quality, $x_{\mathrm{e}} = 0$. The length of the sub-cooled region was evaluated from the energy balance equation, i.e.

$$L_{sub} = \frac{M c_{p,f} (T_{sat,0} - T_{f,in})}{q_{eff} W} \tag{5.1}$$

where M is the mass flow rate, $c_{p,f}$ is the liquid mean specific heat capacity along the sub-cooled length, $T_{f,in}$ is the liquid inlet temperature, q_{eff} is the effective heat flux, W is the width of the test piece, and $T_{sat,0}$ is the saturation temperature at the zero thermodynamic equilibrium quality, corresponding to the local pressure $P_{sat,0}$. Local pressure $P_{sat,0}$ was evaluated from a linear pressure distribution assumption across the test piece. The linear pressure distribution assumption was deduced from the measured inlet pressure, P_{in}, and the measured pressure drop, Δp. Thus

$$p = p_{in} - \Delta p \frac{z}{L} \tag{5.2}$$

where L is the test piece length and z is the distance from the beginning of the test piece. The process was iterative to find out the L_{sub}. Since the test piece had a length L, the boiling length, L_{sat}, was estimated from

$$L_{sat} = L - L_{sub} \tag{5.3}$$

Typical temperature and pressure distribution profiles along the test piece for flow boiling tests are included in Figure 5.1.

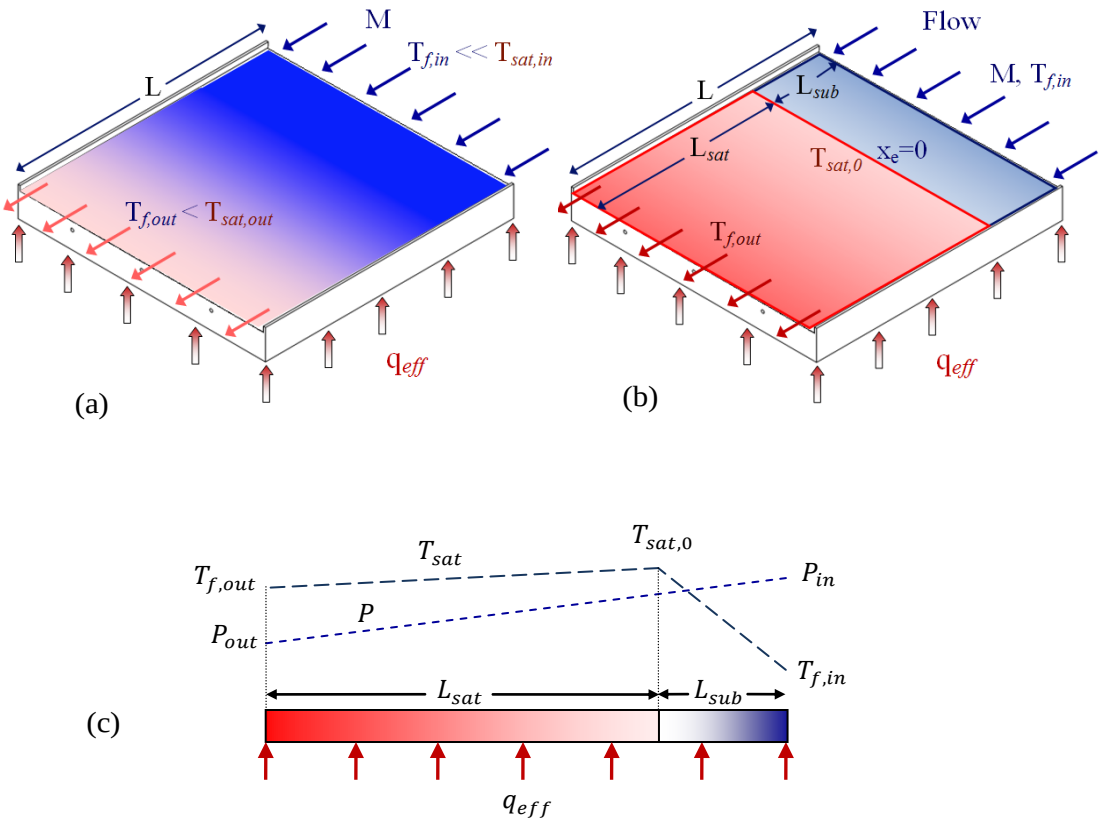

Figure 5.1 Heat load partition, (a) Single-phase tests, (b) Two-phase tests, and (c) Typical temperature and pressure distribution profiles along the test piece for flow boiling tests

5.3.1. Heat Transfer Coefficient Determination

Since determination of the local heat transfer coefficient requires flow passages local wall temperature and local fluid temperature, the heat transfer coefficient precisely evaluated at the location of measured wall temperatures by the type-K thermocouples situated inside the test piece, three close to the inlet and three close to the outlet. Thus two local heat-transfer coefficients deduced for each heat and mass flux set; inlet heat transfer coefficient h_{in}, and outlet heat transfer coefficient h_{out}. Figure 5.2 illustrates the locations of the obtained inlet and outlet heat transfer coefficients for parallel test piece.

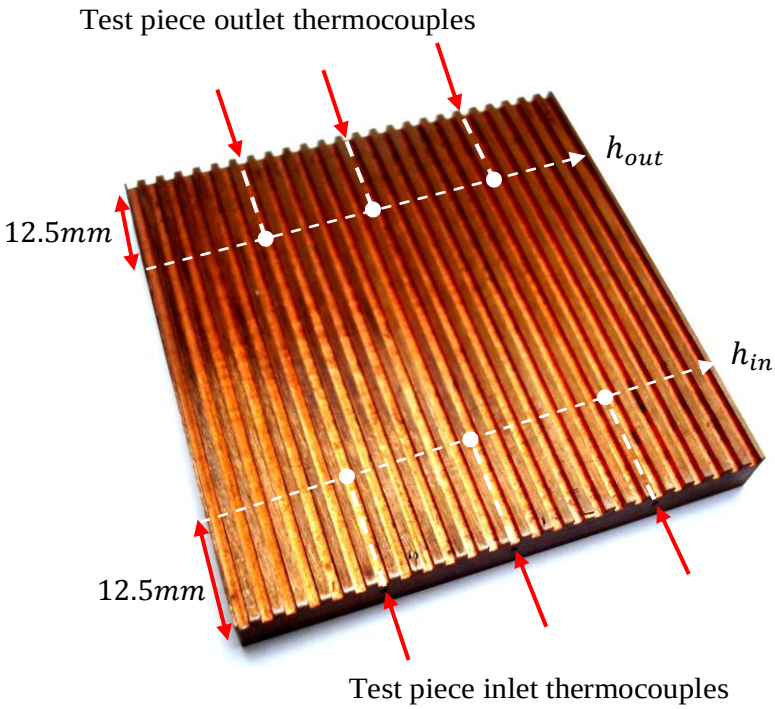

Figure 5.2 Locations of the obtained inlet and outlet heat transfer coefficients

The local heat transfer coefficient was obtained by separating the flow field into cells. Typical two dimensional unit cells at the location of a thermocouple situated inside the test piece for all test pieces is shown in Figure 5.3. The patterns are shown in axial direction, parallel and perpendicular to the flow, and consisted of single/double channels with surrounding walls, aluminium housing and glass cover plate. Figure 5.4 illustrates the top section of the typical unit cells for parallel channel, In-line and off-set pin-fin test pieces. For the plate channel test piece, the unit cell was assumed across the test piece with the width of 50 mm and the length of 2 mm, and can be presented like parallel channel unit cell by Figure 5.4a. The unit cells dimensions are specified in Table 5.2.

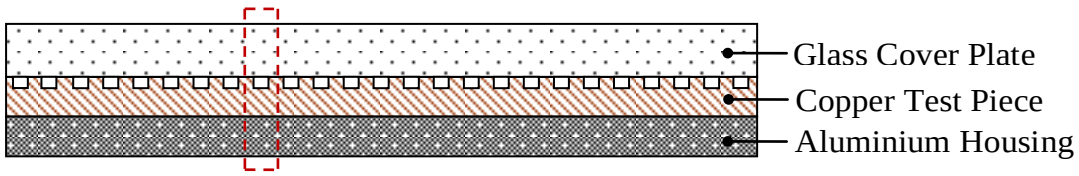

Figure 5.3 Test pieces heat transfer unit cells, (a) In-line off-set pin-fin surface, (b) Plate channel/Parallel channel/In-line pin-fin surfaces

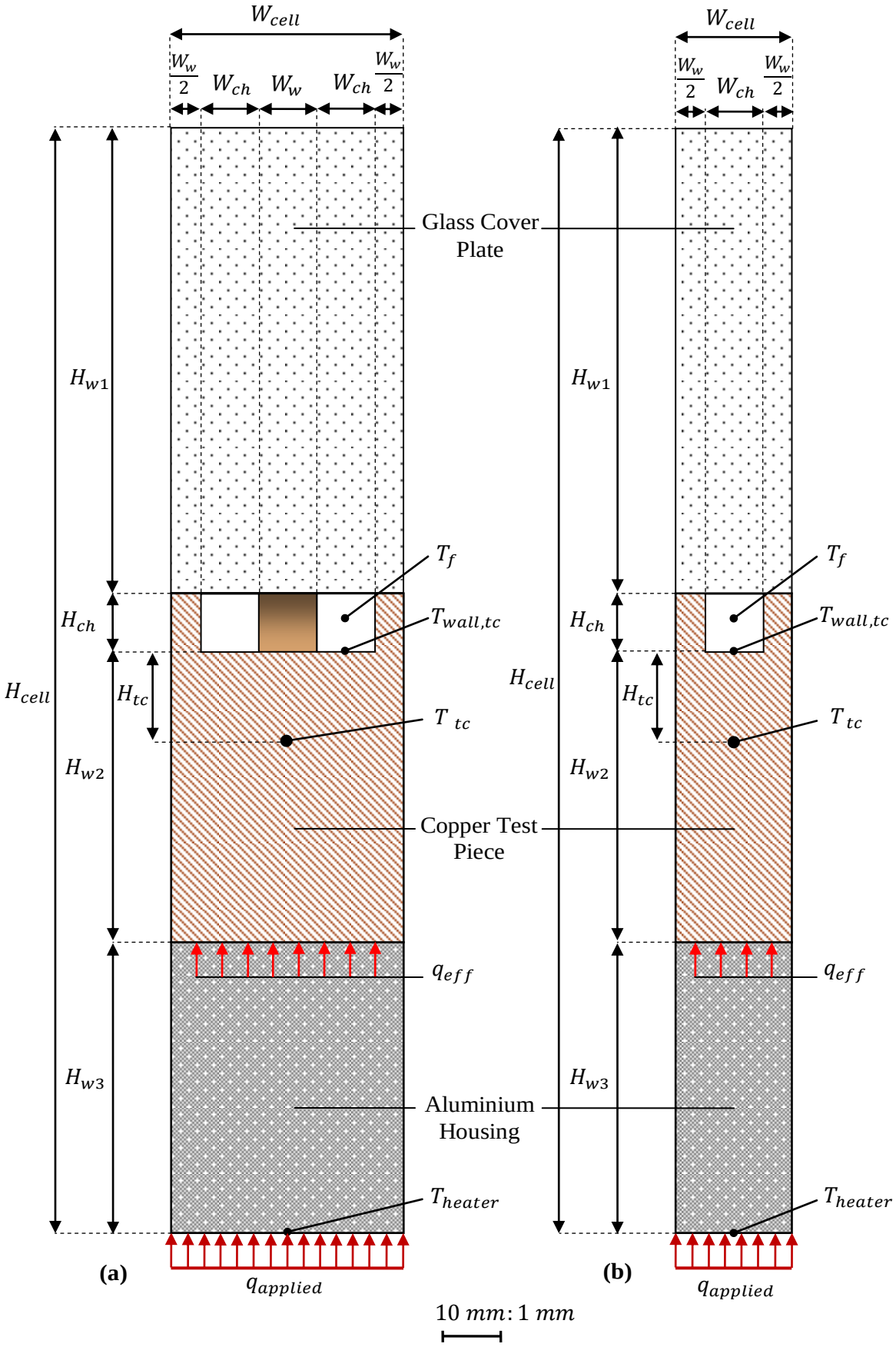

Figure 5.3 (continued) Test pieces heat transfer unit cells, (a) In-line off-set pin-fin surface, (b) Plate channel/Parallel channel/In-line pin-fin surfaces

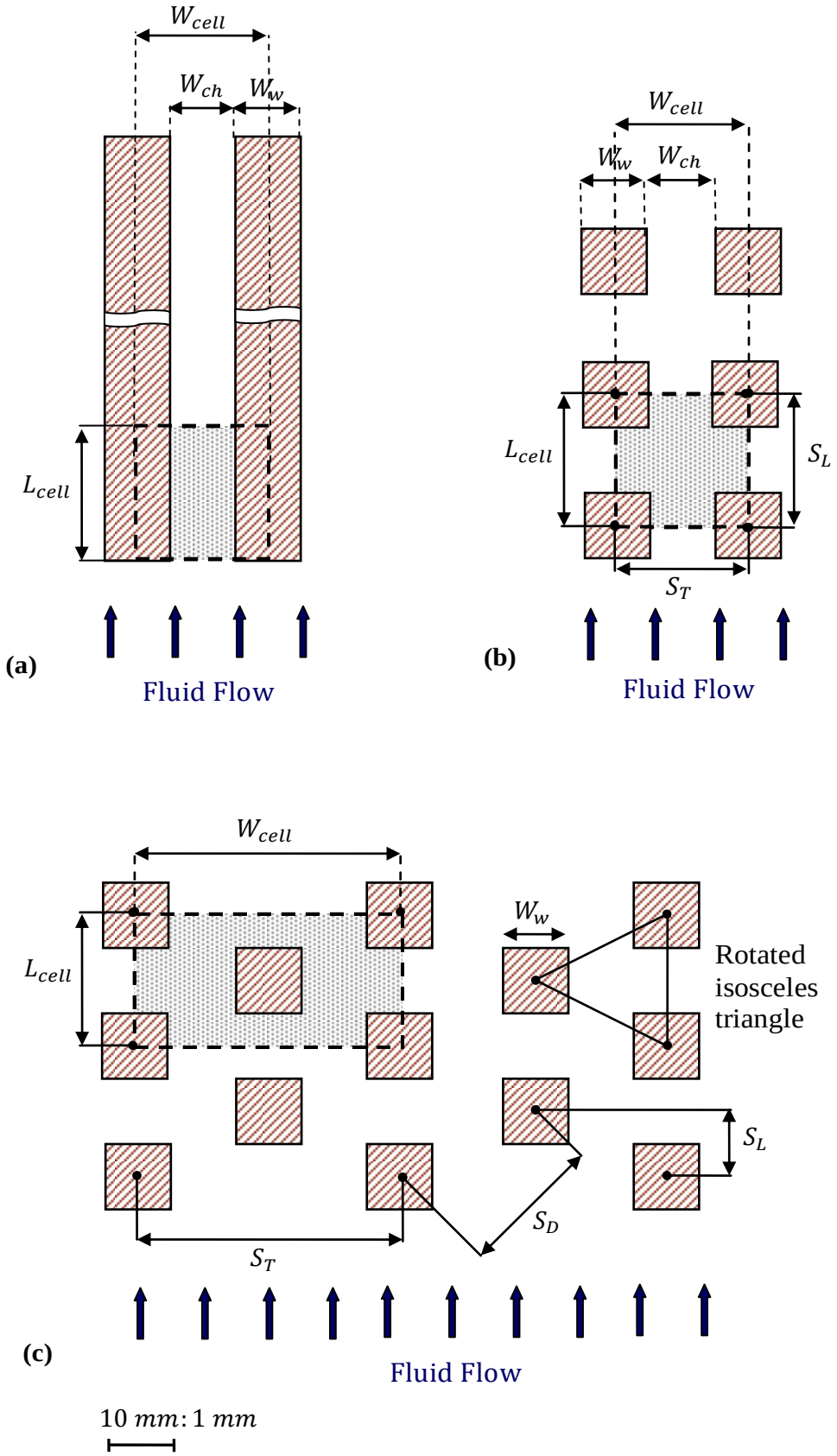

Figure 5.4 Top view of the test pieces heat transfer unit cells, (a) Plate/Parallel channel surface, (b) In-line pin-fin surface, and (c) In-line off-set pin-fin surface

Table 5.2 Dimensions of heat transfer unit cells

Plate channel test piece									
W_w/ mm	W_{ch}/ mm	W_{cell}/ mm	L_{cell}/ mm	H_{w1}/ mm	H_{w2}/ mm	H_{w3}/ mm	H_{ch}/ mm	H_{tc}/ mm	H_{cell}/ mm
0.5	49.0	50.0	2.0	10.0	5.0	5.0	1.0	1.5	21.0

Parallel channel test piece									
W_w/ mm	W_{ch}/ mm	W_{cell}/ mm	L_{cell}/ mm	H_{w1}/ mm	H_{w2}/ mm	H_{w3}/ mm	H_{ch}/ mm	H_{tc}/ mm	H_{cell}/ mm
1.0	1.0	2.0	2.0	10.0	5.0	5.0	1.0	1.5	21.0

In-line pin-fin test piece											
W_w/ mm	W_{ch}/ mm	W_{cell}/ mm	L_{cell}/ mm	H_{w1}/ mm	H_{w2}/ mm	H_{w3}/ mm	H_{ch}/ mm	H_{tc}/ mm	H_{cell}/ mm	S_T/ mm	S_L/ mm
1.0	1.0	2.0	2.0	10.0	5.0	5.0	1.0	1.5	21.0	2.0	2.0

Staggered pin-fin test piece												
W_w/ mm	W_{ch}/ mm	W_{cell}/ mm	L_{cell}/ mm	H_{w1}/ mm	H_{w2}/ mm	H_{w3}/ mm	H_{ch}/ mm	H_{tc}/ mm	H_{cell}/ mm	S_T/ mm	S_L/ mm	S_D/ mm
1.0	1.0	4.0	2.0	10.0	5.0	5.0	1.0	1.5	21.0	4.0	1.0	$\sqrt{5}$

For the parallel channel, in-line and in-line off-set pin-fin test pieces, because of the presence of the fins and channels and because of rectangular shape of the flow passages, the heat flux around the perimeter of the channels and pin fins was non-uniform, therefore the local heat transfer coefficient averaged over the heated surrounding walls of the flow passages and evaluated by using the fin analysis method. Two heat flow paths specified. One was through the base of the test piece to the fluid and the other one was through the channels and pin-fins walls to the fluid. These flow paths allowed the fin analysis method to be applied to the unit cells shown in Figures 5.3 and 5.4. For the plate channel test piece unit cell, the side walls area are negligible in comparison with the whole unit cell's area, therefore no fin analysis method was used for the plate channel test piece. A one-dimensional energy balance through the bottom of the test pieces gave the following equations;

- Plate channel test piece unit cell energy balance;

$$q_{eff} = h\left(T_{w,tc} - T_f\right) \tag{5.4a}$$

- Parallel channel test piece unit cell energy balance;

$$q_{eff}(W_{ch} + W_w) = h\big(T_{w,tc} - T_f\big)[W_{ch} + 2\eta H_{ch}] \quad (5.4b)$$

- In-line and in-line off-set pin-fin test piece unit cell energy balance;

$$q_{eff}(W_{ch} + W_w)^2 = h\big(T_{w,tc} - T_f\big)[(W_{ch} + W_w)^2 - W_w^2 + 4\eta W_w H_{ch}] \quad (5.4c)$$

where h is the local heat transfer coefficient, η is the fin efficiency, T_f is the fluid temperature and $T_{w,tc}$ is the flow passages bottom wall temperature. The left-hand side of the Equation (5.4) represents the heat input to the unit cell and the right-hand side shows the heat removal by the working liquid from the unit cell with neglecting the heat loss from the glass cover plate. The size of the flow passages dimensions in the above equations were given in Table 5.2.

The variation of measured inlet and outlet wall temperatures was typically less than 1 ℃, but could, on occasion, be as large as 2 ℃. A typical variation of the inlet and outlet wall temperatures with time at the location of the test piece thermocouples over a 4 minutes period is shown in Figure 5.5. As is shown, variation of each measured temperature was typically less than 0.2 ℃, and variation of wall inlet or outlet temperatures were typically less than 1.5 ℃. The wall temperature was therefore obtained by averaging the readings from the three wall temperatures at each location, Figure 5.2, near the test piece inlet and outlet to obtain T_{tc}, which was then corrected for depth from the plate surface, H_{tc}, through the following one-dimensional heat conduction equation, i.e.,

$$T_{w,tc} = T_{tc} - \frac{q_{eff} H_{tc}}{k} \quad (5.5)$$

where k is the thermal conductivity of the copper test piece, and H_{tc} is the thermocouples set distance from the plate surface, Figure 5.3. The fluid temperature, T_f, in the above energy equations, Equation(5.4), was obtained from the test piece partition shown in figure 5.1. If the heat balance indicated that the fluid above each set of thermocouples was sub-cooled, the sub-cooled temperature was used for T_f. Otherwise the saturation temperature corresponding to the local pressure was used.

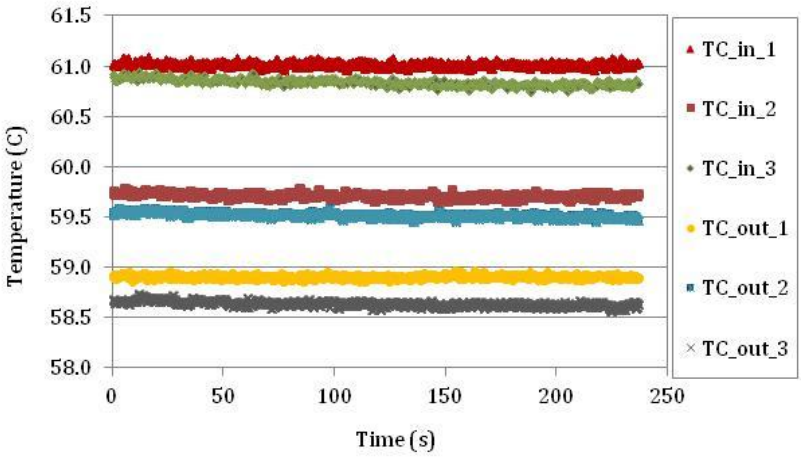

Figure 5.5 Typical variation of the inlet and outlet wall temperatures with time at the location of the test piece thermocouples

Wang et al. (2011) experimentally investigated flow boiling heat transfer of FC-72 and ethanol in high-aspect-ratio rectangular micro-channels. They observed large channel wall temperature fluctuations which resulted from periodic recoiling and re-wetting of the heated surface. In the present study, flow boiling tests were carried out at much higher mass flux ranges using test pieces containing mini flow passages with a larger height (1 mm). The periodic recoiling and re-wetting process was not observed for the present study except for the plate channel tests at low mass fluxes of 50 and 100 kg/m^2s and the highest heat fluxes of 80.4 and 112 kW/m^2.

As expressed in Chapter 4, the effective heat flux was calculated with an allowance made for heat loss, including the heat transfer from the glass cover plate. Therefore, at this stage, the heat transfer from the fin's top wall was neglected in Equation 5.4, as it was considered before. Thus, fin efficiency was given by (Incropera and Dewitt, 2002)

$$\eta = \frac{\tanh\,(mH_{ch})}{mH_{ch}} \tag{5.6}$$

where m is the fin parameter, given by the following equations for parallel and pin-fin surfaces, respectively;

$$m_{parallel} = \sqrt{\frac{2h}{kW_w}} \tag{5.7a}$$

$$m_{pin-fin} = \sqrt{\frac{4h}{kW_w}} \tag{5.7b}$$

As it was shown, the fin parameter is a function of heat transfer coefficient. Thus, the process of obtaining the heat-transfer coefficient was iterative. For two-phase tests, the local mass vapour quality, x, was estimated from

$$x = \frac{q_{eff} W (z - L_{sub})}{M h_{fg}} \tag{5.8}$$

where h_{fg} is the enthalpy of evaporation and W is the test piece width.

5.3.2. Pressure Drop Determination

Since the differential pressure transducer was connected to the pressure tappings which were located just upstream and downstream of the test piece, the measured pressure drop just included the pressure drop across the test piece. Therefore the pressure drop obtained directly from the differential pressure transducer.

A typical variation of the measured pressure drop and absolute pressure with time over a 4 minutes period is shown in Figure 5.6. As is shown, variation of the measured pressure drop was typically less than $4\,mbar$, and variation of the absolute pressure was less than $0.06\,bar$. The pressure drop and absolute pressure were therefore obtained by averaging the readings over a $40\,s$ period, during which 2000 readings of each were obtained.

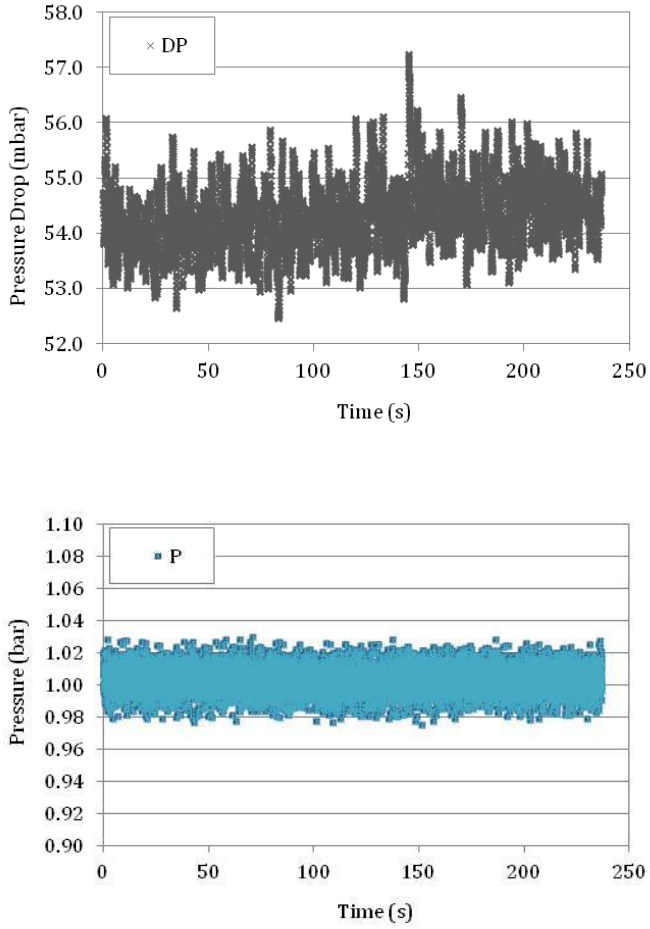

Figure 5.6 Typical variations of the measured pressure drop and absolute pressure with time

CHAPTER 6

EXPERIMENTAL RESULTS AND DISCUSSION

Heat transfer coefficients and pressure drop measurements obtained for single-phase and two-phase tests with R113 and deionised water, and also flow boiling visualizations for these series of tests are presented in this chapter. The results described are based on the test series.

Single-phase heat transfer coefficients were obtained for a range of heat loads and mass fluxes. The heat loads were chosen to provide a reasonable increase in fluid temperature, with a minimum increase of $5\ K$ across the test piece before reaching the saturation temperature corresponding to the local pressure. Single-phase pressure drops were obtained under isothermal conditions for the same mass fluxes. Two-phase heat transfer coefficients and pressure drops were obtained in the steady state conditions for the same mass flux range used for single-phase tests. The working fluid was supplied to the test section at near atmospheric pressure with $2 - 12\ K$ sub-cooling. The heat loads were chosen to provide flow boiling conditions with quite significant mass vapour quality for higher heat loads at the test piece outlet.

The operating conditions for single-phase and flow boiling tests were described in section 5.1 based on the test series, and summarized in Table 5.1. Full details of tests operating conditions and measurements can be found in Appendix E. The operating conditions for flow boiling tests and experimental procedure led to the occurrence of three types of heat-transfer, single-phase, sub-cooled flow boiling and saturated flow boiling heat transfer at the measuring points. Single-phase heat-transfer occurred when the fluid above the thermocouple was sub-cooled liquid and the wall temperature was below the local saturation temperature. Sub-cooled flow boiling heat-transfer occurred when the fluid above the thermocouple was sub-cooled liquid and the wall temperature was above the local saturation temperature. Saturated flow boiling heat-transfer occurred when the fluid above the thermocouple was in a saturated state and the wall temperature was above the local saturation temperature.

Experimental results and flow boiling visualisations for all test series; Plate channel, Parallel channel, in-line pin-fin and in-line off-set pin-fin surfaces with R113, and in-line pin-fin surface with deionised water as working fluid are described in Sections 6.1 to 6.5 respectively.

As it was mentioned before, the test piece wall thermocouples were located 12.5 and 37.5 mm from the test piece's inlet. Inlet and outlet boiling curves and heat-transfer coefficients in the following sections refer respectively to the 12.5 and 37.5 mm locations, Figure 6.1.

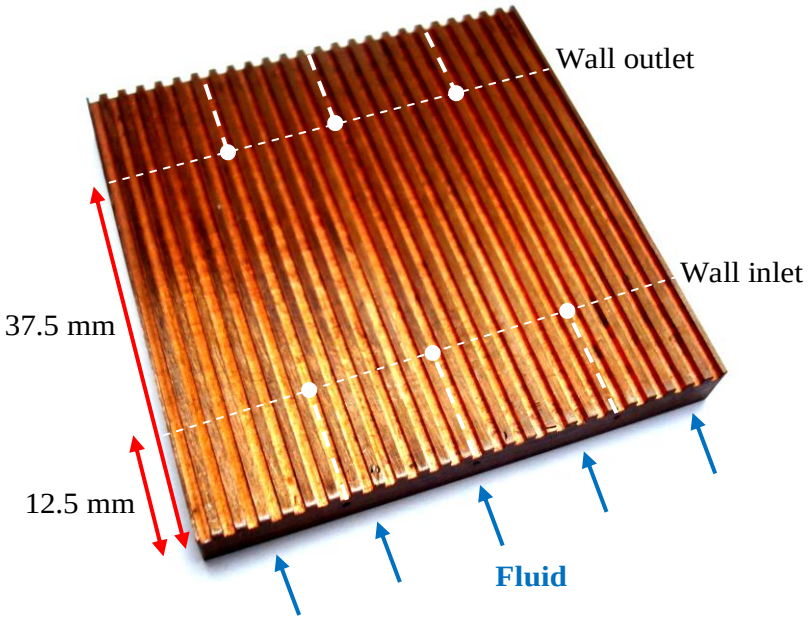

Figure 6.1 Locations of the inlet and outlet readings

6.1. Plate Channel Surface Tests with R113

Plate channel heat transfer coefficients and pressure drop measurements, obtained for single-phase and two-phase tests with R113 as the working fluid, and also flow boiling visualizations for these series of tests, are presented in this section.

6.1.1. Single-Phase Heat Transfer Coefficient

The variation of single-phase heat transfer coefficient with mass flux for the complete range of heat fluxes is shown in Figure 6.2. The estimated error in the heat transfer coefficient is $\pm 10\%$.

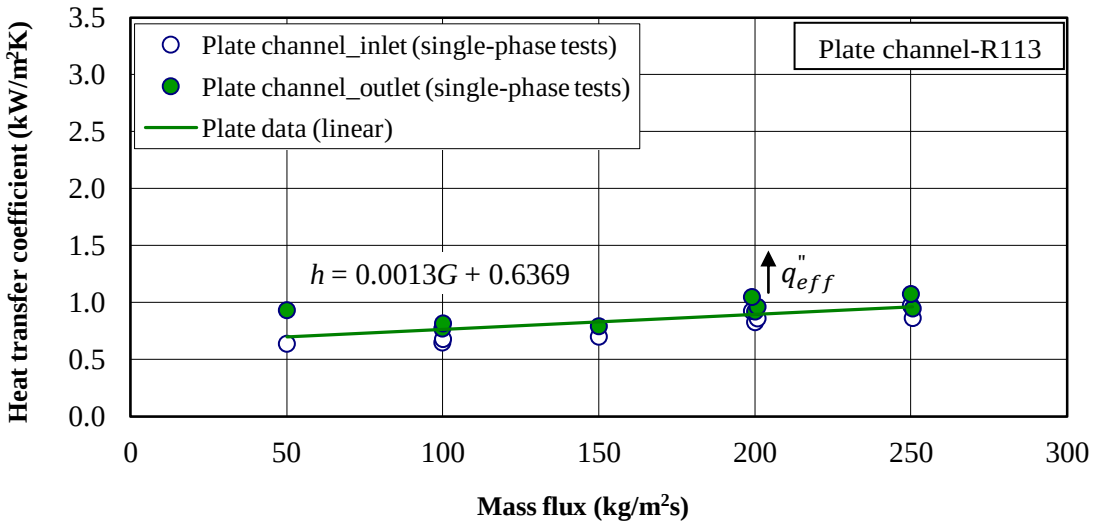

Figure 6.2 Variation of single-phase heat-transfer coefficient with mass flux for plate surface with R113

For all but lowest mass flux of $50\ kg/m^2s$, the single-phase heat-transfer coefficients at the inlet and outlet positions of the plate surface are shown to be similar in magnitude and to increase with increasing mass flux. For a constant mass flux, heat transfer coefficient remains fairly constant or increases only slightly with increasing heat flux. The slight increase in heat transfer coefficient value with increasing heat flux may be attributed to the increase in the average Reynolds number defined as

$$Re_{ave} = \frac{\rho_{f,ave} u_{ave} D_h}{\mu_{f,ave}} \tag{6.1}$$

where the liquid properties were evaluated at the average liquid bulk temperature, $T_{f,ave}$, across the test piece. This is because of reduced liquid density and viscosity, caused by high $T_{f,ave}$, corresponding to high heat fluxes. Wall inlet and outlet single phase heat transfer coefficients values are shown approximately following a linear function of the mass flux.

6.1.2. Single-Phase Pressure Drop

According to the differential pressure transducer reference accuracy, Table 3.11, the minimum measurable pressure drop was around $1\,pa$. For the plate surface most of the measured single-phase pressure drops were below this value, therefore the pressure drops were too small to be measured using the pressure transducer installed in the rig.

6.1.3. Boiling Curve

Figure 6.3 illustrates typical boiling curves for mass fluxes of 150 and 250 kg/m^2s. Boiling curves obtained for steady state conditions at the location of two sets of thermocouples, situated at the test piece wall inlet and outlet. In these curves effective heat flux, q_{eff}, is plotted in terms of the difference between channel base wall temperature, $T_{w,tc}$, and local bulk fluid temperature, $T_{f,tc}$, where $T_{w,tc}$ was obtained from conduction equation, Equation (5.5). If the fluid above each set of thermocouples was sub-cooled, the sub-cooled temperature was used for $T_{f,tc}$, otherwise the saturation temperature corresponding to the local pressure was used.

Two regions featuring fairly different relationships between effective heat flux, q_{eff}, and temperature difference, $(T_{w,tc} - T_{f,tc})$, can be identified. First, a sub-cooled flow boiling region at low heat fluxes, where the local vapour mass fraction is below zero and the slopes of the boiling curves are firstly have a low slope and increase sharply with increasing heat flux thereafter. Afterwards a saturated flow boiling region at higher heat fluxes, where the local vapour mass fraction is above zero.

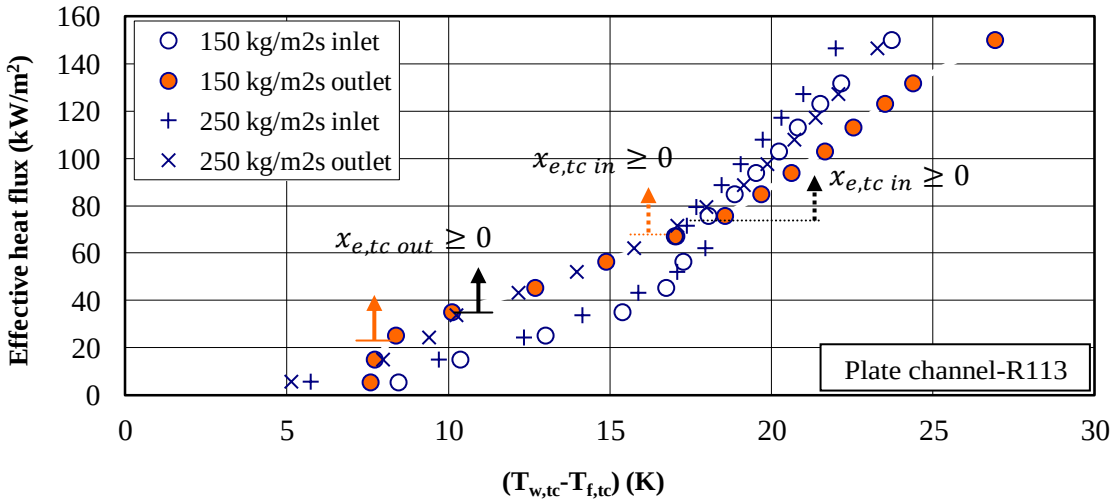

Figure 6.3 Boiling curves at the wall inlet and outlet for representative mass fluxes of 150 and 250 kg/m^2s, obtained from plate surface tests with R113

Figure 6.4 shows variation of plate surface boiling length, the length over which boiling takes place measured from the outlet end of the test piece, with effective heat flux for a range of mass fluxes. As is shown, the boiling length is increased with increasing heat flux. At heat fluxes greater than 80 kW/m^2 the boiling lengths remain quite constant. This was resulted from the needed minimum sub-cooled length, the length which the bulk liquid is in the sub-cooled state and absorbing heat until reaching the onset of nucleate boiling (ONB) and starting the partial nucleate boiling region. As is shown, for a constant heat flux the sub-cooled length is increased with increasing the mass flux.

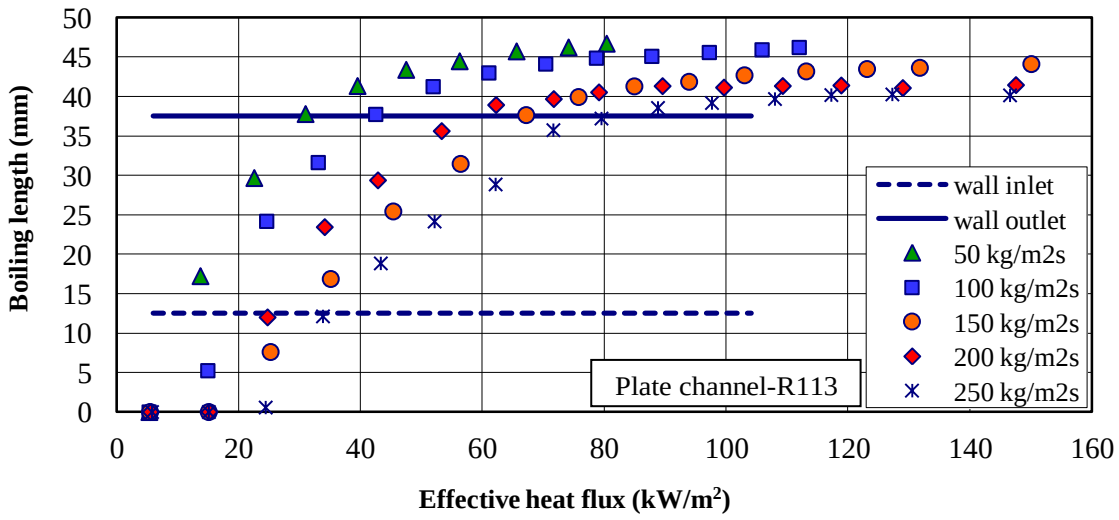

Figure 6.4 Variation of boiling length with effective heat flux for a range of mass fluxes for plate surface with R113

6.1.4. Two-Phase Heat Transfer Coefficient

The variation of the measured heat-transfer coefficients with the effective heat fluxes is shown for each mass flux in Figure 6.5. At the mass flux of $50\ kg/m^2s$, sub-cooled flow boiling is shown to exist at the wall inlet location for heat fluxes in the range $5-23\ kW/m^2$, with saturated flow boiling occurring thereafter. Saturated flow boiling is shown to occur for all heat fluxes at the wall outlet, except for the lowest heat flux of $5\ kW/m^2$, which is in the sub-cooled flow boiling region. In the heat flux range of $5-23\ kW/m^2$, which wall inlet flow is in the sub-cooled flow boiling region, the wall inlet heat-transfer coefficient is shown to rise from levels below the outlet values to the outlet value. Thus, the merging of the heat-transfer coefficients is consistent with the single-phase settling length being longer than the two-phase equivalent. At heat fluxes in the range $23-65\ kW/m^2$, the wall inlet and outlet heat-transfer coefficients are shown to be similar in magnitude, in the saturated boiling region and independent of heat flux.

At heat fluxes greater than $65\ kW/m^2$, the wall inlet and outlet heat transfer coefficients are not independent of heat flux. Instead, a reasonably constant value is maintained until a heat flux of approximately $80\ kW/m^2$ is achieved, after this a dip occurs. Figure 6.9 shows typical observed flow patterns for the plate surface for mass flux of $50\ kg/m^2s$ at effective heat fluxes in the range $23-86\ kW/m^2$. As is shown in this figure, the plate surface contains dried out areas covering relatively large areas. These dried out areas appeared at lower heat fluxes and grew in size and dominance until the plate surface heat-transfer coefficient decreased at a heat flux of around $75\ kW/m^2$ and the local vapour mass fraction of 0.53. The drop in heat transfer coefficient for mass flux of $100\ kg/m^2s$ at heat flux of $106\ kW/m^2$ and local vapour mass fraction of 0.37 is also associated with the onset of dry-out.

As the mass flux increases, the range of heat fluxes in the sub-cooled flow boiling region increases. This results from the increased amount of absolute sensible enthalpy change that is required to reach saturation as a consequence of the mass flux increase. At these larger mass fluxes, the description given for mass flux of $50\ kg/m^2s$ is, in the main, repeated with this major difference that, the region where the heat-transfer coefficient is reasonably independent of heat flux decreases as the mass flux increases.

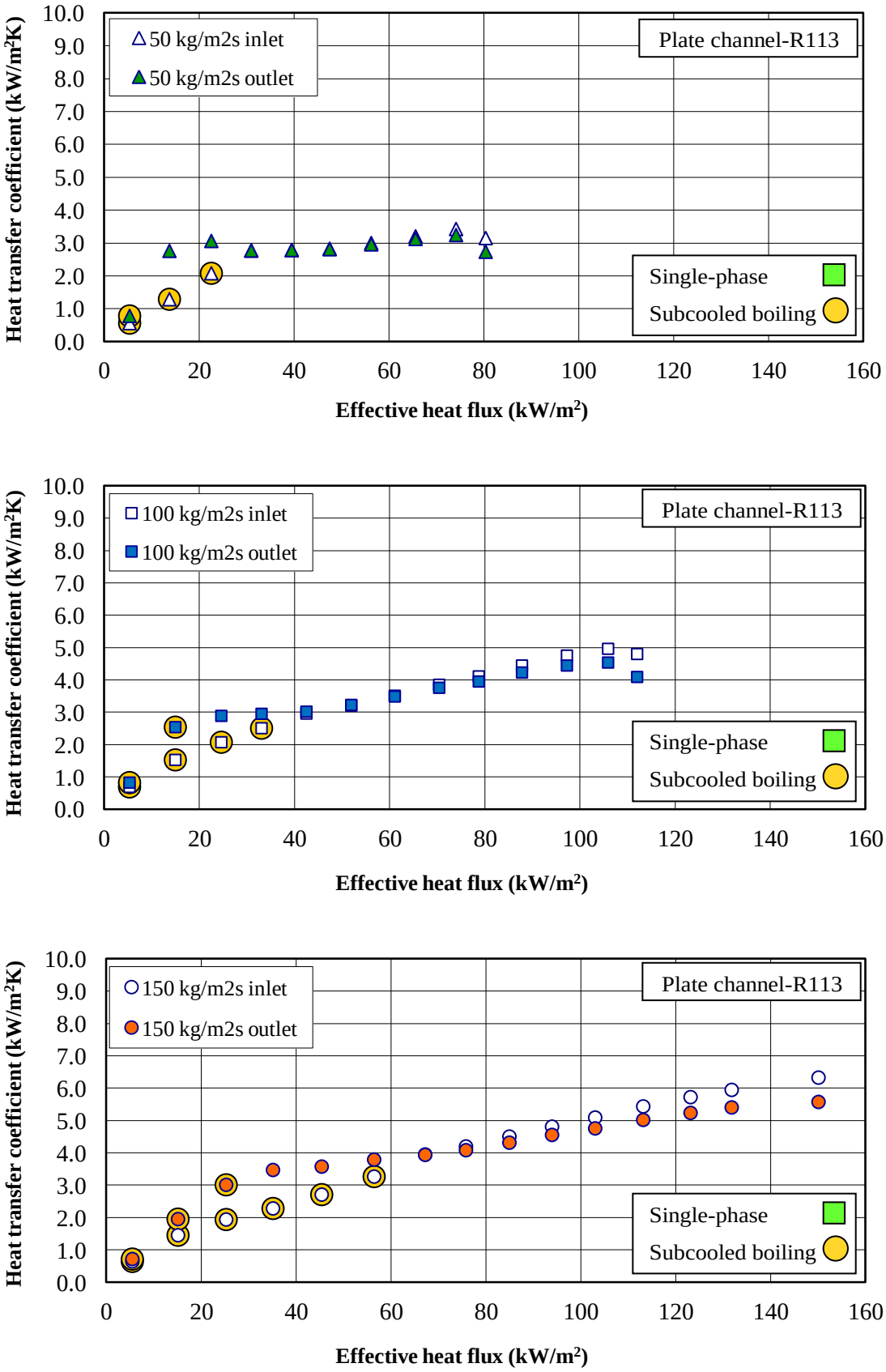

Figure 6.5 Variation of heat transfer coefficient with effective heat flux for a range of mass fluxes for plate surface with R113

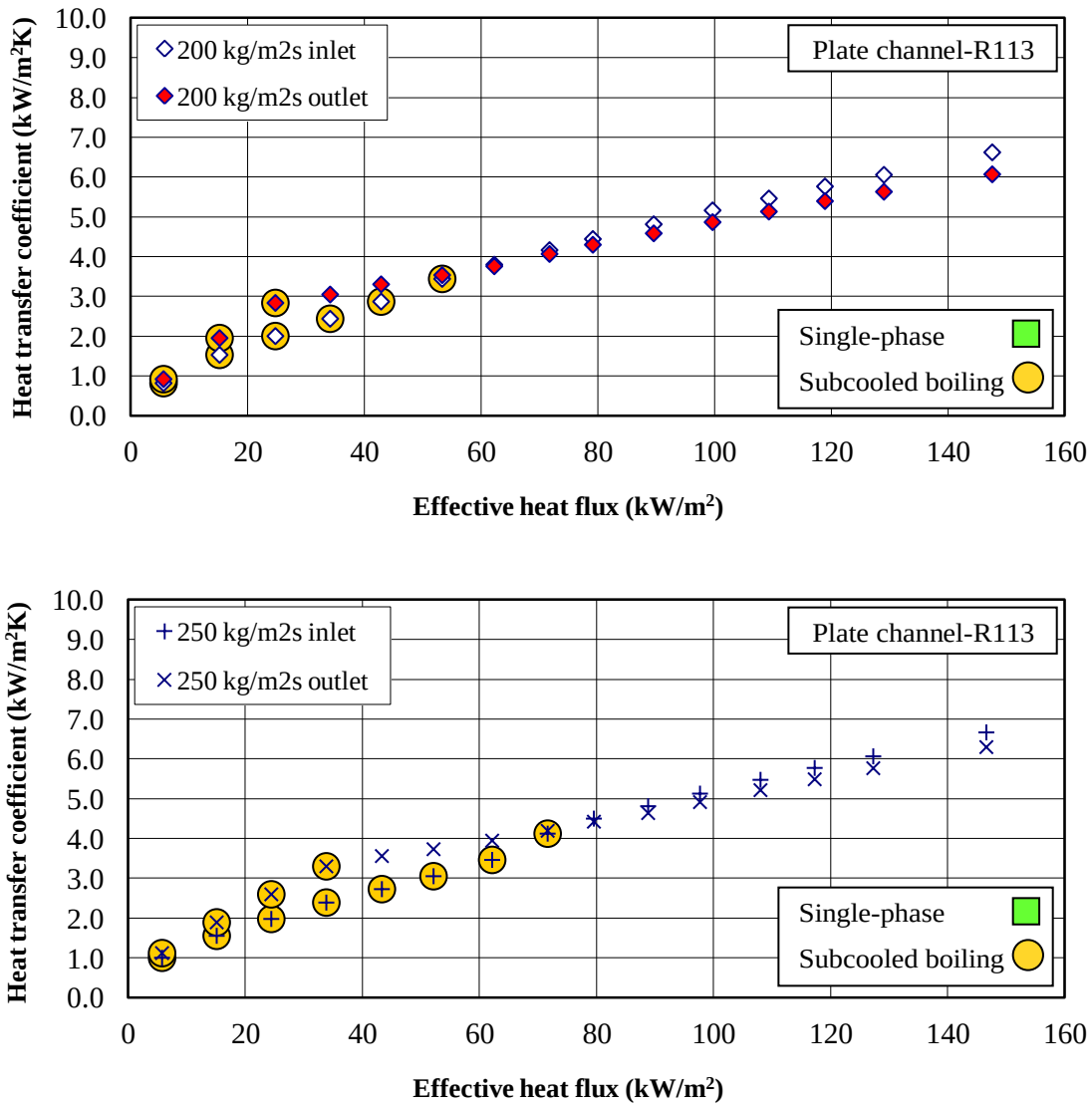

Figure 6.5 (continued) Variation of heat transfer coefficient with effective heat flux for a range of mass fluxes for plate surface with R113

The region where the saturated flow boiling heat-transfer coefficients are reasonably independent of heat flux could be consistent with the convective enhancement to a confined bubble or annular flow regime, where the convective flow boiling heat transfer mechanism is dominant. Then these flow regimes break up to new flow patterns with nucleation and lead to a region where the heat transfer coefficients are strongly dependent on heat flux.

Figure 6.6 illustrates the variation of saturated boiling heat transfer coefficient with local vapour mass fraction for a range of mass fluxes. The range of vapour mass fractions is reduced at the larger mass fluxes. For mass flux $50\,kg/m^2s$, the vapour

mass fractions at the wall inlet and outlet locations are approximately 0.08 and 0.3 respectively at a heat flux of $65\,kW/m^2$ while, the saturated boiling heat transfer coefficients at these locations are quite the same. Thus, for each mass flux, the saturated boiling heat transfer coefficients are fairly independent of vapour mass fraction.

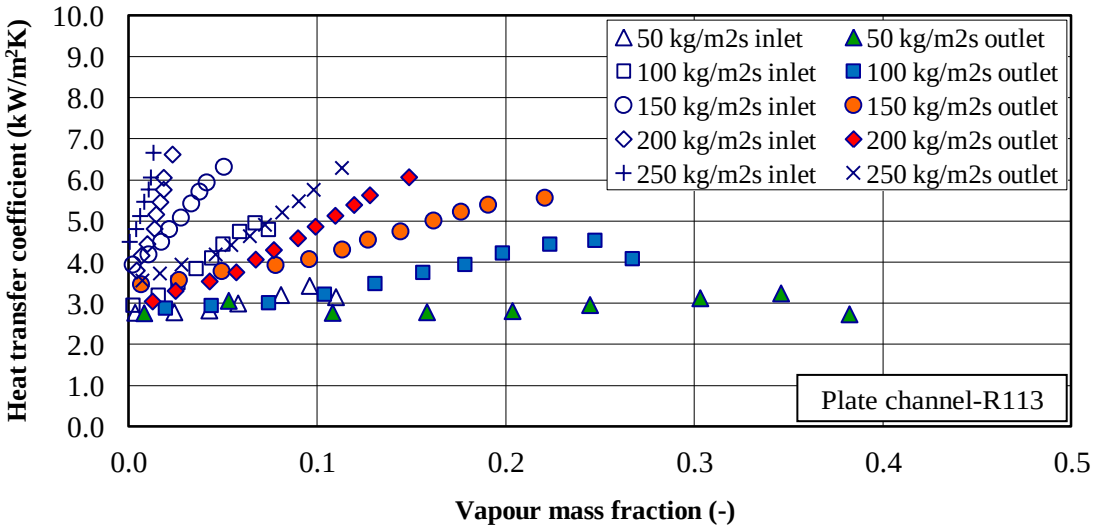

Figure 6.6 Variation of saturated boiling heat transfer coefficient with local vapour mass fraction for a range of mass fluxes for plate surface with R113

All of the saturated boiling data identified in Figure 6.5, are reproduced in Figure 6.7. A power law function is also passed through the data. As is shown, data are reasonably independent of location and mass flux and follow the power law relationship

$$h = 0.556 q_{eff}^{0.467} \tag{6.2}$$

to within $\pm 10\%$ of the measured values. Equation (6.2) is based on the effective heat flux. For the plate surface the effective and actual heat fluxes are the same. Actual heat flux is the heat flux based on the actual heat transfer area. It therefore seems likely that the dominating heat-transfer mechanism in the saturated boiling flow regime is nucleate boiling. This result agrees with that found by Kew et al. (2006). They suggested that rate of vapour generation determines heat transfer and that this, for a single geometry is proportional to heat flux. It is worth mentioning that, the region where the heat-transfer coefficients were reasonably independent of heat flux could be consistent with the domination of convective boiling heat transfer mechanism.

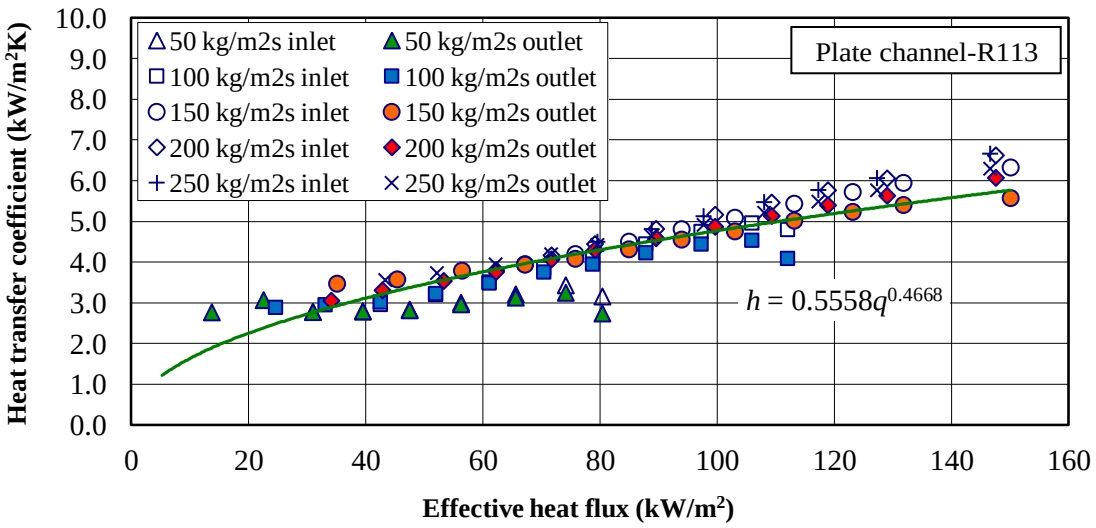

Figure 6.7 Variation of saturated boiling heat transfer coefficient with effective heat flux for plate surface with R113

6.1.5. Two-Phase Pressure Drop

The variation of two-phase pressure drop with heat flux for a range of mass fluxes is shown in Figure 6.8. At the heat flux of approximately $5\ kW/m^2$, most of the plate surface is in sub-cooled flow boiling region and the two-phase pressure drop is shown to decrease with increasing mass flux. In the heat flux range of $5-23\ kW/m^2$ for all mass fluxes, pressure drop is close to zero. For heat fluxes greater than $23\ kW/m^2$, the pressure drop is shown to be reasonably proportional to heat flux and increase with increasing heat flux.

For all mass fluxes, the pressure drop is shown not following a clear trend with increasing mass flux. There are two opposing effects that could cause this to occur. The first is that pressure drop increases with increasing mass flux. The second is that the pressure drop increases with increasing vapour content. For the same heat flux, as the mass flux increases, the vapour content decreases, leading to the trends shown in Figure 6.8. For mass fluxes of 50 and $100\ kg/m^2s$, is shown at high heat fluxes with the appearance of dried out areas and growing at the surface, the pressure drop starts to decrease.

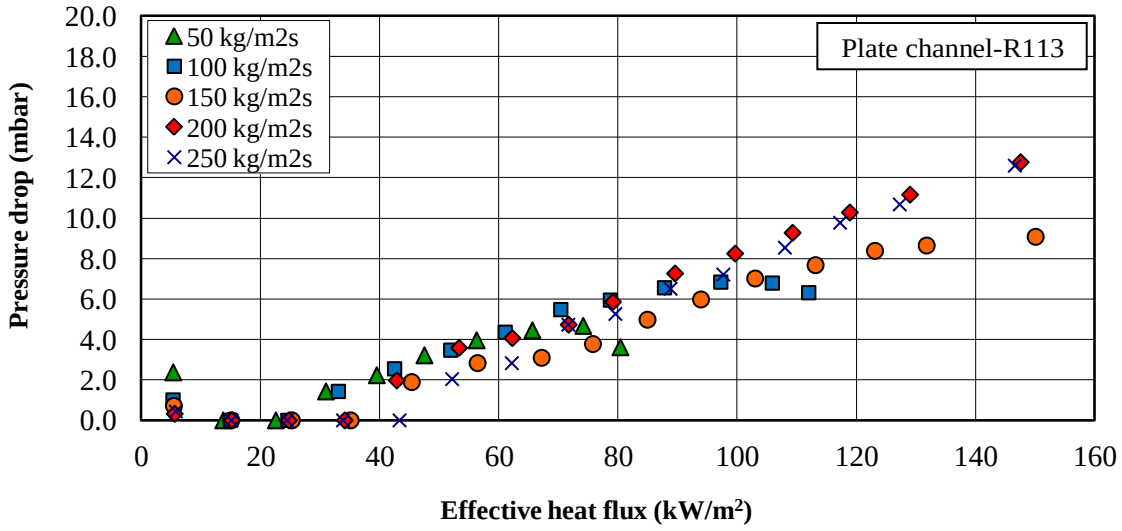

Figure 6.8 Variation of pressure drop with effective heat flux at various mass fluxes for plate surface with R113

6.1.6. Flow Boiling Visualisation

Figure 6.9 shows typical observed flow patterns for mass flux of $50\,kg/m^2s$ at effective heat fluxes in the range $23-86\,kW/m^2$. As it is shown, the plate surface contains dried out areas in light gray colour, covering relatively large areas. These dried out areas appeared at lower heat fluxes and grew in size with increasing heat flux. For heat fluxes larger than $80\,kW/m^2$, the wall temperature increases sharply and continuously.

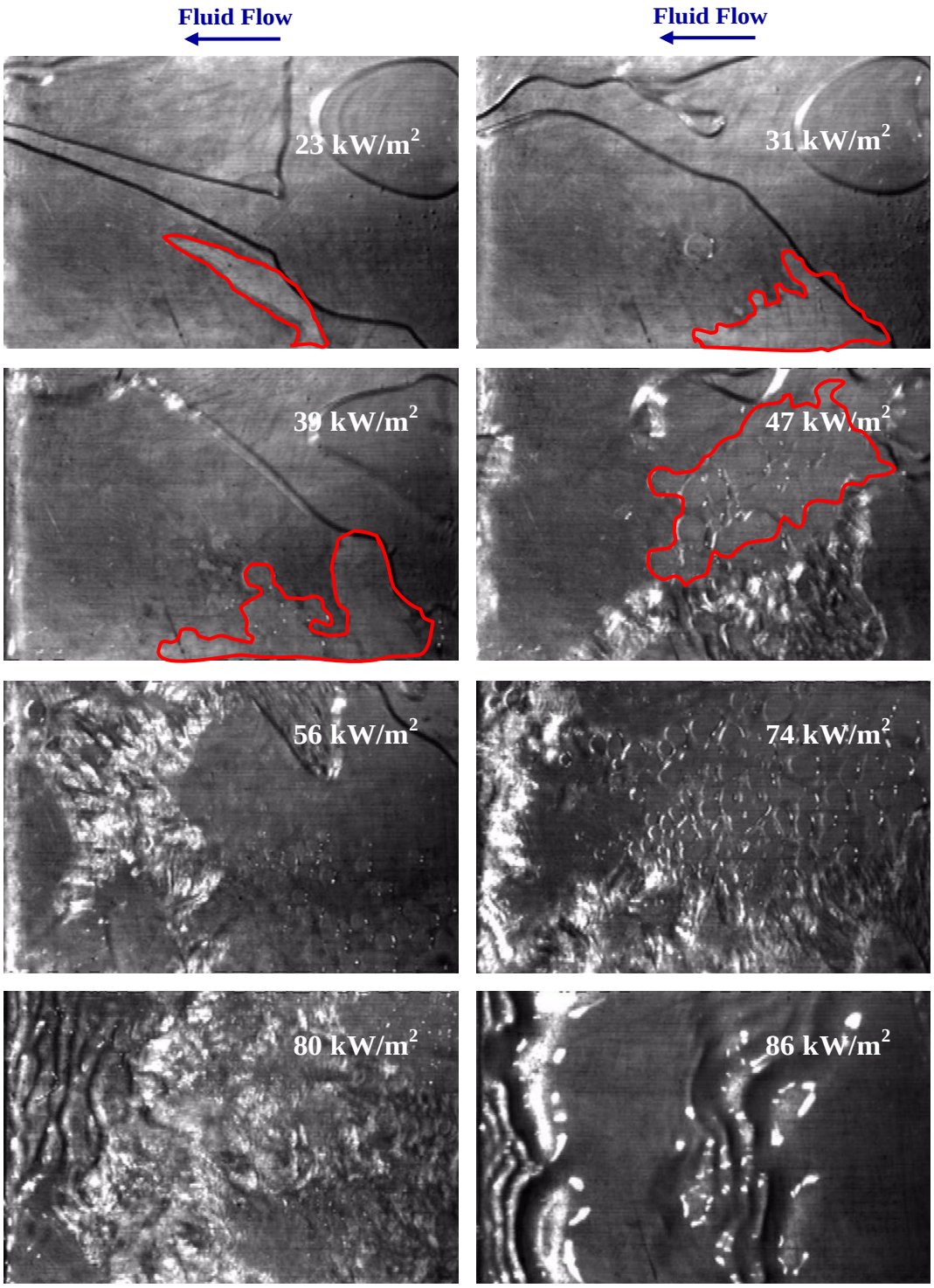

Figure 6.9 Typical views of the flow for mass flux of 50 kg/m^2s at effective heat fluxes in the range $23 - 86\ kW/m^2$, for plate surface with R113

6.2. Parallel Channel Surface Tests with R113

Parallel channel surface heat transfer coefficients and pressure drop measurements, obtained for single-phase and two-phase tests with R113 as working fluid, and also flow boiling visualisation for these series of tests are presented in this section.

6.2.1. Single-Phase Heat Transfer Coefficient

Figure 6.10 shows the variation of the measured single-phase heat transfer coefficient with mass flux for a range of heat fluxes. The estimated error in the heat transfer coefficient is $\pm 10\%$.

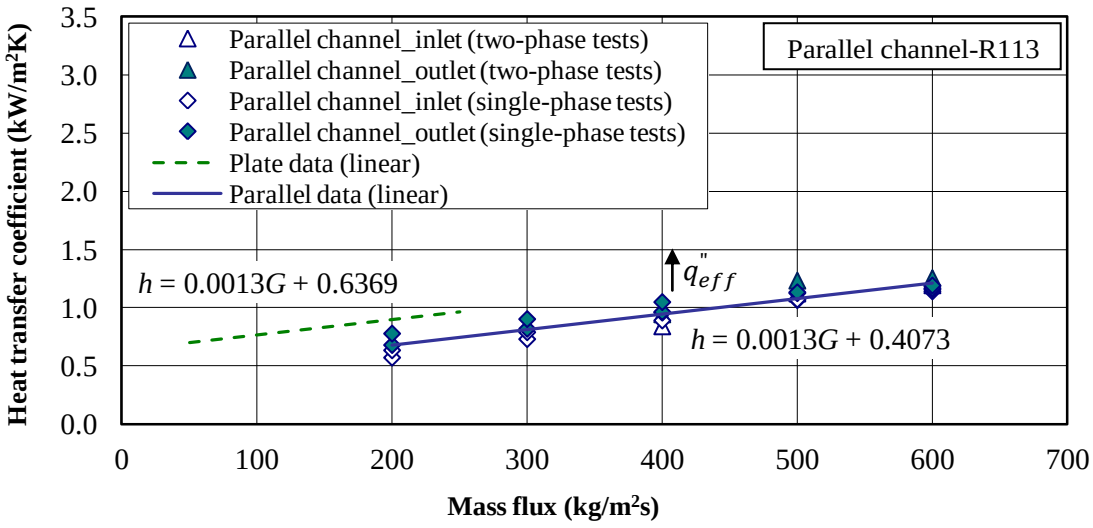

Figure 6.10 Variation of single-phase heat-transfer coefficient with mass flux for parallel channel surface with R113

The parallel channel surface single-phase heat-transfer coefficients are shown to be similar in magnitude and to increase with increasing mass flux, similar to those obtained with the plate surface. As it is shown, for a constant mass flux, parallel channel surface heat transfer coefficient remains fairly constant or increases only slightly with increasing heat flux, caused by increasing the average Reynolds number. Parallel channel surface wall inlet and outlet values are shown following a single linear function of the mass flux.

The plate surface linear trend line is included in Figure 6.10. For the same mass fluxes the plate surface single-phase heat transfer coefficients are a little bit larger than the parallel channel surface values with following a linear function containing exactly the same slope as parallel trend line. However, as the parallel channel surface has a 1.5 times larger heat transfer area than the plate surface, for constant heat transfer rates, smaller temperature values are achieved at the heater surface.

6.2.2. Single-Phase Pressure Drop

The variation of single-phase pressure drop with mass flux is shown for the parallel channel surface in Figure 6.11. According to the operating conditions, Reynolds number for these series of tests was less than 841, indicative of laminar flow through the channels. In the laminar flow range the pressure drop is directly proportional to the velocity (Massey, 2006). The pressure drop is shown to be a linear function of the mass flux, as would be expected for laminar flow in channels.

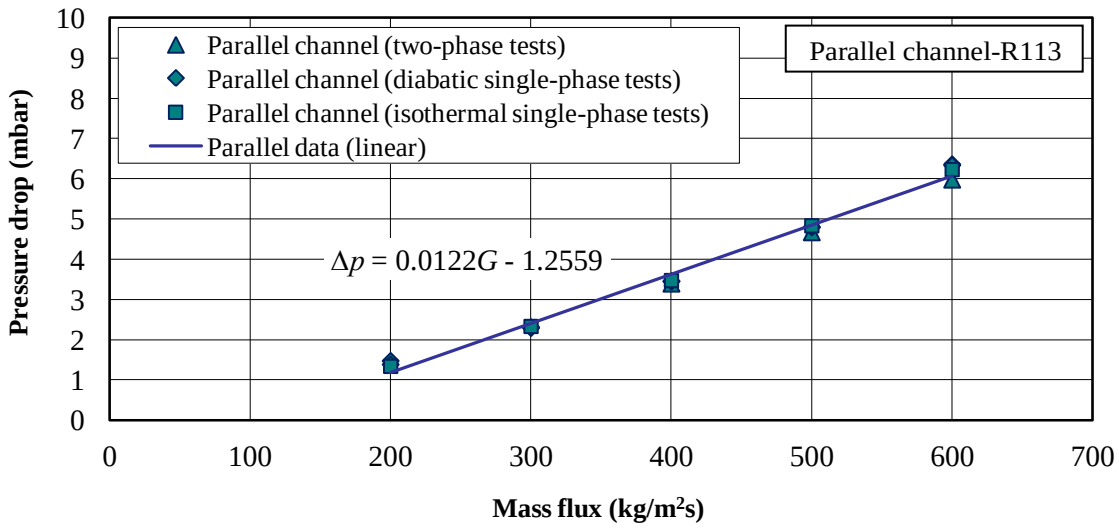

Figure 6.11 Variation of single-phase pressure drop with mass flux for parallel channel surface with R113

6.2.3. Boiling Curve

Figure 6.12 shows typical boiling curves obtained for steady state conditions at the wall inlet and outlet thermocouples sets locations for each mass flux. Effective heat flux is plotted in terms of the difference between channel base wall temperature, $T_{w,tc}$, and local bulk fluid temperature, $T_{f,tc}$. For all mass fluxes, except 300 kg/m^2s, three regions featuring fairly different relationships between effective heat flux, q_{eff}, and temperature difference, $(T_{w,tc} - T_{f,tc})$, can be identified.

For lowest mass flux of 200 kg/m^2s, at lowest heat flux, the temperature difference $(T_{w,tc} - T_{f,tc})$ at the wall inlet is small and separated from the rest of the curve's data. A single-phase region is identified in this location. For intermediate heat fluxes, the slope of the wall inlet boiling curve sharply increases, indicative of sub-cooled flow boiling region. At the wall outlet, for low heat fluxes, due to a sharp rise in the convective heat transfer coefficient, the slope of the wall outlet boiling curve is negative, indicative of sub-cooled flow boiling region. At both the wall inlet and outlet locations, for higher heat fluxes the local vapour mass fraction, $x_{e,tc}$, is above zero and the slopes of the boiling curves are positive and fairly constant, indicative of saturated flow boiling region.

For larger mass fluxes, the description given for mass flux 200 kg/m^2s is, in the main, repeated. There are few differences. At mass flux of 300 kg/m^2s, the single-phase region cannot be identified and two sub-cooled and saturated flow boiling regions occur for both inlet and outlet flows. For mass fluxes of 400 kg/m^2s and above, at lowest heat flux, the single-phase region is identified at both the wall inlet and outlet locations. For these mass fluxes, except at the lowest heat flux for which wall inlet data are in single-phase region, for other heat fluxes the wall inlet data are in sub-cooled flow boiling region and no saturated flow boiling region occurs for inlet location. Despite the similarity in the shape of the boiling curves for these mass fluxes, considerable difference is viewed between the two inlet and outlet curves, which is resulted from the two different regions at these locations.

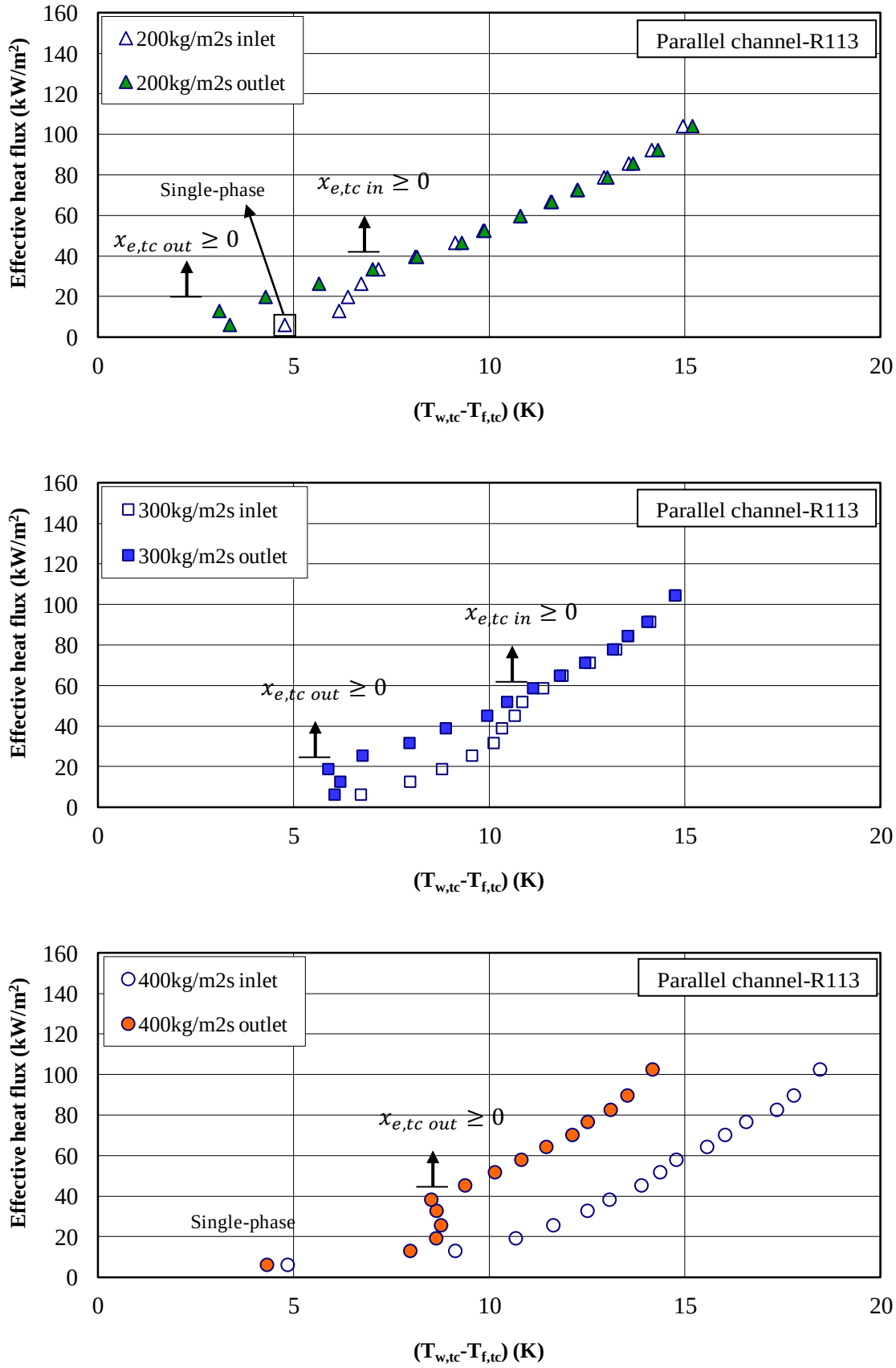

Figure 6.12 Boiling curves at the wall inlet and outlet for a range of mass fluxes, obtained from parallel channel surface tests with R113

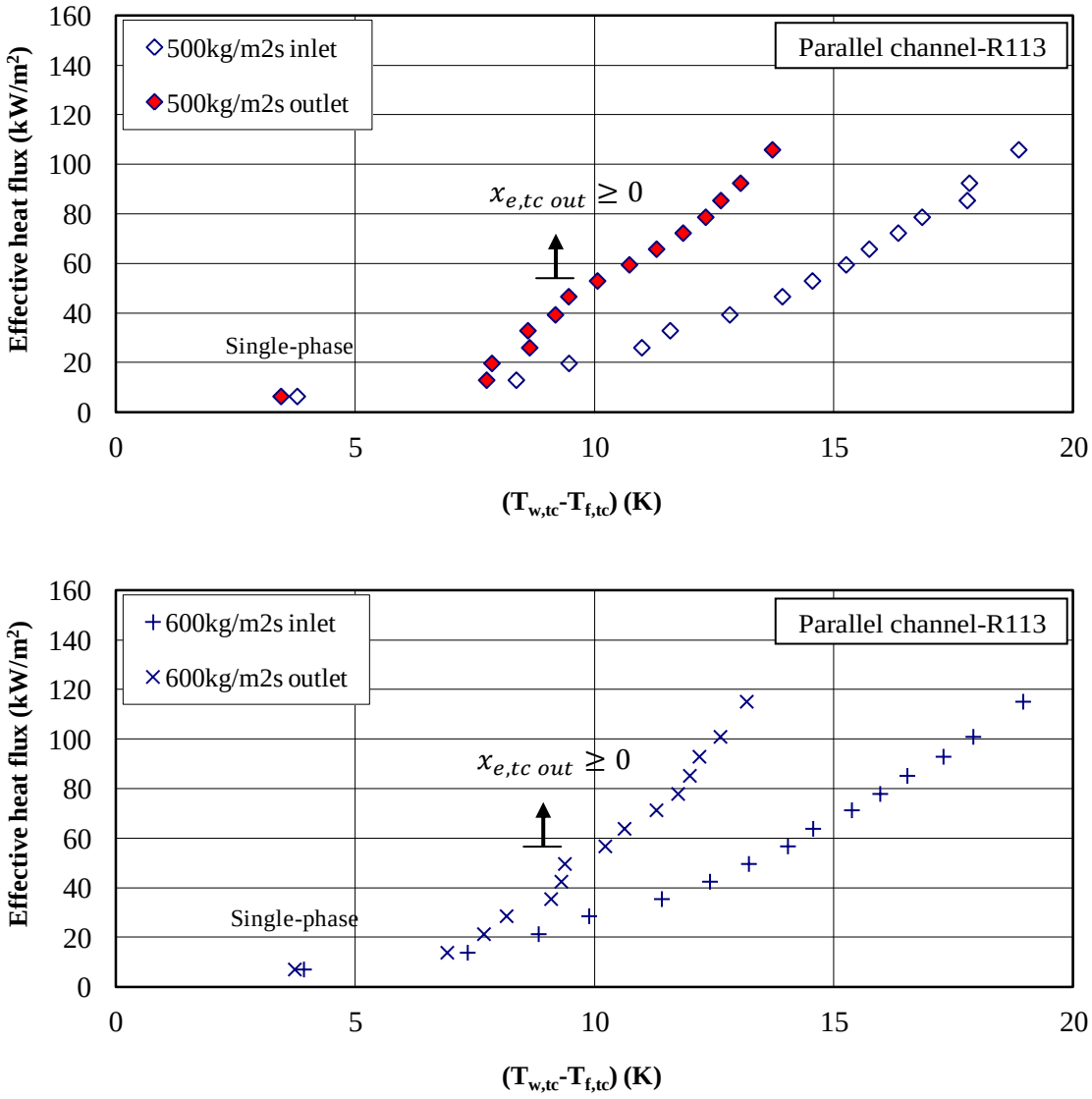

Figure 6.12 (continued) Boiling curves at the wall inlet and outlet for a range of mass fluxes, obtained from parallel channel surface tests with R113

Figure 6.13 shows variation of parallel channel surface boiling length with effective heat flux for a range of mass fluxes. As it is shown, the boiling length is increased with increasing heat flux, and for a constant heat flux, boiling length is decreased with increasing mass flux.

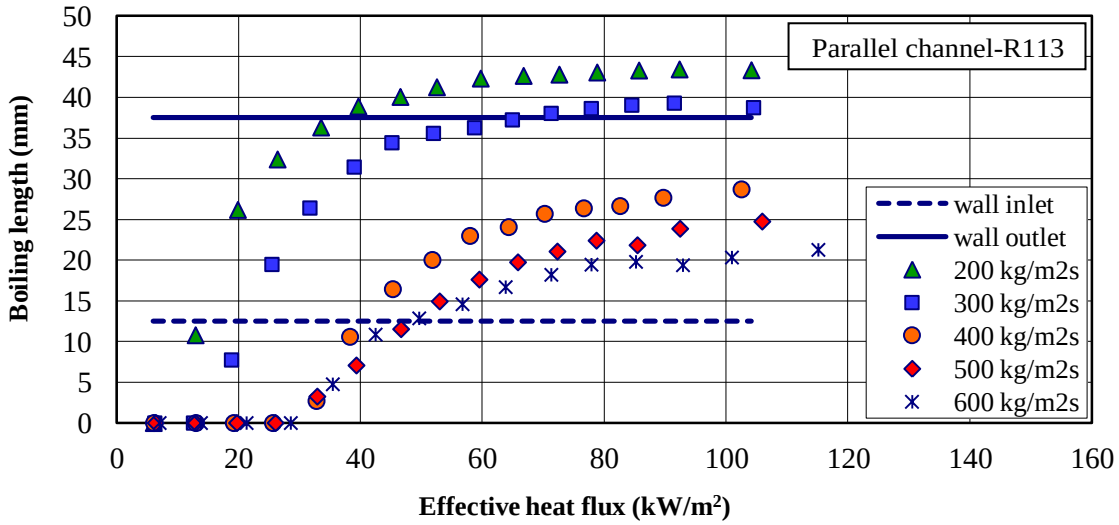

Figure 6.13 Variation of boiling length with effective heat flux for a range of mass fluxes for parallel channel surface with R113

6.2.4. Two-Phase Heat Transfer Coefficient

Figure 6.14 shows the variation of the measured heat-transfer coefficients with the effective heat fluxes for each mass flux. For the lowest mass flux of $200\ kg/m^2s$, single-phase convection occurs only at the wall inlet location, at a heat flux of approximately $6\ kW/m^2$. Sub-cooled flow boiling is shown to exist at the wall inlet for heat fluxes in the range $13-34\ kW/m^2$, with saturated flow boiling occurring thereafter. At the wall outlet location, saturated flow boiling is shown to occur for heat fluxes larger than $19\ kW/m^2$, and sub-cooled flow boiling occurring before. At heat fluxes in the range $19-40\ kW/m^2$, which wall inlet and outlet are in sub-cooled and saturated flow boiling regions respectively, wall outlet heat transfer coefficients are independent of heat flux, while the wall inlet values increases with increasing heat flux and merge to outlet values. This region where the wall outlet heat transfer coefficient is reasonably independent of heat flux does not exist for higher mass fluxes.

For mass flux of $300\ kg/m^2s$, both the inlet and outlet values are in sub-cooled and saturated flow boiling regions, and no single-phase region occurs at this mass flux. For both mass fluxes of 200 and $300\ kg/m^2s$, which the wall inlet transfers from sub-cooled to saturated flow boiling regime with increasing the heat flux, the wall inlet heat-transfer coefficients at the sub-cooled flow boiling regime are shown to rise from levels below the outlet values to the outlet values at the saturated flow boiling regime. At the

merging points and thereafter, the wall inlet and outlet heat-transfer coefficients are shown to be similar in magnitude and increase with increasing heat flux.

For mass fluxes of 400 kg/m^2s and above, single-phase convection occurs at both the wall inlet and outlet locations at the lowest heat flux of approximately 6 kW/m^2, while at higher heat fluxes, the rest of the wall inlet values are in the sub-cooled flow boiling region. As at higher heat fluxes for these mass fluxes, the inlet and outlet locations are in different regions, sub-cooled and saturated flow boiling regions respectively, wall inlet and outlet heat transfer coefficients are not similar in magnitude and following different curves. The curves are quite parallel and do not merge with increasing heat flux. The wall outlet heat transfer coefficient values increase with quite sharper slope than the wall inlet values.

For all mass fluxes, as the mass flux increases, the range of heat fluxes in the sub-cooled flow boiling region increases. This results from the increased amount of absolute sensible enthalpy change that is required to reach saturation as a consequence of the mass flux increase.

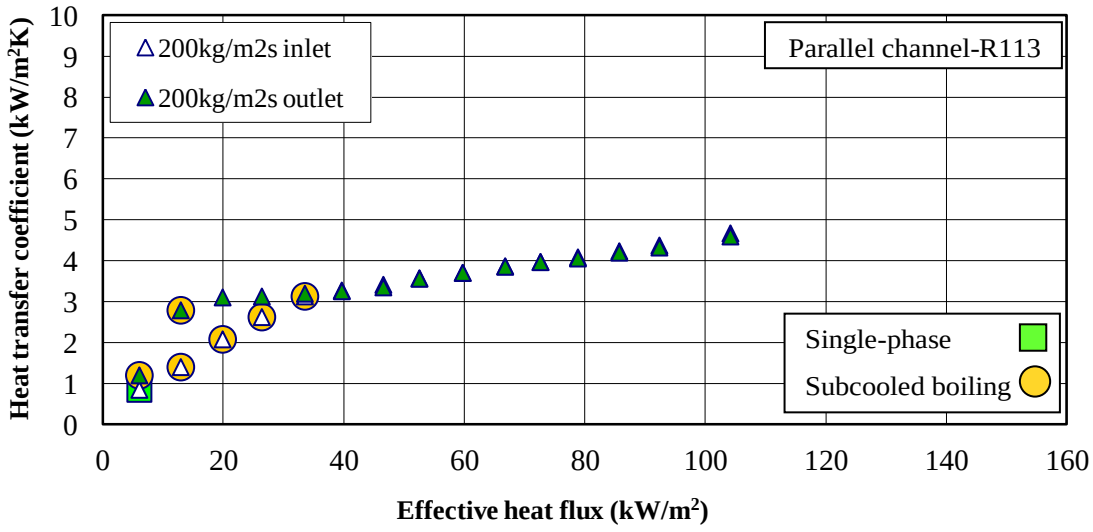

Figure 6.14 Variation of heat transfer coefficient with effective heat flux for a range of mass fluxes for parallel channel surface with R113

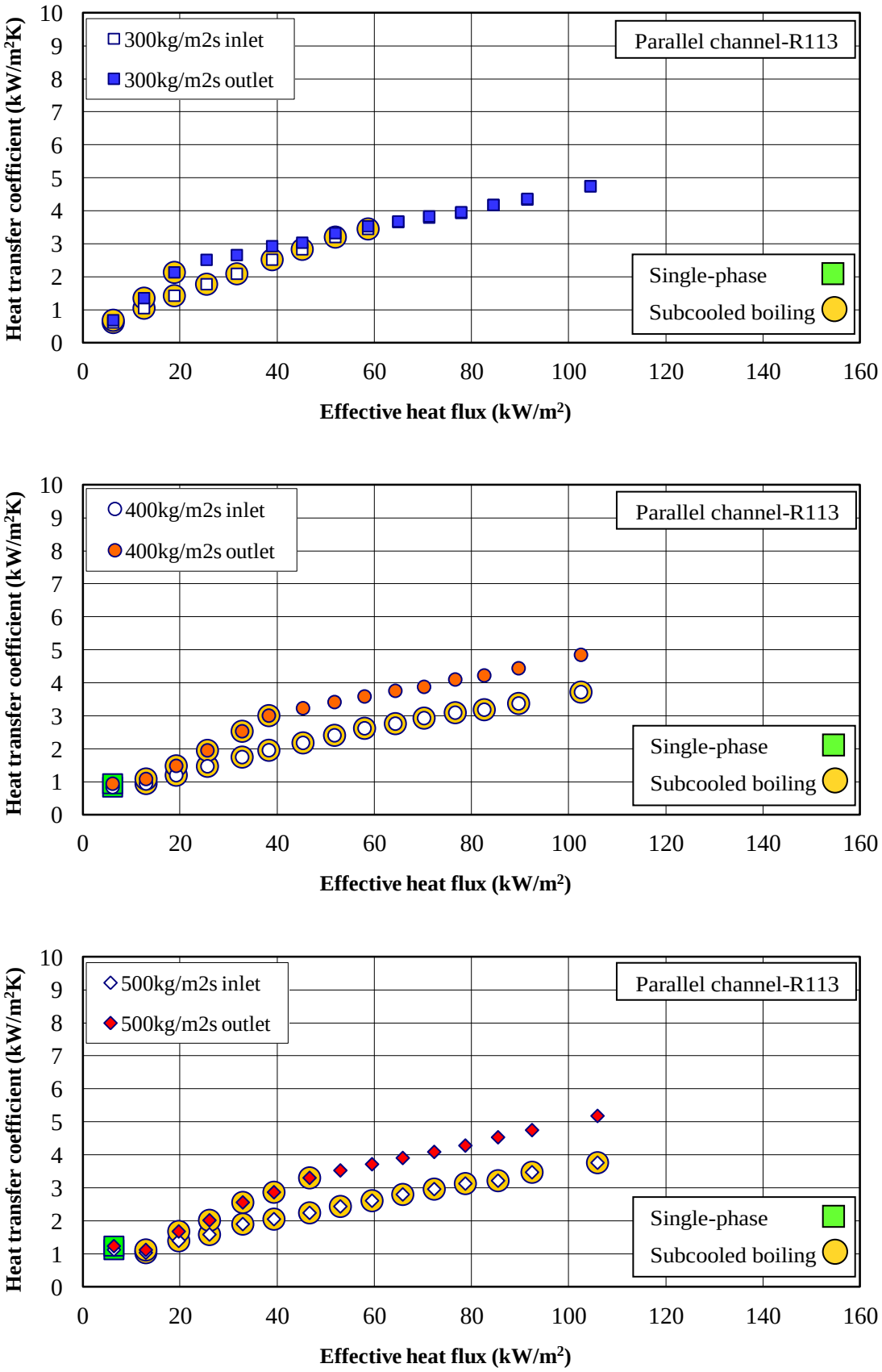

Figure 6.14 (continued) Variation of heat transfer coefficient with effective heat flux for a range of mass fluxes for parallel channel surface with R113

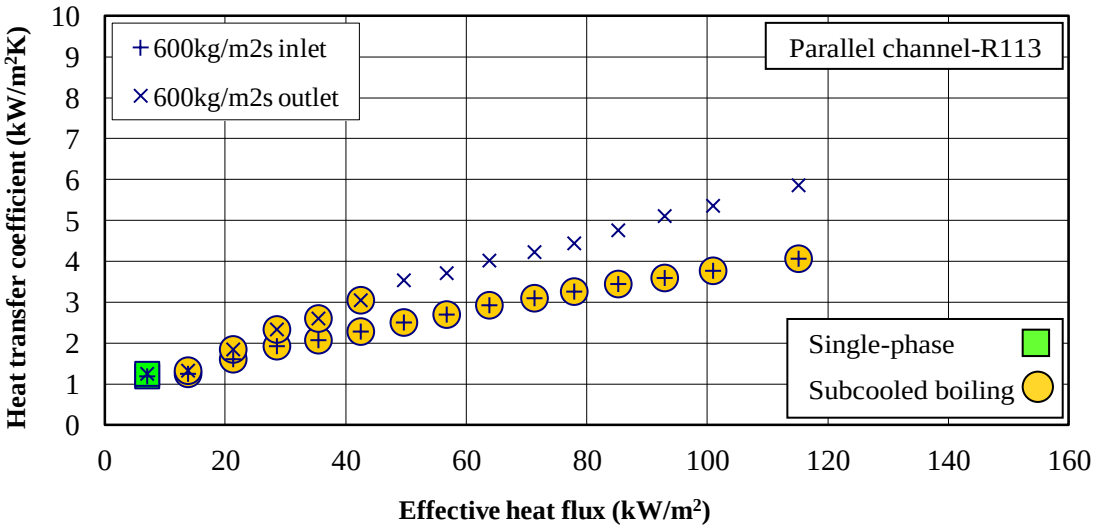

Figure 6.14 (continued) Variation of heat transfer coefficient with effective heat flux for a range of mass fluxes for parallel channel surface with R113

Figure 6.15 illustrates the variation of saturated boiling heat transfer coefficient with local vapour mass fraction. The range of wall inlet and outlet vapour mass fractions is reduced as the mass flux increases. For each mass flux, for a constant heat flux, the vapour mass fractions at the wall inlet and outlet locations are different in magnitude but the saturated boiling heat-transfer coefficients are shown to be similar in magnitude and remain fairly independent of vapour mass fraction.

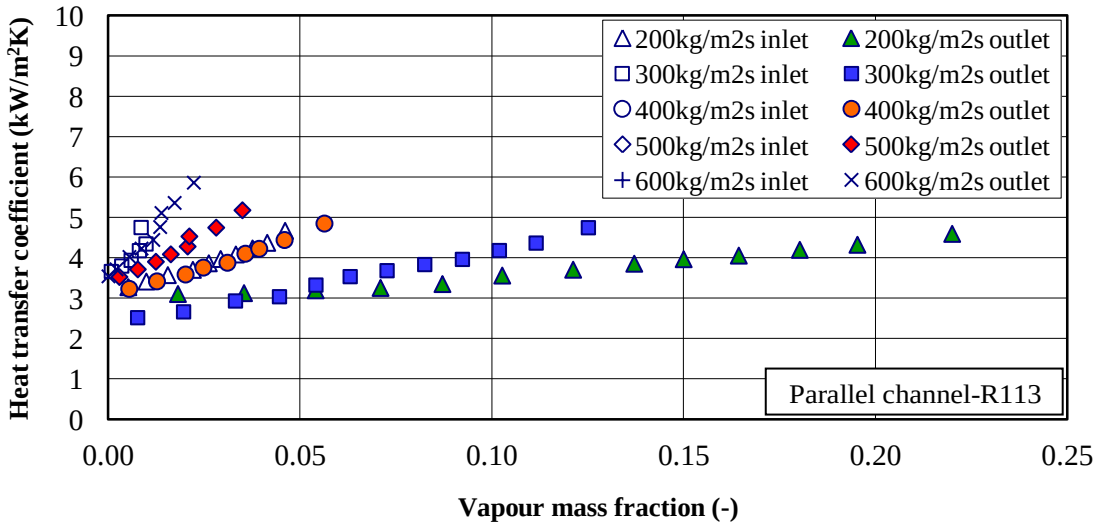

Figure 6.15 Variation of saturated boiling heat transfer coefficient with local vapour mass fraction at various mass fluxes for parallel channel surface with R113

The same as plate surface, all of the parallel channel surface saturated boiling data identified in Figure 6.14, are reproduced in Figure 6.16. As it is shown, the parallel channel surface data are reasonably independent of location and mass flux and follow the power law relationship

$$h = 0.8667 q_{act}^{0.3985} \tag{6.3}$$

to within $\pm 10\%$ of the measured values. Equation (6.3) is based on the actual heat flux, q_{act}, i.e., the heat flux based on the actual heat transfer area. It therefore seems likely that similar to the plate surface, the dominating heat-transfer mechanism in the saturated boiling flow regime is nucleate boiling for parallel channel surface.

The plate surfaces power law is included in Figure 6.16. The plate surface data trend is similar to the parallel channel surface data sets, with lower values. This indicates that the parallel channel surface improves heat transfer by increasing the surface area and the heat transfer coefficient.

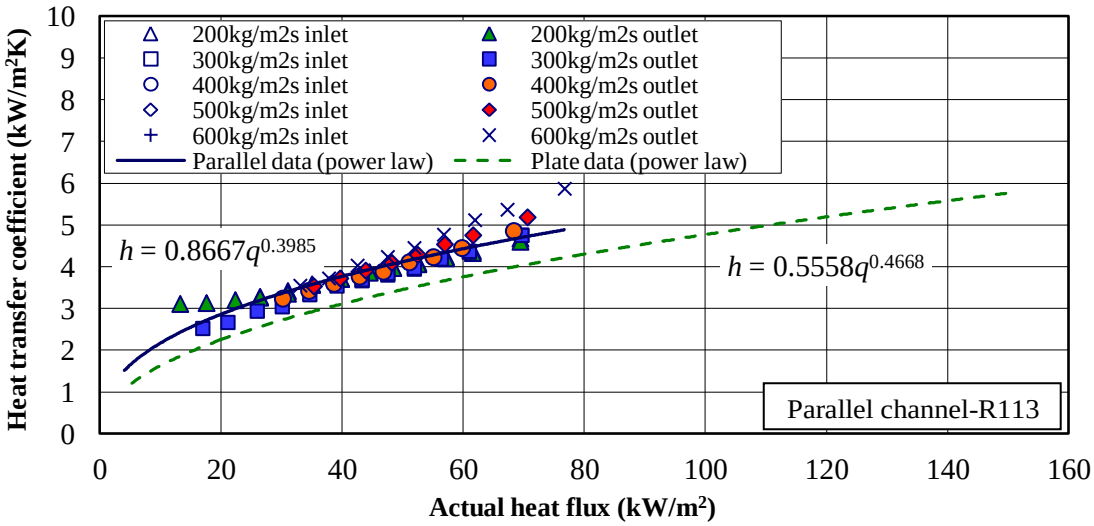

Figure 6.16 Variation of saturated boiling heat transfer coefficient with actual heat flux at various mass fluxes for parallel channel surface with R113

6.2.5. Two-Phase Pressure Drop

The variation of two-phase pressure drop with heat flux for a range of mass fluxes for parallel channel surface is shown in Figure 6.17. For most of the mass fluxes at the heat flux of approximately $6\ kW/m^2$, most of the parallel channel surface area is in the single-phase region and the single-phase pressure drop is shown to increase with increasing mass flux. With increasing heat flux to the heat flux of approximately $12\ kW/m^2$, the region transforms from single-phase to sub-cooled flow boiling region and pressure drop slightly increases for all mass fluxes. In the heat flux range of $12-35\ kW/m^2$, most of the parallel channel surface area is in sub-cooled boiling region. In this heat flux range, the two-phase pressure drop for mass fluxes of $300\ kg/m^2s$ and $600\ kg/m^2s$ decreases, while for other mass fluxes it slightly increases and then decreases. For heat fluxes greater than $35\ kW/m^2$, most of the surface area is in saturated flow boiling region and the pressure drop is shown to be reasonably proportional to heat flux and increases with increasing heat flux. Similar to the plate surface, as it was discussed in section 6.1.5, for all mass fluxes, the pressure drop is shown not following a special trend with increasing mass flux.

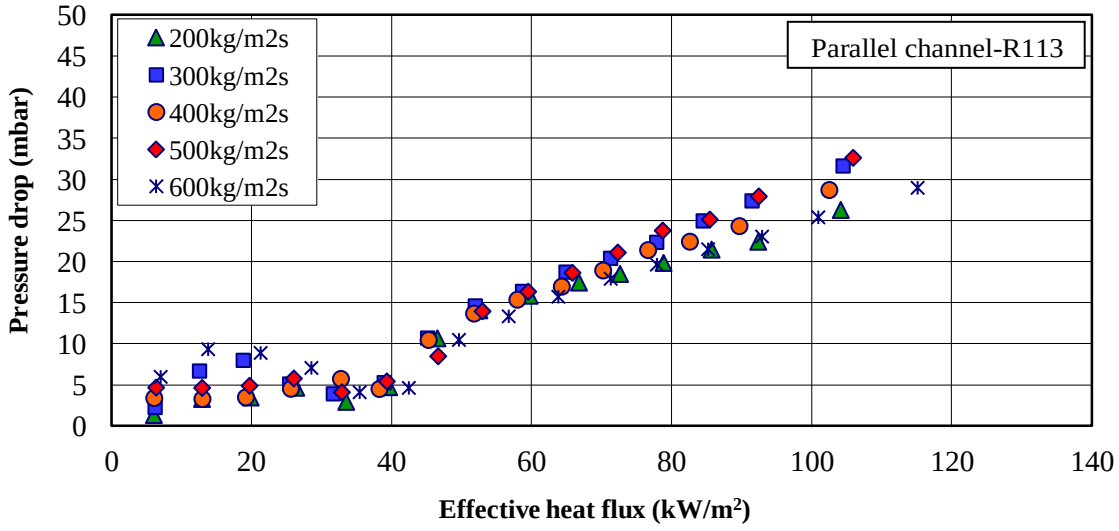

Figure 6.17 Variation of pressure drop with effective heat flux at various mass fluxes for parallel channel surface with R113

6.2.6. Flow Boiling Visualisation

Figure 6.18 shows typical observed flow patterns for mass fluxes of 200 kg/m^2s and 600 kg/m^2s, at similar effective heat fluxes in equal intervals.

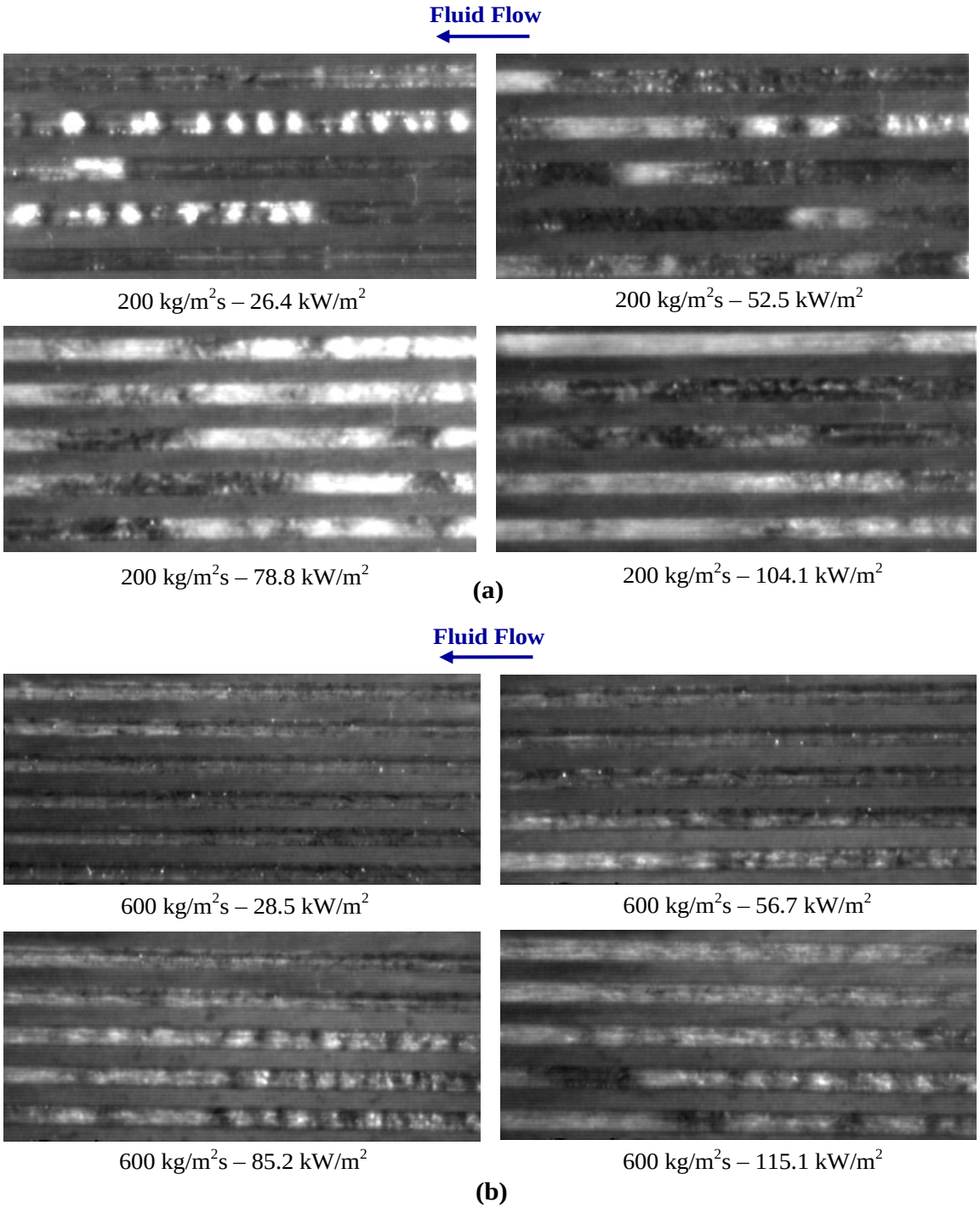

Figure 6.18 Typical views of the flow for mass fluxes of, (a) 200, and (b) 600 kg/m^2s at various heat fluxes, for parallel channel surface with R113

As it is shown for each mass flux the vapour mass fraction increases with increasing the heat flux. For all mass fluxes, similar to a previous study by Cornwell and Kew (1993), three different flow patterns were observed; isolated bubble, confined bubble, and slug/annular flow patterns. Many others have observed these three basic flow patterns, such as Damianides and Westwater (1988) for a $1mm$ tube, Mertz et al. (1996) with water and R-141b evaporating in multi-micro-channels, Kasza et al. (1997) for a single rectangular channel of $2.5\ mm$ by $6\ mm$, Lin et al. (1998) using a single round tube of $2.1\ mm$ diameter, and Sheng and Palm (2001) for 1 to $4\ mm$ tubes.

6.3. Conclusions for Plate and Parallel Channel Surfaces

As was discussed in literature review, Chapter 2, various flow patterns including bubbly/isolated bubble, confined bubble (plug, slug, and elongated bubble), churn, slug-annular (liquid ring and liquid lump flow), wispy annular, annular, liquid film nucleation, and dry out flows were reported for flow boiling phenomena in single and multiple mini and micro-channels. A number of researchers such as Tran et al. (1993), Kew and Corwell (1997, 1998), Steinke and Kandlikar (2003, 2004), and many more researches reported that the saturated flow boiling heat transfer coefficients in mini and micro-channels were dependent nearly exclusively on heat flux and saturation pressure, and only slightly dependent on mass flux and vapour quality. This observation led to the conclusion that nucleate boiling controls flow boiling phenomena in these flow passages. The nucleate boiling heat transfer mechanism is consistent with the isolated bubble (bubbly/individual bubble) flow regime.

Some other researchers such as Jacobi and Thome (2002), and Qu and Mudawar (2003) reported that the saturated flow boiling heat transfer coefficients in mini and micro-channels were a strong function of mass flux and only a weak function of heat flux. This observation led to the conclusion that the dominant heat transfer mechanism for these mini and micro-channel heat sinks was convective boiling and not nucleates boiling. The convective boiling heat transfer mechanism is consistent with the confined bubble (slug, elongated bubbles), slug-annular (liquid ring, liquid lump), and annular flow regimes.

Other researchers such as Lee and Mudawar (2005) reported that the saturated flow boiling heat transfer coefficients in mini and micro-channels is associated with different mechanisms for low, Medium and high quality flows; Bubbly flow and dominant nucleate boiling at very low qualities and low heat fluxes, bubbly/slug flow and a combination of nucleate and convective boiling at medium qualities and heat fluxes, and finally annular/local dry-out flow and dominant convective boiling at high vapour quality and high heat fluxes.

As has been discussed in the previous sections, the present study investigation of flow boiling in plate and parallel mini-channels have shown that the saturated flow boiling heat transfer coefficients were almost independent of vapour quality, weakly dependent on mass flux, and strongly dependent on heat flux. Such trend proposes the nucleate boiling as the dominant heat transfer mechanism.

6.4. In-Line Pin-Fin Surface Tests with R113

In-line pin-fin surface heat transfer coefficients and pressure drop measurements, obtained for single-phase and two-phase tests with R113, and also flow boiling visualisation for these series of tests are presented in this section.

6.4.1. Single-Phase Heat Transfer Coefficient

The single-phase heat transfer coefficients are shown for the range of mass fluxes in Figure 6.19. The inlet and outlet heat-transfer coefficients are shown to be different in magnitude, with both following a power law function of the mass flux. The estimated error in the heat transfer coefficient is $\pm 10\%$.

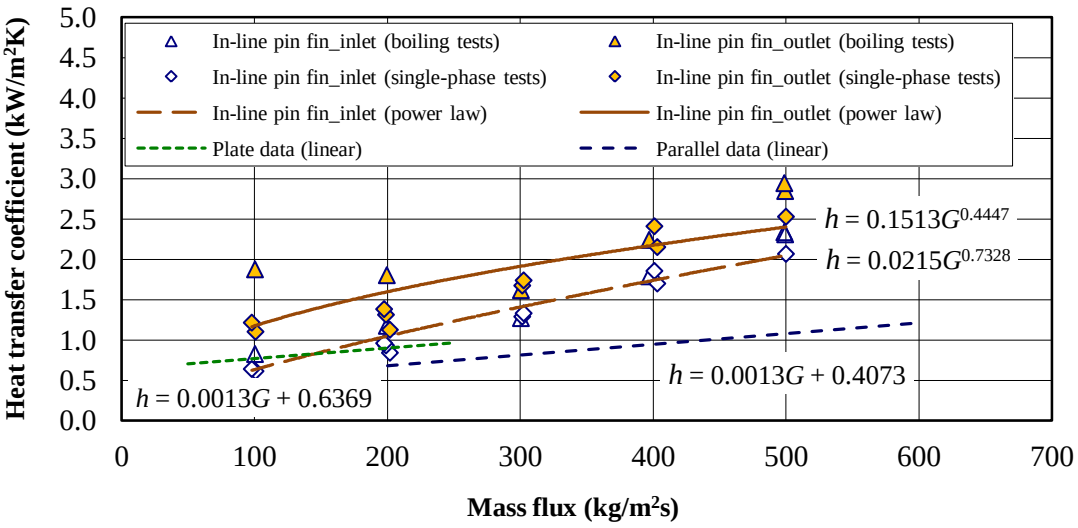

Figure 6.19 Variation of single-phase heat-transfer coefficient with mass flux for in-line pin-fin surface with R113

As it is shown, the same as the other surfaces, the in-line pin fin single-phase heat transfer coefficient increases with mass flux and is independent of wall heat flux. For a constant mass flux, heat transfer coefficient remains fairly constant or increases only slightly with increasing heat flux, resulted from increasing the average Reynolds number.

The plate and parallel channel surface linear functions are included in Figure 6.19 as well. For the plate and parallel channel surfaces, wall inlet and outlet values follow single linear functions, while the in-line pin-fin wall inlet and outlet values are shown to be different in magnitude, with both following a power law function of the mass flux. Since, unlike the plate and parallel data the in-line pin fin data do not follow single curves, and as the wall inlet data are corresponding to the 7th row of pin fins and the

wall outlet to the 19th, the difference is probably a settling length effect caused by the pin fins.

6.4.2. Single-Phase Pressure Drop

The variation of single-phase pressure drop with mass flux for the in-line pin fin surface is shown in Figure 6.20. The pressure drop is shown to be a power law function of the mass flux, as would be expected. The parallel channel surface linear function is included in Figure 6.20. Both data sets trends are quite similar, with the in-line pin fin values being higher.

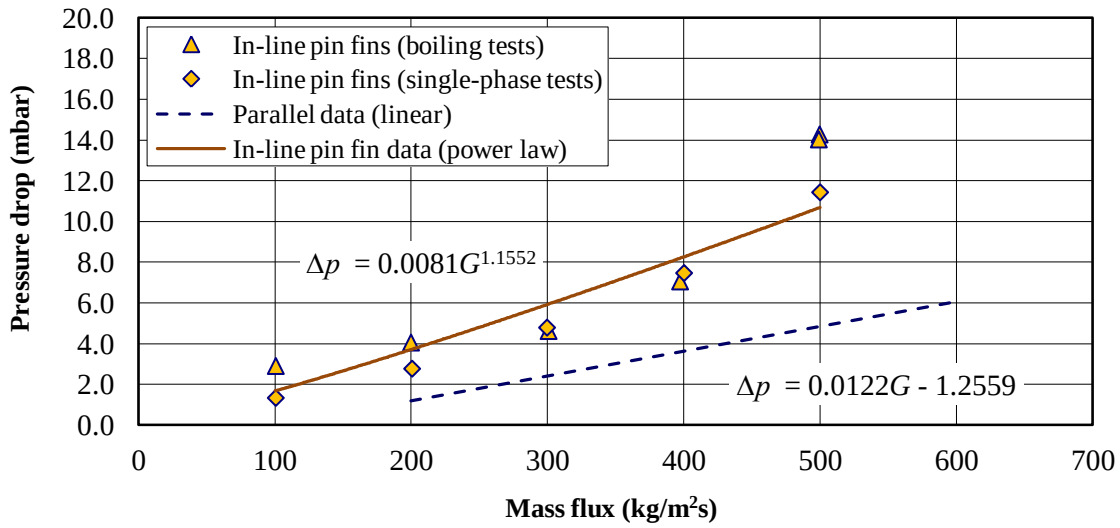

Figure 6.20 Variation of single-phase pressure drop with mass flux for in-line pin fin surface with R113

6.4.3. Boiling Curve

The boiling curves, obtained for steady state conditions at the in-line pin fin wall inlet and outlet thermocouples locations, are illustrated for each mass flux in Figure 6.21. At low mass fluxes of 100 and 200 kg/m^2s, two regions were identified for wall outlet curves. A single-phase region at the lowest heat flux of approximately 6 kW/m^2 and a saturated flow boiling region thereafter. As is

shown, both regions have quite similar positive slopes. At the highest mass flux of $500\ kg/m^2s$, two single-phase and sub-cooled flow boiling regions were identified for wall inlet curve. The single-phase region has a small and fairly constant slope, while due to a sharp rise in the convective heat transfer coefficient at the sub-cooled flow boiling region, the slope increases.

For the rest of the curves, three regions were identified at the inlet and outlet wall thermocouples locations. Firstly, a single-phase region at the low heat fluxes, where the slopes of the boiling curves are small, positive and fairly constant. As is shown in Figure 6.21, this region can be readily identified for the highest mass flux of $500\ kg/m^2s$. Secondly, a sub-cooled flow boiling region at the intermediate heat fluxes, where the slopes of the boiling curves increases and tend to become negative due to a quick rise in the convective heat transfer coefficient, and finally a saturated flow boiling region at higher heat fluxes, where the local vapour mass fraction, $x_{e,tc}$, is above zero and the slopes of the boiling curves are positive and fairly constant.

As is shown, transition from one region to another occurs at a lower heat flux value at the wall outlet than that at wall inlet, indicating that the boiling front propagated from downstream to upstream. At high heat fluxes, where the saturated flow boiling region is identified for both wall inlet and outlet, boiling curves for all mass fluxes are similar in magnitude and following quite similar slope, with the wall outlet values being slightly sharper than that at the wall inlet.

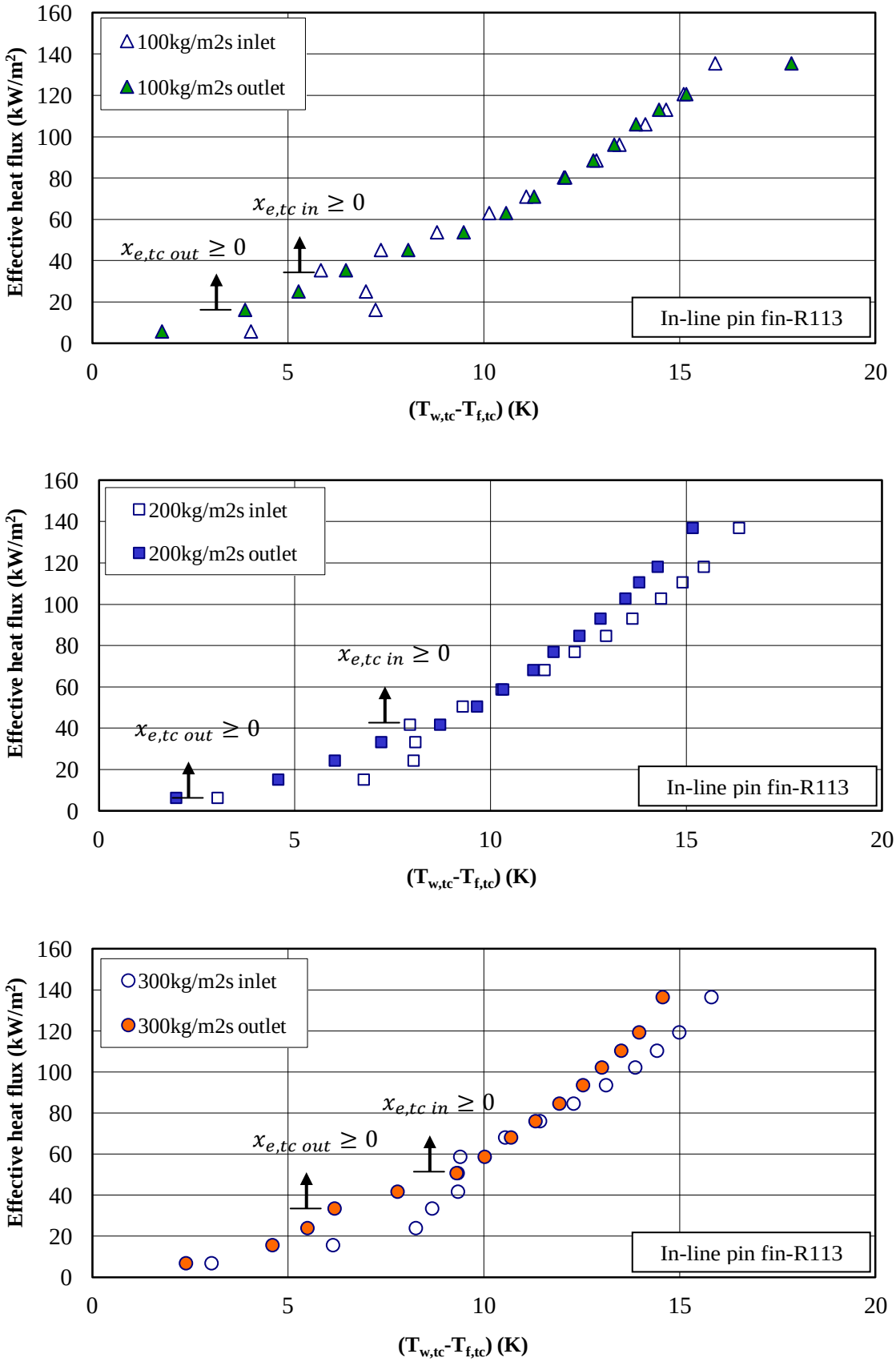

Figure 6.21 Boiling curves at the wall inlet and outlet for a range of mass fluxes, obtained from in-line pin fin surface tests with R113

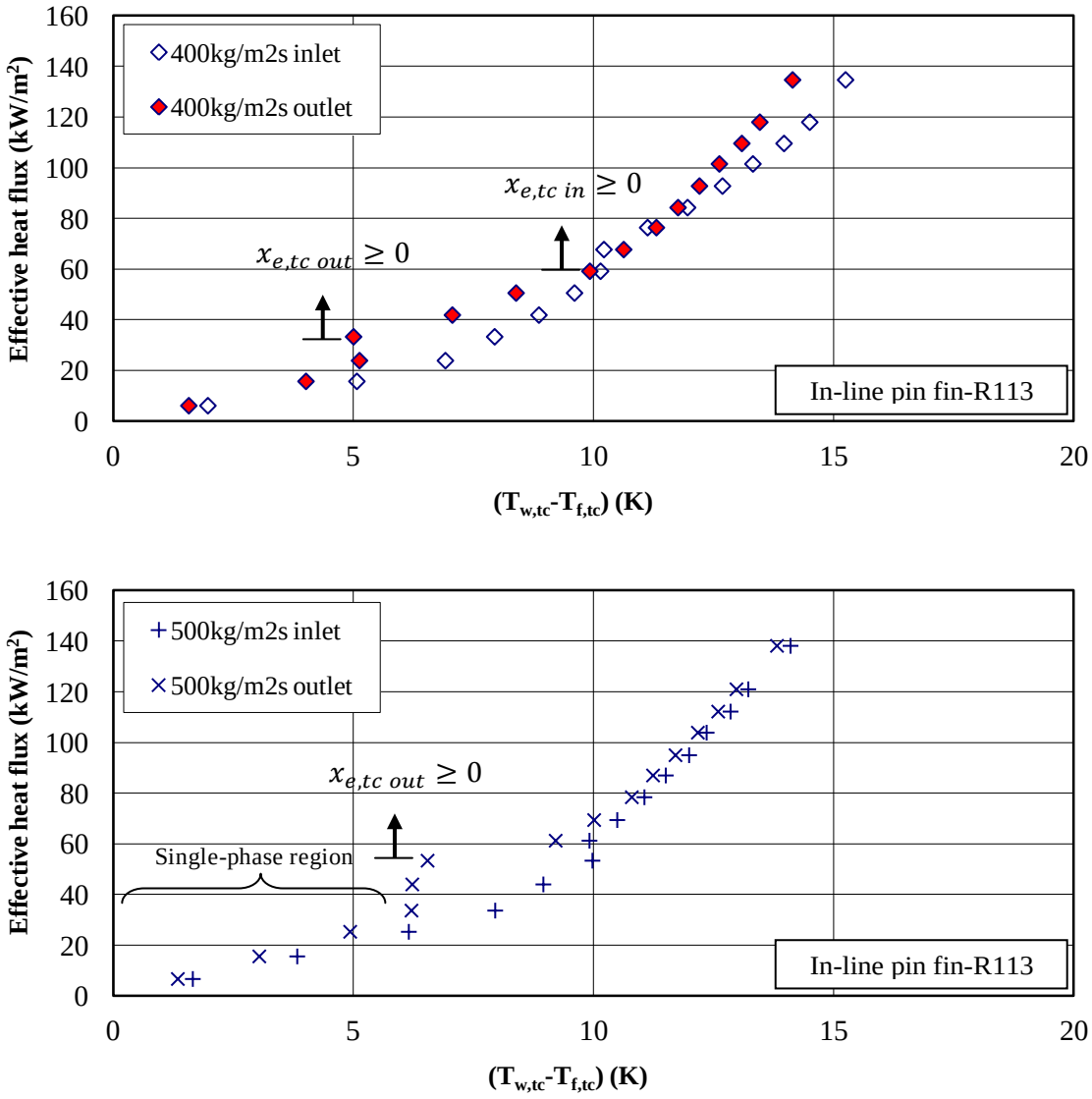

Figure 6.21 (continued) Boiling curves at the wall inlet and outlet for a range of mass fluxes, obtained from in-line pin fin surface tests with R113

Figure 6.22 shows variation of boiling length with effective heat flux for a range of mass fluxes. For a constant heat flux, boiling length is decreased with increasing mass flux.

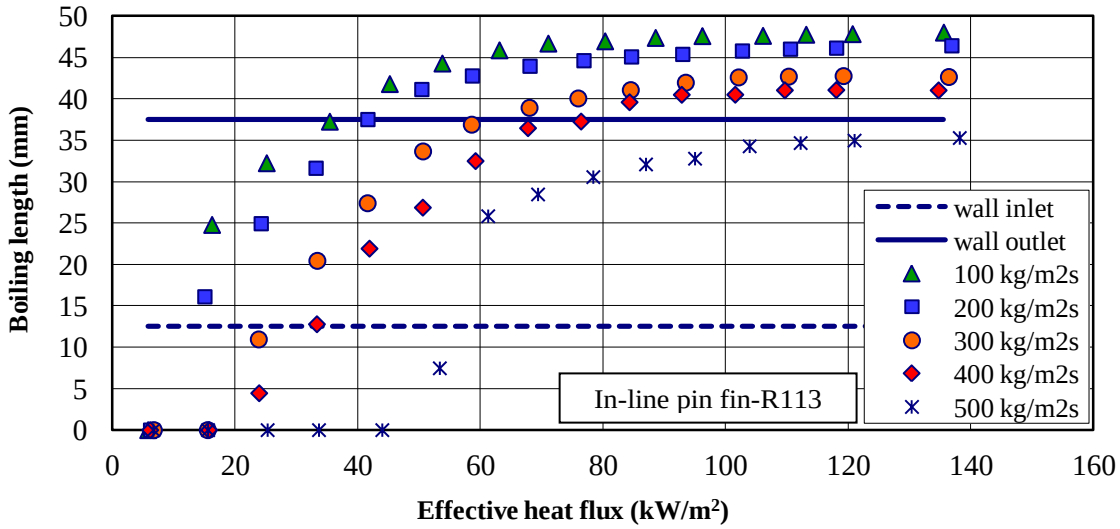

Figure 6.22 Variation of boiling length with effective heat flux for a range of mass fluxes for in-line pin fin surface with R113

6.4.4 Two-Phase Heat Transfer Coefficient

The variation of the measured heat-transfer coefficients with the effective heat fluxes for in-line pin fin surface is shown for each mass flux in Figure 6.23. The same as parallel channel surface, the in-line pin fin surface was subjected to all three heat transfer types. The plate surface had a smaller heat-transfer surface than the in-line pin fin and the parallel channel surfaces, thus for a constant heat flux, the wall temperatures were higher; giving only sub-cooled and saturated boiling heat transfer on the plate surface. As it is shown, unlike the plate and parallel channel surfaces, the in-line pin fin wall inlet and outlet single-phase values are different in magnitude. The difference is probably a settling length effect, caused by the pin fins rows between the two sets of wall inlet and outlet thermocouples locations.

For all mass fluxes except $500\ kg/m^2s$, single-phase convection occurs just at the lowest heat flux of approximately $6\ kW/m^2$, but for $500\ kg/m^2s$, single-phase convection occurs at the wall inlet and outlet locations in the heat flux range of $6-26\ kW/m^2$ and $6-16\ kW/m^2$, respectively. At higher heat fluxes for all mass fluxes, the wall inlet heat-transfer coefficient is shown to rise from levels below the wall outlet values to the wall outlet value. Within this range, the wall inlet flow is shown to be in the sub-cooled boiling regime. Thus, the merging of the heat-transfer coefficients is

consistent with the single-phase settling length being longer than the two-phase equivalent.

For mass flux of $100\ kg/m^2s$, at heat fluxes in the range $35-60\ kW/m^2$, the wall inlet and outlet heat-transfer coefficients are shown to be similar in magnitude, in the saturated flow boiling region and independent of heat flux. As the mass flux increases, this region decreases. At high heat fluxes the wall inlet and outlet heat transfer coefficients are again similar in magnitude and in the saturated boiling region. However, they are not independent of heat flux. At the highest mass flux of $500\ kg/m^2s$, the wall outlet sub-cooled boiling heat-transfer coefficient over-shoots the saturated boiling value.

As the mass flux increases, the number of wall inlet points in the sub-cooled flow boiling region increases. At mass fluxes of $300\ kg/m^2s$ and above, an increasing number of the wall outlet points are also in this regime. This results from the increased amount of absolute sensible enthalpy change that is required to reach saturation as a consequence of the mass flux increase.

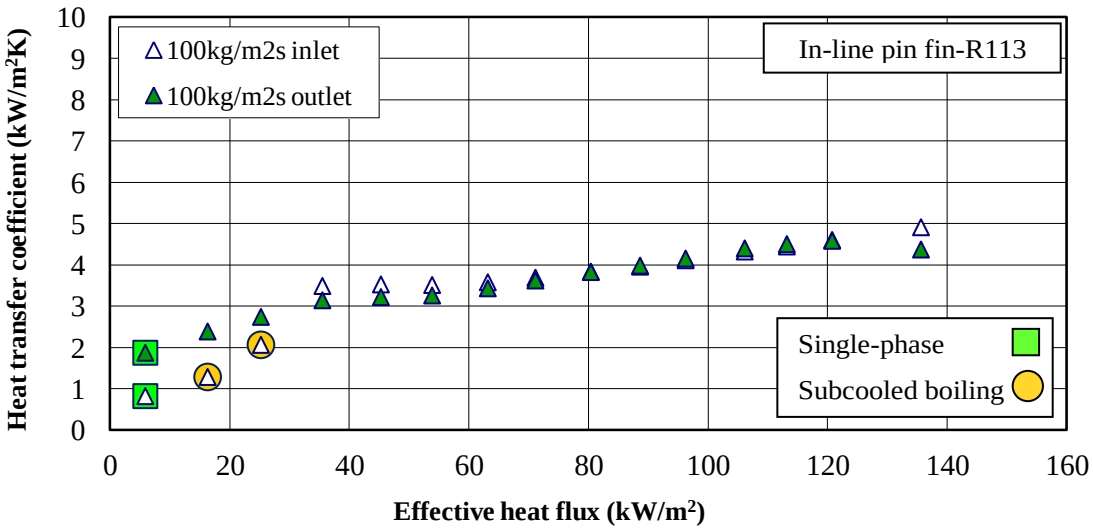

Figure 6.23 Variation of heat transfer coefficients with effective heat flux for a range of mass fluxes, for in-line pin fin surface with R113

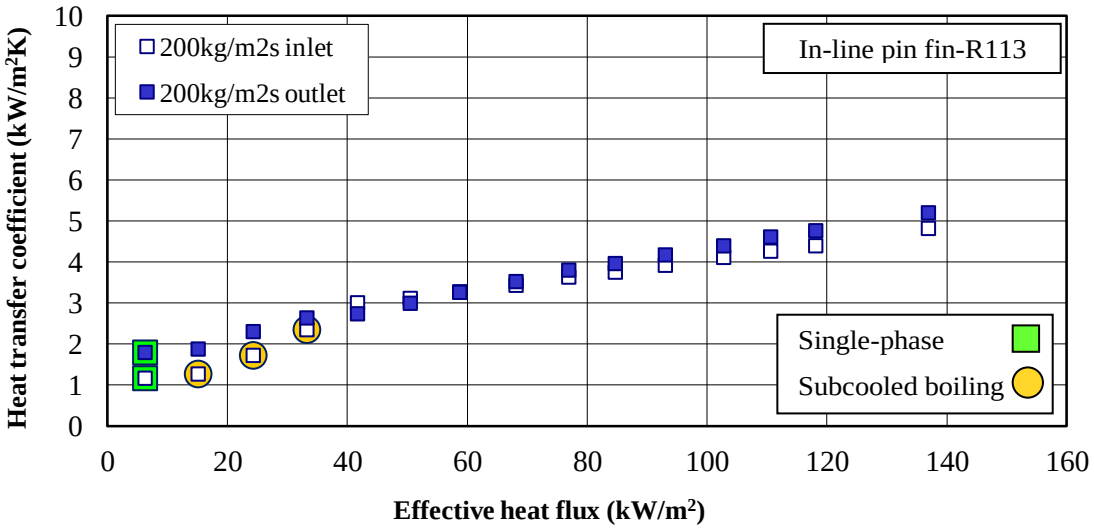

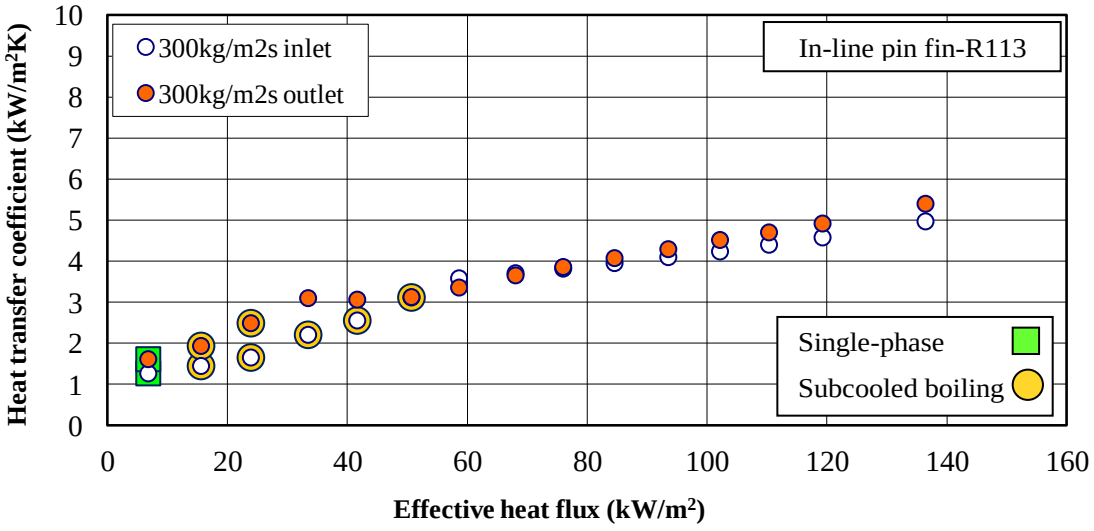

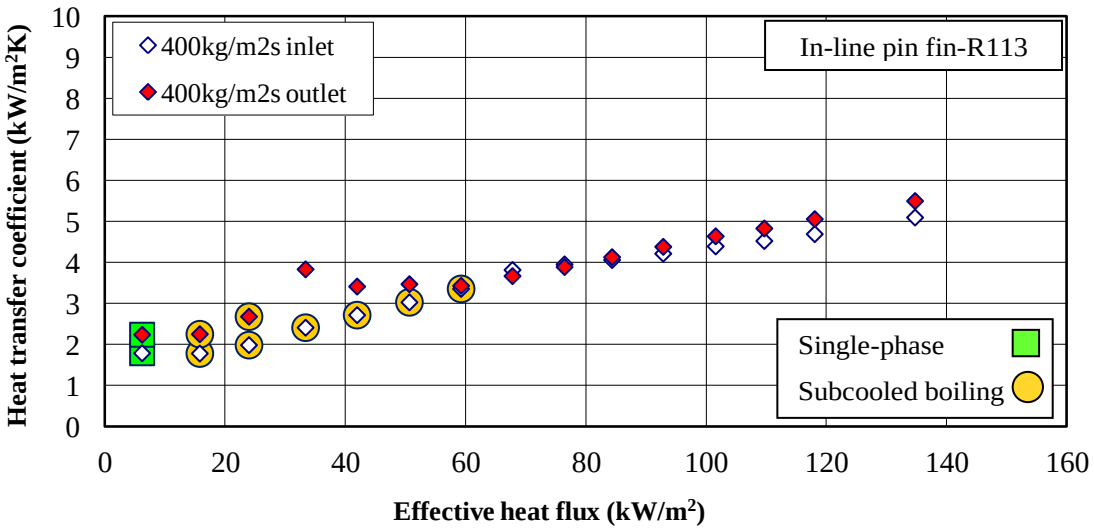

Figure 6.23 (continued) Variation of heat transfer coefficients with effective heat flux for a range of mass fluxes, for in-line pin fin surface with R113

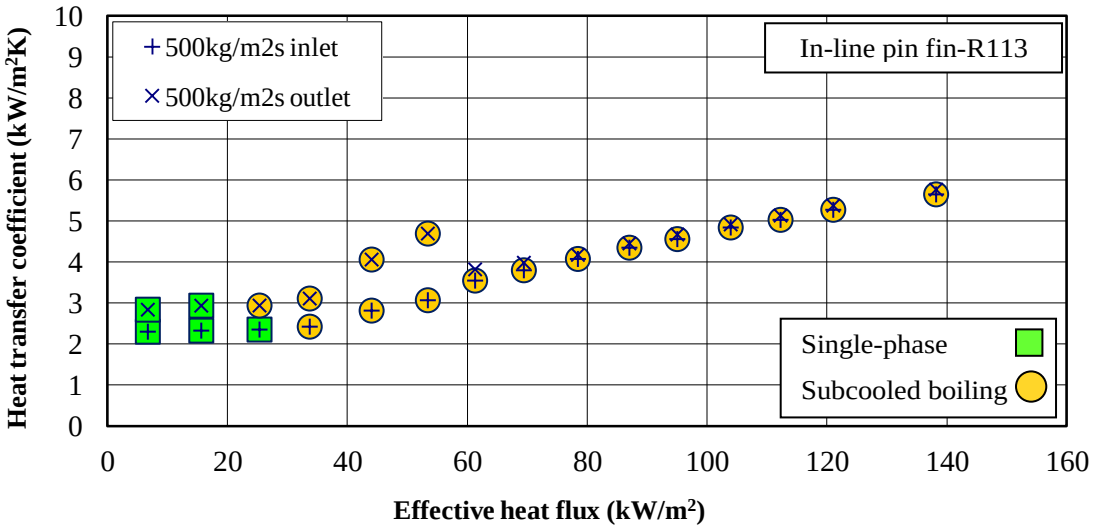

Figure 6.23 (continued) Variation of heat transfer coefficients with effective heat flux for a range of mass fluxes, for in-line pin fin surface with R113

Figure 6.24 illustrates the variation of saturated boiling heat transfer coefficient with local vapour mass fraction for in-line pin fin surface. The range of wall inlet and outlet vapour mass fractions is reduced as the mass flux increases. At each mass flux, for a constant heat flux, the vapour mass fractions at the wall inlet and outlet locations are different, while the saturated boiling heat-transfer coefficients remain fairly independent of it.

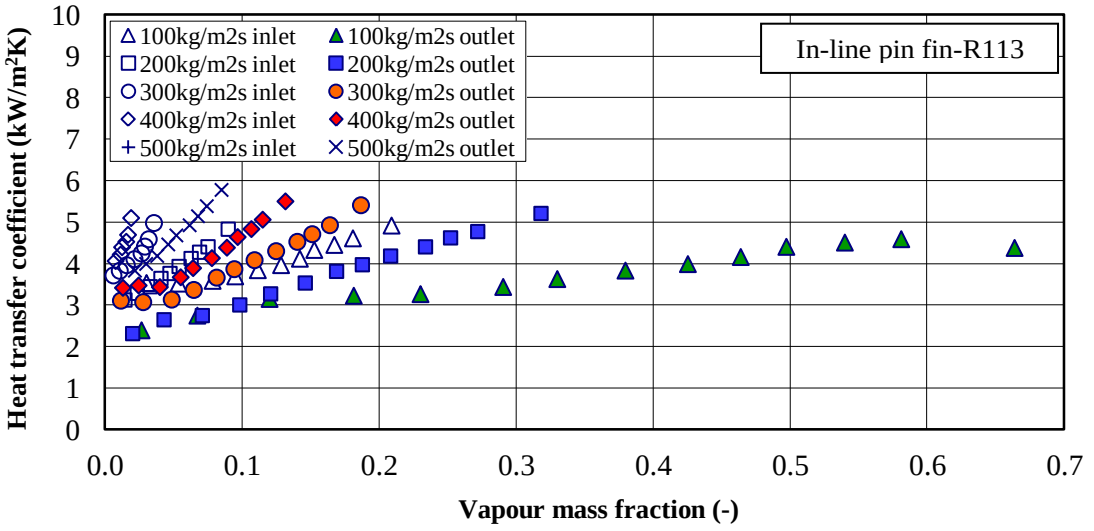

Figure 6.24 Variation of saturated boiling heat transfer coefficient with local vapour mass fraction at various mass fluxes, for in-line pin fin surface with R113

All of the in-line pin fin surface saturated boiling data identified in Figure 6.23, are reproduced in Figure 6.25. As is shown, the in-line pin fin surface data are reasonably independent of vapour quality, weakly dependent on mass flux, and strongly dependent on heat flux and follow the power law relationship

$$h = 0.8998 q_{act}^{0.3905} \tag{6.4}$$

to within $\pm 10\%$ of the measured values. Equation (6.4) is based on the actual heat flux, q_{act}. The same as other surfaces, it therefore seems likely that the dominating heat-transfer mechanism in the saturated boiling flow regime is nucleate boiling for the in-line pin fin surface as well.

The plate and parallel channel surfaces power laws are included in Figure 6.25 as well. Both parallel and pin-fin data sets are the same in magnitude and following a very similar curve. The plate surface data set trend is similar to the in-line pin fin and parallel channel surfaces data sets, with lower values. This indicates that the pin-fin and parallel channel surfaces similarly improve heat transfer by increasing the surface area and the heat transfer coefficient.

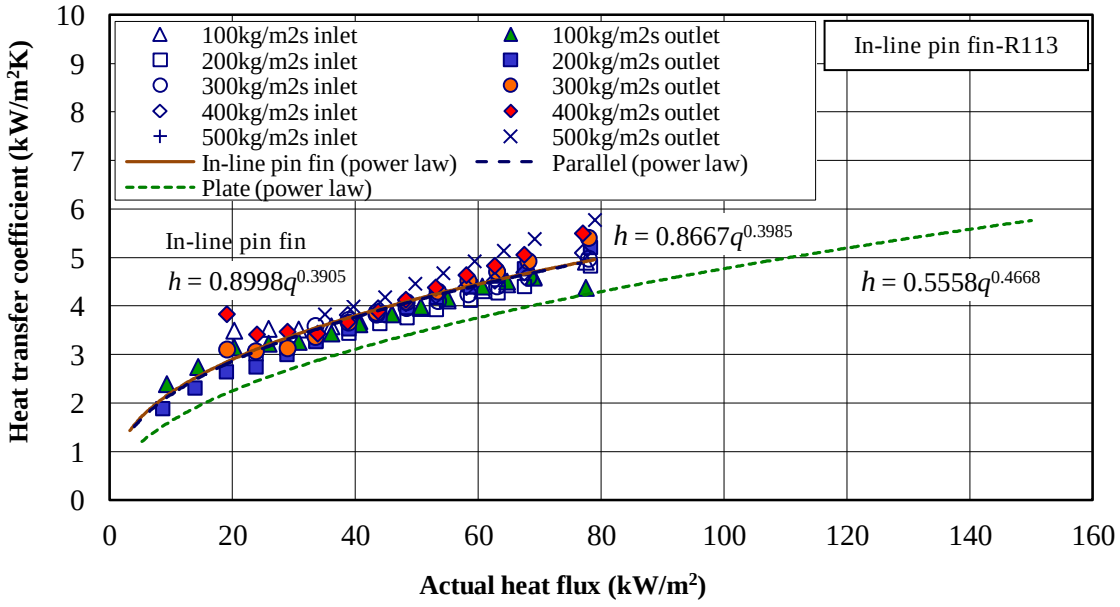

Figure 6.25 Variation of saturated boiling heat transfer coefficient with actual heat flux at various mass fluxes, for in-line pin fin surface with R113

6.4.5 Two-Phase Pressure Drop

The variation of in-line pin fin two-phase pressure drop with heat flux for a range of mass fluxes is shown in Figure 6.26. The same as other surfaces the in-line pin-fin pressure drop is shown to increase with increasing heat flux. For all but the highest mass flux, the pressure drop is also shown to increase with mass flux. As it was mentioned before, pressure drop increases with increasing mass and vapour content. For a constant heat flux, as the mass flux increases, the vapour content decreases, leading to the trends shown in Figure 6.26. The in-line pin fin data are considerably larger than the plate and parallel data by a factor of about 6.3 and 2, respectively.

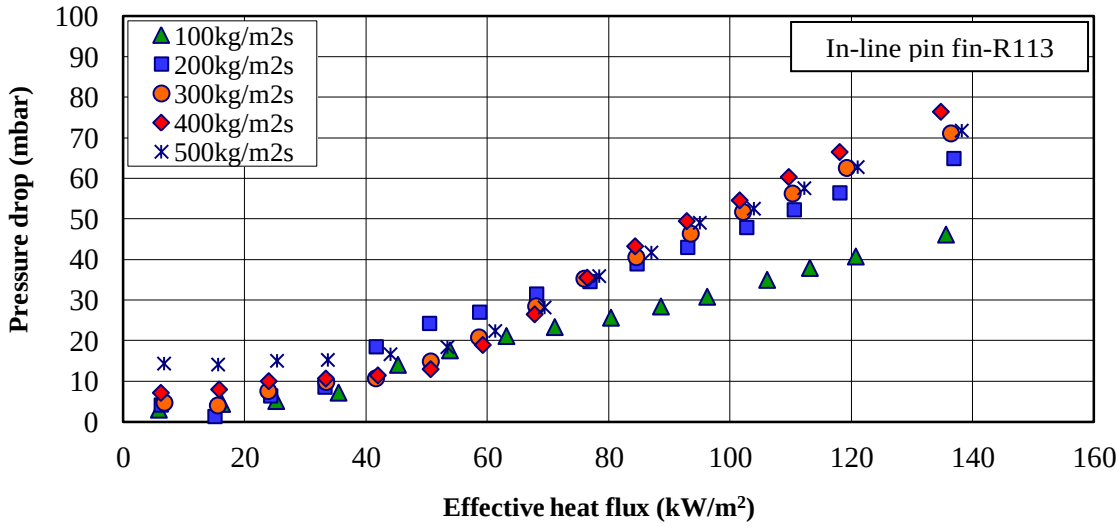

Figure 6.26 Variation of pressure drop with effective heat flux at various mass fluxes, for in-line pin fin surface with R113

6.4.6 Flow Boiling Visualisation

Figure 6.27 shows video images of flow boiling region development at nominally equal heat fluxes, for all mass fluxes in the range $100 - 500\ kg/m^2s$. As is shown, for a quite constant heat flux, as the mass flux increases the boiling length decreases. This results from the increased amount of absolute sensible enthalpy change that is required to reach saturation as a consequence of the mass flux increase.

Figure 6.28 shows typical observed flow patterns for mass fluxes of 100 and $500\ kg/m^2s$, at quite similar effective heat fluxes in equal intervals. For each mass flux the vapour mass fraction increases with increasing the heat flux. As is shown, at low heat fluxes, the in-line pin-fin surface contains small bubbles generating between pin fins. As the heat flux increases, bubbles are expanded, collated and elongated. These elongated bubbles move between the fins. Three different flow patterns were observed. Flow patterns were quite similar to those observed by Krishnamurthy and Peles (2007). They studied adiabatic nitrogen-water two-phase flow patterns across a staggered array of circular micro-pin fins. The observed flow patterns were bubbly slug (isolated bubbles/confined bubbles), vapour-slug, and annular flows. The bubbly slug was dispersed bubbles in the liquid with the size of less than or equal to the spacing between the pin-fins. The gas-slug was the continuous bubbles which covered four or more pin-fins. At higher heat fluxes, the annular flow was observed along the channels.

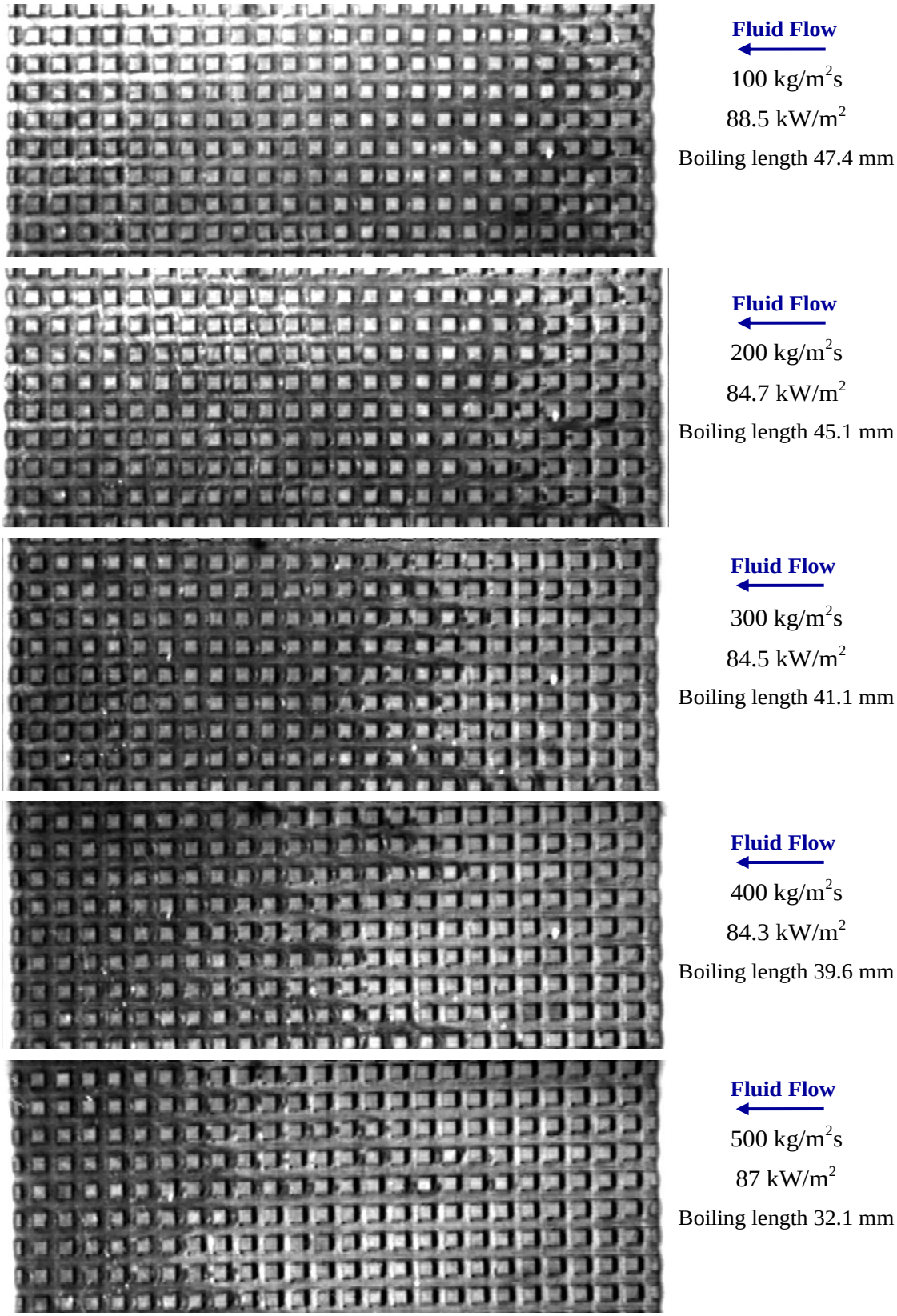

Figure 6.27 Video images of flow boiling region development at quite equal heat fluxes, at various mass fluxes, for in-line pin fin surface with R113

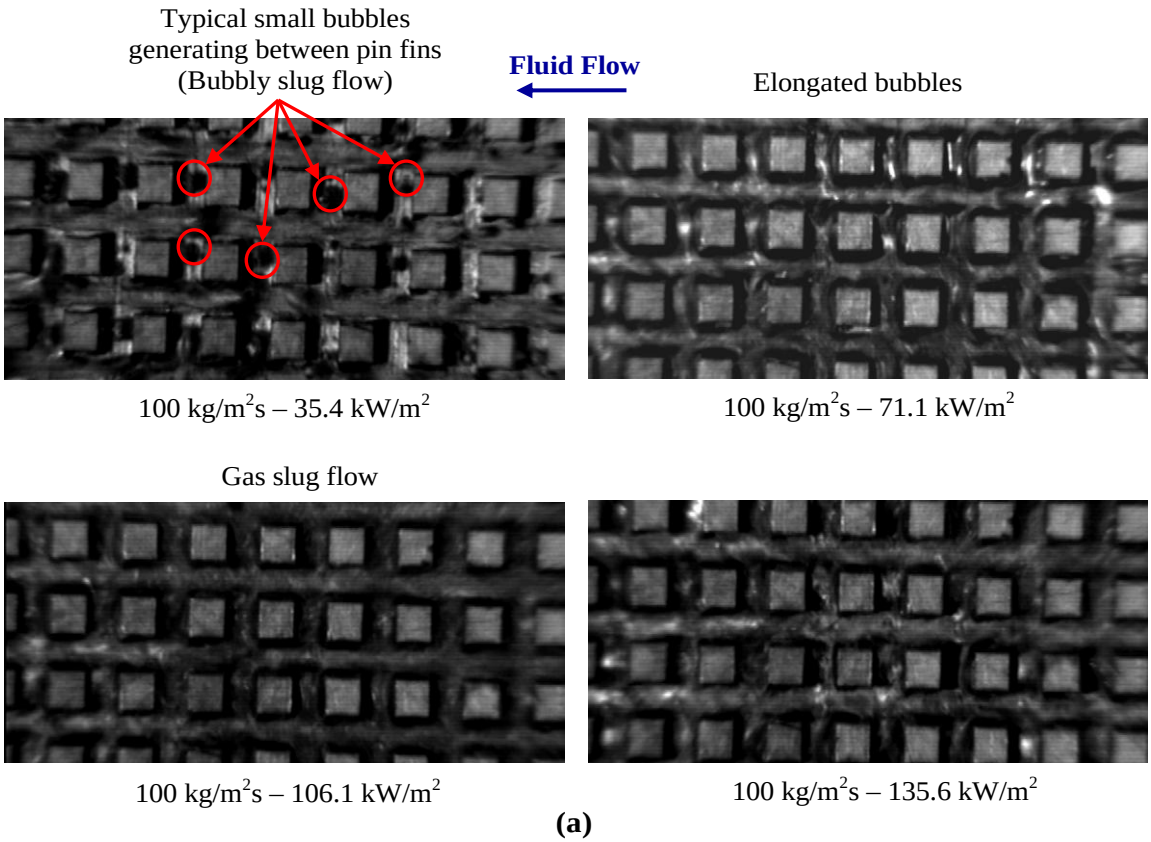

(a)

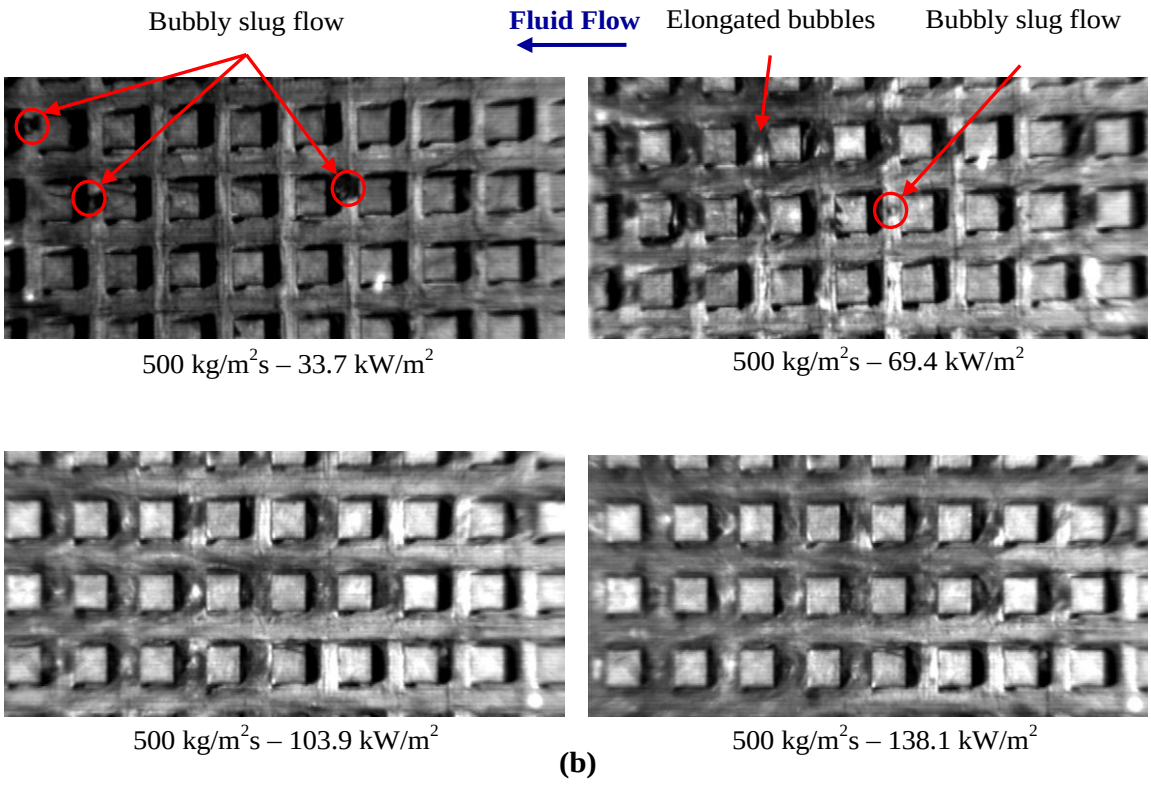

(b)

Figure 6.28 Typical views of the flow for mass fluxes of, (a) 100 and (b) 500 kg/m^2s at various heat fluxes, for in-line pin fin surface with R113

6.5 In-Line Off-Set Pin-Fin Surface Tests with R113

In-line off-set pin-fin surface heat transfer coefficients and pressure drop measurements, obtained for single-phase and two-phase tests with R113, and also flow boiling visualisation for these series of tests are presented in this section. For a better distinction between the two pin-fin surfaces, the in-line off-set referred to hereafter as off-set.

6.5.1 Single-Phase Heat Transfer Coefficient

The off-set pin fin surface single-phase heat transfer coefficients are shown for the range of mass fluxes in Figure 6.29. The plate, parallel and in-line surfaces linear and power law functions are included in the figure as well. Unlike the in-line pin fin surface, the off-set pin fin wall inlet and outlet heat-transfer coefficients are similar in magnitude, with both following a power law function of the mass flux. The estimated error in the heat transfer coefficient is $\pm 10\%$.

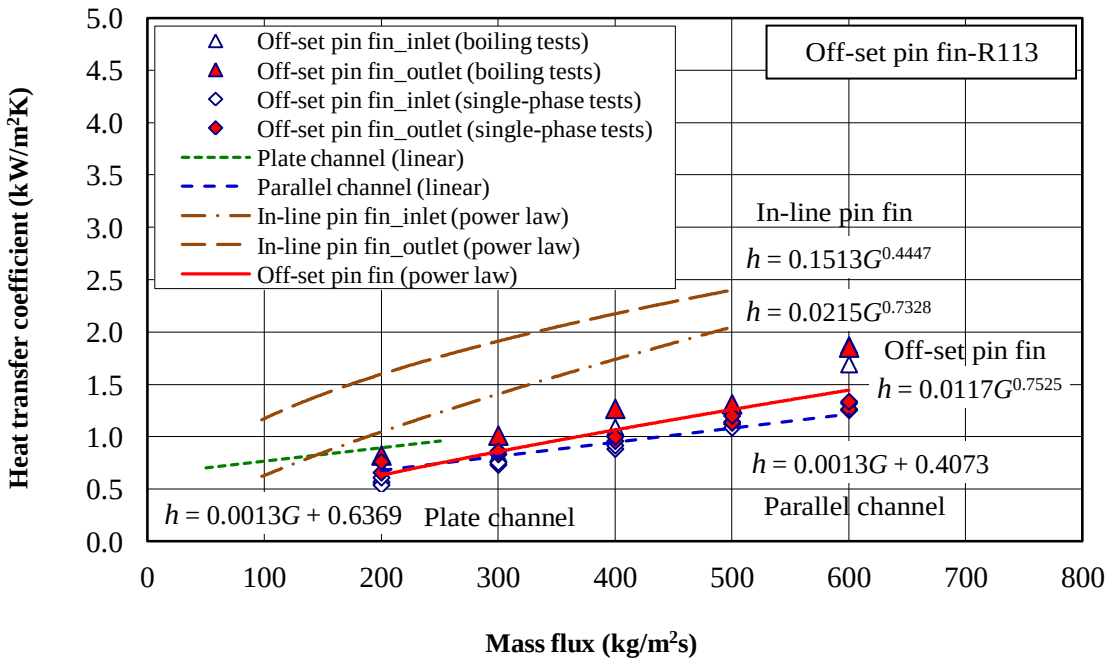

Figure 6.29 Variation of single-phase heat-transfer coefficient with mass flux for off-set pin-fin surface with R113

As is shown, the same as other surfaces the single-phase heat transfer coefficient increases with mass flux and is independent of wall heat flux, as for a constant mass flux, heat transfer coefficient remains fairly constant.

6.5.2 Single-Phase Pressure Drop

The variation of single-phase pressure drop with mass flux for the off-set pin fin surface is shown in Figure 6.30. The same as the in-line surface, the pressure drop for off-set pin fin surface is shown to be a power law function of the mass flux, as would be expected. The parallel and in-line surfaces linear and power law functions respectively are included in the figure. All data sets are similar in magnitude, but the in-line pin fin values are higher, while the parallel values are slightly lower.

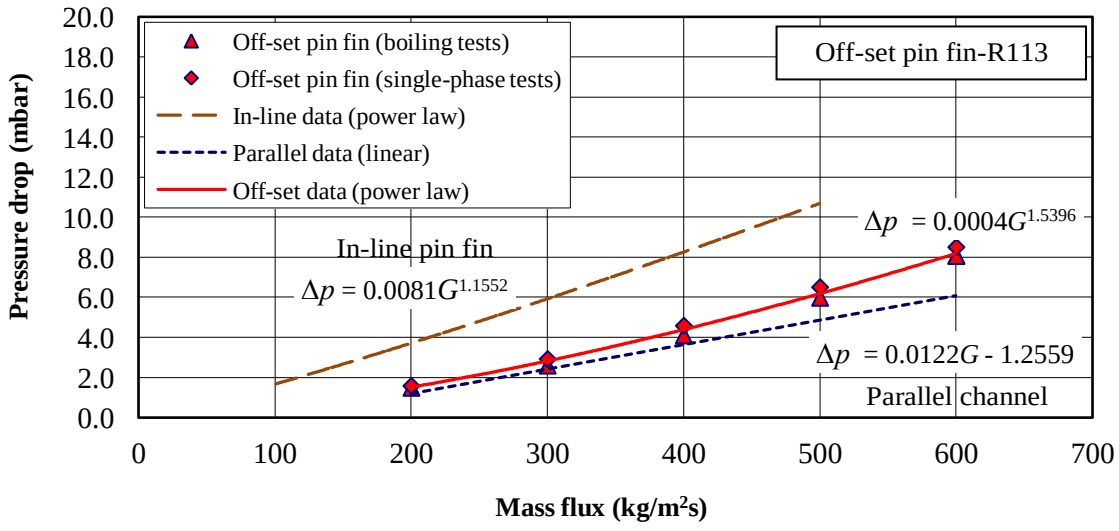

Figure 6.30 Variation of single-phase pressure drop with mass flux for off-set pin fin surface with R113

6.5.3 Boiling Curve

The boiling curves, obtained at the wall inlet and outlet thermocouples locations, are illustrated for each mass flux in Figure 6.31. The same as the in-line pin fin and parallel channel surfaces, for most of the curves, three regions can be identified at inlet and outlet wall thermocouples locations. Firstly, a single-phase region at the low heat fluxes, where the slopes of the boiling curves are positive and fairly constant. This region can be readily identified for mass fluxes of 500 and 600 kg/m^2s. As for these mass fluxes single-phase occurs at two lowest heat fluxes, while for lower mass fluxes, it occurs at just the lowest heat flux, at both wall inlet and outlet locations. Secondly, a sub-cooled flow boiling region at intermediate heat fluxes, where the slopes of the boiling curves increase and become negative in most of the curves due to a quick rise in the convective heat transfer coefficient. And finally, a saturated flow boiling region at higher heat fluxes, where the local vapour mass fraction, $x_{e,tc}$, is above zero and the slopes of the boiling curves become positive and fairly constant again. At high heat fluxes, where the saturated flow boiling region is identified for both wall inlet and outlet, boiling curves are similar in magnitude and following quite similar slope, with the outlet values being slightly sharper than that at inlet.

For mass fluxes of 400 kg/m^2s and above at high heat fluxes, sub-cooled flow boiling regime were identified for wall inlet data, while the wall outlet data are in saturated boiling regime, therefore the wall inlet boiling curves at these high heat fluxes do not rise to the wall outlet curves and similarly follow the wall outlet curves with lower values. While for lower mass fluxes of 300 kg/m^2s and below, at high heat fluxes, both the wall inlet and outlet data are in saturated flow boiling regime, therefore both wall inlet and outlet curves following quite the same slope, with the same magnitude.

As it was mentioned before the boiling curves obtained for steady state conditions. Typical error bars with $\pm 10\%$ error range for the wall inlet data at the lowest mass flux of 200 kg/m^2s are included in Figure 6.31.

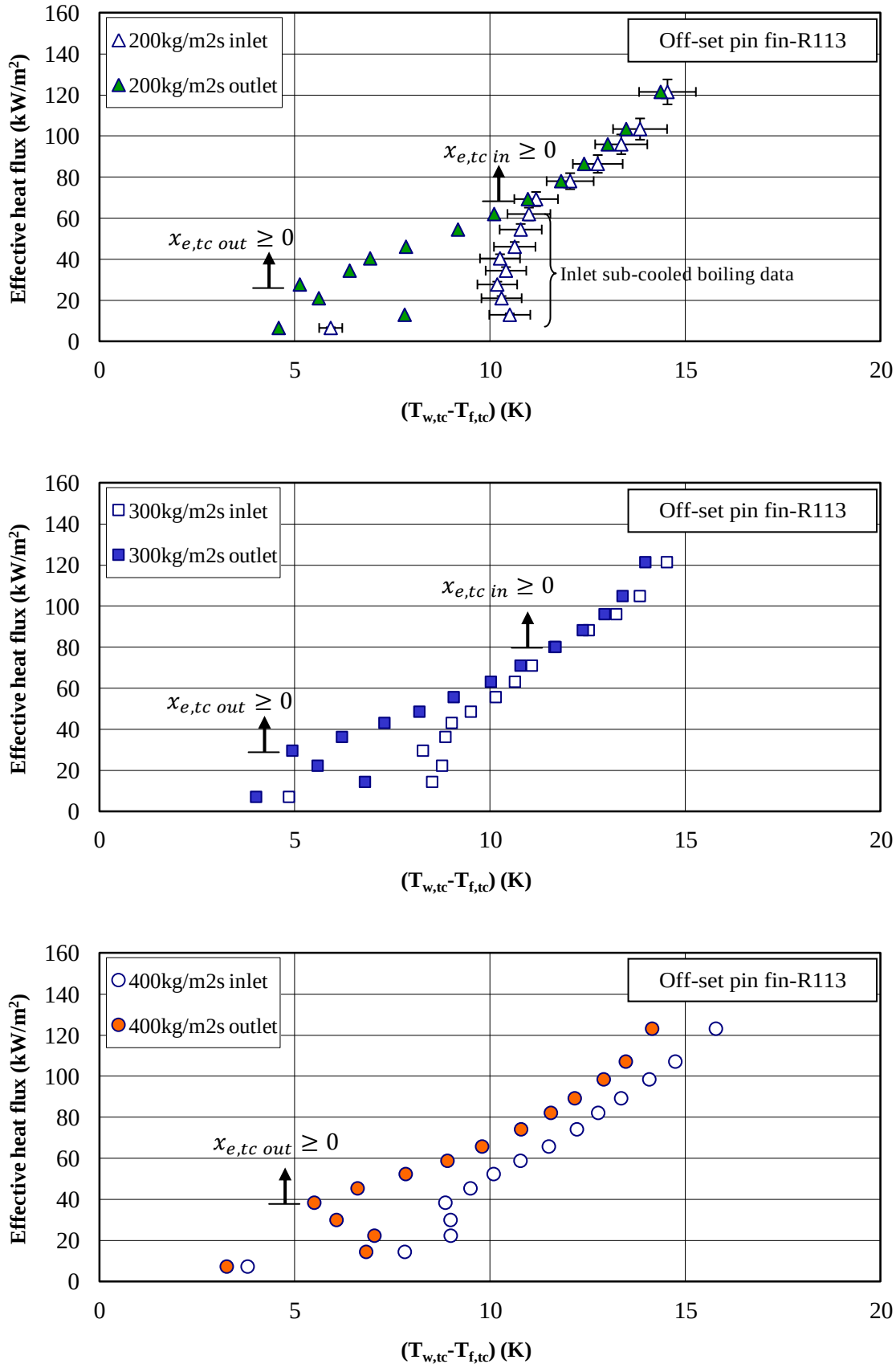

Figure 6.31 Boiling curves at the wall inlet and outlet for a range of mass fluxes, obtained from off-set pin fin surface tests with R113

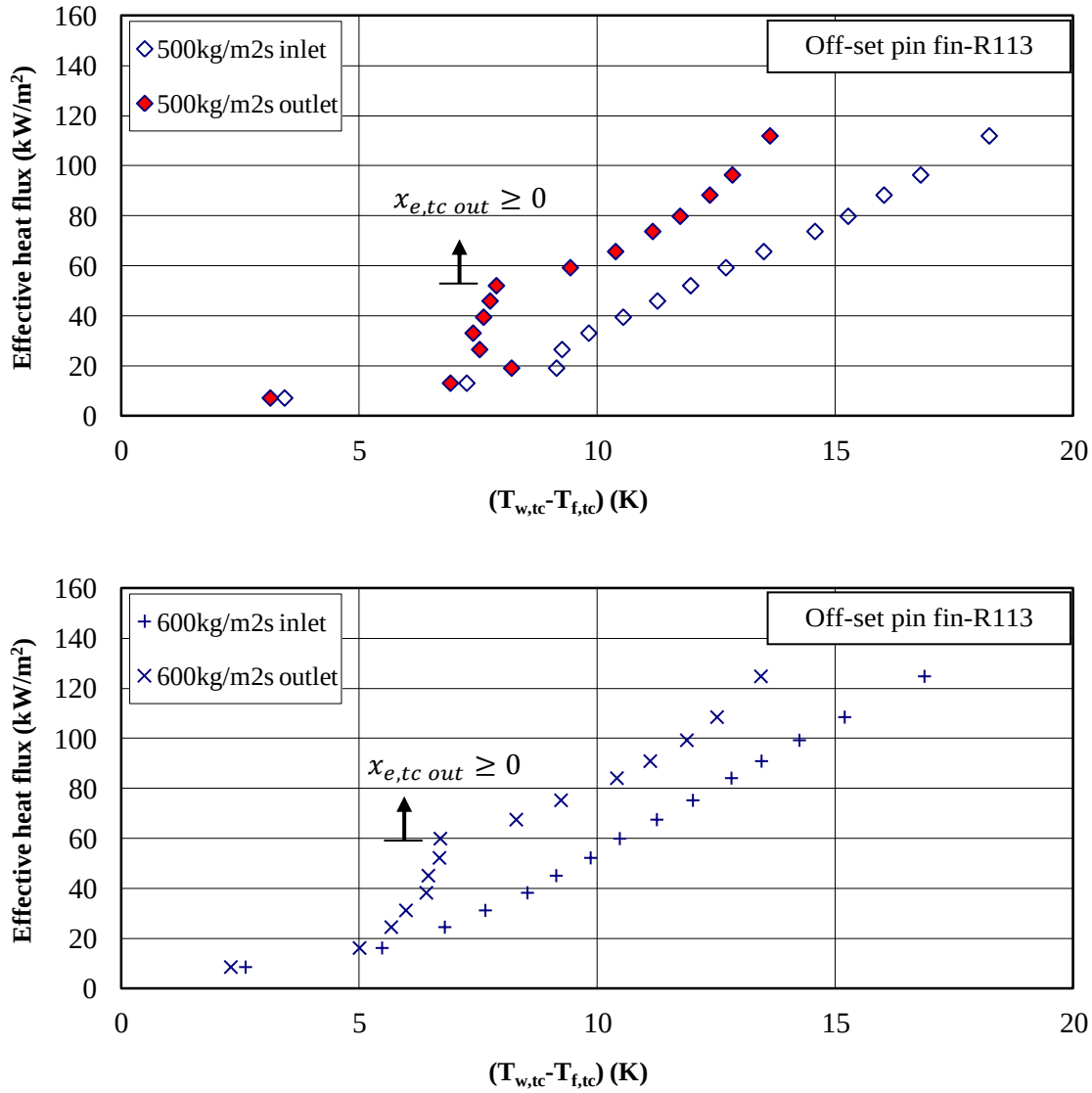

Figure 6.31 (continued) Boiling curves at the wall inlet and outlet for a range of mass fluxes, obtained from off-set pin fin surface tests with R113

Figure 6.32 shows variation of boiling length with effective heat flux for a range of mass fluxes. For a constant heat flux, boiling length is decreased with increasing mass flux.

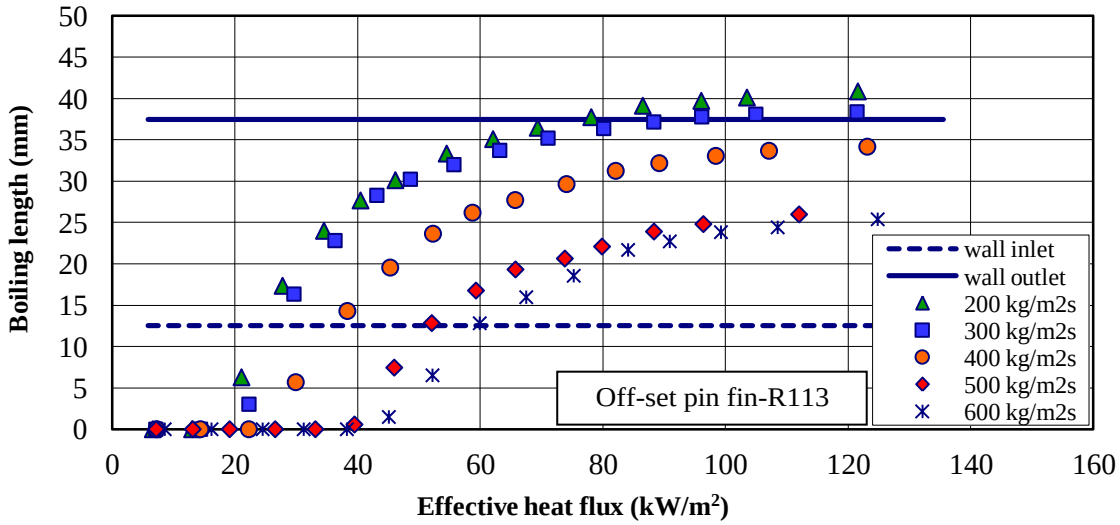

Figure 6.32 Variation of boiling length with effective heat flux for a range of mass fluxes for off-set pin fin surface with R113

6.5.4 Two-Phase Heat Transfer Coefficient

The variation of the measured heat-transfer coefficients with the effective heat fluxes for off-set pin fin surface is shown for each mass flux in Figure 6.33. As is shown, the off-set pin-fin surface was subjected to all three heat transfer types, the same as parallel and in-line pin fin surfaces. The off-set pin fin surface heat transfer coefficients characteristics are similar to that obtained with the in-line pin fin surface. Therefore the description given for the in-line pin fin surface two-phase heat transfer coefficients is, in the main, repeated for off-set pin-fin surface. But there are some significant differences.

Unlike the in-line pin fin surface, the off-set pin fin surface wall inlet and outlet single-phase values are similar in magnitude, like the plate and parallel channel surfaces data. The pin fins rows between the two sets of wall inlet and outlet thermocouples locations do not cause any considerable difference on the off-set surface single-phase heat transfer coefficients data.

For mass fluxes of 500 and 600 kg/m^2s, single-phase occurs at the two lowest heat fluxes, while for lower mass fluxes, single-phase occurs at both the wall inlet and outlet, just at the lowest heat flux of approximately 7 kW/m^2. For mass fluxes of 200 and 300 kg/m^2s, as the heat flux increases, the off-set wall inlet heat-transfer coefficient is shown to rise from levels below the outlet values to the outlet value, similar to the in-

line pin fin surface. The merging characteristic of the off-set pin fin surface is similar to that obtained with the in-line pin fin surface. Within this range, where the inlet and outlet flows are shown to be in the sub-cooled and saturated flow boiling regimes respectively, the wall outlet heat-transfer coefficients are shown to be independent of heat flux.

As the mass flux increases, for mass flux of $400\,kg/m^2s$ and above, at high heat fluxes, the wall inlet values remain in the sub-cooled flow boiling region and do not rise to the wall outlet value. Unlike the in-line pin fin surface, the region where the heat transfer coefficient is reasonably independent of heat flux increases as the mass flux increases.

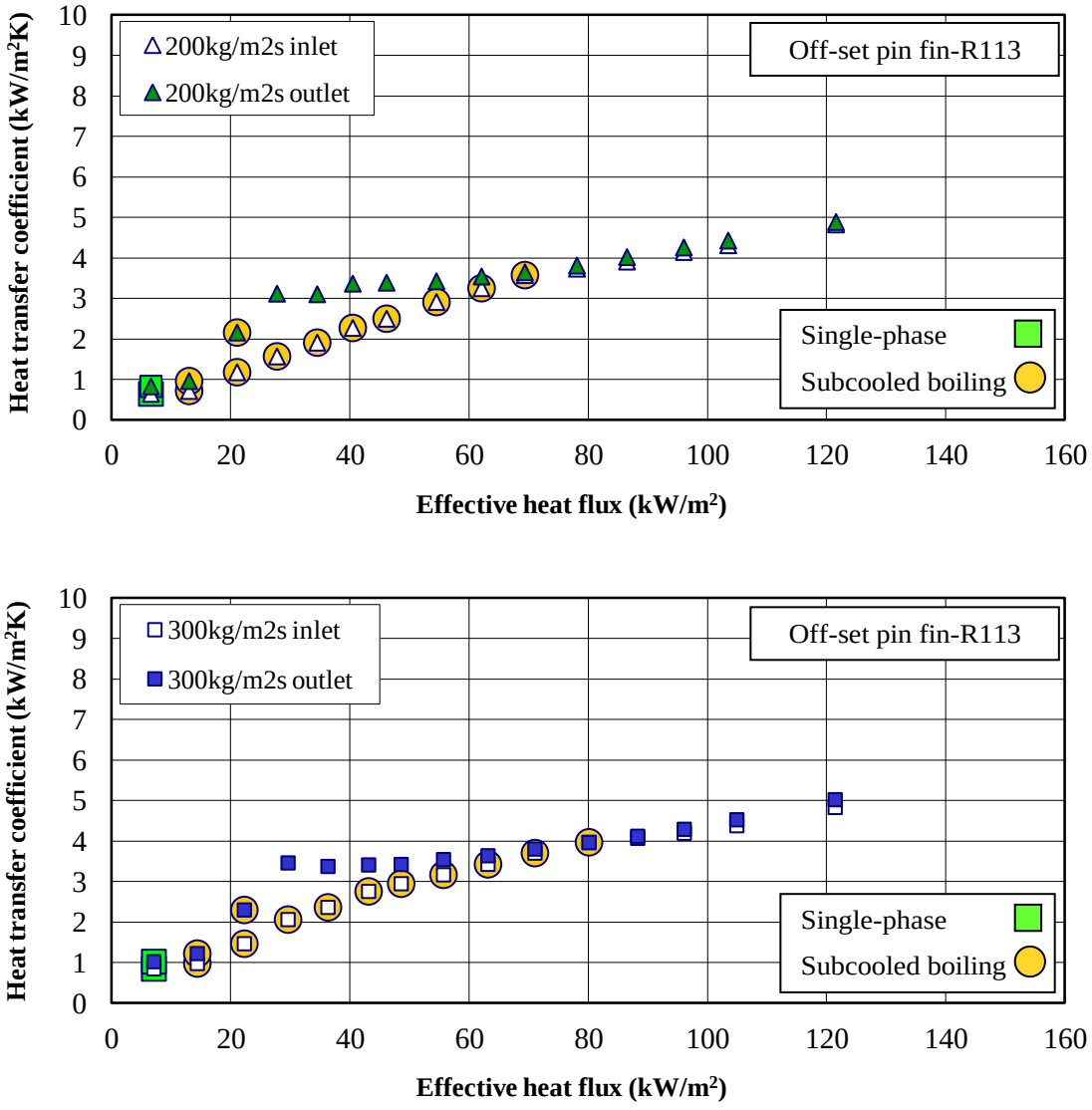

Figure 6.33 Variation of heat transfer coefficients with effective heat flux for a range of mass fluxes, for off-set pin fin surface with R113

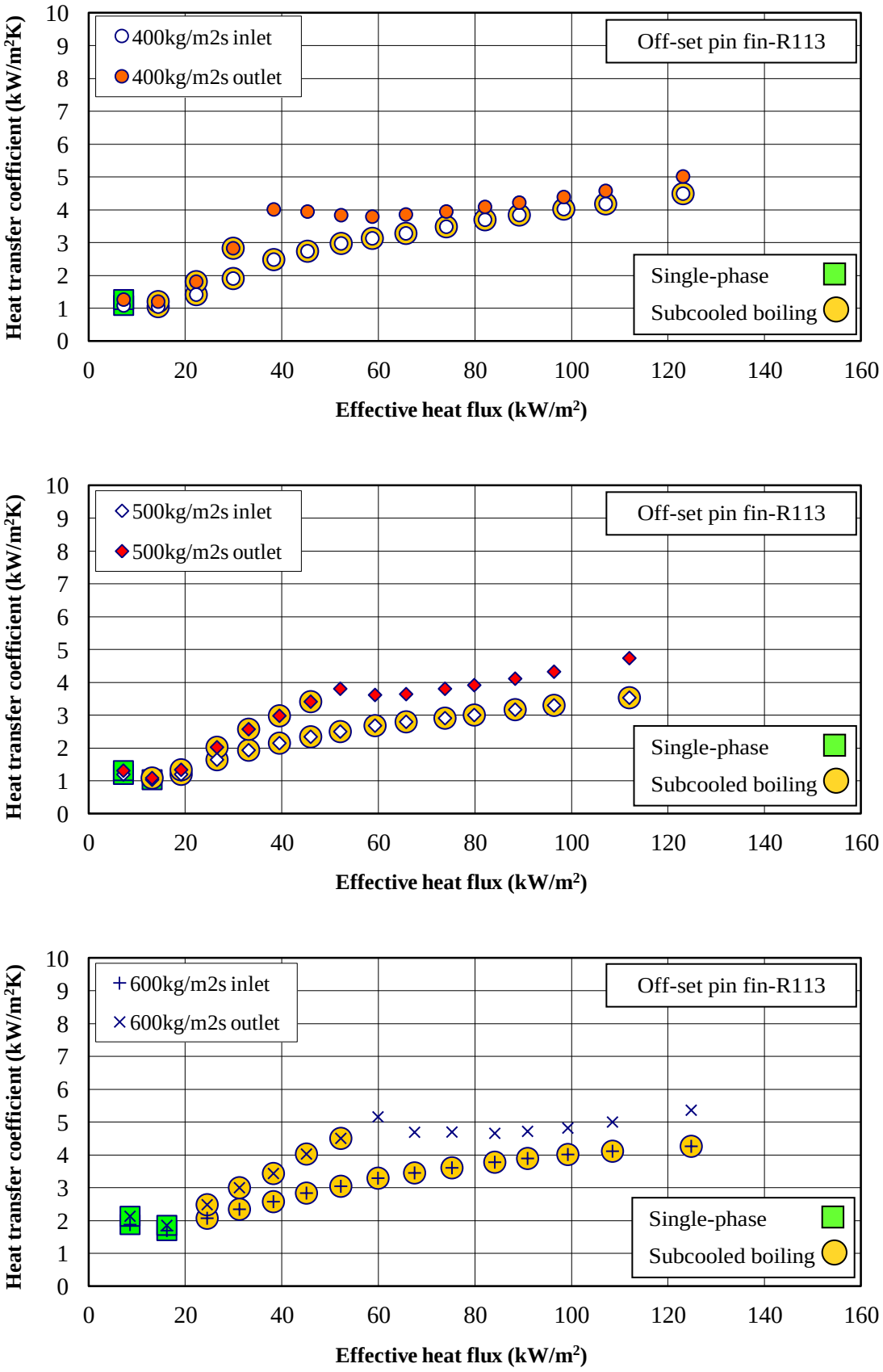

Figure 6.33 (continued) Variation of heat transfer coefficients with effective heat flux for a range of mass fluxes, for off-set pin fin surface with R113

Figure 6.34 illustrates the variation of saturated boiling heat transfer coefficient with local vapour mass fraction for off-set pin fin surface. Similar to the other surfaces, the range of vapour mass fractions is reduced at the larger mass fluxes, but the saturated boiling heat-transfer coefficients remain fairly independent of it.

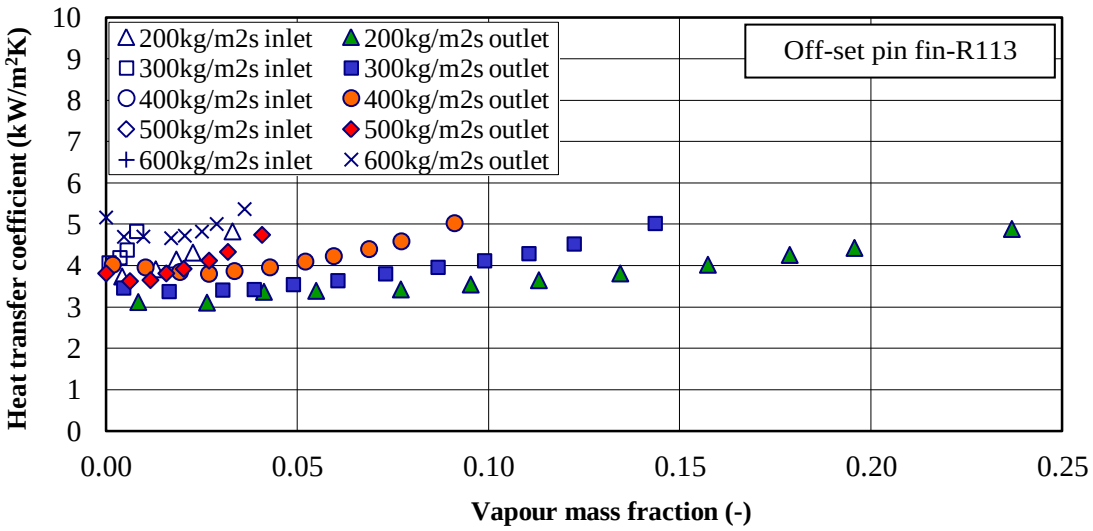

Figure 6.34 Variation of saturated boiling heat transfer coefficient with local vapour mass fraction at various mass fluxes, for off-set pin fin surface with R113

All of the off-set pin fin surface saturated boiling data identified in Figure 6.33 are reproduced in Figure 6.35. As is shown, the same as other surfaces, off-set pin fin surface data are reasonably independent of location and mass flux and follow the power law relationship

$$h = 1.4066 q_{act}^{0.284} \tag{6.5}$$

to within $\pm 10\%$ of the measured values. Equation (6.5) is based on the actual heat flux, q_{act}. The same as other surfaces, it therefore seems likely that the dominating heat-transfer mechanism in the saturated boiling flow regime is nucleate boiling for the off-set pin fin surface as well.

The other surfaces power laws are included in Figure 6.35. As is shown, the off-set pin fin surface data set trend is similar to the other surfaces data sets, with slightly higher values at lower heat fluxes. As the heat flux increases, the off-set pin fin heat transfer coefficients values merge with the parallel and in-line pin fin surfaces

data. This indicates that the off-set pin-fin surface heat transfer coefficient is similar to the parallel channel and in-line pin fin surfaces values to within the experimental uncertainty.

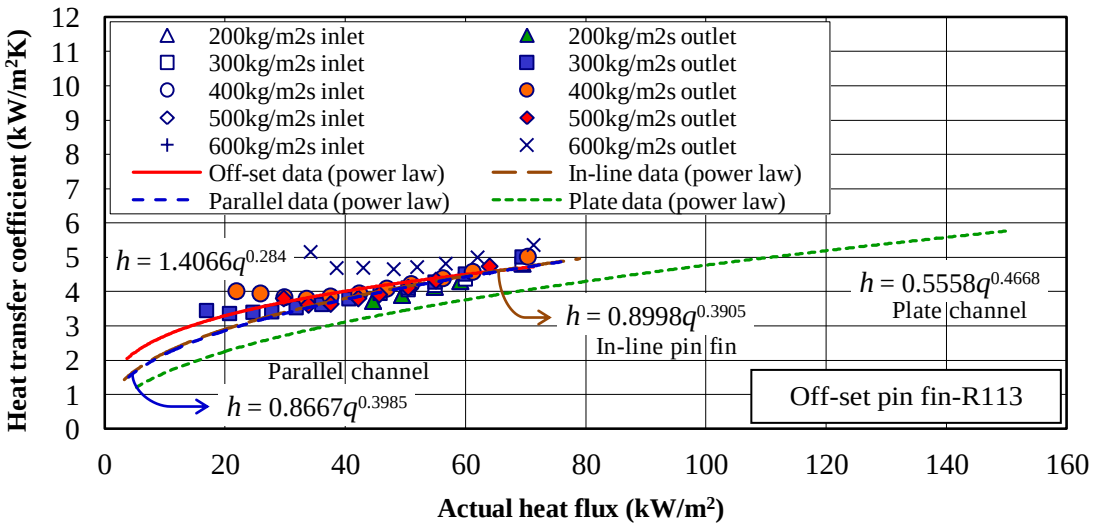

Figure 6.35 Variation of saturated boiling heat transfer coefficient with actual heat flux at various mass fluxes, for off-set pin fin surface with R113

6.5.5 Two-Phase Pressure Drop

Figure 6.36 illustrate the variation of two-phase pressure drop with heat flux for a range of mass fluxes for off-set pin fin surface. The same as other surfaces, the off-set pin-fin pressure drop is shown to increase with increasing heat flux. For all mass fluxes, except 500 kg/m^{2}s, the pressure drop is also shown to increase with mass flux. The off-set pin fin data are slightly smaller than the in-line pin fin data and considerably larger than the plate and parallel data by a factor of about 5 and 1.8 respectively.

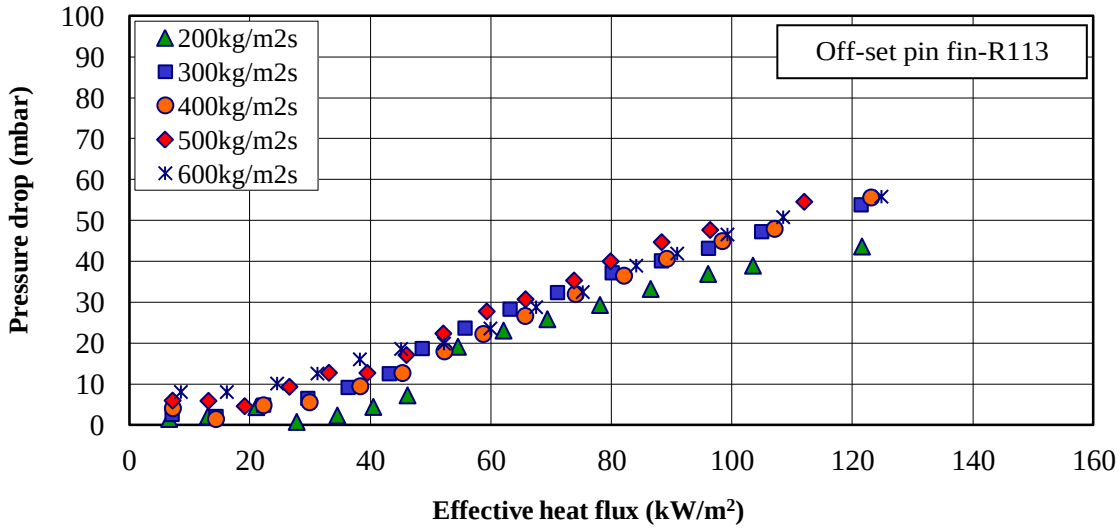

Figure 6.36 Variation of pressure drop with effective heat flux at various mass fluxes, for the off-set pin fin surface with R113

6.5.6 Flow Boiling Visualisation

Figure 6.37 shows video images of flow boiling region development at quite equal heat fluxes, for all mass fluxes in the range $200 - 600\ kg/m^2s$. As is shown for a quite constant heat flux, as the mass flux increases the boiling area decreases. This results from the increased amount of absolute sensible enthalpy change that is required to reach saturation as a consequence of the mass flux increase.

Figure 6.38 shows typical observed flow patterns for lowest mass flux of $200\ kg/m^2s$, at various heat fluxes in equal intervals. As it is shown, the vapour mass fraction increases with increasing the heat flux. At low heat fluxes, the off-set pin fin surface contains small bubbles generating between pin fins, perpendicular to the flow direction. The isolated bubbles are expanded and start to move. The fins arrangement causes the bubbles mostly move between the fins, parallel to the flow direction. At higher heat fluxes, similar to the in-line pin fin surface, bubbles are expanded, collated and elongated. These elongated bubbles move between the fins, parallel and perpendicular to the flow direction. Similar to the in-line pin fin surfaces, three flow patterns were observed; bubbly slug (isolated bubbles/confined bubbles), gas-slug, and annular flows.

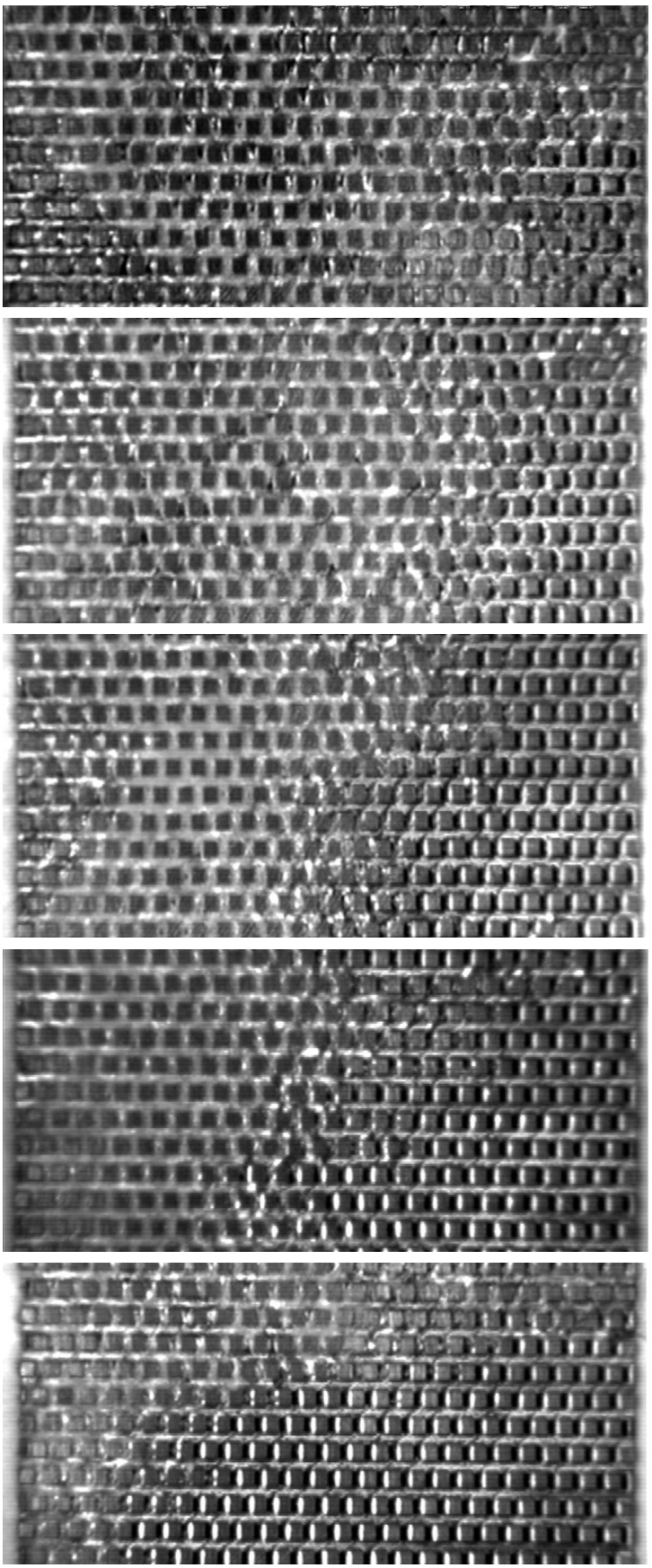

Figure 6.37 Video images of flow boiling region development at quite similar heat fluxes, at various mass fluxes, for off-set pin fin surface with R113

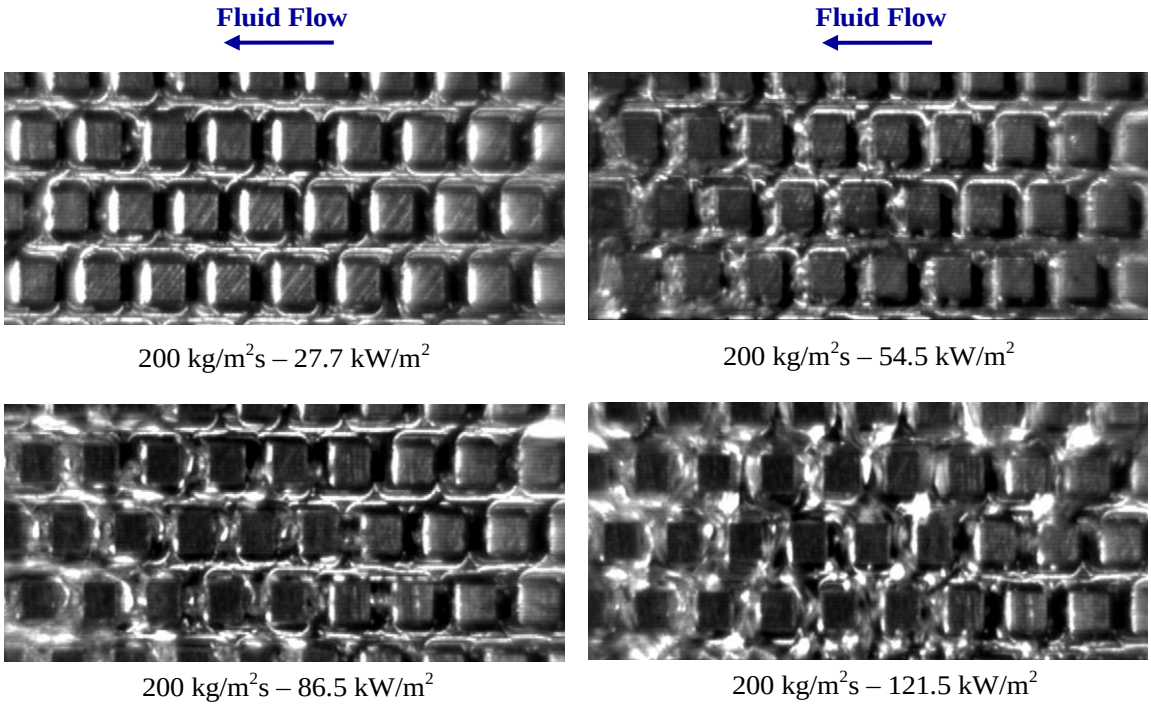

Figure 6.38 Typical views of the flow for mass fluxes of 200 kg/m^2s at various heat fluxes, for off-set pin fin surface with R113

6.6 In-Line Pin-Fin Surface Tests with Deionised Water

The In-line pin-fin surface heat transfer coefficients and pressure drop measurements, obtained for single-phase and two-phase tests with deionised water are presented in this section. As it was mentioned in Chapter 2, deionised water has a much higher surface tension than R113. The Bond number for water is much less than that for R113. Therefore based on the Bond number, the water data should be more consistent with the micro-scale channels. Thus, deionised water was selected to make comparisons with R-113 data.

6.6.1 Single-Phase Heat Transfer Coefficient

The single-phase heat transfer coefficients are shown for the range of mass fluxes in Figure 6.39. Similar to the data sets obtained from in-line pin fin surface tests with R113, the wall inlet and outlet heat-transfer coefficients are shown to be different in magnitude, with both following a power law function of the mass flux. The estimated error in the heat transfer coefficient is $\pm 10\%$.

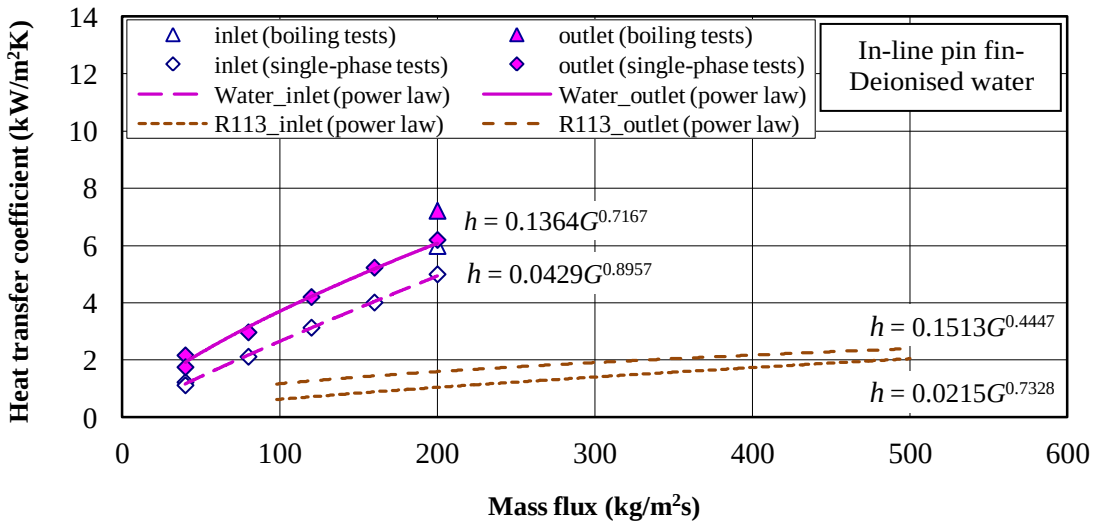

Figure 6.39 Variation of single-phase heat-transfer coefficient with mass flux, for in-line pin-fin surface with deionised water

As is shown, similar to the tests with R113, the single-phase heat transfer coefficient increases with mass flux and is independent of wall heat flux for water tests as well. The wall inlet and outlet power laws for the in-line pin fin surface tests with R113 are included in Figure 6.39. Both water and R113 data sets trend are similar, but the water heat transfer coefficients are considerably higher and increase with a sharper slope than the R113 values. This results from the higher specific heat capacity and thermal conductivity of water than R113.

6.6.2 Single-Phase Pressure Drop

The variation of single-phase pressure drop with mass flux is shown for the in-line pin fin surface tests with deionised water in Figure 6.40. The same as the R113 data, pressure drop is shown to be a power law function of the mass flux, as would be expected. The in-line pin fin surface power law for tests with R113 is included in Figure 6.40. Both water and R113 data sets are similar in magnitude, with the R113 values being slightly higher. This results from the R113 higher density and lower viscosity than those for water, which cause higher frictional pressure drop.

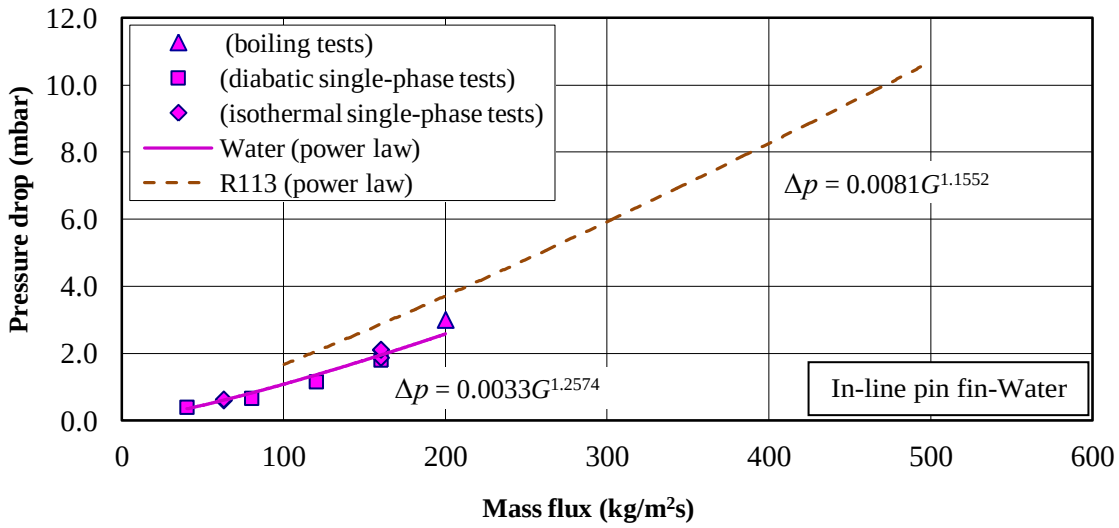

Figure 6.40 Variation of single-phase pressure drop with mass flux for in-line pin fin surface with deionised water

6.6.3 Boiling Curve

The boiling curves, obtained at the wall inlet and outlet thermocouples locations, are illustrated for each mass flux in Figure 6.41. The boiling curves trend for in-line pin fin surface data with water is, in the main, quite similar to the other surfaces boiling curves trend. There is one major difference. For all mass fluxes except 40 kg/m^2s, at high saturated flow boiling region, where the slopes of the boiling curves are positive and the local vapour mass fraction is above zero, similar to the R113 tests, the wall inlet and outlet boiling curves are similar in magnitude for each mass flux and following quite a similar slope, while for a constant effective heat flux unlike the R113 data, the wall inlet temperature difference ($T_{w,tc} - T_{f,tc}$) is slightly less than the wall outlet values and with increasing the mass flux this difference increases. But for each mass flux as the heat flux increases, the wall inlet values tend to the outlet values.

For all mass fluxes, at both wall inlet and outlet locations except for wall outlet data at mass flux of 40 kg/m^2s and wall inlet and outlet data at mass flux of 200 kg/m^2s, two regions were identified. Firstly, a sub-cooled flow boiling region at low heat fluxes where the slopes of the boiling curves are negative in low mass fluxes or sharply begins to increase first and then become negative due to a sharp rise in the convective heat transfer coefficient. And secondly, a saturated

flow boiling region thereafter, where the slopes of the boiling curves are again positive and fairly constant and the local vapour mass fraction is above zero.

For the mass flux of 40 kg/m^2s, just a saturated flow boiling region is identified for the wall outlet boiling curve as it has a fairly constant positive slope and for all effective heat fluxes, the local vapour mass fraction is above zero. For the highest mass flux of 200 kg/m^2s, three regions were identified; a single-phase region at both the wall inlet and outlet locations for the lowest heat flux of 32.5 kg/m^2s, and as the heat flux increases, sub-cooled and saturated flow boiling regions were identified thereafter.

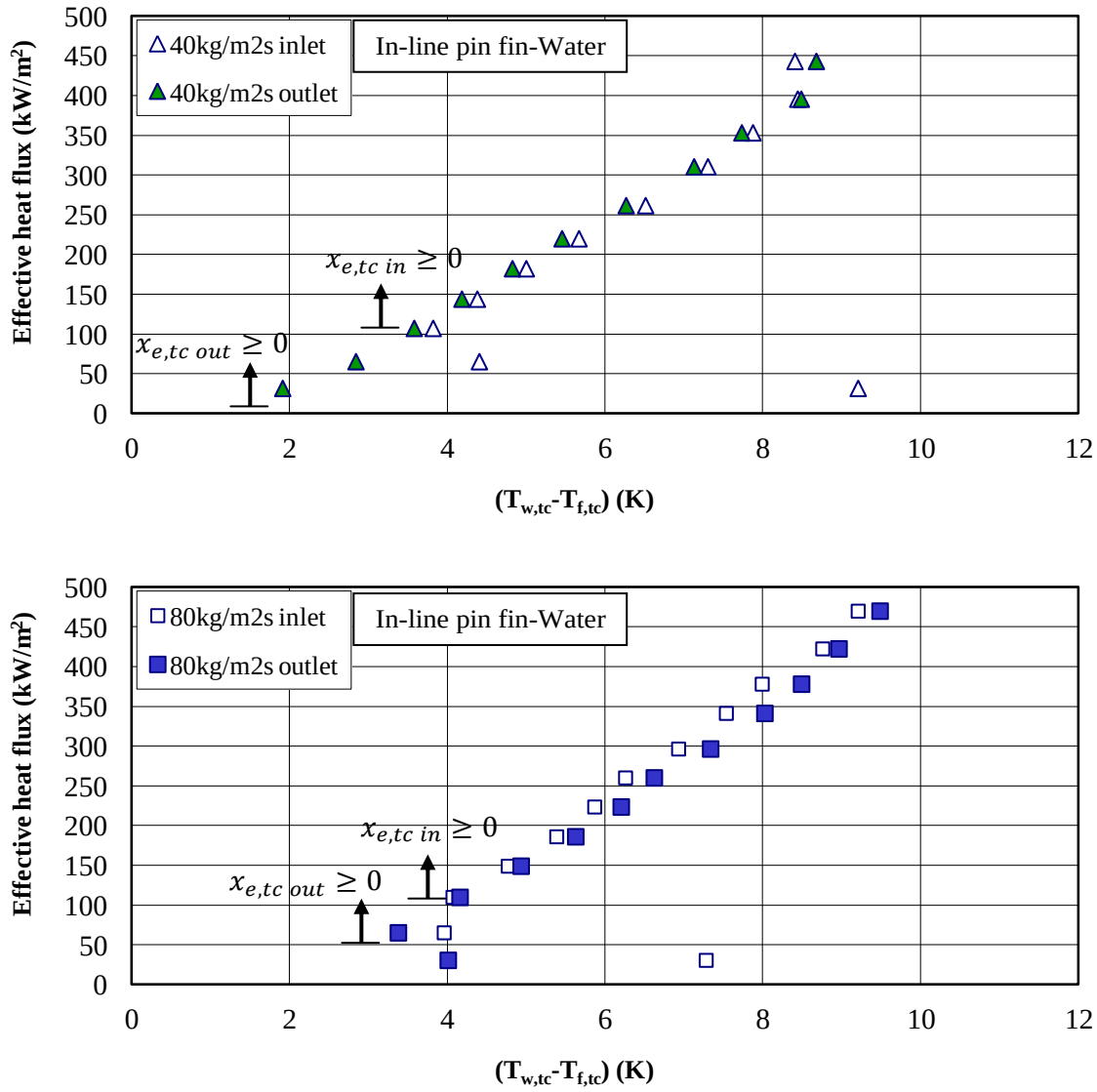

Figure 6.41 Boiling curves at the wall inlet and outlet for a range of mass fluxes, obtained from in-line pin fin surface tests with deionised water

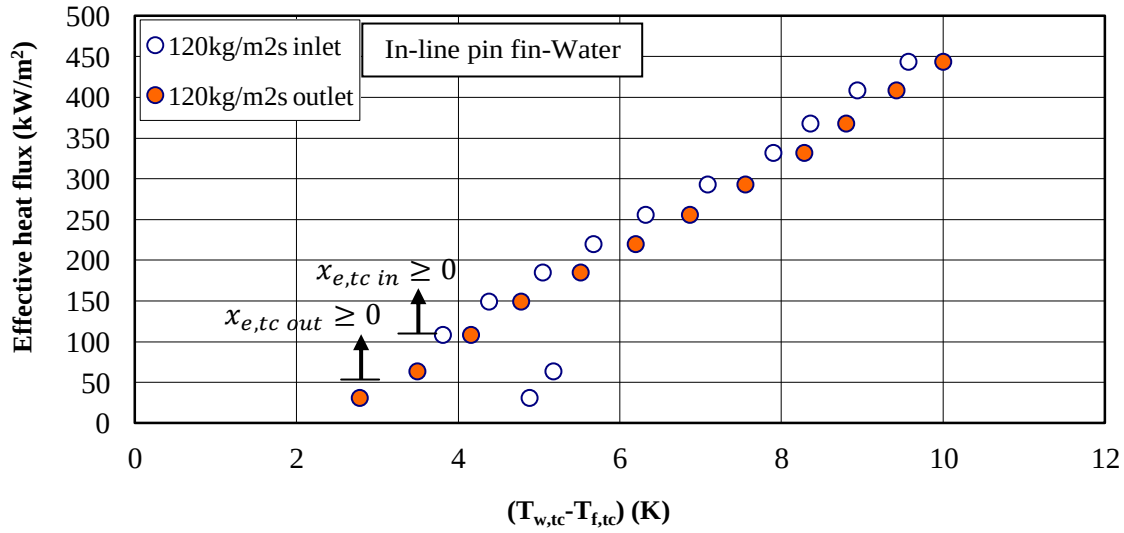

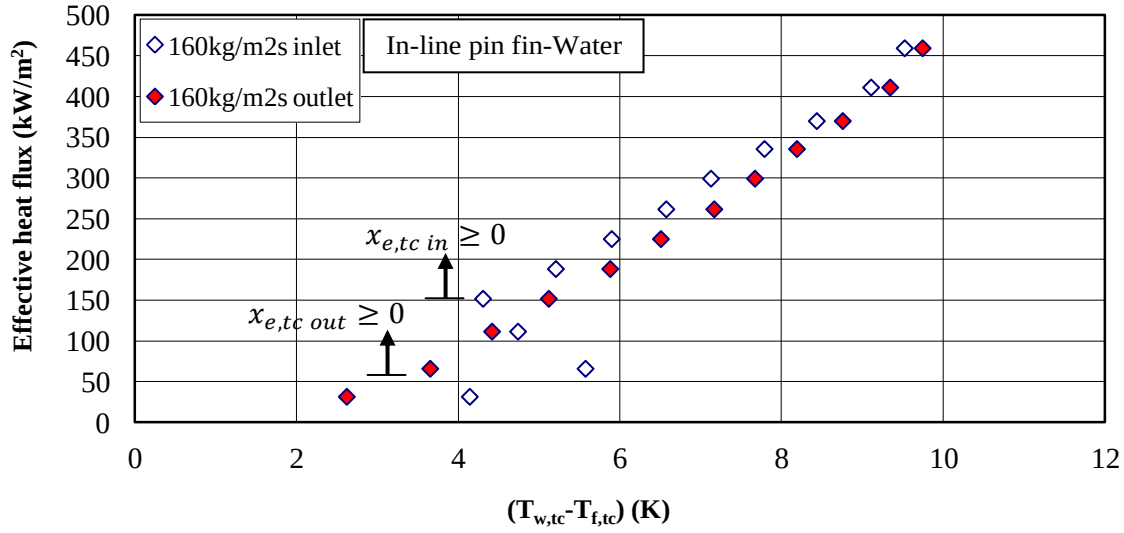

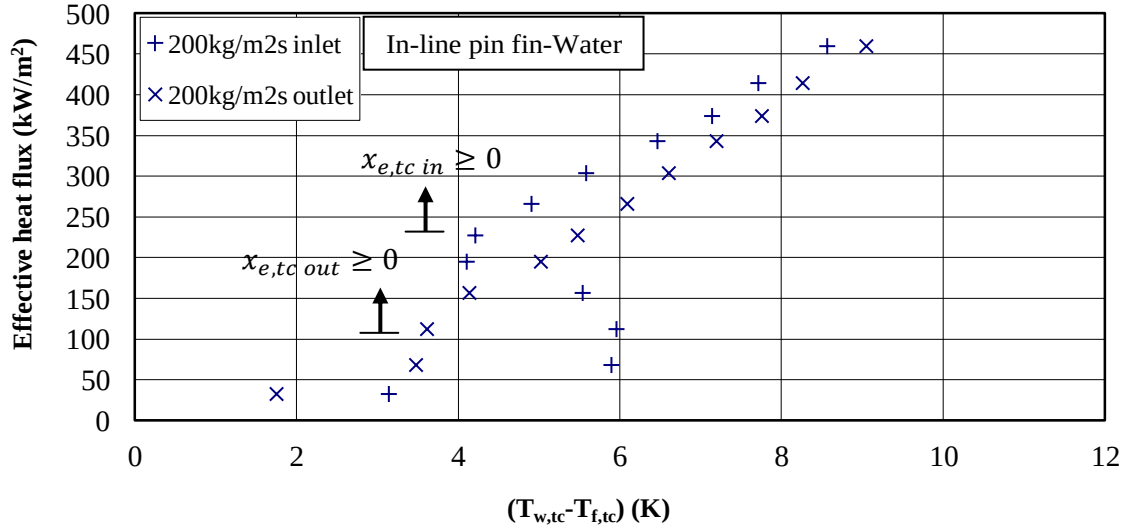

Figure 6.41 (continued) Boiling curves at the wall inlet and outlet for a range of mass fluxes, obtained from in-line pin fin surface tests with deionised water

Figure 6.42 shows variation of boiling length with effective heat flux for a range of mass fluxes. As it is shown, for a constant heat flux, boiling length is decreased with increasing mass flux.

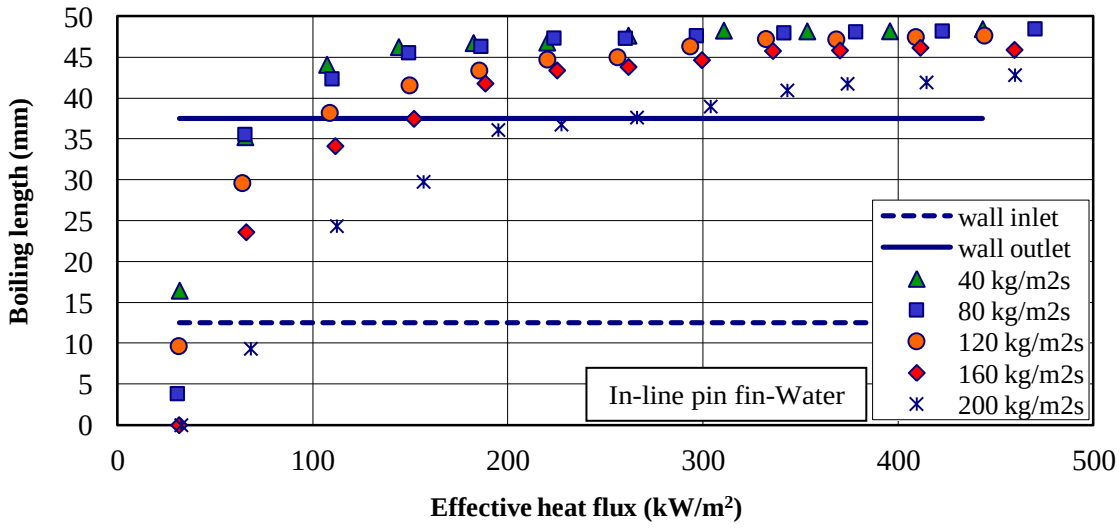

Figure 6.42 Variation of boiling length with effective heat flux for a range of mass fluxes, for in-line pin fin surface with deionised water

6.6.4 Two-Phase Heat Transfer Coefficient

The variation of the measured heat-transfer coefficients with the effective heat fluxes for in-line pin fin surface tests with water is shown for each mass flux in Figure 6.43. At all mass fluxes, the general trend shown for the in-line pin fin tests with R113 is repeated. There are few major differences.

Firstly, the region where the heat transfer coefficient for R113 tests were reasonably independent of heat flux, disappeared for water tests, and the wall inlet and outlet heat transfer coefficients continuously increase with increasing heat flux, except for the highest mass flux of 200 kg/m^2s at the wall inlet. Secondly, for all mass fluxes except 40 kg/m^2s, at high heat fluxes where the saturated flow boiling region occurs at both wall inlet and outlet locations, unlike the R113 data, the wall inlet heat transfer coefficients values are slightly higher than the wall outlet values. As the mass flux increases, this difference increases. At each mass flux, as the heat flux increases this difference decreases and the wall inlet values tend to the outlet values. For the highest mass flux of 200 kg/m^2s, at heat flux of approximately 195 kW/m^2, the wall inlet

heat transfer coefficient in sub-cooled flow boiling region over-shoot the wall outlet values in saturated flow boiling region.

As it was resulted from boiling curves and is shown in Figure 6.43, for all mass fluxes except $40\ kg/m^2s$ at wall outlet, and $200\ kg/m^2s$ at both wall inlet and outlet, two regions were identified; a low sub-cooled flow boiling region and a high saturated flow boiling region. For mass flux of $40\ kg/m^2s$, at all heat fluxes, just saturated flow boiling regime occurs at the wall outlet. While, for the highest mass flux of $200\ kg/m^2s$, three single-phase, sub-cooled and saturated flow boiling regimes occurred at both the wall inlet and outlet. Similar to the obtained data from the in-line pin fin surface tests with R113, the wall inlet and outlet single-phase heat transfer coefficients are shown to be different in magnitude. The difference is probably a settling length effect caused by the pin fins.

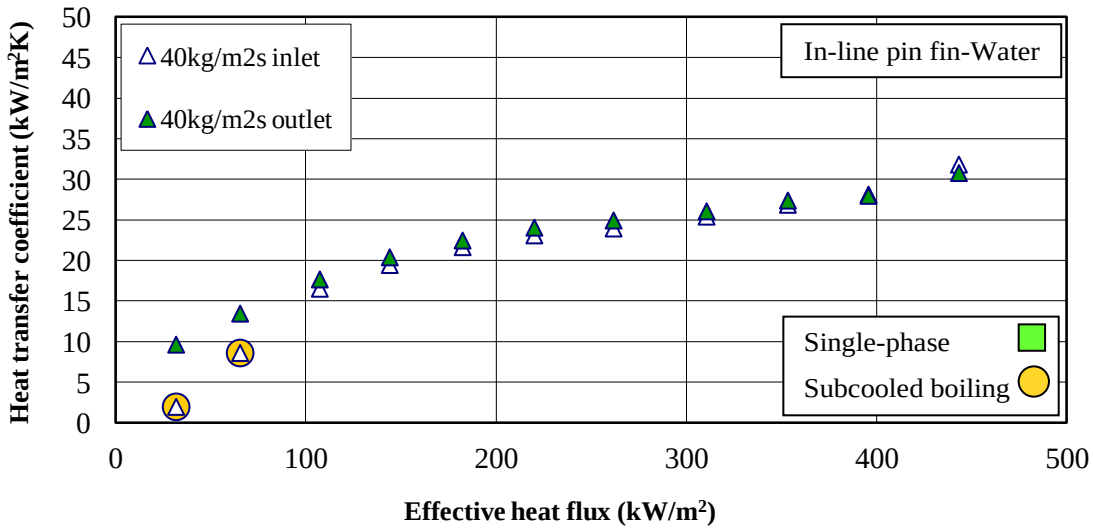

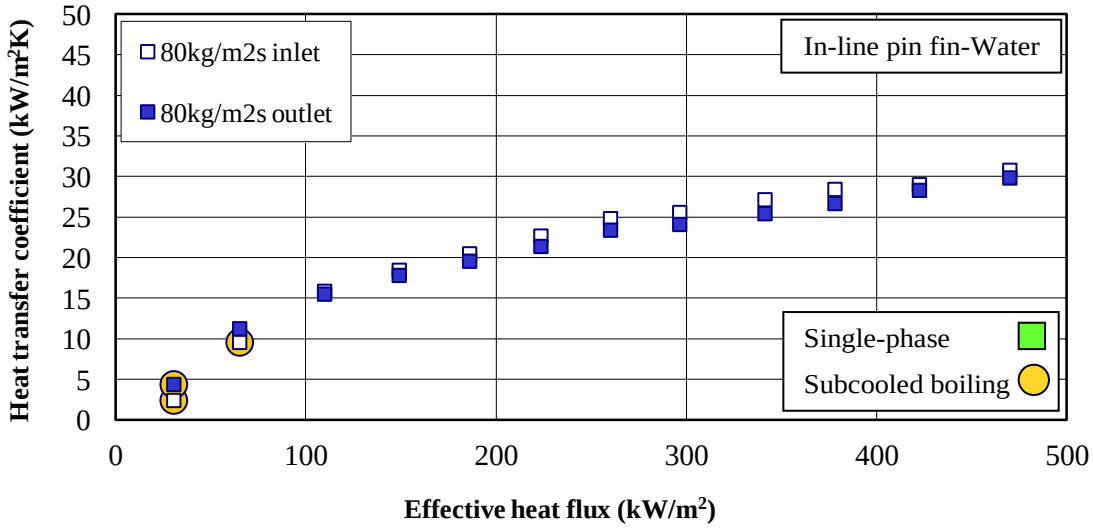

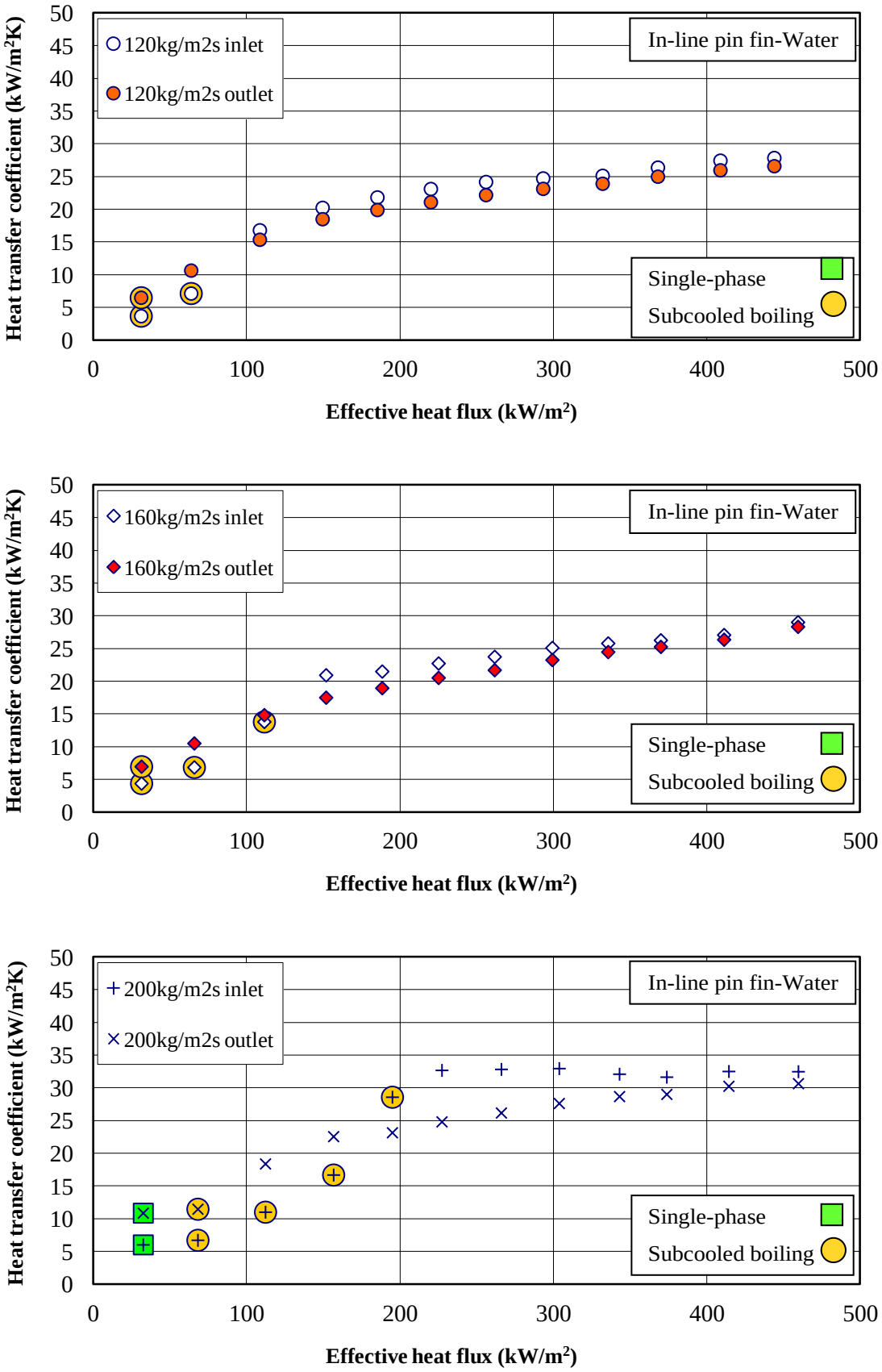

Figure 6.43 Variation of heat transfer coefficients with effective heat flux for a range of mass fluxes, for in-line pin fin surface with deionised water

Figure 6.44 illustrates the variation of saturated boiling heat transfer coefficient with local vapour mass fraction for in-line pin fin surface tests with deionised water. Similar to the other surfaces flow boiling tests, the range of wall inlet and outlet vapour mass fractions is reduced as the mass flux increases. At each mass flux, for a constant heat flux, the vapour mass fractions at the wall inlet and outlet locations are different, while the saturated boiling heat-transfer coefficients remain fairly independent of it.

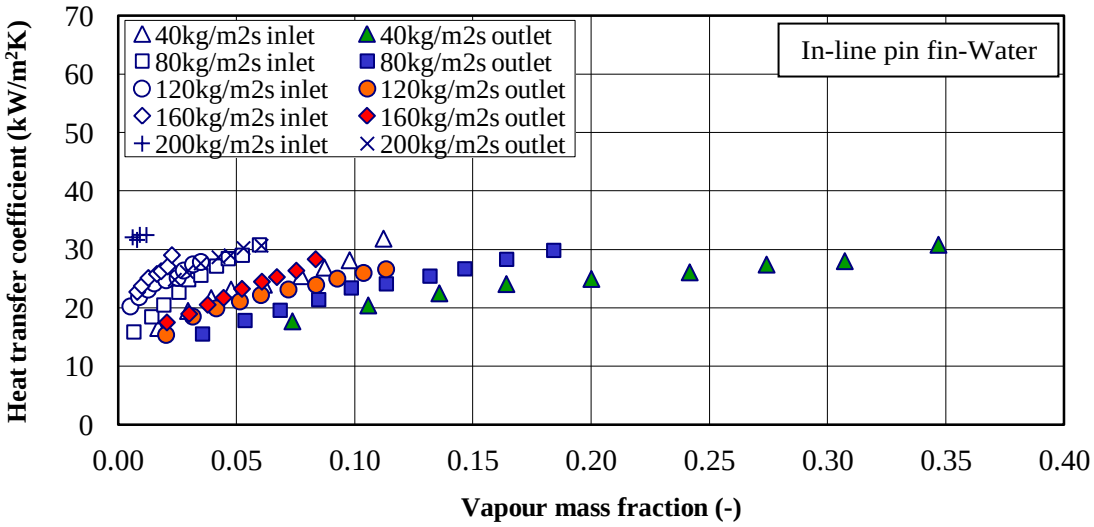

Figure 6.44 Variation of saturated boiling heat transfer coefficient with local vapour mass fraction at various mass fluxes, for in-line pin fin surface with deionised water

All of the saturated flow boiling data identified in Figure 6.43 are reproduced in Figure 6.45. As is shown, the same as other surfaces, in-line pin fin surface data for tests with deionised water are follow the power law relationship

$$h = 0.9711 q_{act}^{0.6355} \tag{6.6}$$

to within $\pm 20\%$ of the measured values. It seems likely that the dominating heat-transfer mechanism in the saturated flow boiling regime is nucleate boiling.

The in-line pin fin data obtained from flow boiling tests with R113 power law is included in Figure 6.45 as well. Both R113 and water data sets are following quite similar increasing trend, but the water data sets are much higher than the R113

data. This indicates that the water as the working fluid improve heat transfer by increasing the heat transfer coefficient.

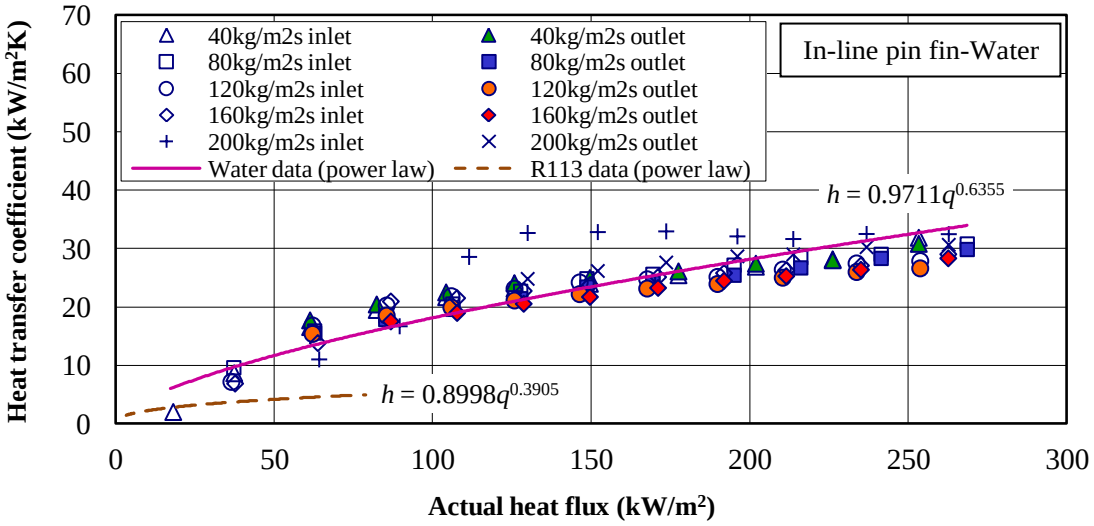

Figure 6.45 Variation of saturated boiling heat transfer coefficient with actual heat flux at various mass fluxes, for in-line pin fin surface with deionised water

A number of previous flow boiling investigations in mini and micro-scale pin-fin heat sinks which were described in Chapter 2, literature review, have been carried out with water as the working fluid (Krishnamurthy and Peles (2008); Qu and Siu-Ho (2009a, 2009b); and Kosar et al. (2010)). Unlike the present study, the two-phase forced convection associated with annular flow was postulated to be the governing heat transfer mechanism for the saturated flow boiling data in these three studies. The hydraulic diameters of the flow passages in these studies were much less than the present study flow passages hydraulic diameter. The operating conditions were also quite different. None-the-less Krishnamurthy and Peles (2008) saturated flow boiling data were chosen as a typical flow boiling study with water in a micro-scale pin-fin heat sink to be compared with the present study data. Krishnamurthy and Peles (2008) reported flow boiling of water across staggered circular pin fins with diameter of 100 μm and a height of 250 μm. The test piece specifications and tests operating conditions were mentioned in Chapter 2 in more details. The comparison between the present study water tests saturated flow boiling heat transfer coefficients and Krishnamurthy and Peles (2008) data is

shown in Figure 6.46. Since the Krishnamurthy and Peles (2008) data were consistent with the convective enhancement and the heat sink's flow passages were much smaller than the present study flow passages, and also the applied heat flux range was also different, the Krishnamurthy and Peles (2008) heat transfer coefficients were significantly different than that for the present study water data.

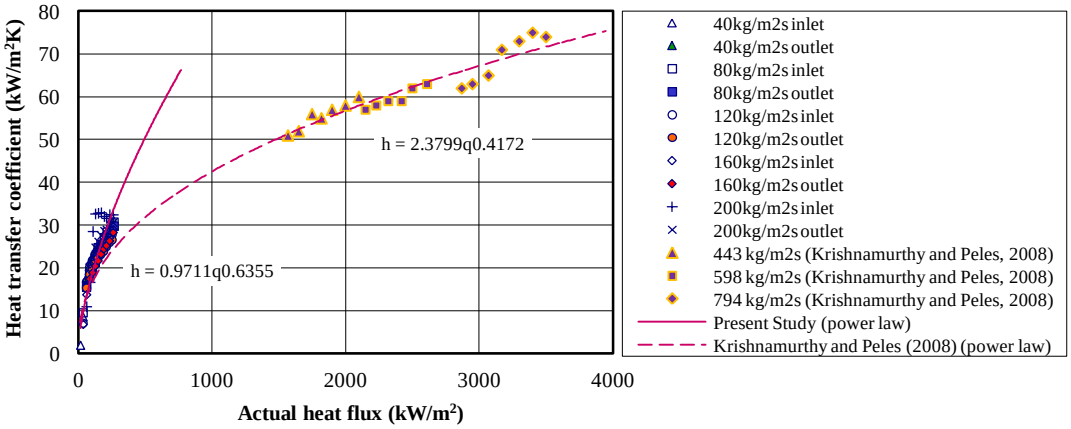

Figure 6.46 Saturated flow boiling heat transfer coefficients comparisons with Krishnamurthy and Peles (2008) data for tests with water as working fluid

6.6.5 Two-Phase Pressure Drop

The variation of two-phase pressure drop with heat flux for a range of mass fluxes, obtained from in-line pin fin surface tests with water, is shown in Figure 6.47. The same as other boiling tests the in-line pin-fin pressure drop is shown to increase with increasing heat flux. For all but the highest mass flux, the pressure drop is also shown to increase with mass flux. At heat fluxes larger than $180\ kW/m^2$, this trend occurs for the highest mass flux as well. As it was mentioned before, pressure drop increases with increasing mass and vapour content. For a constant heat flux, as the mass flux increases, the vapour content decreases, leading to the trends for lower heat fluxes. The R113 data for the same range of heat flux are much larger than the water data by a factor of about 5.

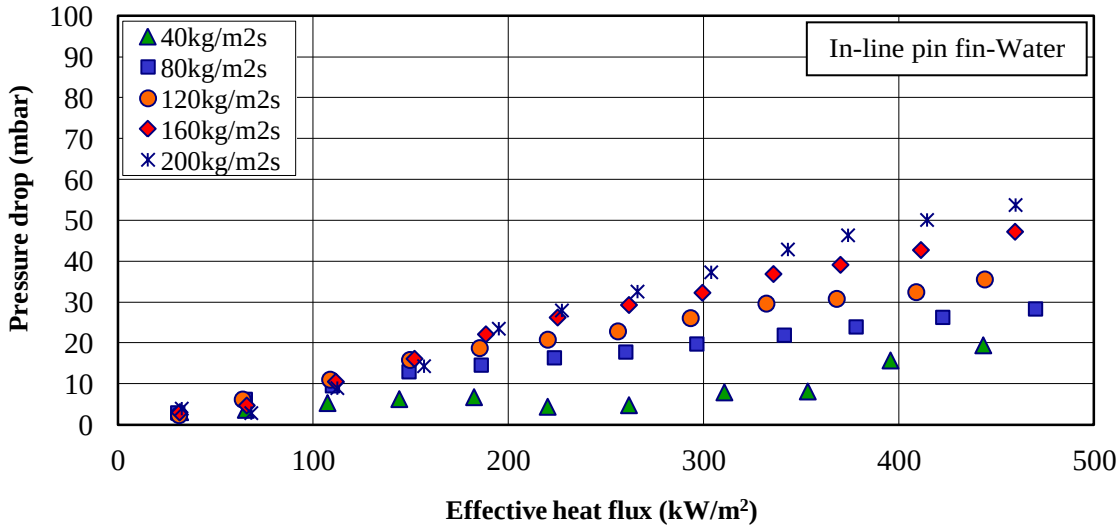

Figure 6.47 Variation of pressure drop with effective heat flux at various mass fluxes for in-line pin fin with deionised water

6.7 General Conclusion

Flow boiling heat transfer coefficient and pressure drop measurements in small-scale multi-channel geometries with and without interconnecting passages were investigated in this Chapter. It was found that, the saturated flow boiling heat transfer coefficients for all surfaces were similar in magnitude, with the plate channel surface values being lower, all dependent on heat flux and almost independent of mass flux and vapour mass fraction. This indicated that the dominant heat-transfer mechanism in the saturated boiling flow regime was nucleate boiling for all surfaces. The parallel channel and in-line and off-set pin-fin surfaces saturated flow boiling heat transfer coefficients were similar to within the experimental uncertainty and considerably higher than the plate channel surface data. Pin-fin surfaces and parallel channel surface areas were 75% and 50% larger than the plate channel surface respectively, and their heat-transfer coefficients were considerably larger, allowing a much lower surface temperature for the same heat flux. Thus, parallel channel and pin-fin surfaces improved the heat transfer by increasing the heat-transfer surface area and the heat-transfer coefficient.

For the plate and parallel channel surfaces isolated bubbles were generated at low heat fluxes, departed from the channels' walls and moved towards the channels outlet. With increasing the mass flux the speed of bubbles departure increased, while the bubbles

departure diameters were decreased. For a constant mass flux, as the heat flux increased the generated bubbles coalesced into larger sizes and formed the confined bubble (slug, and elongated bubble) and slug-annular flow regimes. For pin-fin surfaces the flow boiling behaviour is different. At low heat fluxes, the isolated bubbles were generated between the pin-fins, perpendicular to the flow direction. The isolated bubbles were expanded and started to move. The fins arrangement caused the bubbles move between the fins. At higher heat fluxes, bubbles were expanded, collated and elongated. These elongated bubbles moved between the fins, parallel and perpendicular to the flow direction. Pin-fins gave enhanced heat transfer because vapour trapped between the fins provided additional nucleation sites. Additionally, these spaces retained vapour for longer, giving enhanced heat transfer. For pin-fin surfaces three flow patterns were observed; bubbly slug (isolated bubbles/confined bubbles), gas-slug, and annular flows.

The two-phase pressure drops in the parallel channel and pin-fin surfaces were much larger than that for the plate. Thus, the reduction in wall temperature is achieved by a significant pressure drop penalty. The conclusions obtained from this chapter are stated in Chapter 8 in more details.

CHAPTER 7

DATA ANALYSIS

Single-phase and two-phase heat transfer coefficients and pressure drop measurements which were presented in Chapter 6, are analysed in this chapter. For the plate and parallel channel surfaces, several popular macro- and micro-channel correlations for the heat transfer coefficient and pressure drop were compared with the experimental data. For the in-line and in-line offset pin fin surfaces, as the geometries have some similarities with tube bundles, the data were compared to tube bundle standard methods for the heat transfer coefficient and pressure drop. Several macro-scale tube bundle and micro-pin-fin correlations were compared with these series of data.

7.1. Plate and Parallel Channel Surfaces

The comparison between the single-phase and two-phase experimental results and the predictions and empirical correlations for the plate and parallel channel surfaces are presented in this section.

7.1.1. Single-Phase Flow Heat Transfer Predictions

For the plate surface, Ansys CFX 11 was used to deduce the heat transfer coefficient. A two-dimensional simulation of a channel $70\,mm$ long and $1\,mm$ high was made. This allowed the $20\,mm$ of settling length upstream of the plate to be included. A uniform velocity inlet was assumed along with a constant pressure exit. The mesh size was systematically halved until the solution was independent of grid size. Temperature dependent fluid properties were used. The resultant predicted heat-transfer coefficients are shown in Figure 7.1. The agreement is reasonable.

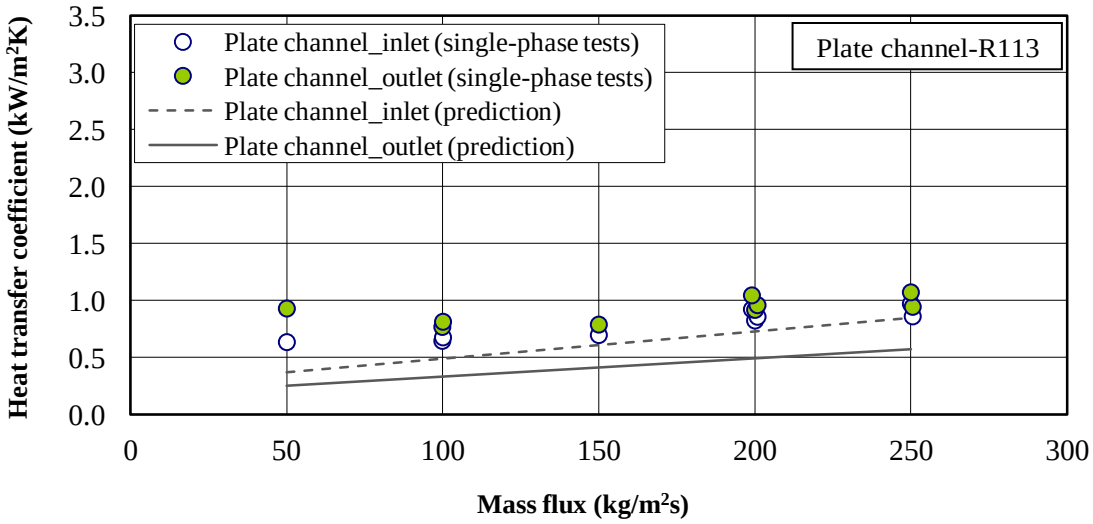

Figure 7.1 Comparison of single-phase heat transfer coefficient data with predictions for plate channel surface tests with R113

For the parallel surface, the single-phase heat transfer coefficient was evaluated from

$$h_{sp} = Nu\frac{k_f}{D_h} \tag{7.1}$$

where D_h is the hydraulic diameter of the channel in the presence of heat transfer process, given by

$$D_h = \frac{4H_{ch}W_{ch}}{2H_{ch}+W_{ch}} \tag{7.2}$$

Nu and k_f in Equation (7.1) represent the local Nusselt number and liquid thermal conductivity at the wall thermocouple sets locations, respectively. Nu is calculated from

$$Nu_{lam} = Constant(Nu_3) \qquad \text{for } Re_f < 2{,}000 \tag{7.3}$$

$$Nu_{tur} = 0.023Re_f^{0.8}Pr_f^{0.4} \qquad \text{for } Re_f \geq 2{,}000 \tag{7.4}$$

where Pr_f and Re_f are the liquid Prandtl number and Reynolds number based on local flow, i.e.,

$$Pr_f = \frac{C_{p,f}\mu_f}{k_f} \tag{7.5}$$

$$Re_f = \frac{GD_h}{\mu_f} \tag{7.6}$$

where $c_{p,f}$ is the liquid specific heat capacity at constant pressure, μ_f is the liquid dynamic viscosity, and G is the mass flux.

It should be noted that the shape of the parallel channels examined in the present study are rectangular with three walls heating, as the top wall is characteristically adiabatic, thus, Nu_3 in Equation (7.3) is the single-phase fully developed laminar Nusslet number for the condition of three wall heating (Shah and London, 1978) and is evaluated from

$$Nu_3 = 8.235(1 - 1.883\beta + 3.767\beta^2 - 5.814\beta^3 + 5.361\beta^4 - 2.0\beta^5) \tag{7.7}$$

While, the single-phase fully developed laminar Nusslet number for the condition of four wall heat transfer, Nu_4 (Shah and London, 1978), defined as

$$Nu_4 = 8.235(1 - 2.042\beta + 3.085\beta^2 - 2.477\beta^3 + 1.058\beta^4 - 0.186\beta^5) \tag{7.8}$$

where β is the ratio of channel depth to width

$$\beta = \frac{H_{ch}}{W_{ch}} \tag{7.9}$$

The parallel surface single-phase heat transfer coefficients were predicted and the resultant predicted values are shown in Figure 7.2. As is shown, the agreement between the obtained and predicted heat transfer coefficients is quite reasonable. As it was mentioned in Chapter 5 as well, parallel channel single-phase tests were carried out for Reynolds number in the range of $349 - 1104$, therefore the flow was laminar over the range tested and no discontinuity was observed in the heat transfer coefficients.

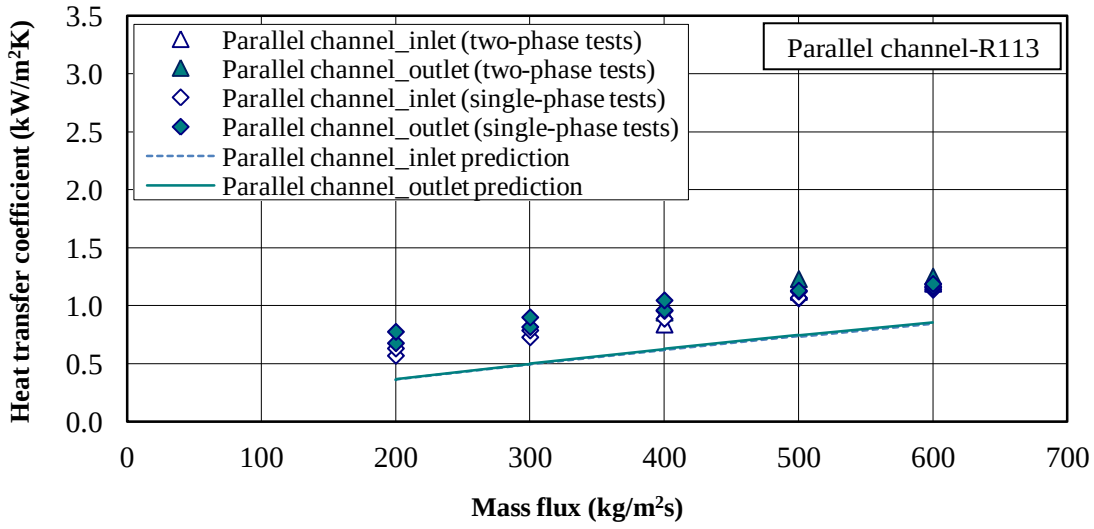

Figure 7.2 Comparison of single-phase heat transfer coefficient data with predictions for parallel channel surface tests with R113

7.1.2. Single-Phase Flow Pressure Drop Predictions

Since the differential pressure transducer was connected to the pressure tappings which were located just upstream and downstream of the test piece, the measured pressure drop just included the pressure drop across the test piece. Because of presence of a $2cm$ settling length before the test piece and small mass fluxes corresponding to the operating conditions which result the small inlet Reynolds number values, the inlet flow was assumed as fully developed flow. For single-phase tests the total predictive pressure drop across the test piece was just consisted of frictional component.

As it was mentioned in Chapter 6, the plate surface single-phase pressure drops were too small to be measured and compared. For the parallel channel surface, the total single-phase pressure drop evaluated from

$$\Delta P_{tot,sp} = \frac{2L_{ch}}{D_h} f_f G^2 \nu_f \tag{7.10}$$

where L_{ch} is the length of the channel, ν_f is specific volume of the liquid, and D_h is the hydraulic diameter in the absence of heat transfer process, given by

$$D_h = \frac{4H_{ch}W_{ch}}{2(H_{ch}+W_{ch})} \tag{7.11}$$

f_f in Equation (7.10) is the friction factor and evaluates from

$$f_f = \frac{24}{Re_f}[1 - 1.3553\beta + 1.9467\beta^2 - 1.7012\beta^3 + 0.9564\beta^4 - 0.2537\beta^5]$$

for $Re_f < 2{,}000$, (7.12a)

$f_f = 0.079 Re_f^{-0.25}$ for $2{,}000 \leq Re_f < 10^5$, and (7.12b)

$f_f = 0.046 Re_f^{-0.2}$ for $10^5 \leq Re_f < 10^6$ (7.12c)

Figure 7.3 shows the comparison of the resultant predicted single-phase pressure drops to the experimental data. The agreement between the obtained and predicted single-phase pressure drops is quite reasonable. At lower mass fluxes the agreement is better. As the mass flux increases the divergence increases. As is shown, both values are following similar linear functions with different slops. The measured values are slightly higher.

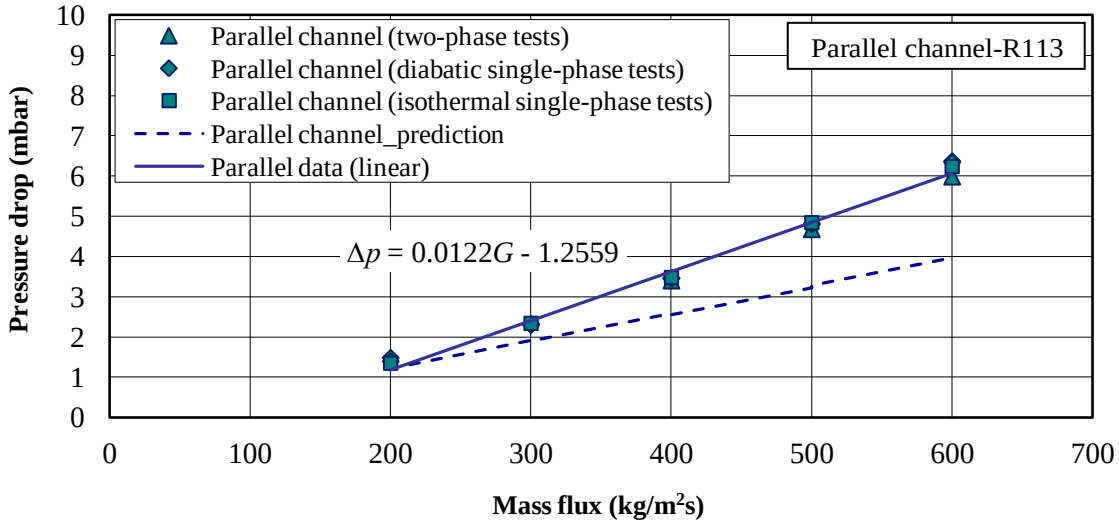

Figure 7.3 Comparison of single-phase pressure drop data with predictions for parallel channel surface tests with R113

7.1.3. Two-Phase Flow Heat Transfer Comparisons with Existing Correlations

For the plate and parallel channel surfaces, the obtained saturated flow boiling heat transfer coefficients were compared with several popular published correlations for conventional and unconventional scale channels. These correlations are summarized in Table 7.1. Most of these correlations were developed for circular tubes with uniform circumferential heating. Since the shape of channels examined in the present study are rectangular with three walls heating, as the top wall is characteristically adiabatic, the heat transfer coefficients were corrected using the following relation

$$h_{tp} = h_{tp,cor} \frac{Nu_3}{Nu_4} \tag{7.13}$$

where $h_{tp,cor}$ is the heat transfer coefficient directly evaluated from a correlation, and Nu_3 and Nu_4 are the single-phase fully developed laminar flow Nusselt numbers for the conditions of three and four walls heating, respectively, and evaluated from Equation (7.7) and (7.8) (Shah and London, 1978).

The first two correlations in Table 7.1, Mostinski (1963) and Cooper (1984) correlations are popular for determining the nucleate pool boiling heat transfer coefficients. The surface roughness parameter in Cooper correlation was chosen unity to remove the surface roughness dependency from the Cooper prediction. The next three correlations, Chen (1966); Kandlikar (1990) and Liu and Winterton (1991), are popular for determining the flow boiling heat transfer coefficient for macro-channels. The single-phase heat transfer coefficient term, h_{sp}, in these correlations is based on turbulent liquid flow prevalent in conventional channels, while in micro- and mini-scale channels the liquid is almost laminar. The last seven correlations, Lazarek and Black (1982); Tran et al. (1996); Lee and Lee (2001); Yu et al. (2002); Warrier et al. (2002); Kosar et al. (2005a) and Lee and Mudawar (2005b), are based on saturated flow boiling heat transfer in mini- and micro-channels. Notice that Lazarek and Black (1982); Tran et al. (1996) and Yu et al. (2002) correlations assume heat transfer is dominated by nucleate boiling, while two correlations of Kosar et al. (2005a) are based on nucleate and convective boiling and the three remaining correlations of Lee and Lee (2001); Warrier et al. (2002) and Lee and Mudawar (2005b) are based on a form similar to that of conventional channel correlations.

Table 7.1 Two-phase heat transfer coefficient correlations corresponding to the plate and parallel channel surfaces

Correlation number	Reference	Recommended channel size Heat transfer mechanism	Correlation
1	Mostinski (1963)	Conventional channels Nucleate boiling	$h_{nb} = 0.525\, P_{crit}^{0.69}\,(1.8P_r^{0.17} + 4P_r^{1.2} + 10P_r^{10})\, q"_{eff}^{0.7}\,[\frac{W}{m^2K}]$, $P_r = \frac{P}{P_{crit}}$ (reduced pressure)
2	Cooper (1984)	Conventional channels Nucleate boiling	$h_{nb} = 55P_r^{(0.12-0.2\log R_p)}\left(-log_{10}(P_r)\right)^{-0.55} M_W^{-0.5} q"_{eff}^{0.67}\left[\frac{W}{m^2K}\right]$ $P_r = \frac{P}{P_{crit}}$ (reduced pressure), $R_p = 1$ (surface roughness in micro-meter), M_W; molecular weight
3	Chen (1966) Edelstein et al. (1984)	Conventional channels Nucleate and Convective boiling	$h_{tp} = \frac{Nu_3}{Nu_4}(Eh_{sp} + Sh_{nb})$ $h_{sp} = Nu\frac{k_f}{D_h}$, Nu_{lam} = Constant (Refer to Eq. (7.7)), $Nu_{tur} = 0.023Re_f^{0.8}Pr_f^{0.4}$ $h_{nb} = 0.00122\left(\frac{k_f^{0.79}c_{p,f}^{0.45}v_g^{0.24}}{\sigma^{0.5}\mu_f^{0.29}h_{fg}^{0.24}v_f^{0.49}}\right)\Delta T_{sat}^{0.24}\Delta P_{sat}^{0.75}$ $E = \left(1 + \frac{1}{X^{0.5}}\right)^{1.78}$, $X = \left[(dp/dz)_f/(dp/dz)_g\right]^{0.5} = \left(\frac{f_f}{f_g}\right)^{0.5}\left(\frac{v_f}{v_g}\right)^{0.5}\left(\frac{1-x_e}{x_e}\right)$ $S = 0.9622 - 0.5822tan^{-1}\left(\frac{Re_f E^{1.25}}{6.18\times10^4}\right)$ $f_f = \frac{24}{Re_f}[1 - 1.3553\beta + 1.9467\beta^2 - 1.7012\beta^3 + 0.9564\beta^4 - 0.2537\beta^5]$ for $Re_f < 2{,}000$, $f_f = 0.079Re_f^{-0.25}$ for $2{,}000 \le Re_f < 10^5$, and $f_f = 0.046Re_f^{-0.2}$ for $10^5 \le Re_f < 10^6$ $f_g = \frac{24}{Re_g}[1 - 1.3553\beta + 1.9467\beta^2 - 1.7012\beta^3 + 0.9564\beta^4 - 0.2537\beta^5]$ for $Re_g < 2{,}000$, $f_g = 0.079Re_g^{-0.25}$ for $2{,}000 \le Re_g < 10^5$, and $f_g = 0.046Re_g^{-0.2}$ for $10^5 \le Re_g < 10^6$ $Re_f = \frac{G(1-x_e)D_h}{\mu_f}$, $Re_g = \frac{Gx_eD_h}{\mu_g}$, $Pr_f = \frac{C_{p,f}\mu_f}{k_f}$

Correlation number	Reference	Recommended channel size Heat transfer mechanism	Correlation
4	Kandlikar (1990)	Conventional channels Nucleate and Convective boiling	$h_{tp} = \frac{Nu_3}{Nu_4} max(E, S) h_{sp}$ $h_{sp} = Nu \frac{k_f}{D_h}$, Nu_{lam} = Constant (Refer to Eq. (7.7)), $Nu_{tur} = 0.023 Re_f^{0.8} Pr_f^{0.4}$ $E = 0.6683 Co^{-0.2} f(Fr_{fo}) + 1058 Bo^{0.7}$ (Convective boiling) $S = 1.136 Co^{-0.9} f(Fr_{fo}) + 667.2 Bo^{0.7}$ (Nucleate boiling) $Fr_{fo} = \frac{(G v_f)^2}{g D_h}$, $Bo = \frac{q''_{act}}{G h_{fg}}$, $Co = \left(\frac{1-x_e}{x_e}\right)^{0.8} \left(\frac{v_f}{v_g}\right)^{0.5}$ $f(Fr_{fo}) = 1$ $(Fr_{fo} \geq 0.04)$ or $f(Fr_{fo}) = (25 Fr_{fo})^{0.3}$ $(Fr_{fo} < 0.04)$
5	Liu and Winterton (1991)	Conventional channels Nucleate and Convective boiling	$h_{tp} = \frac{Nu_3}{Nu_4} ((E h_{sp})^2 + (S h_{nb})^2)^{0.5}$ $h_{sp} = Nu \frac{k_f}{D_h}$, Nu_{lam} = Constant (Refer to Eq. (7.7)), $Nu_{tur} = 0.023 Re_{fo}^{0.8} Pr_f^{0.4}$ $h_{nb} = 55 P_r^{0.12} (-log_{10}(P_r))^{-0.55} M_W^{-0.5} q''^{0.67}_{act}$, $P_r = \frac{P}{P_{crit}}$, M_W; molecular weight $E = \left(1 + x_e Pr_f \left(\frac{v_g}{v_f} - 1\right)\right)^{0.35}$ $S = \left(1 + 0.055 E^{0.1} Re_{fo}^{0.16}\right)^{-1}$ If $Fr_{fo} \leq 0.05$, replace E by $E Fr_{fo}^{0.1-2Fr_f}$ and S by $S Fr_{fo}^{0.5}$, respectively $Re_{fo} = \frac{G D_h}{\mu_f}$, $Fr_{f0} = \frac{(G v_f)^2}{g D_h}$
6	Lazarek and Black (1982)	Circular, $D_h = 3.15\ mm$ Nucleate boiling	$h_{tp} = \frac{Nu_3}{Nu_4} \left(30 Re_{f0}^{0.857} Bo^{0.714} \frac{k_f}{D_h}\right)$
7	Tran et al. (1996)	Circular, $D_h = 2.46\ mm$ Rectangular, $D_h = 2.4\ mm$ Nucleate boiling	$h_{tp} = \frac{Nu_3}{Nu_4} \left(8.4 \times 10^5 (Bo^2 We_{fo})^{0.3} \left(\frac{v_g}{v_f}\right)^{-0.4}\right)$, $We_{fo} = \frac{v_f G^2 D_h}{\sigma}$

Correlation number	Reference	Recommended channel size Heat transfer mechanism	Correlation
8	Lee and Lee (2001)	Rectangular, $D_h = 0.78 - 3.63\ mm$ Convective boiling	$h_{tp} = \frac{Nu_3}{Nu_4}(Eh_{sp})$ $h_{sp} = Nu\frac{k_f}{D_h}$, Nu_{lam} = Constant (Refer to Eq. (7.7)), $Nu_{tur} = 0.023Re_{fo}^{0.8}Pr_f^{0.4}$ $E = 10.3\beta^{0.398}\phi_f^{0.598}$ $\phi_f^2 = \left(1 + \frac{C}{X} + \frac{1}{X^2}\right)$, $C = 6.185 \times 10^{-2}Re_{fo}^{0.726}$, $X = \left[(dp/dz)_f/(dp/dz)_g\right]^{0.5} = \left(\frac{f_f}{f_g}\right)^{0.5}\left(\frac{v_f}{v_g}\right)^{0.5}\left(\frac{1-x_e}{x_e}\right)$ $f_f = \frac{24}{Re_f}[1 - 1.3553\beta + 1.9467\beta^2 - 1.7012\beta^3 + 0.9564\beta^4 - 0.2537\beta^5]$ for $Re_f < 2{,}000$, $f_f = 0.079Re_f^{-0.25}$ for $2{,}000 \le Re_f < 10^5$, and $f_f = 0.046Re_f^{-0.2}$ for $10^5 \le Re_f < 10^6$ $f_g = \frac{24}{Re_g}[1 - 1.3553\beta + 1.9467\beta^2 - 1.7012\beta^3 + 0.9564\beta^4 - 0.2537\beta^5]$ for $Re_g < 2{,}000$, $f_g = 0.079Re_g^{-0.25}$ for $2{,}000 \le Re_g < 10^5$, and $f_g = 0.046Re_g^{-0.2}$ for $10^5 \le Re_g < 10^6$
9	Yu et al. (2002)	Circular, $D_h = 2.98\ mm$ Nucleate boiling	$h_{tp} = \frac{Nu_3}{Nu_4}\left(6.4 \times 10^6(Bo^2We_{fo})^{0.24}\left(\frac{v_g}{v_f}\right)^{-0.2}\right)$, $We_{fo} = \frac{v_f G^2 D_h}{\sigma}$
10	Warrier et al. (2002)	5 parallel rectangular channels, $D_h = 0.75\ mm$ Sub-cooled and saturated nucleate boiling	$h_{tp} = \frac{Nu_3}{Nu_4}(Eh_{sp})$ $h_{sp} = Nu\frac{k_f}{D_h}$, Nu_{lam} = Constant (Refer to Eq. (7.7)), $Nu_{tur} = 0.023Re_{fo}^{0.8}Pr_f^{0.4}$ $E = 1 + 6Bo^{1/16} + f(Bo)x_e^{0.65}$ $f(Bo) = -5.3(1 - 855Bo)$

Correlation number	Reference	Recommended channel size Heat transfer mechanism	Correlation
11	Kosar et al. (2005a)	5 parallel rectangular channels, $D_h = 0.223\ mm$ Convective and nucleate boiling	(a) $h_{tp} = 4.068 \times 10^4 \left(Re_{fo}\right)^{0.12} (1 - x_e)^{0.8} \left(\frac{1-x_e}{x_e}\right)^{0.02}$ [in W/m^{2}K] Convective boiling (b) $h_{tp} = 1.068 q^{"0.64}$ [in W/m^{2}K] Nucleate boiling
12	Lee and Mudawar (2005b)	53 parallel rectangular channels, $D_h = 0.398\ mm$ Nucleate boiling and annular film evaporation (convective flow boiling)	If $0 \le x_e < 0.05$ $h_{tp} = 3.856 X^{0.267} h_{sp,f}$ If $0.05 \le x_e < 0.55$ $h_{tp} = 436.48\, Bo^{0.522} We_{fo}^{0.351} X^{0.665} h_{sp,f}$ If $0.55 \le x_e \le 1.0$ $h_{tp} = max\{(108.6\, X^{1.665} h_{sp,g}), h_{sp,g}\}$ $h_{sp,f} = Nu_3 \frac{k_f}{D_h}$ $h_{sp,g} = Nu \frac{k_g}{D_h}$, Nu_{lam} = Constant (Refer to Eq. (7.7)), $Nu_{tur} = 0.023 Re_g^{0.8} Pr_g^{0.4}$ $X = \left[(dp/dz)_f / (dp/dz)_g\right]^{0.5} = \left(\frac{f_f}{f_g}\right)^{0.5} \left(\frac{v_f}{v_g}\right)^{0.5} \left(\frac{1-x_e}{x_e}\right)$, $Bo = \frac{q"_{act}}{G h_{fg}}$, $We_{fo} = \frac{v_f G^2 D_h}{\sigma}$

Comparisons between predictions from the correlations and experimental data are shown in Figures 7.4 and 7.5 for plate and parallel channel surfaces, respectively. Figures include the root mean square error, RMS, for each correlation which defined as

$$RMS = \left[\frac{1}{N}\sum_{i=1}^{N}\varepsilon_i^2\right]^{\frac{1}{2}} \tag{7.14}$$

where N is the number of data point and ε is the error, evaluates from

$$\varepsilon = \frac{measured\ value - predicted\ value}{predicted\ value} \tag{7.15}$$

Apart from RMS, Table 7.2 includes average error for each correlation, which is defined as

$$Average\ error = \frac{1}{N}\sum_{i=1}^{N}\varepsilon_i \tag{7.16}$$

As can be seen in Figures 7.4 and 7.5, predictions of the correlations by Mostinski (1963) and Cooper (1984) for both surfaces are close to measurements. The nucleate boiling correlation of Mostinski (1963) under predicts the data for all mass fluxes, while the nucleate boiling correlation of Cooper (1984) under predicts the data for all mass fluxes at low heat fluxes and as the heat flux increases, reasonably predicts the data at higher heat fluxes and quality range.

The three macro-channel correlations of Chen (1966), Liu and Winterton (1991) and Kandlikar (1990) under predict most of the data. The predictions of the first two correlations, Chen (1966) and Liu and Winterton (1991), for both surfaces are reasonably close to the experimental data, as Liu and Winterton (1991) predicts parallel channel surface data with a RMS error of 21.32%. The nucleate boiling term of Liu and Winterton (1991) correlation is based on Cooper (1984) correlation and show a better agreement in compare with the other macro-scale channel correlations. The Kandlikar (1990) correlation predictions are quite dispersed. Although these correlations are based on macro-scale tubes and the size of tubes were used to develop these correlations are much larger than the present study channels' size, and also these correlations are based on turbulent single-phase heat transfer coefficients, since turbulent flow is prevalent in macro-scale channels, while flow in small channels is mostly laminar because of small channel size and

low flow rates, the agreement between the predictions and measurements indicating these correlations may be transferable for channels with hydraulic diameter of the order of $1\,mm$, although more surfaces will need to be tested before this can be stated conclusively.

For the last seven correlations which are based on saturated flow boiling heat transfer in mini- and micro-channels, predictions of the correlations by Lazarek and Black (1982) and Tran et al. (1996) are reasonably in a good agreement with the experimental data for both plate and parallel channel surfaces. These two correlations are based on nucleate boiling heat transfer in circular and rectangular channels with the hydraulic diameter of $d_h = 3.15$ and $2.41\,mm$, respectively. Correlation by Yu et al. (2002) is also based on nucleate boiling heat transfer in circular channel with a hydraulic diameter of $d_h = 2.98\,mm$, but predicts very large values for both surfaces compared to the data. The convective boiling correlation by Kosar et al. (2005a), Correlation 11(a), is based on micro-scale channels and predicts very large values for both surfaces. The nucleate boiling correlations by Warrier et al. (2002) and Kosar et al. (2005a), Correlations 10 and 11(b) respectively, are based on channels with hydraulic diameters smaller than $1\,mm$, and under predict data for both surfaces. The correlation by Mudawar (2005b), is based on nucleate and convective flow boiling and has been developed for channels with hydraulic diameters smaller than $1\,mm$. The last three named correlations by Warrier et al. (2002), Kosar et al. (2005a) and Mudawar (2005b) do not show good agreement with experimental data.

The correlations by Lazarek and Black (1982) and Tran et al. (1996), which are based on nucleate boiling heat transfer in channels with hydraulic diameters larger than $1\,mm$ provide the best agreement with the data among all seven correlations for small-scale channels. Lazarek and Black (1982) correlation shows the best agreement among all 12 tested correlations with an average error of 11.46% and 8.98%, for plate and parallel channel surfaces, respectively. The correlation by Cooper (1984) provides the second best agreement with the data among all correlations tested, with average errors of 12.90% and 12.81% for plate and parallel channel surfaces, respectively. This agreement shows that the heat transfer mechanism is dominated by nucleate boiling. It is worthy of note that Cooper (1984) correlation is a general correlation while the Lazarek and Black (1982)

correlation was derived for single condition and fluid (R113), So may not be as good for other fluids.

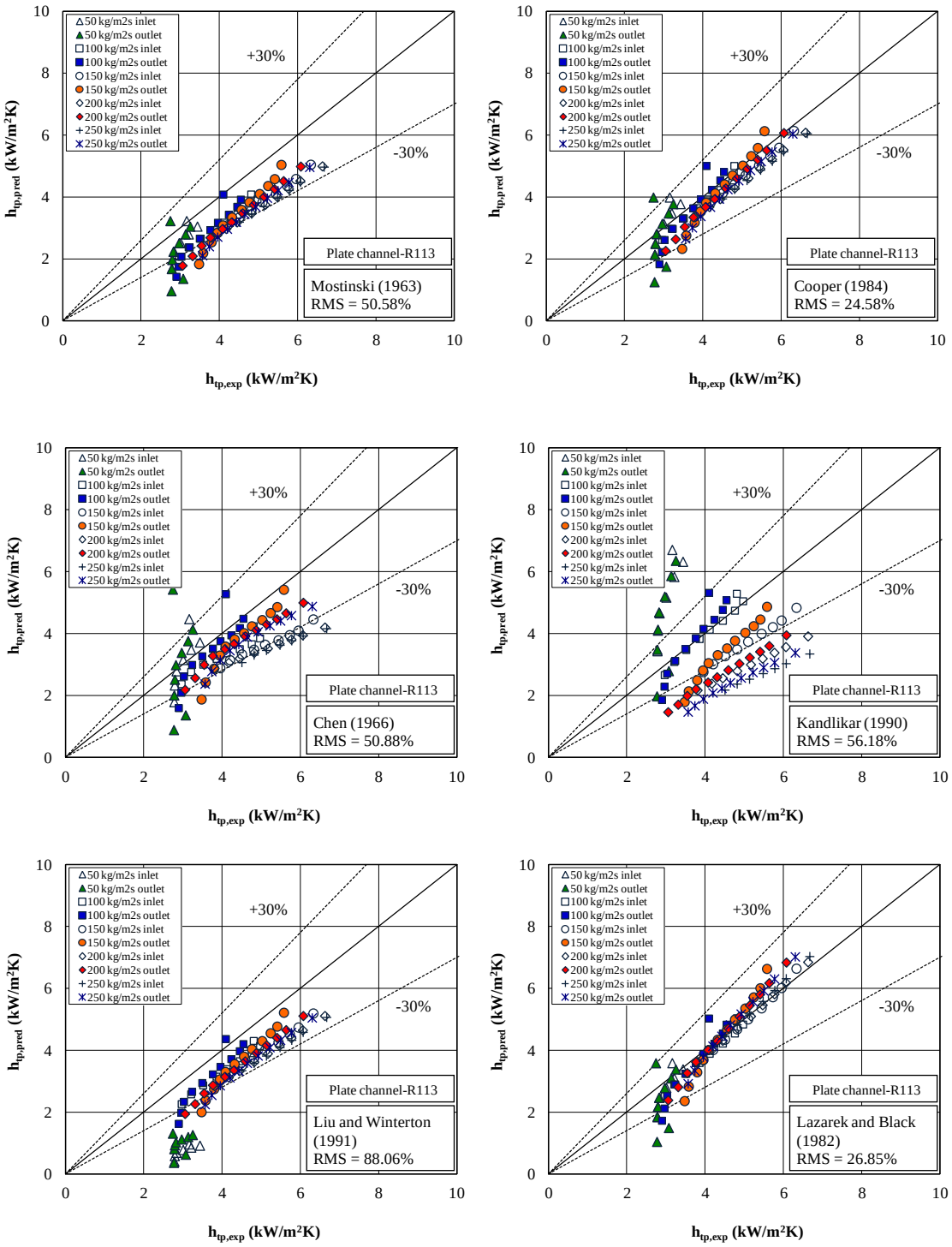

Figure 7.4 Saturated flow boiling heat transfer coefficients comparisons with existing correlations for plate channel surface tests with R113

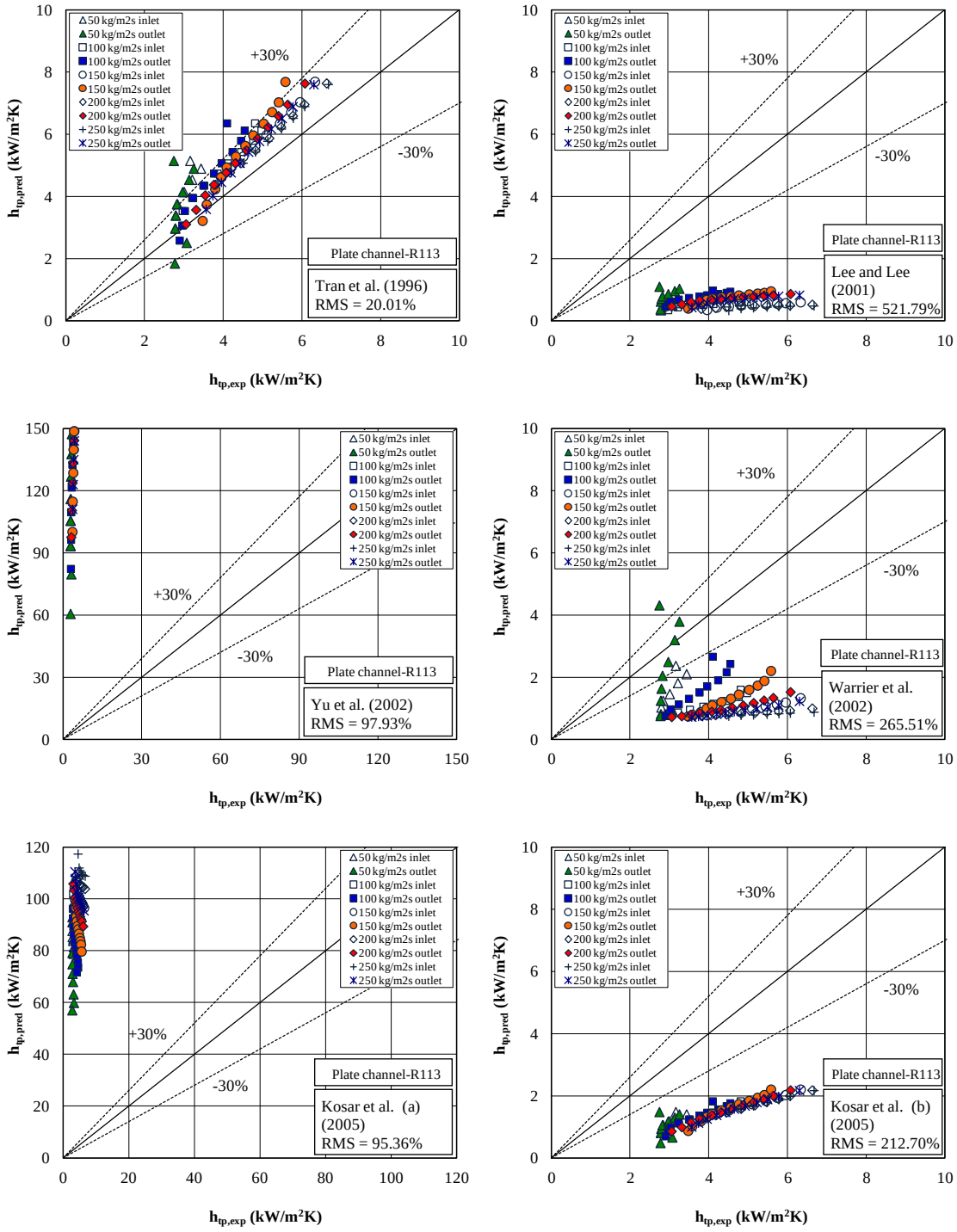

Figure 7.4 (continued) Saturated flow boiling heat transfer coefficients comparisons with existing correlations for plate channel surface tests with R113

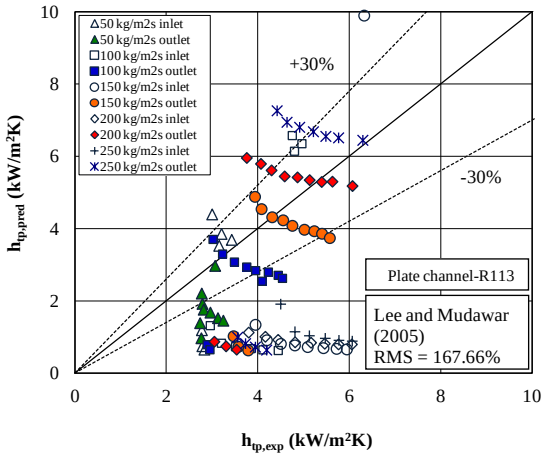

Figure 7.4 (continued) Saturated flow boiling heat transfer coefficients comparisons with existing correlations for plate channel surface tests with R113

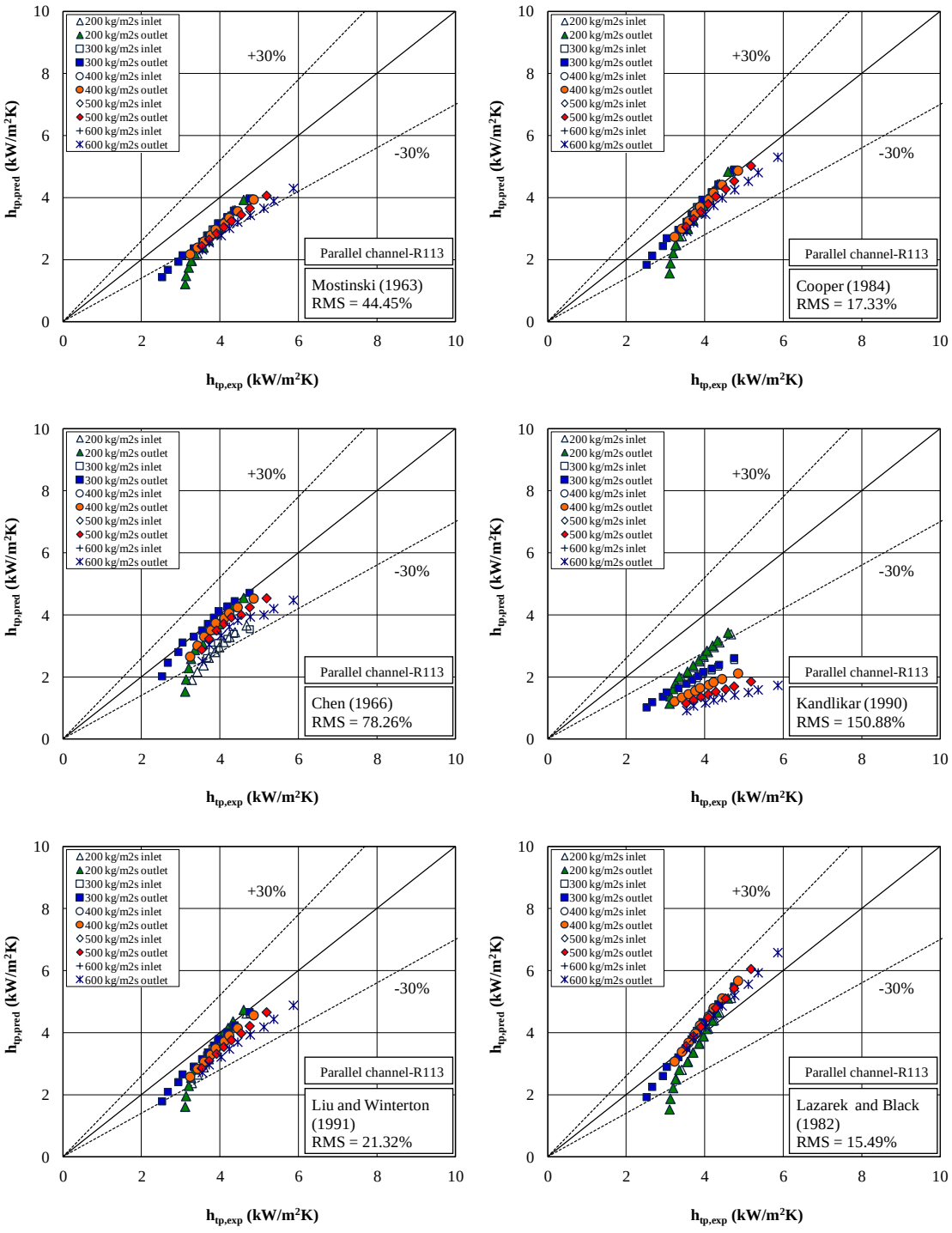

Figure 7.5 Saturated flow boiling heat transfer coefficients comparisons with existing correlations for parallel channel surface tests with R113

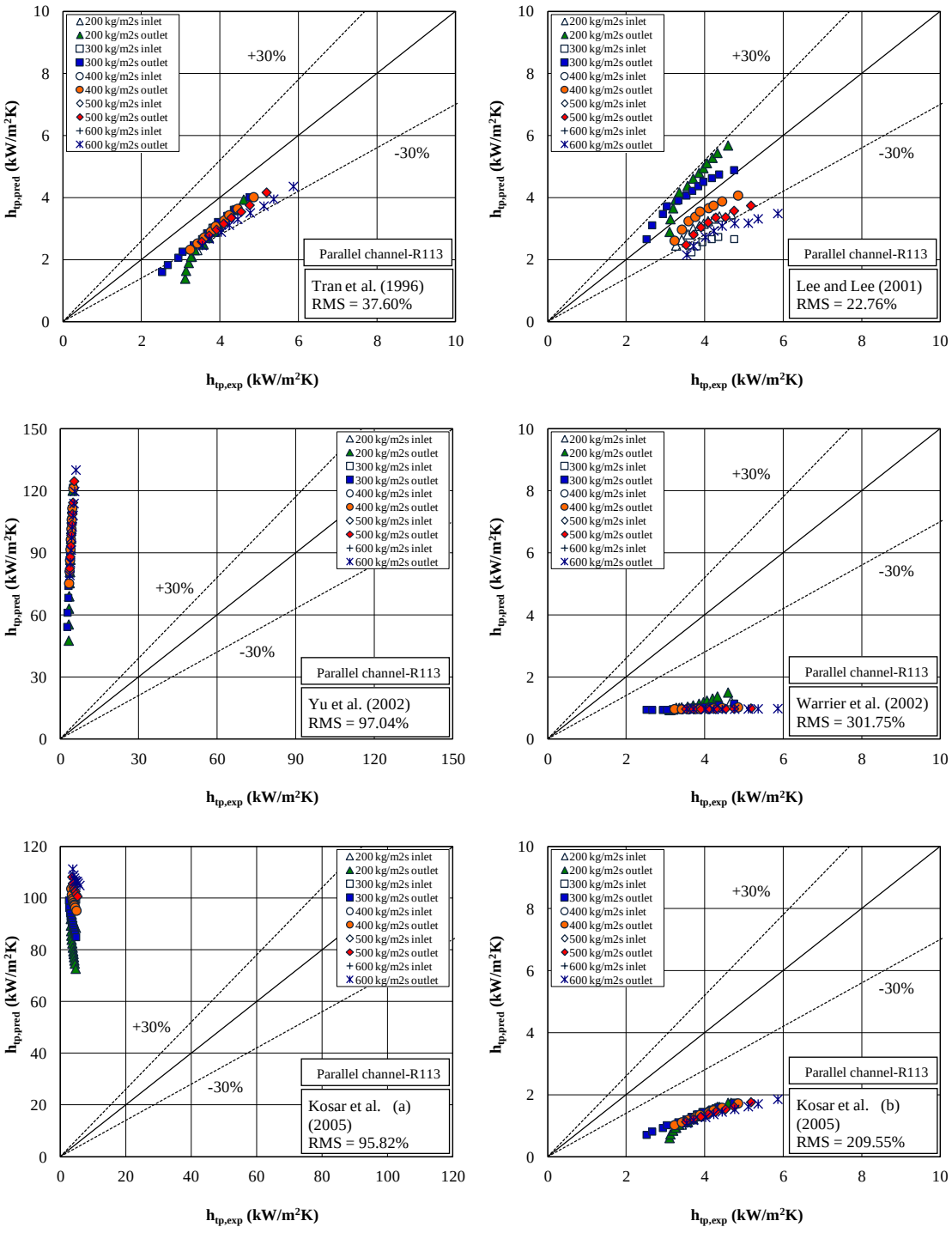

Figure 7.5 (continued) Saturated flow boiling heat transfer coefficients comparisons with existing correlations for parallel channel surface tests with R113

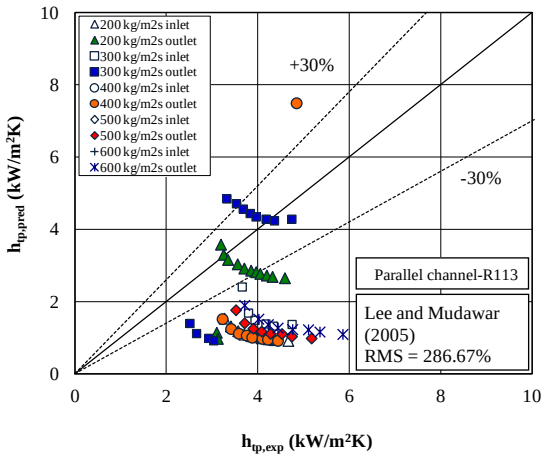

Figure 7.5 (continued) Saturated flow boiling heat transfer coefficients comparisons with existing correlations for parallel channel surface tests with R113

Table 7.2 Plate and parallel channel surfaces' RMS and average errors for comparisons between the Table 7.1 correlations predictions and experimental data

Corr.	Reference	Plate Channel		Parallel Channel	
		RMS Error%	Average Error%	RMS Error%	Average Error%
1	Mostinski (1963)	50.58	40.87	44.45	40.94
2	Cooper (1984)	24.58	12.90	17.33	12.81
3	Chen (1966) Edelstein et al. (1984)	50.88	36.06	78.26	75.29
4	Kandlikar (1990)	56.18	48.27	150.88	148.28
5	Liu and Winterton (1991)	88.06	74.52	21.32	17.57
6	Lazarek and Black (1982)	26.85	11.46	15.49	8.98
7	Tran et al. (1996)	20.01	14.71	37.60	35.27
8	Lee and Lee (2001)	521.79	517.48	22.76	21.74
9	Yu et al. (2002)	97.93	97.92	97.04	97.03
10	Warrier et al. (2002)	265.51	250.99	301.75	298.17
11a	Kosar et al. (2005a) (Convective boiling)	95.36	95.35	95.82	95.82
11b	Kosar et al. (2005a) (Nucleate boiling)	212.70	203.93	209.55	206.98
12	Lee & Mudawar (2005b)	167.66	77.50	143.73	115.90

7.1.4. Two-Phase Flow Pressure Drop Predictions

For two-phase tests, working liquid was delivered into the test piece in a sub-cooled state and divided the test piece into upstream single-phase and downstream two-phase regions, Figure 5.1(b). Therefore the total predictive test piece pressure drop can be expressed as;

$$\Delta P_{\mathrm{tot,tp}} = \Delta P_{\mathrm{sp}} + \Delta P_{\mathrm{tp}} \tag{7.17}$$

where ΔP_{sp} and ΔP_{tp} are the single-phase and the two-phase regions pressure drops, respectively. As it was mentioned, because of the presence of the $2cm$ settling length before the test piece and the small channel size and low flow rates, the upstream single-phase region is assumed as fully developed region. Thus, for the plate and parallel channel surfaces, the upstream single-phase pressure drop is evaluated by Equation (7.10), where L_{ch} is substituted with the length of the upstream single-phase region, L_{sub}. Therefore upstream single-phase pressure drop is given by

$$\Delta P_{sp} = \frac{2L_{sub}}{D_h} f_f G^2 \nu_f \tag{7.18}$$

The two-phase region pressure drop consists of frictional and accelerational components which are predicted from the simultaneous integration of the pressure gradient, $\frac{dP}{dz}$, and the differential form of energy equation. This approach allows the variation of physical properties to be included. Therefore the two-phase region pressure drop is given by

$$\Delta P_{\mathrm{tp}} = \int_{L_{sub}}^{L_{ch}} \left(\frac{dP}{dz}\right)_{tp} dz \tag{7.19}$$

where $\left(\frac{dP}{dz}\right)_{tp}$ is evaluated from

$$\left(\frac{dP}{dz}\right)_{tp} = \left(\frac{dP}{dz}\right)_{F} + \left(\frac{dP}{dz}\right)_{A} \tag{7.20}$$

where $\left(\frac{dP}{dz}\right)_{F}$ is the pressure gradient due to friction and $\left(\frac{dP}{dz}\right)_{A}$ is the pressure gradient due to acceleration. Differential form of energy equation is given by

$$\frac{dx_e}{dz} = \frac{q_{eff}}{Gh_{fg}H_{ch}} \tag{7.21}$$

The two-phase frictional pressure gradient, $\left(\frac{dP}{dz}\right)_F$, in Equation (7.20) is obtained from the two-phase multiplier method of Chisholm (1983), with the single-phase pressure gradient, $\left(\frac{dP}{dz}\right)_f$, found from laminar channel flow theory. Therefore $\left(\frac{dP}{dz}\right)_F$ is evaluated from

$$\left(\frac{dP}{dz}\right)_F = \left(\frac{dP}{dz}\right)_f \phi_f^2 \tag{7.22}$$

where the single-phase pressure gradient, $\left(\frac{dP}{dz}\right)_f$, is obtained from

$$\left(\frac{dP}{dz}\right)_f = \frac{2(1-x_e)^2}{D_h} f_f G^2 \nu_f \tag{7.23}$$

where x_e is thermodynamic equilibrium quality and f_f is friction factor based on local liquid flow rate and is evaluated from Equation (7.12). Reynolds number, Re_f in Equation (7.12) is based on local liquid flow, therefore for two-phase region is evaluated from

$$Re_f = \frac{G(1-x_e)D_h}{\mu_f} \tag{7.24}$$

ϕ_f^2 in Equation (7.22) is two-phase frictional multiplier based on local liquid flow rate and was obtained from method of Chisholm (1983), i.e.,

$$\phi_f^2 = \left(1 + \frac{C}{X} + \frac{1}{X^2}\right) \tag{7.25}$$

where C is Martinelli-Chisholm constant and is evaluated from Table 7.3.

Table 7.3 Values of C in Equation (7.25)

Regime	X	Liquid	Gas	C
(vv)	X_{vv}	Laminar	Laminar	5
(tv)	X_{tv}	Turbulent	Laminar	10
(vt)	X_{vt}	Laminar	Turbulent	12
(tt)	X_{tt}	Turbulent	Turbulent	20

X in Equation (7.25) is Martinelli parameter and is evaluated from

$$X = \left[(dp/dz)_f/(dp/dz)_g\right]^{0.5} \tag{7.26}$$

where $(dp/dz)_f$ and $(dp/dz)_g$ are the single-phase liquid and vapour pressure gradients, respectively, based on local flow. $(dp/dz)_f$ is calculated from Equation (7.23), while $(dp/dz)_g$ is evaluated from

$$\left(\frac{dP}{dz}\right)_g = \frac{2{x_e}^2}{D_h} f_g G^2 v_g \tag{7.27}$$

where v_g is vapour specific volume and f_g is friction factor based on local vapour flow rate and given by

$$f_g = \frac{24}{Re_g}[1 - 1.3553\beta + 1.9467\beta^2 - 1.7012\beta^3 + 0.9564\beta^4 - 0.2537\beta^5]$$

for $Re_g < 2{,}000$, (7.28a)

$f_g = 0.079Re_g^{-0.25}$ for $2{,}000 \leq Re_g < 10^5$, and (7.28b)

$f_g = 0.046Re_g^{-0.2}$ for $10^5 \leq Re_g < 10^6$ (7.28c)

where Re_g is the Reynolds number based on local vapour flow rate, i.e.,

$$Re_g = \frac{G x_e D_h}{\mu_g} \tag{7.29}$$

Substituting Equations (7.23) and (7.27) into Equation (7.26) gives the general Equation of X as,

$$X = \left(\frac{f_f}{f_g}\right)^{0.5} \left(\frac{v_f}{v_g}\right)^{0.5} \left(\frac{1-x_e}{x_e}\right) \tag{7.30}$$

By substituting Equations (7.12) and (7.28) into Equation (7.30) for different liquid and vapour flow regimes, Equation (7.30) can be expressed as following equations;

$$X_{vv} = \left(\frac{\mu_f}{\mu_g}\right)^{0.5} \left(\frac{v_f}{v_g}\right)^{0.5} \left(\frac{1-x_e}{x_e}\right)^{0.5} \tag{7.31a}$$

$$X_{vt} = \left(\frac{f_f}{f_g}\right)^{0.5} \left(\frac{v_f}{v_g}\right)^{0.5} \left(\frac{1-x_e}{x_e}\right) \tag{7.31b}$$

$$X_{tt} = \left(\frac{\mu_f}{\mu_g}\right)^{0.1} \left(\frac{v_f}{v_g}\right)^{0.5} \left(\frac{1-x_e}{x_e}\right)^{0.9} \tag{7.31c}$$

The acceleration pressure drop, $\left(\frac{dP}{dz}\right)_A$, in Equation (7.20) was obtained from the integration of acceleration pressure gradient based on the homogeneous equilibrium flow model, i.e.,

$$\left(\frac{dP}{dz}\right)_A = G^2 \frac{dv_m}{dz} \tag{7.32}$$

where v_m is the mean specific volume of the homogeneous fluid and is evaluated from

$$v_m = \frac{x_e^2}{\alpha} v_g + \frac{(1-x_e)^2}{(1-\alpha)} v_f \tag{7.33}$$

where α is the void fraction given by

$$\alpha = \frac{x_e v_g}{x_e v_g + (1-x_e) v_f} \tag{7.34}$$

The two-phase pressure drops for both plate and parallel channel surfaces were predicted and the resultant predicted values are shown in Figures 7.6 and 7.7, respectively. For the plate surface the agreement between the measured and predicted values is reasonable. The plate surface predicted two-phase pressure drop components for different flow rates and heat fluxes are presented in Table F.1, Appendix F. The acceleration component accounts for up to 84% of the total, and is always significantly higher than the corresponding friction component. Thus, the homogeneous equilibrium flow model is shown to be reasonable for plate channel surface.

For the parallel surface, Figure 7.7, the agreement between the measured and predicted two-phase pressure drop is reasonable at low heat fluxes and is not too bad at higher heat fluxes. As the heat flux increases, the vapour quality increases. On one hand, increasing in vapour quality in such small-scale channels increases both static and dynamic instabilities such as, density wave, flow pattern transition and oscillations. On the other hand rapid bubble growth cause back flows at high

vapour quality. Thus, these instabilities and back flows cause the measured two-phase pressure drop at high heat fluxes becomes higher than the predicted values obtained from the homogeneous equilibrium flow model. For the parallel surface the predicted two-phase pressure drop components are presented in Table F.2, Appendix F. Similar to the plate surface, the predictions are dominated by acceleration component, accounting for up to 75% of the total. As the parallel channel's hydraulic diameter is smaller than the plate channel, for similar mass fluxes the surface tension forces are higher, therefore the percentage of the parallel surface friction components is higher than the plate surface ones.

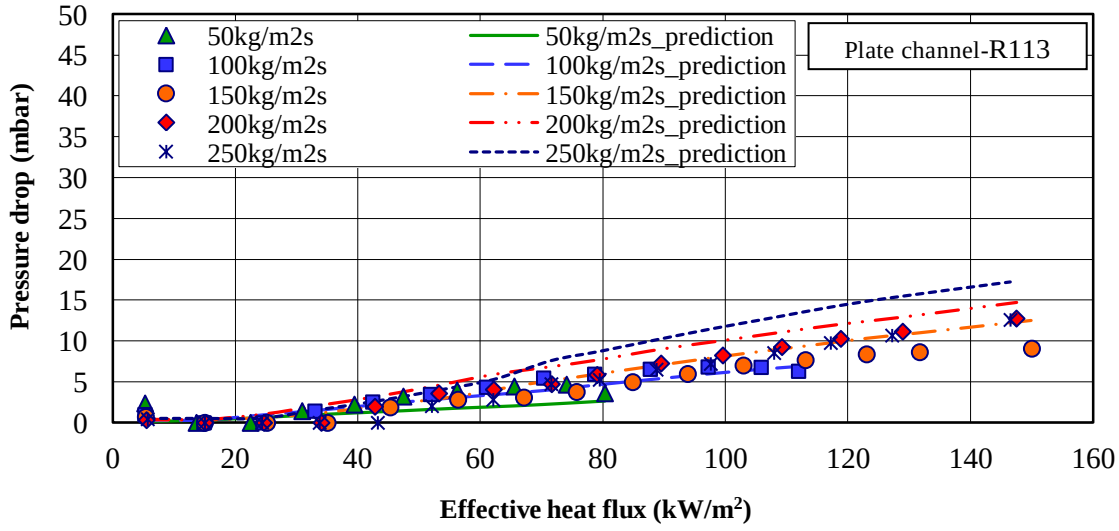

Figure 7.6 Comparison of two-phase pressure drop data with predictions for plate channel surface tests with R113

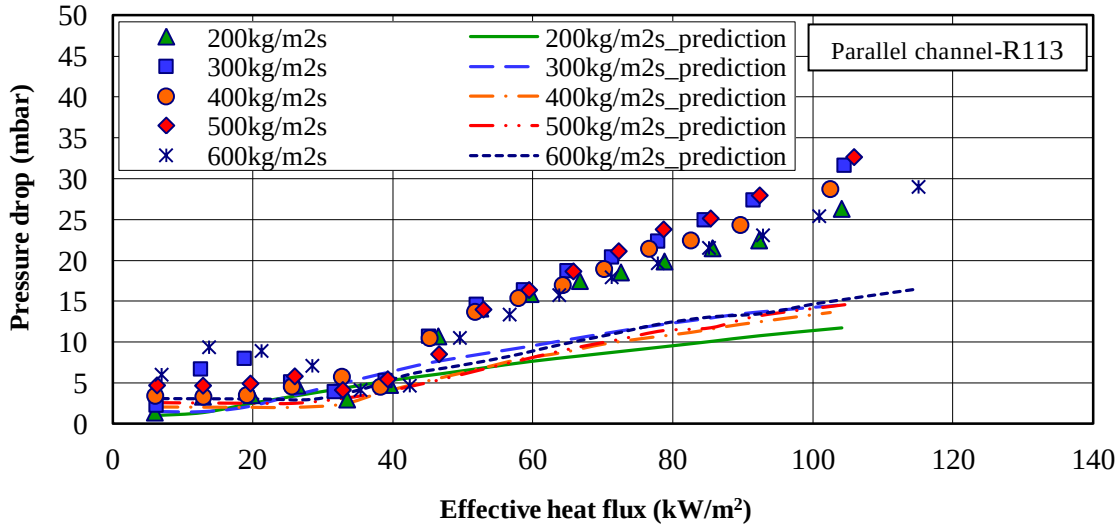

Figure 7.7 Comparison of two-phase pressure drop data with predictions for parallel channel surface tests with R113

7.1.5. Two-Phase Flow Pressure Drop Comparisons with Existing Correlations

The two-phase pressure drops obtained in the current study for plate and parallel channel surfaces were compared with nine published empirical correlations, Table 7.4. The correlations were developed based on the homogeneous equilibrium flow model and the separated flow model and evaluate both friction and acceleration pressure drop components.

The first three correlations in Table 7.4, Homogeneous model (Collier and Thome, 1994); Lockhart-Martinelli (Lockhart and Martinelli, 1949; Chisholm, 1983) and Friedel (1979), are popular for determining the two-phase pressure drop for macro-channels. Homogeneous model correlation (Collier and Thome, 1994) is based on the homogeneous equilibrium flow model, while the other two are based on the separated flow model and evaluate acceleration pressure drop component using Martinelli void fraction correlation. The homogeneous equilibrium flow model considers the two-phase mixture behaves as a single-phase fluid possessing mean fluid properties, while the separated flow model considers the two-phase mixture separated into two streams of liquid and vapour phases with different mean velocities.

The next four correlations in Table 7.4, Mishima and Hibiki (1996); Tran et al. (2000); Lee and Lee (2001) and Yu et al. (2002), are based on the separated flow model and were developed based on mini-channels data, channels with the hydraulic diameter of $0.8\,mm$ up to $6.7\,mm$. The Zivi (1964) void fraction correlation was used in all these correlations to evaluate acceleration pressure drop component. The last two correlations in Table 7.4, Qu and Mudawar (2003c) and Lee and Mudawar (2005a), are based on the separated flow model and were developed based on the micro-channels data, channels with hydraulic diameter of $0.35\,mm$.

Table 7.4 Two-phase pressure drop correlations corresponding to the plate and parallel channel surfaces

Correlation number	Reference, Remarks	Frictional Component, $\Delta P_{tp,F}$	Accelerational Component, $\Delta P_{tp,A}$
1	Homogeneous model (Collier and Thome, 1994)	$\Delta P_{tp,F} = \frac{2 f_{tp} G^2 L_{tp} v_f}{D_h}\left[1 + \frac{x_{e,out}}{2}\left(\frac{v_{fg}}{v_f}\right)\right], \quad f_{tp} = 0.003$	$\Delta P_{tp,A} = G^2 v_f x_{e,out}$
2	Lockhart-Martinelli (Lockhart and Martinelli, 1949; Chisholm, 1983) Fluids: water, benzene, kerosene, oil, etc. $D_h = 1.49 - 25.83\ mm$	$\Delta P_{tp,F} = \frac{L_{sat}}{x_{e,out}} \int_{x_{e,0}}^{x_{e,out}} \frac{2 f_f G^2 (1-x_e)^2 v_f}{D_h} \phi_f^2\, dx_e$ $f_f = \frac{24}{Re_f}[1 - 1.3553\beta + 1.9467\beta^2 - 1.7012\beta^3 + 0.9564\beta^4 - 0.2537\beta^5]$ for $Re_f < 2{,}000$, $f_f = 0.079 Re_f^{-0.25}$ for $2{,}000 \le Re_f < 10^5$, and $f_f = 0.046 Re_f^{-0.2}$ for $10^5 \le Re_f < 10^6$ $\phi_f^2 = \left(1 + \frac{C}{X} + \frac{1}{X^2}\right)$ $X = \left[(dp/dz)_f / (dp/dz)_g\right]^{0.5} = \left(\frac{f_f}{f_g}\right)^{0.5}\left(\frac{v_f}{v_g}\right)^{0.5}\left(\frac{1-x_e}{x_e}\right)$ $f_g = \frac{24}{Re_g}[1 - 1.3553\beta + 1.9467\beta^2 - 1.7012\beta^3 + 0.9564\beta^4 - 0.2537\beta^5]$ for $Re_g < 2{,}000$, $f_g = 0.079 Re_g^{-0.25}$ for $2{,}000 \le Re_g < 10^5$, and $f_g = 0.046 Re_g^{-0.2}$ for $10^5 \le Re_g < 10^6$ $Re_f = \frac{G(1-x_e)D_h}{\mu_f}, \quad Re_g = \frac{G x_e D_h}{\mu_g}$	$\Delta P_{tp,A} = G^2 v_f \left[\frac{x_{e,out}^2}{\alpha_{out}}\left(\frac{v_g}{v_f}\right) + \frac{(1-x_{e,out})^2}{1-\alpha_{out}} - 1\right]$ $\alpha_{out} = 1 - \frac{1}{\sqrt{1 + \frac{C}{X} + \frac{1}{X^2}}}$ Regime / Liquid / Gas / C (vv) / Laminar / Laminar / 5 (tv) / Turbulent / Laminar / 10 (vt) / Laminar / Turbulent / 2 (tt) / Turbulent / Turbulent / 20

Correlation number	Reference, Remarks	Frictional Component, $\Delta P_{tp,F}$	Accelerational Component, $\Delta P_{tp,A}$
3	Friedel (1979) $D_h \geq 4\ mm$	$\Delta P_{tp,F} = \frac{2 f_{fo} G^2 v_f}{D_h} \frac{L_{sat}}{x_{e,out}} \int_{x_{e,0}}^{x_{e,out}} \phi_{fo}^2\ dx_e$ $\phi_{fo}^2 = A_1 + \frac{3.24 A_2 A_3}{Fr_H^{0.045} We_H^{0.035}}$ $A_1 = (1-x_e)^2 + x_e^2 \left(\frac{v_g}{v_f}\right)\left(\frac{\mu_g}{\mu_f}\right),\ A_2 = x_e^{0.78}(1-x_e)^{0.224}$ $A_3 = \left(\frac{v_g}{v_f}\right)^{0.91} \left(\frac{\mu_g}{\mu_f}\right)^{0.19} \left(1-\frac{\mu_g}{\mu_f}\right)^{0.7}$ $Fr = \frac{G^2}{g D_h \bar{\rho}_f^2},\quad We = \frac{G^2 D_h}{\bar{\rho}_f \sigma},\ \bar{\rho} = \frac{1}{x_e v_g + (1-x_e) v_f}$ $f_{fo} = \frac{24}{Re_{fo}}[1 - 1.3553\beta + 1.9467\beta^2 - 1.7012\beta^3 + 0.9564\beta^4 - 0.2537\beta^5]$ for $Re_{fo} < 2{,}000$, $f_{fo} = 0.079 Re_{fo}^{-0.25}$ for $2{,}000 \leq Re_{fo} < 10^5$, and $f_{fo} = 0.046 Re_{fo}^{-0.2}$ for $10^5 \leq Re_{fo} < 10^6$	$\Delta P_{tp,A} = G^2 v_f \left[\frac{x_{e,out}^2}{\alpha_{out}}\left(\frac{v_g}{v_f}\right) + \frac{(1-x_{e,out})^2}{1-\alpha_{out}} - 1\right]$ $\alpha_{out} = 1 - \frac{1}{\sqrt{1 + \frac{C}{X} + \frac{1}{X^2}}}$ Regime / Liquid / Gas / C (vv) / Laminar / Laminar / 5 (tv) / Turbulent / Laminar / 10 (vt) / Laminar / Turbulent / 12 (tt) / Turbulent / Turbulent / 20
4	Mishima and Hibiki (1996) Fluid: air-water mixture, $D_h = 1 - 4\ mm$	$\Delta P_{tp,F} = \frac{L_{sat}}{x_{e,out}} \int_{x_{e,0}}^{x_{e,out}} \frac{2 f_f G^2 (1-x_e)^2 v_f}{D_h} \phi_f^2\ dx_e$ $\phi_f^2 = \left(1 + \frac{C}{X} + \frac{1}{X^2}\right)$ $C = 21[1 - \exp(-0.319 \times 10^3 D_h)]$ $X = \left[(dp/dz)_f / (dp/dz)_g\right]^{0.5} = \left(\frac{f_f}{f_g}\right)^{0.5} \left(\frac{v_f}{v_g}\right)^{0.5} \left(\frac{1-x_e}{x_e}\right)$	$\Delta P_{tp,A} = G^2 v_f \left[\frac{x_{e,out}^2}{\alpha_{out}}\left(\frac{v_g}{v_f}\right) + \frac{(1-x_{e,out})^2}{1-\alpha_{out}} - 1\right]$ $\alpha_{out} = \frac{1}{1 + \left(\frac{1-x_{e,out}}{x_{e,out}}\right)\left(\frac{v_f}{v_g}\right)^{2/3}}$

Correlation number	Reference, Remarks	Frictional Component, $\Delta P_{tp,F}$	Accelerational Component, $\Delta P_{tp,A}$
5	Tran et al. (2000) Fluid: R-134a, R-12, and R-113 Two circular tubes: $D = 2.46\ and\ 2.92$ And a rectangular tube: $D_h = 2\ mm$ $(4.06 \times 1.7\ mm)$	$\Delta P_{tp,F} = \frac{2 f_{fo} G^2 v_f}{D_h} \frac{L_{sat}}{x_{e,out}} \int_{x_{e,0}}^{x_{e,out}} \phi_{fo}^2\, dx_e$ $\phi_{fo}^2 = 1 + (4.3\Gamma^2 - 1)\left[N_{conf} x_e^{0.875} (1 - x_e)^{0.875} + x_e^{1.75}\right]$ $\Gamma = \left(\frac{v_g}{v_f}\right)^{0.5} \left(\frac{\mu_g}{\mu_f}\right)^{0.5}$, $N_{conf} = \left[\frac{\sigma}{g(\rho_f - \rho_g)}\right]^{0.5} / D_h$ $f_{fo} = \frac{24}{Re_{fo}} [1 - 1.3553\beta + 1.9467\beta^2 - 1.7012\beta^3 + 0.9564\beta^4 - 0.2537\beta^5]$ for $Re_{fo} < 2{,}000$, $f_{fo} = 0.079 Re_{fo}^{-0.25}$ for $2{,}000 \le Re_{fo} < 10^5$, and $f_{fo} = 0.046 Re_{fo}^{-0.2}$ for $10^5 \le Re_{fo} < 10^6$ $Re_{fo} = \frac{G D_h}{\mu_f}$	$\Delta P_{tp,A} = G^2 v_f \left[\frac{x_{e,out}^2}{\alpha_{out}} \left(\frac{v_g}{v_f}\right) + \frac{\left(1 - x_{e,out}\right)^2}{1 - \alpha_{out}} - 1\right]$ $\alpha_{out} = \frac{1}{1 + \left(\frac{1 - x_{e,out}}{x_{e,out}}\right)\left(\frac{v_f}{v_g}\right)^{2/3}}$
6	Lee and Lee (2001) Fluid: R-113 Wide horizontal rectangular channels: $D_h = 0.78, 6.67\ mm$ $(0.4 - 2\ mm \times 20\ mm)$	$\Delta P_{tp,F} = \frac{L_{sat}}{x_{e,out}} \int_{x_{e,0}}^{x_{e,out}} \frac{2 f_f G^2 (1 - x_e)^2 v_f}{D_h} \phi_f^2\, dx_e$ $\phi_f^2 = \left(1 + \frac{C}{X} + \frac{1}{X^2}\right)$ $C = 6.185 \times 10^{-2} Re_{fo}^{0.726}$ $X = \left[(dp/dz)_f / (dp/dz)_g\right]^{0.5} = \left(\frac{f_f}{f_g}\right)^{0.5} \left(\frac{v_f}{v_g}\right)^{0.5} \left(\frac{1 - x_e}{x_e}\right)$	$\Delta P_{tp,A} = G^2 v_f \left[\frac{x_{e,out}^2}{\alpha_{out}} \left(\frac{v_g}{v_f}\right) + \frac{\left(1 - x_{e,out}\right)^2}{1 - \alpha_{out}} - 1\right]$ $\alpha_{out} = \frac{1}{1 + \left(\frac{1 - x_{e,out}}{x_{e,out}}\right)\left(\frac{v_f}{v_g}\right)^{2/3}}$

Correlation number	Reference, Remarks	Frictional Component, $\Delta P_{tp,F}$	Accelerational Component, $\Delta P_{tp,A}$
7	Yu et al. (2002) Fluid: Water A circular horizontal tube, $D_h = 2.98\ mm$	$\Delta P_{tp,F} = \frac{L_{sat}}{x_{e,out}} \int_{x_{e,0}}^{x_{e,out}} \frac{2 f_f G^2 (1-x_e)^2 v_f}{D_h} \phi_f^2\ dx_e$ $\phi_f^2 = \frac{1}{X^{1.9}}$ $X = \left[(dp/dz)_f / (dp/dz)_g\right]^{0.5} = \left(\frac{f_f}{f_g}\right)^{0.5} \left(\frac{v_f}{v_g}\right)^{0.5} \left(\frac{1-x_e}{x_e}\right)$	$\Delta P_{tp,A} = G^2 v_f \left[\frac{x_{e,out}^2}{\alpha_{out}} \left(\frac{v_g}{v_f}\right) + \frac{\left(1-x_{e,out}\right)^2}{1-\alpha_{out}} - 1\right]$ $\alpha_{out} = \frac{1}{1 + \left(\frac{1-x_{e,out}}{x_{e,out}}\right) \left(\frac{v_f}{v_g}\right)^{2/3}}$
8	Qu and Mudawar (2003c) Fluid: Water 21 parallel rectangular micro-channels, $D_h = 0.349\ mm$ $(231 \times 713\ \mu m)$	$\Delta P_{tp,F} = \frac{L_{sat}}{x_{e,out}} \int_{x_{e,0}}^{x_{e,out}} \frac{2 f_f G^2 (1-x_e)^2 v_f}{D_h} \phi_f^2\ dx_e$ $\phi_f^2 = \left(1 + \frac{C}{X} + \frac{1}{X^2}\right)$ $C = 21[1 - \exp(-0.319 \times 10^3 D_h)](0.00418G + 0.0613)$ $X = \left[(dp/dz)_f / (dp/dz)_g\right]^{0.5} = \left(\frac{f_f}{f_g}\right)^{0.5} \left(\frac{v_f}{v_g}\right)^{0.5} \left(\frac{1-x_e}{x_e}\right)$	$\Delta P_{tp,A} = G^2 v_f \left[\frac{x_{e,out}^2}{\alpha_{out}} \left(\frac{v_g}{v_f}\right) + \frac{\left(1-x_{e,out}\right)^2}{1-\alpha_{out}} - 1\right]$ $\alpha_{out} = \frac{1}{1 + \left(\frac{1-x_{e,out}}{x_{e,out}}\right) \left(\frac{v_f}{v_g}\right)^{2/3}}$
9	Lee and Mudawar (2005a) Fluid: R-134a 53 parallel rectangular micro-channels, $D_h = 0.349\ mm$ $(231 \times 713\ \mu m)$	$\Delta P_{tp,F} = \frac{L_{sat}}{x_{e,out}} \int_{x_{e,0}}^{x_{e,out}} \frac{2 f_f G^2 (1-x_e)^2 v_f}{D_h} \phi_f^2\ dx_e$ $\phi_f^2 = \left(1 + \frac{C}{X} + \frac{1}{X^2}\right)$ $C_{vv} = 2.16 Re_{fo}^{0.047} We_{fo}^{0.6}, \quad C_{vt} = 1.45 Re_{fo}^{0.25} We_{fo}^{0.23}$ $X = \left[(dp/dz)_f / (dp/dz)_g\right]^{0.5} = \left(\frac{f_f}{f_g}\right)^{0.5} \left(\frac{v_f}{v_g}\right)^{0.5} \left(\frac{1-x_e}{x_e}\right)$	$\Delta P_{tp,A} = G^2 v_f \left[\frac{x_{e,out}^2}{\alpha_{out}} \left(\frac{v_g}{v_f}\right) + \frac{\left(1-x_{e,out}\right)^2}{1-\alpha_{out}} - 1\right]$ $\alpha_{out} = \frac{1}{1 + \left(\frac{1-x_{e,out}}{x_{e,out}}\right) \left(\frac{v_f}{v_g}\right)^{2/3}}$

The comparison between two-phase pressure drop predictions from these correlations and experimental data is shown in Figures 7.8 and 7.9 for both plate and parallel channel surfaces, respectively. These figures include the RMS error, defined by Equation 7.14, for each correlation. Both the RMS and average errors for comparisons between the correlations predictions and experimental data, for each correlation are shown in Table 7.5. In addition to the correlations comparisons, the comparisons between the two-phase pressure drops predictions presented in section 7.1.4, and experimental data are included in Figures 7.8 and 7.9 for both surfaces.

As is shown in Figures 7.8 and 7.9, the Homogeneous flow model (Collier and Thome, 1994) predicts very small values for both surfaces, compared to the experimental data. The correlation of Lockhart-Martinelli (Lockhart and Martinelli, 1949; Chisholm, 1983) reasonably predicts the experimental data at low heat fluxes. As the heat flux increase, the Lockhart-Martinelli (Lockhart and Martinelli, 1949; Chisholm, 1983) correlation over predicts the experimental data for plate channel surface and under predicts the data for parallel channel surface. The Friedel (1979) correlation over predict most of the data for both surfaces. As can be seen among all these three popular macro-channel correlations, better agreement is achieved with the Lockhart-Martinelli (Lockhart and Martinelli, 1949; Chisholm, 1983) correlation, with an average error of 17.11%, for the plate channel surface, while for the parallel channel surface, Friedel (1979) correlation shows better agreement among all these three macro-channel correlations with an average error of 31.46%. A possible reason is that the Lockhart-Martinelli correlation was developed for both laminar and turbulent flow, while the Friedel (1979) correlation was developed for turbulent flow, which is prevalent in macro-channels, while according to the size of the mini-channels and tests' low flow rates, the mini-channels dominated by mostly laminar flow for the liquid phase and laminar or turbulent flow for the vapour phase. But for the parallel channel tests, back flow occurred, which caused some instabilities and fluctuations and increased the pressure drop. Therefore this better agreement between the Friedel (1979) correlation and parallel channel surface data resulted from these resultant higher pressure drops.

The correlation of Mishima and Hibiki (1996) accounts for channel size effect by incorporating channel hydraulic diameter in the Martinelli-Chisholm constant C. For the Lee and Lee (2001) correlation, the liquid Reynolds number, Re_{fo}, which contains the effect of both channel size and liquid flow rate, is in corporate into the Martinelli-Chisholm constant C. Both Mishima and Hibiki (1996) and Lee and Lee (2001) correlations reasonably predict the experimental data at low heat fluxes. As the heat flux increase, the correlations over predict the experimental data for plate channel surface and under predict the data for parallel channel surface. Both correlations show a quite better agreement with the plate channel surface data. Correlations of Tran et al. (2000) and Yu et al. (2002) under predict data for all heat and mass fluxes. For the parallel channel surface, correlation of Yu et al. (2002) predicts very small values compared to the data.

Predictions of Qu and Mudawar (2003c) and Lee and Mudawar (2005a) correlations, for plate channel surface are close to measurements at low heat fluxes. At higher heat fluxes both correlations over predict the data for plate channel surface. For parallel channel surface, both correlations under predict most of the data with a reasonable agreement. With an average error of 4.07% and 20.18% for the plate and parallel channel surfaces respectively, the correlation of Qu and Mudawar (2003c) yields the most accurate predictions among the all previous correlations in total, Table 7.5.

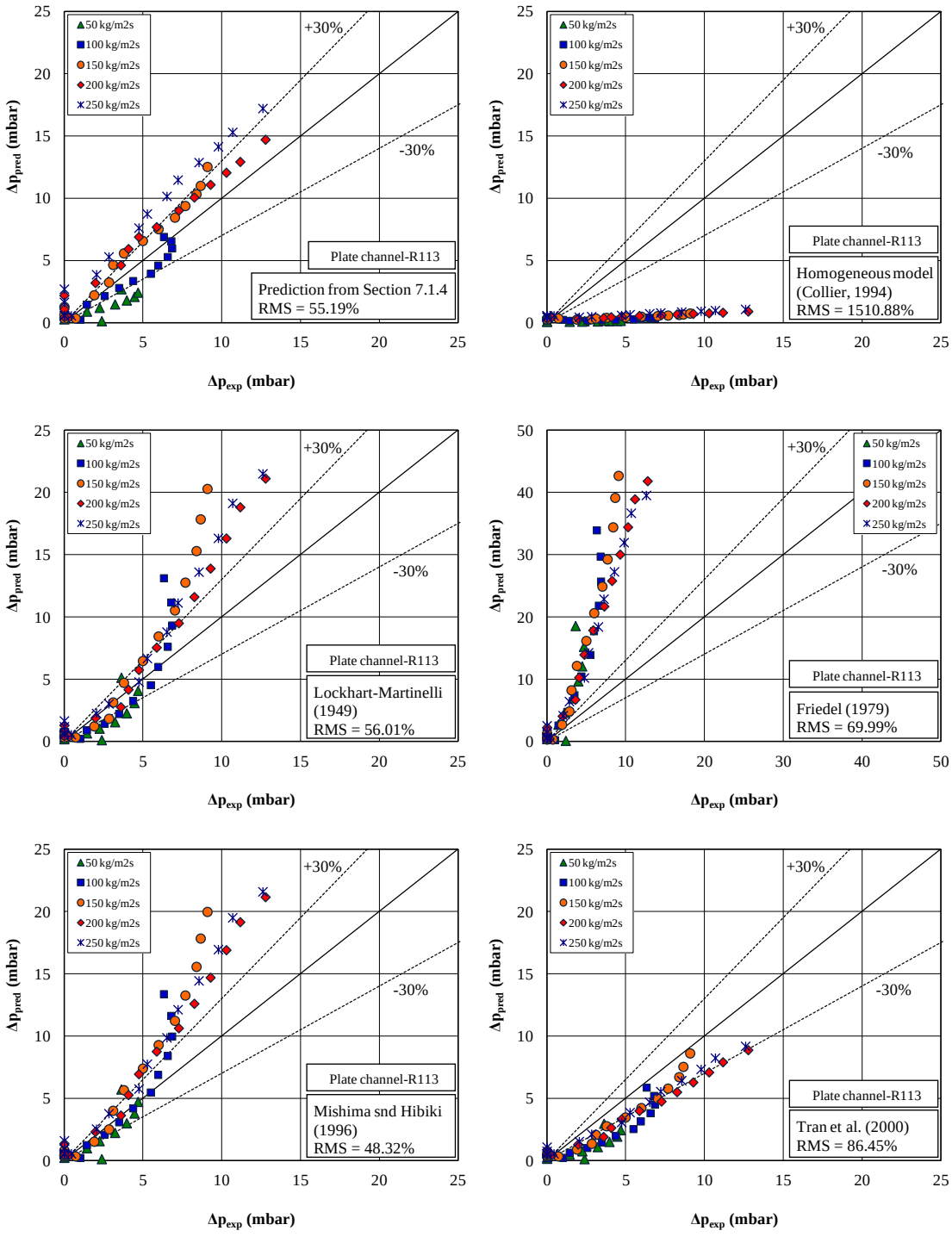

Figure 7.8 Pressure drop comparisons with existing correlations for plate channel surface tests with R113

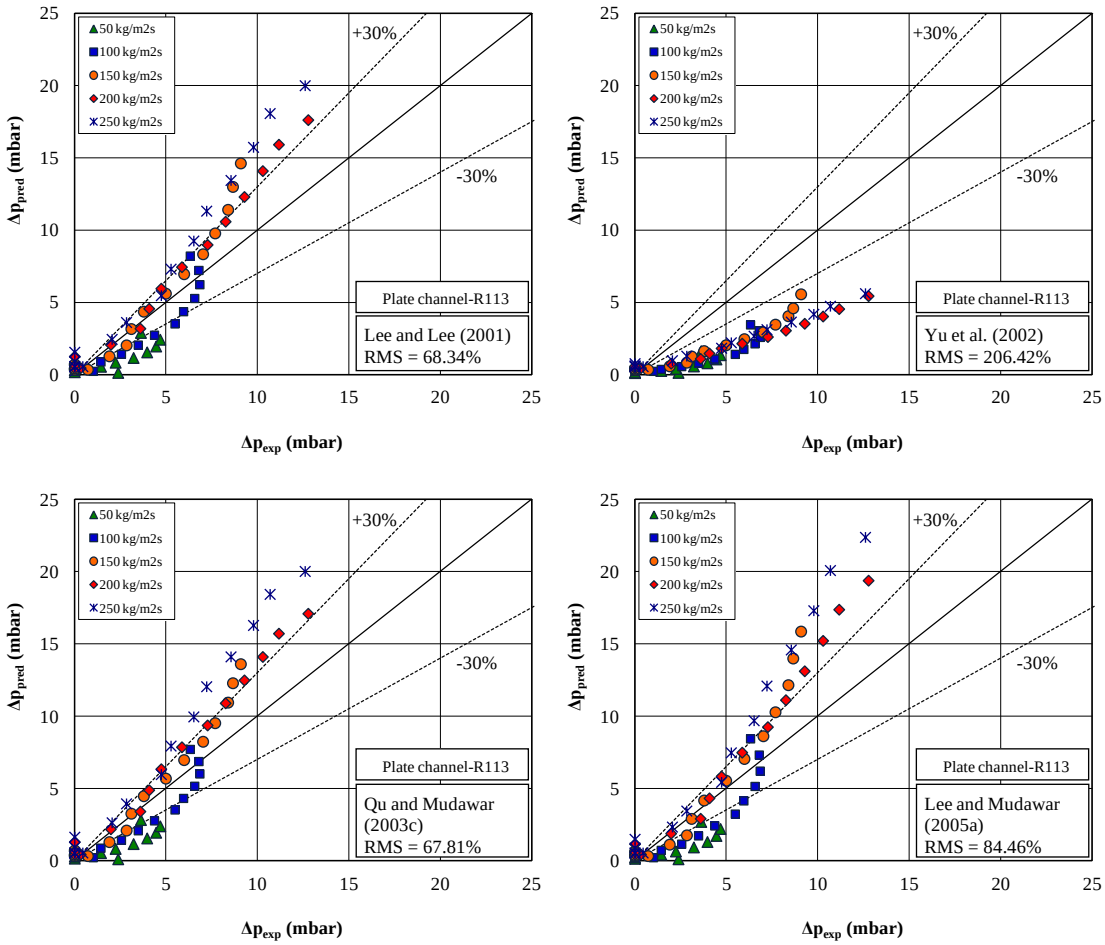

Figure 7.8 (continued) Pressure drop comparisons with existing correlations for plate channel surface tests with R113

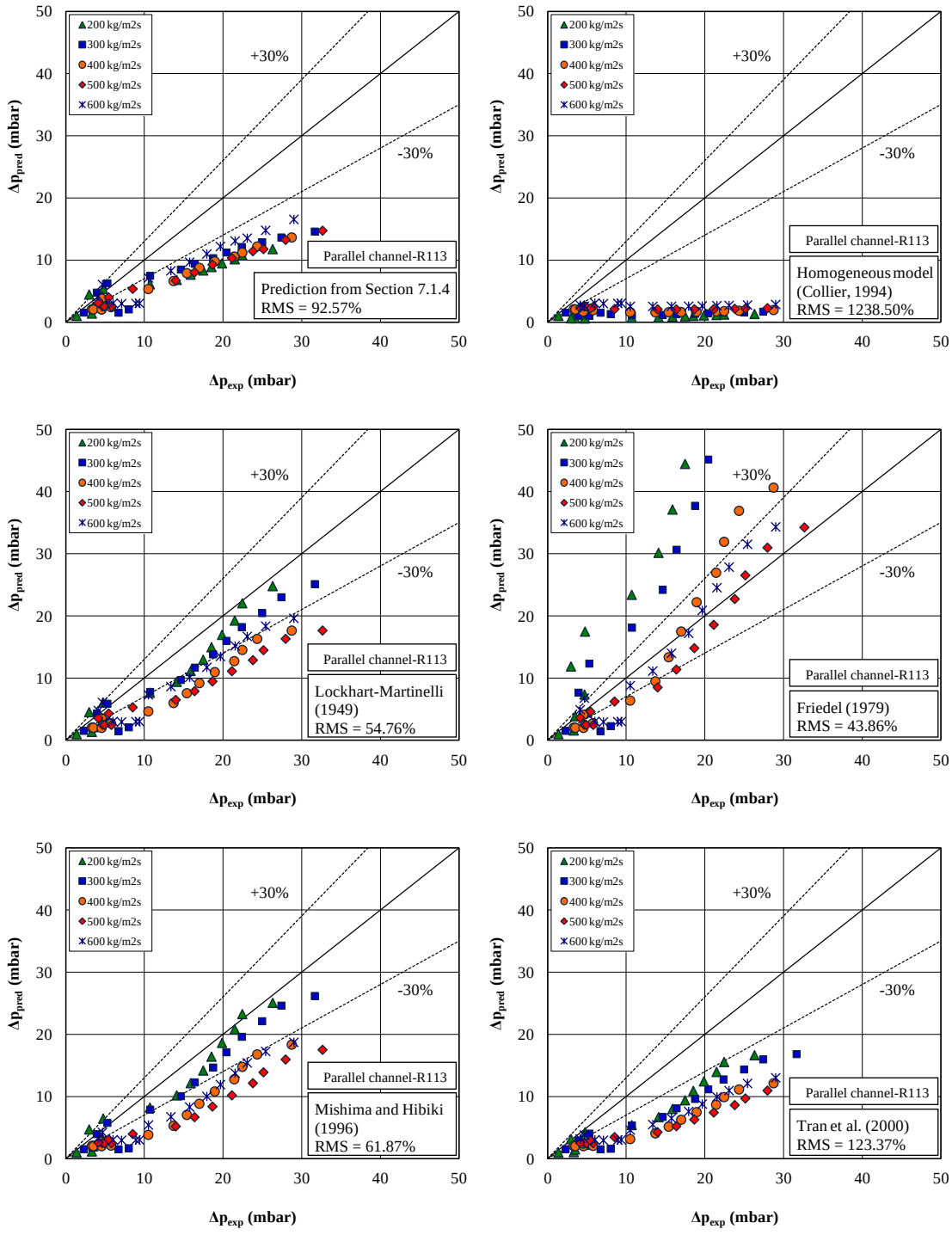

Figure 7.9 Pressure drop comparisons with existing correlations for parallel channel surface tests with R113

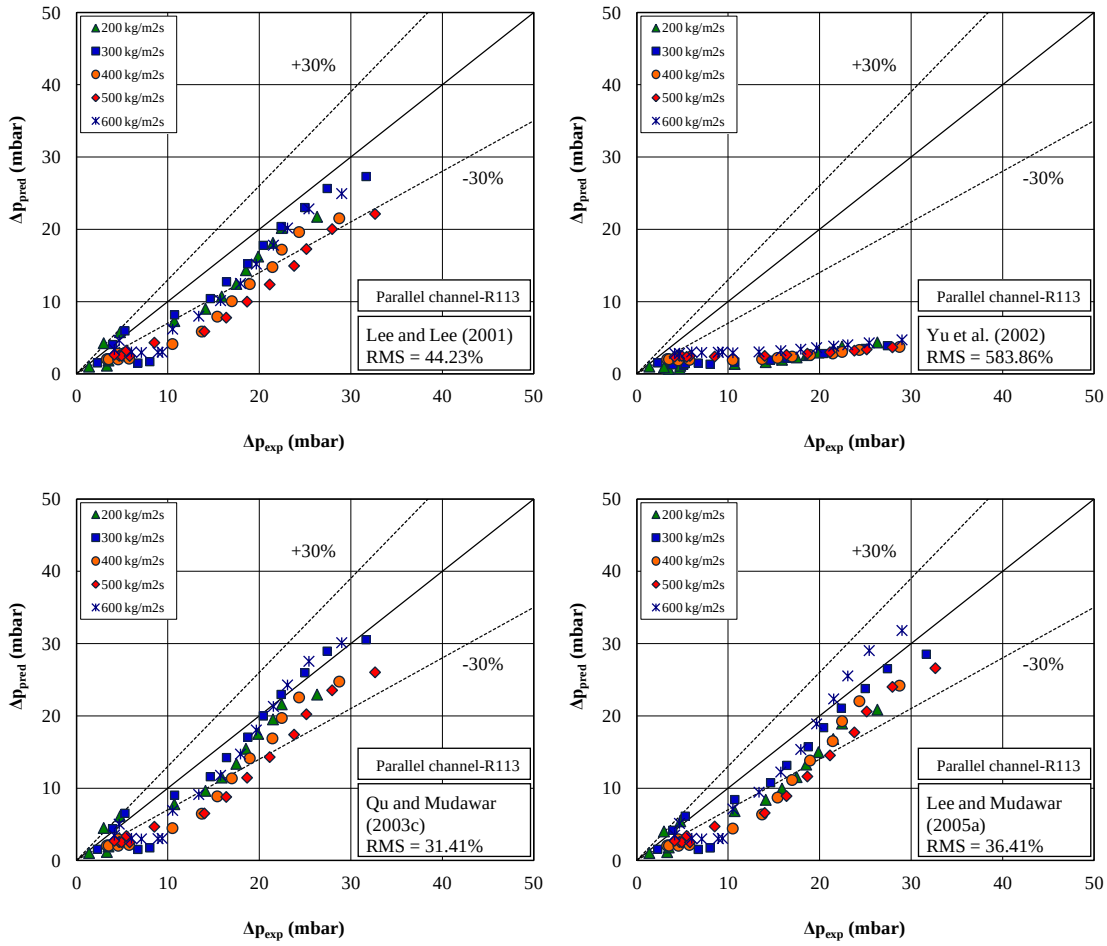

Figure 7.9 (continued) Pressure drop comparisons with existing correlations for parallel channel surface tests with R113

Table 7.5 Plate and parallel channel surfaces' RMS and average errors for comparisons between the Table 7.4 correlations predictions and experimental data

	Reference	Plate Channel		Parallel Channel	
		RMS Error%	Average Error%	RMS Error%	Average Error%
1	Homogeneous model	1510.88	1186.66	1238.50	1168.89
2	Lockhart-Martinelli (1949)	56.01	17.11	54.76	45.40
3	Friedel (1979)	69.99	67.76	43.86	31.46
4	Mishima and Hibiki (1996)	48.32	31.12	61.87	47.76
5	Tran et al. (2000)	86.45	41.95	123.37	113.49
6	Lee and Lee (2001)	68.34	2.62	44.23	35.09
7	Yu et al. (2002)	206.41	146.28	583.86	573.88
8	Qu and Mudawar (2003c)	67.81	4.07	31.41	20.18
9	Lee and Mudawar (2005a)	84.45	4.55	36.41	26.10

7.2. In-Line and In-Line Off-Set Pin-Fin Surfaces

The comparison between the single-phase and two-phase experimental results and predictions and empirical correlations for the in-line and in-line off-set pin fin surfaces are presented in this section. For clarity the two pin fin surfaces, are hereafter referred to as in-line and off-set.

7.2.1. Single-Phase Flow Heat Transfer Predictions

For the in-line and off-set pin-fin surfaces, the single-phase heat transfer coefficient method of ESDU (1973) was used to predict the obtained experimental results. The ESDU (1973) method was deduced for convective heat transfer of cross-flow over tube banks of circular cylinders under conditions of negligible thermal radiation and zero heat generation within the fluid. However, the case of forced convection heat transfer is covered in this method, but no data are available to cover the combined forced and free (mixed) convection heat transfer. The method defined as 'Mean Heat-Transfer Data for Separate Rows' was used to predict the single-phase heat transfer coefficients for particular rows at the wall inlet and outlet locations. When free convection effect can be ignored, the Nusselt number can be related to the flow parameters, fluid properties and tube bank geometry and can be expressed as

$$\overline{Nu} = Nu_r \times F_1 \times F_3 \times F_4 \tag{7.35}$$

where F_1, F_3, and F_4 are the fluid property variation factor, tube inclination factor, and row to row variation in Nusselt number factor, respectively, and Nu_r is the average Nusselt number based on the following reference conditions;

- Constant fluid properties corresponding to bulk fluid conditions,
- Tube bank having 10 tube rows with at least 6 tubes in each row,
- Tube bank normal to oncoming flow,
- $\frac{L_{tube}}{D} > 5$

As it was mentioned before, the geometry of the in-line and off-set pin fin surfaces has some similarities with tube bundles. The similarities have limitations. The method of ESDU (1973) has been developed for conventional tube bundles, and is valid for a

range of reference conditions which were mentioned above. These conditions have two major differences with the both pin-fin surfaces' dominating conditions in the present study. Firstly, the in-line and off-set pin fin surfaces contain 25 and 50 rows respectively, while in the method of ESDU (1973), mean heat transfer coefficient for a particular row can be calculated based on an average of 10 row bank. Secondly, the ESDU (1973) method can be used for tube bundles length to diameter ratios, $\frac{L_{tube}}{D}$, larger than 5, while for the pin-fin arrangements length to diameter ratio, $\frac{H_{ch}}{D_{eq}}$, is 0.78, which is much smaller than the tube bundles minimum valid value.

None-the-less, the data were compared to standard tube bundle methods to evaluate if macro-scale knowledge of this type is transferable to the current length scale. To do this, the equivalent diameter for a square pin was chosen to give the same circumference as an equivalent circular tube.

$$D_{eq} = \frac{4 \times W_w}{\pi} \tag{7.36}$$

The average Nusselt number, Nu_r, in Equation (7.35) is given by

$$Nu_r = aRe_b^m Pr_b^{0.34} \tag{7.37}$$

where Re_b and Pr_b are Reynolds number and Prandtl number based on bulk fluid conditions. Re_b is based on the maximum fluid velocity between the fins, V_{max}, i.e.,

$$Re_b = \frac{G_{max} D_{eq}}{\mu_b} \tag{7.38}$$

Values of the parameters a and m in Equation (7.37) are given in Table 7.6. The ESDU (1973) method was developed for in-line and staggered tube arrangements. Because of some similarities between staggered and off-set arrangements, the staggered tube arrangement parameters values were used for the off-set pin-fin arrangement in this study.

Table 7.6 Values of the parameters to be used in Equation (7.37)

In-line tube arrangement				
Range of Re_b	X_T	X_L	a	m
$10 - 3 \times 10^2$	$1.2 - 4$	≥ 1.15	0.742	0.431
$3 \times 10^2 - 2 \times 10^5$	$1.2 - 4$	≥ 1.15	0.211	0.651
$2 \times 10^5 - 2 \times 10^6$	$1.2 - 4$	≥ 1.15	0.116	0.700
Staggered tube arrangement				
Range of Re_b	X_T	X_L	a	m
$10 - 3 \times 10^2$	All values between 0.6 and 4		1.309	0.360
$3 \times 10^2 - 2 \times 10^5$			0.273	0.635
$2 \times 10^5 - 2 \times 10^6$			0.124	0.700

where X_T and X_L are transverse, S_T, and longitudinal, S_L, pitches to equivalent diameter ratio, respectively, i.e.,

$$X_T = \frac{S_T}{D_{eq}} \tag{7.39a}$$

$$X_L = \frac{S_L}{D_{eq}} \tag{7.39b}$$

In this study, X_T and X_L are 1.571 for the in-line pin-fin surface and 3.142 and 0.785, respectively, for the off-set pin fin surface. The fluid property variation factor of F_1 in Equation (7.35), for both in-line and staggered tube banks for $Re_b > 10$ and $Pr_b < 600$ is given by

$$F_1 = \left[\frac{Pr_b}{Pr_w}\right]^{0.26} \tag{7.40}$$

where Pr_w is Prandtl number based on fluid conditions at wall of a tube/pin-fin. The tube/pin-fin inclination factor, F_3, in Equation (7.35) is given by

$$F_3 = \frac{\overline{Nu}_\theta}{\overline{Nu}_{\theta=90^\circ}} \tag{7.41}$$

As the flow is normal to the pin-fins' axes, the tube/pin-fin inclination factor, F_3, is unit, $F_3 = 1$. Factor F_4 in Equation (7.35) relates the performance of a particular row (nth row) to the average for a 10 row bank,

$$F_4 = \frac{Nu_n}{\overline{Nu}_{N=10}} \tag{7.42}$$

where Nu_n is the mean Nusselt number for the nth row. Values of the factor F_4 are given in Figure 7.10.

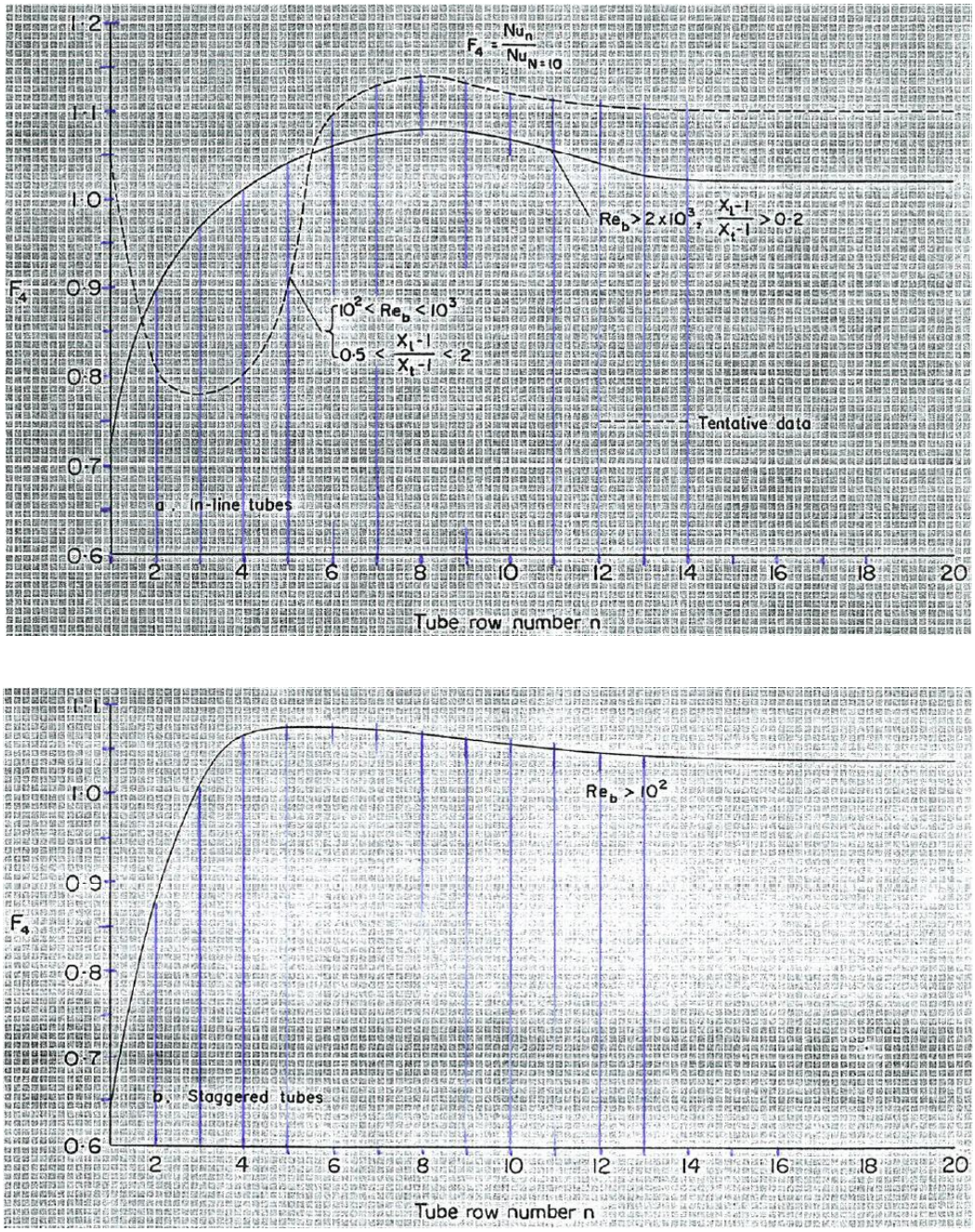

Figure 7.10 Row to row variation of heat transfer reproduced from ESDU (1973); (a) in-line tubes, (b) staggered tubes

The single-phase heat transfer coefficients for both the in-line and off-set pin fin surfaces were predicted and the resultant predicted values are shown in Figure 7.11. The pin-fin surfaces heat transfer coefficients' power law functions are included in the figures as well. The estimated error in the heat transfer coefficient is $\pm 10\%$.

For the off-set pin fin surface, turbulence created in the first few rows of pin-fins will cause an increase in the heat transfer coefficient, but this effect will become constant after the first few rows. Therefore the wall inlet and outlet heat-transfer coefficients corresponding to the 13^{th} and 37^{th} row are similar in magnitude and follow similar curves. For the in-line pin fin surface at low Reynolds numbers, the predictions of the wall inlet and outlet heat-transfer coefficients slightly differ as they are row dependent. The first row contributes a great proportion of the overall heat transfer because of a shielding effect on subsequent rows. This process continuous for inner rows and the heat transfer coefficient slightly decrease along the test piece.

The agreement between the measured and the predicted heat-transfer coefficient is quite good for the in-line surface tests with R113, and is reasonable for tests with water, indicating that correlations for this surface may be similar to those derived from macro-scale data, while for the off-set pin fin surface, the staggered tube/pin-fin arrangement predictions do not show good agreement with the off-set measured heat-transfer coefficients, indicating that correlations for off-set pin-fin surface cannot be informed by macro-scale knowledge of staggered tube arrangement.

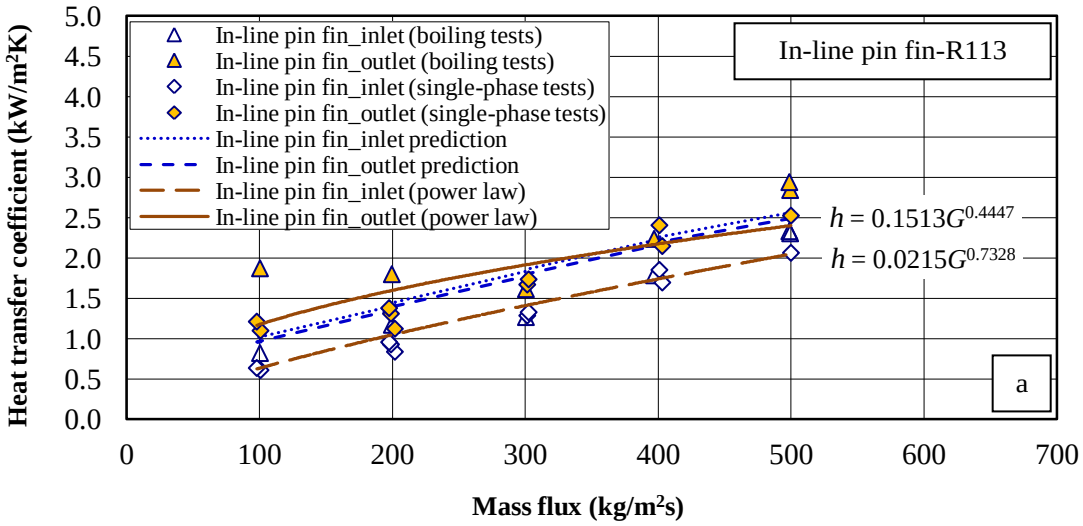

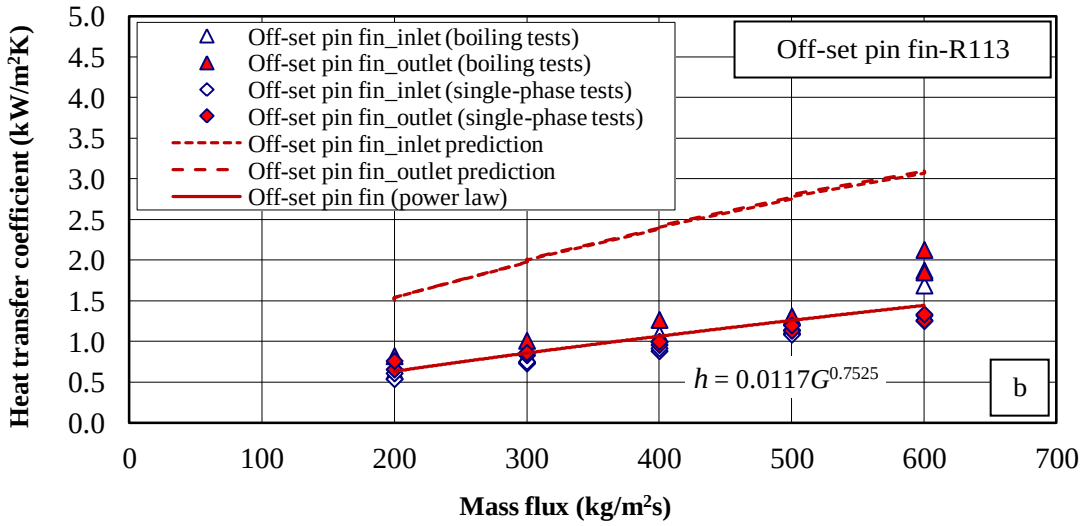

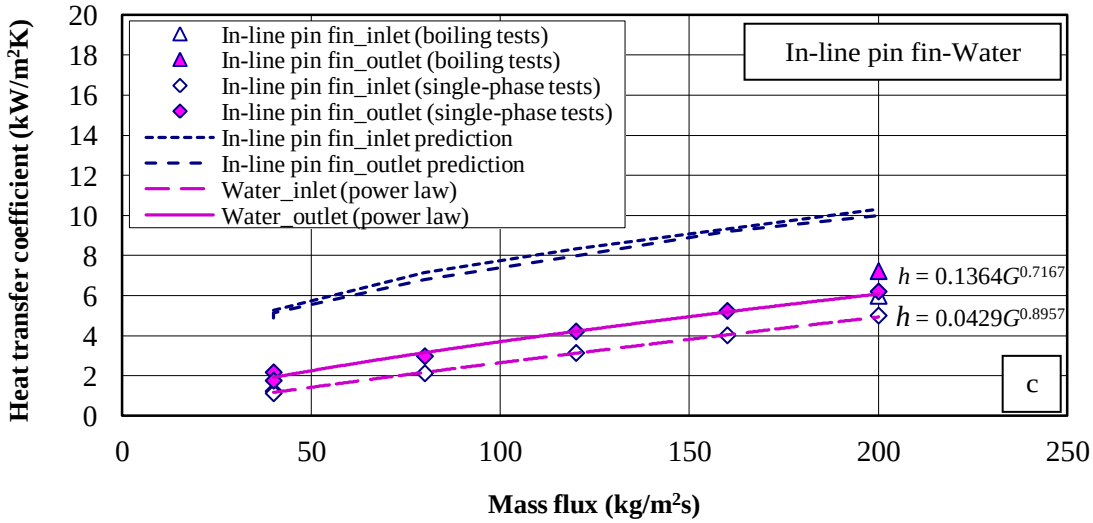

Figure 7.11 Comparison of single-phase heat transfer coefficients with predictions obtained from ESDU method, (a) in-line pin-fin surface tests with R113, (b) off-set pin-fin surface tests with R113 and (c) in-line pin-fin surface tests with deionised water

7.2.2. Single-Phase Flow Pressure Drop Predictions

For the in-line and off-set pin-fin surfaces, the single-phase pressure drops were predicted from the single-phase pressure drop method of ESDU (1979). The method was deduced from the pressure loss characteristics of single-phase Newtonian fluids flowing across banks of tubes set in arrangements commonly employed in shell-and-tube heat exchangers. As is shown in Table 7.7, the off-set pin fin surface has a rotated isosceles triangle arrangement, which is not covered by the ESDU (1979) method. Thus, the rotated equilateral triangle tube arrangement was assumed for the off-set pin-fin surface, while, square in-line tube arrangement was applied to the in-line pin-fin surface. The applied arrangements to the pin fin surfaces are shown in Table 7.7.

Table 7.7 ESDU method tube arrangements according to the pin-fin surfaces arrangements

ESDU tube arrangements	Pin-fin arrangements	S_L	S_T or S_D
Flow 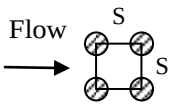 Square in-line	Flow 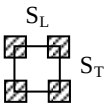 Square in-line	2 mm	2 mm
Flow 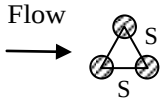 Rotated equilateral triangle	Flow 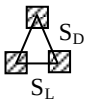 Rotated isosceles triangle	2 mm	$\sqrt{5}$ mm

The ESDU (1979) method covers a range of pitch to diameter ratio ($X = S/D$) from 1.2 to 3.0. Thus, the in-line and off-set pin fin arrangements, having 1.571 and 1.756 pitch to diameter ratios ($X = S/D_{eq}$), are covered by the ESDU method.

As it was mentioned in Section 7.1.2, the total predictive pressure drop across the test piece for single-phase tests is just consisted of frictional component. The total single-phase Pressure drops obtained from the integration of the pressure gradient, $\frac{dp}{dz}$, along the test piece, thus

$$\Delta P_{\mathrm{tot,sp}} = \int_0^{\mathrm{L}} \frac{dp}{dz} dz \tag{7.43}$$

where L is the length of the test piece in the flow direction. The pressure gradient $\frac{dp}{dz}$ is given by

$$\frac{dp}{dz} = -C\frac{\frac{1}{2}\rho U^2}{D_{eq}} \tag{7.44}$$

where superficial velocity U is the fluid flow velocity based on the unrestricted flow area, a flow area calculated ignoring the area occupied by the fins. D_{eq} is the pin-fin equivalent diameter, given by Equation (7.36), and C is the pressure loss coefficient which composed of a reference value, C', and three correction factors, ϕ_1, ϕ_2 and ϕ_3, i.e.,

$$C = C'\,\phi_1\,\phi_2\,\phi_3 \tag{7.45}$$

The correction factors ϕ_1, ϕ_2, and ϕ_3 are the viscosity ratio factor, the flow inclination factor and the fins surface roughness factor, respectively. ϕ_1 is a function of the superficial Reynolds number, Re, and the viscosity ratio, $\frac{\mu_w}{\mu_b}$, i.e.,

$$\phi_1 = \left(\frac{\mu_w}{\mu_b}\right)^{0.38Re^{-0.24}} \tag{7.46}$$

where the μ_w and μ_b are dynamic viscosity of fluid appropriate to value at wall temperature and bulk conditions, respectively. The superficial Reynolds number, Re, is calculated based on the fluid flow superficial velocity, U.

$$Re = \frac{\rho U D_{eq}}{\mu_b} \tag{7.47}$$

As the flow is normal to the plane of the pin-fin axes and the pin-fins are clean and assumed to have a nominal roughness ratio $\epsilon/D_{eq} = 5 \times 10^{-5}$, therefore the ϕ_2, and ϕ_3 values are unity, $\phi_2 = \phi_3 = 1.0$.

The loss coefficient reference value C' in Equation (7.45) for the in-line square pin-fin arrangement evaluates from

$$C' = YF\left(\frac{D_v}{D_{eq}}\right)_{\square}\frac{1}{(X-1)^3} \tag{7.48}$$

where parameter F is ratio of C' for rotated square to C' for in-line square arrays. Thus, parameter F for the in-line pin-fin arrangement is unity, F=1. Parameter Y representing the effect of superficial Reynolds number, given by

$$Y = \left[\frac{\left\{ \frac{0.1Re}{Re+100} \right\}^2}{\left\{ \frac{a^2}{[0.5(1+0.6a)]^2} + \frac{1}{(1+3a)^2} \right\}} + \frac{49}{Re^{1.95}} \right]^{1/2} \tag{7.49}$$

where parameter a is given by

$$a = \frac{Re}{(Re+10^4)} \tag{7.50}$$

D_v in Equation (7.48) is the modified volumetric diameter. The ratio $\left(\frac{D_v}{D_{eq}}\right)_{\square}$ is given by

$$\left(\frac{D_v}{D_{eq}}\right)_{\square} = \frac{4X^2}{\pi} - \frac{Re}{Re+1{,}000} \tag{7.51}$$

where X is the pitch to equivalent diameter ratio and given by

$$X = S/D_{eq} \tag{7.52}$$

As for the in-line square pin-fin arrangement, longitudinal and transverse pitch values are equal, therefore $S = S_L = S_T = 2\ mm$.

For rotated equilateral triangle pin-fin arrangement, the loss coefficient reference value C' in Equation (7.45) evaluated from

$$C' = Y \left(\frac{D_v}{D_{eq}}\right)_{\triangle} \frac{1}{(X-1)^3} \tag{7.53}$$

where Y is given by

$$Y = \left[\frac{3.61}{Re^{0.7}} \left(1 + \frac{5}{Re^{0.8}}\right)^2 + 0.0625(1-a)^2 + 0.01 \right]^{1/2} \tag{7.54}$$

and the ratio $\left(\frac{D_v}{D_{eq}}\right)_{\triangle}$ is given by

$$\left(\frac{D_v}{D_{eq}}\right)_{\Delta} = \frac{2\sqrt{3}X^2}{\pi} - \frac{Re}{Re+10} \tag{7.55}$$

Figure 7.12 shows the variation of measured single-phase pressure drops with mass flux for both the in-line and off-set pin fin surfaces. For the tests with R113, both in-line and off-set pin-fin surfaces data sets are similar in magnitude. The in-line pin fin values are higher. This can be attributed to the pin-fins arrangement in the off-set surface. The pin-fins are staggered in the longitudinal direction, which in comparison to the in-line arrangement, causes a reduced disturbance to the flow, giving pressure drops that are slightly smaller. A comparison between in-line pin fin surface tests with R113 and water indicate that both water and R113 data sets are similar in magnitude, with the R113 values being slightly higher. This could be resulted from the experimental uncertainties.

For both surfaces, single-phase pressure drop predictions, obtained from method of ESDU, and also power law functions are included in the figure. The agreement between the measured and the predicted pressure drops for the in-line pin fin surface tests with both R113 and water is good, while for the off-set pin fin surface does not show a good agreement. However, more geometrical variations would need to be tested before its applicability can be considered general.

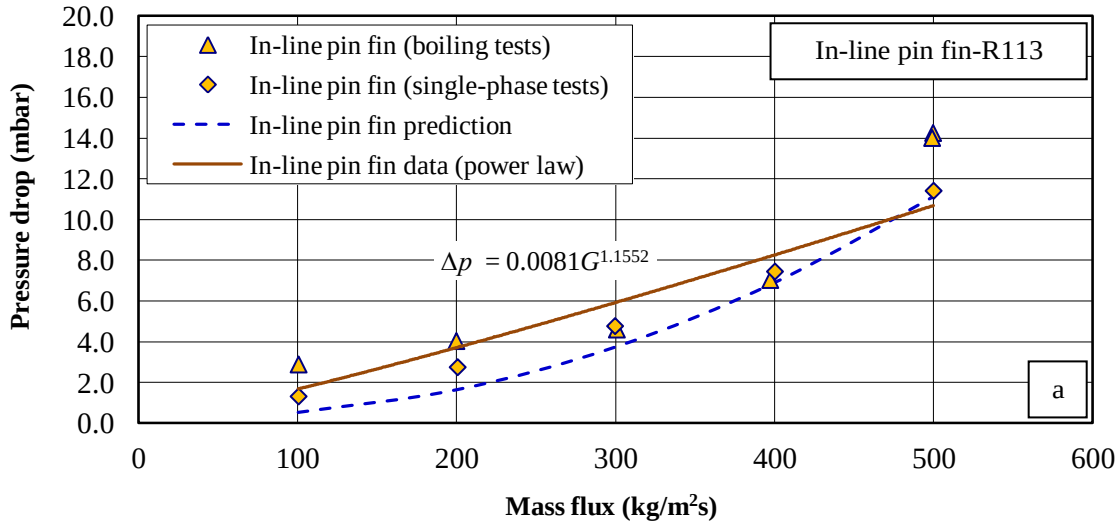

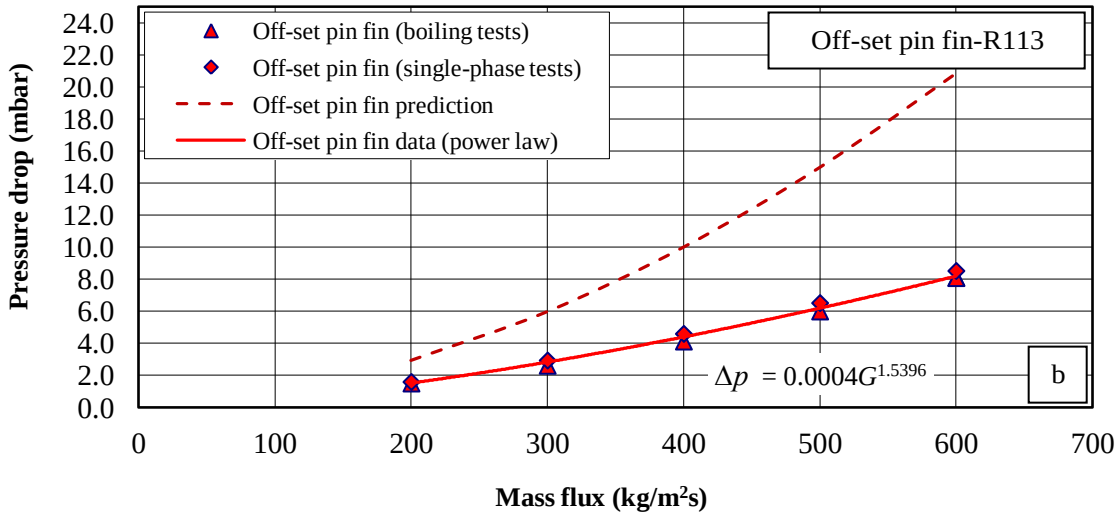

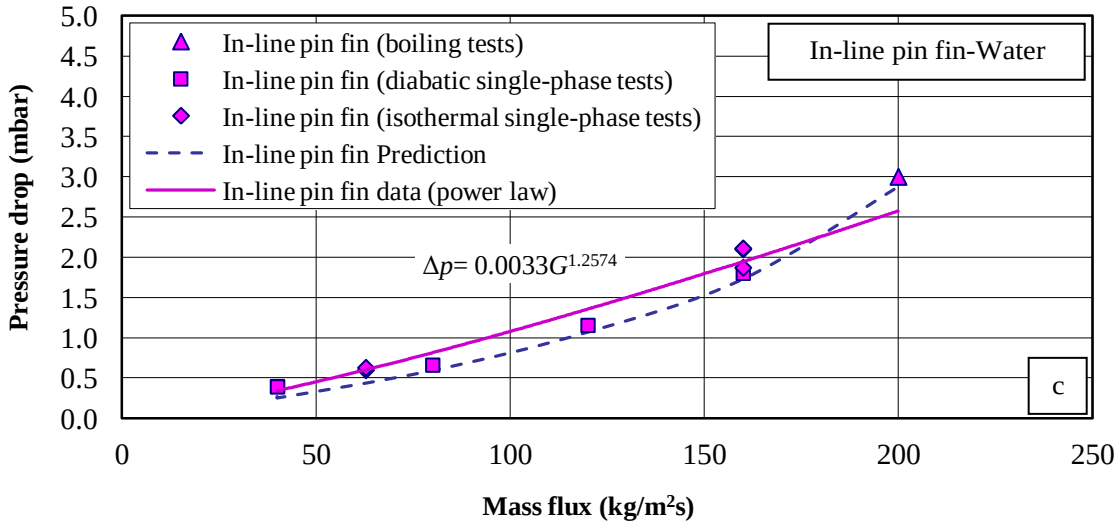

Figure 7.12 Comparison of single-phase pressure drops with predictions obtained from ESDU method, (a) in-line pin-fin surface tests with R113, (b) off-set pin-fin surface tests with R113, and (c) in-line pin-fin surface tests with deionised water

7.2.3. Two-Phase Flow Heat Transfer Predictions

For both pin-fin surfaces, the saturated flow boiling heat transfer coefficients were predicted from tube bundle methods. Conventional scale boiling correlations for cross-flow of fluids over tube bundles generally fall into two categories, the asymptotic correlations used by Kim et al. (2002), i.e.,

$$h = (h_{cv}^n + h_{nb}^n)^{1/n} \tag{7.56}$$

and the Chen-type correlations (Chen, 1966) used by Jensen and Hsu (1988); Gupta et al. (1995); Huang and Witte (2001); Gupta (2005). In the present study, the pin fin surfaces two-phase heat transfer coefficient, h, was evaluated from a Chen-type correlation, which is contributions of nucleate boiling and single-phase convective mechanisms, i.e.,

$$h = Eh_{cv} + Sh_{nb} \tag{7.57}$$

where h_{cv} and h_{nb} are the single-phase convective heat-transfer coefficient and the nucleate boiling heat transfer coefficient, respectively, E is the convective enhancement factor, and S is the nucleate boiling suppression factor. Convective enhancement factor E is defined by:

$$E = \left(\phi_f^2\right)^{0.36} \tag{7.58}$$

where the two-phase multiplier, ϕ_f^2, was obtained from Ishihara et al. (1980), i.e.,

$$\phi_f^2 = 1 + \frac{8}{X_{tt}} + \frac{1}{X_{tt}^2} \tag{7.59}$$

where Martinelli parameter X_{tt} was obtained from Equation (7.31c). The nucleate boiling suppression factor S was obtained from the method of Bennett et al. (1980), i.e.,

$$S = \left(\frac{k_f}{E\alpha_{cv}X_o}\right)\left(1 - exp\left(-\frac{E\alpha_{cv}X_o}{k_f}\right)\right) \tag{7.60}$$

where X_o is the bubble growth parameter, given by

$$X_o = 0.041\left(\frac{\sigma}{g(\rho_f - \rho_g)}\right)^{0.5} \tag{7.61}$$

The single-phase convective heat-transfer coefficient, h_{cv}, in Equation (7.57) was obtained from the method of ESDU (1973), described in Section 7.2.1, by assuming that only the liquid component flowed in the heat exchanger. The nucleate boiling heat transfer coefficient, h_{nb}, in Equation (7.56) was obtained from the method of Mostinski (1963), i.e.,

$$h_{nb} = 0.525\, P_{crit}^{0.69}\, (1.8P_r^{0.17} + 4P_r^{1.2} + 10P_r^{10})\, q"_{act}^{0.7} \tag{7.62}$$

where h_{nb} is in W/m^2K, $q"_{act}$ the heat flux in W/m^2, P_{crit} the critical pressure of the fluid in kN/m^2, and P_r is the reduced pressure, local pressure to the critical pressure ratio ($P_r = P/P_{crit}$).

Comparisons between the measured heat transfer coefficients and the saturated boiling data predictions, obtained from the tube bundle methods, for the in-line and off-set pin fin surfaces tests with R113 and the in-line pin fin surface tests with water are shown in Figures 7.13, 7.14, and 7.15, respectively.

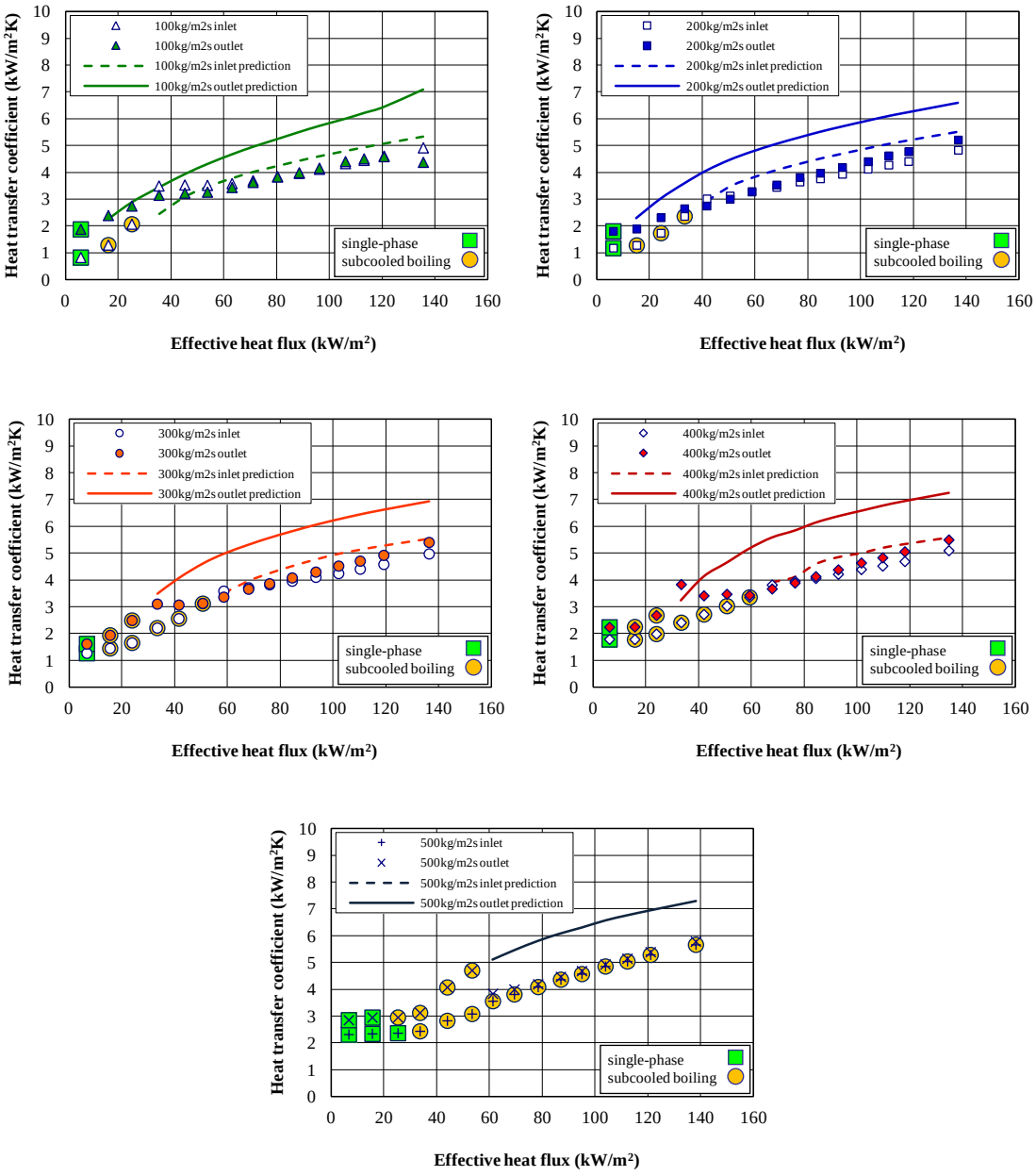

Figure 7.13 Comparison of measured two-phase heat transfer coefficients with predictions for the in-line pin fin surface tests with R113

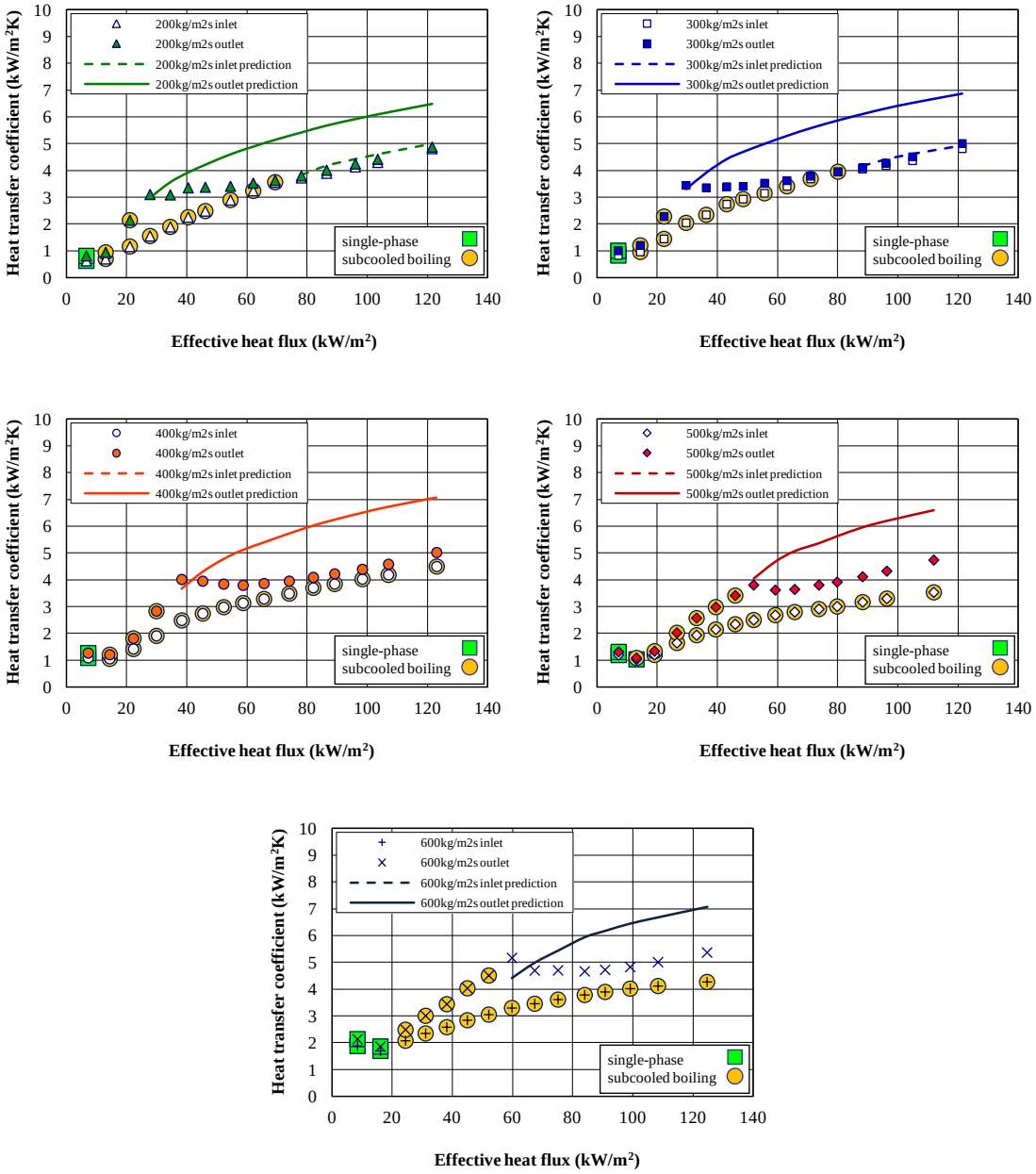

Figure 7.14 Comparison of measured two-phase heat transfer coefficients with predictions for the off-set pin fin surface tests with R113

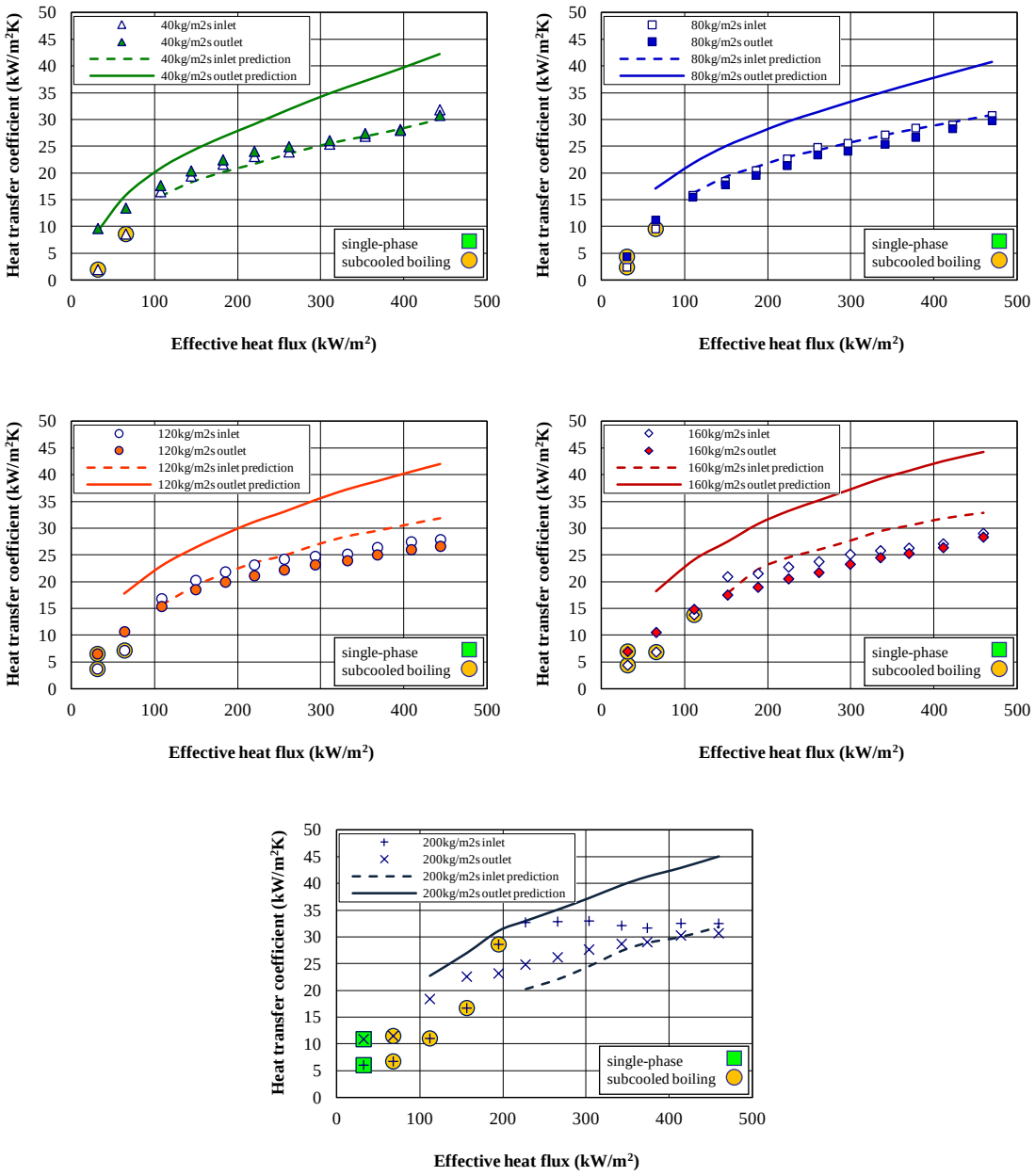

Figure 7.15 Comparison of measured two-phase heat transfer coefficients with predictions for the in-line pin fin surface tests with deionised water

For all pin-fin surfaces with different working fluids, the comparison with the experimental data shows that the predictions for the wall inlet conditions are in reasonable agreement with the measured values at the wall inlet and outlet, except for the in-line pin fin surface tests with water at the highest mass flux of 200 kg/m^2s, which the wall inlet prediction is in reasonable agreement only with the measured values at the wall outlet.

The agreement between the wall inlet predictions and the measured values at the wall inlet and outlet results from the nucleate suppression of Mostinski (1963) balancing with the convective enhancement of ESDU (1973). The wall outlet predictions are quite in reasonable agreement with the measured outlet values at lower heat fluxes, which cause small gas mass-fraction values. As the heat flux increases, the gas mass-fraction increases and the wall outlet predictions become significantly larger than the measured outlet values.

Since the wall outlet gas mass-fraction is significantly larger than the wall inlet value, the difference between the wall inlet and outlet predictions is due to convective enhancement. Thus, the measured data are consistent with predictions in the absence of convective enhancement. Unlike the conventionally-sized tube bundles, the convective enhancement does not occur for the present study's mini-pin-fin surfaces, supporting nucleate boiling domination.

7.2.4. Two-Phase Flow Heat Transfer Comparisons with Existing Correlations

For both the in-line and off-set pin fin surfaces, the saturated boiling heat transfer data were compared with several popular published correlations for conventional tube bundles and micro-scale pin-fin arrangements. These correlations are summarized in Table 7.8. The saturated boiling heat transfer data were also compared with the nucleate pool boiling correlations of Mostinski (1963) and Cooper (1984), which were presented in Table 7.1.

The first five correlations in Table 7.8, Hwang and Yao (1986); Hsu (1987); Gupta et al. (1995); Dowlati et al. (1996) and Gupta (2005) are popular for determining the flow boiling heat transfer coefficient for conventional tube bundles, while the last two correlations of Kosar and Peles (2007) and Krishnamurthy and Peles (2008) have been developed based on the micro-scale pin fin surfaces data.

Table 7.8 Two-phase heat transfer coefficient correlations corresponding to the in-line and off-set pin fin surfaces

Correlation number	Reference	Shape and geometry of pin fins	Working fluid	Correlation
1	Hwang and Yao (1986)	Circular, horizontal, staggered, $S_L/D = S_T/D = 1.5$, $G = 132 - 242\ kg/m^2s$ $0 < x < 0.05$	R-113	$h_{tp} = 0.2086 q"_{act}^{0.75}$, $q"_{act}$ heat flux based on the heat transfer surface area of the device, W/cm^2
2	Hsu (1987)	Circular, horizontal, in-line, $S_L/D = S_T/D = 1.3$, $G = 50 - 675\ kg/m^2s$ $0 < x < 0.36$	R-113	$h_{tp} = Eh_{sp} + Sh_{nb}$ h_{sp} = experimental average single-phase heat transfer coefficient $h_{nb} = 0.5261 q"_{act}^{0.5353}$ $S = \left(\frac{k_f}{Eh_{sp}X_o}\right)\left(1 - exp\left(-\frac{Eh_{sp}X_o}{k_f}\right)\right)$ $E = \left(\phi_f^2\right)^{\frac{m}{2-n}}$, $m = 0.694$, $n = 0.674$, $\phi_f^2 = \left(1 + \frac{8}{X_{tt}} + \frac{1}{X_{tt}^2}\right)$ $X_{tt} = \left(\frac{\mu_f}{\mu_g}\right)^{0.1}\left(\frac{v_f}{v_g}\right)^{0.5}\left(\frac{1-x_e}{x_e}\right)^{0.9}$, $X_o = 0.041\left(\frac{\sigma}{g(\rho_f - \rho_g)}\right)^{0.5}$
3	Gupta et al. (1995)	Circular, horizontal, in-line, $S_L/D = 1.5$, $G = 0 - 10\ kg/m^2s$	Water	$h_{tp} = Eh_{sp} + h_{mic}$ h_{sp} = experimental average single-phase heat transfer coefficient $h_{mic} = 13.035\left(S\left(\overline{T_{tp}} - T_{sat}\right)\right)^{2.881}$, $S = \left(\frac{k_f}{Eh_{sp}X_o}\right)\left(1 - exp\left(-\frac{Eh_{sp}X_o}{k_f}\right)\right)$ $E = 851.38\, Bo^{0.707}\left(\frac{S_L}{D}\right)^{-0.245} N_{row}^{0.577}$, $Bo = \frac{q"_{act}}{Gh_{fg}}$ $X_o = 0.041\left(\frac{\sigma}{g(\rho_f - \rho_g)}\right)^{0.5}$
4	Dowlati et al. (1996)	Circular, horizontal, in-line, $S_L/D = S_T/D = 1.3$, $G = 50 - 970\ kg/m^2s$ $0 < x < 0.3$	R-113	$h_{tp} = 0.41 q"_{act}^{0.58}$, $q"_{act}$ heat flux based on the heat transfer surface area of the device, W/cm^2

Correlation number	Reference	Shape and geometry of pin fins	Working fluid	Correlation
5	Gupta (2005)	Circular, horizontal, in-line, $S_L/D = 1.5$, $G = 0 - 10\ kg/m^2s$	Water	$h_{tp} = Eh_{sp} + h_{mic}$ h_{sp} = experimental average single-phase heat transfer coefficient $h_{mic} = 13.035\left(S\left(\overline{T_{tp}} - T_{sat}\right)\right)^{2.881}$, $S = \left(\frac{k_f}{Eh_{sp}X_o}\right)\left(1 - exp\left(-\frac{Eh_{sp}X_o}{k_f}\right)\right)$ $E = 134.24\,Bo^{0.469}\left(\frac{S_L}{D}\right)^{-0.311}\frac{N_{row}^{0.946}}{1.946}\frac{N_{column}^{0.304}}{1.304}$, $Bo = \frac{q"_{act}}{Gh_{fg}}$ $X_o = 0.041\left(\frac{\sigma}{g(\rho_f - \rho_g)}\right)^{0.5}$
6	Kosar and Peles (2007)	Hydrofoil-based, micro-pin-fins, staggered, $G = 976 - 2349\ kg/m^2s$ $0 < x < 0.98$	R-123	a) $\bar{h}_{tp} = a_1 q"_{act}^{a_2} + a_3 \bar{h}_{sp}^{a_4}$ $a_1 = \frac{3.42\times10^7}{G^{1.16}h_{fg}^{1.16}}$, $a_2 = 1.01$, $a_3 = 0.12$, $a_4 = 0.7$ b) $\bar{h}_{tp} = b_1(Re_{Lo})^{b_2}(1 - x_e)^{b_3}\left(\frac{1-x_e}{x_e}\right)^{b_4}$, $Re_{Lo} = \frac{G_{max}D_h}{\mu_f}$ $b_1 = 819$, $b_2 = 0.6$, $b_3 = 0.22$, $b_4 = 0.01$
7	Krishnamurthy and Peles (2008)	Circular, micro-pin-fins, staggered $S_L/D = S_T/D = 1.5$, $G = 346 - 794\ kg/m^2s$ $0 < x < 0.17$	Water	$h_{tp} = Eh_{sp}$ $E = \xi\left(\phi_f^2\right)^{0.2475}Pr_f^{0.333}$, $\xi = 1.4$ $h_{sp} = 0.76\left(\frac{S_T}{D_{eq}}\right)^{0.16}\left(\frac{S_L}{D_{eq}}\right)^{0.2}\left(\frac{L}{D_{eq}}\right)^{-0.11}Re^{0.33}\frac{k_f}{D_{eq}}$ a) $\phi_f^2 = 1 + \frac{C_1 Re_f}{X_{vv}} + \frac{1}{X_{vv}^2}$ for $Re_f < 50$ (Krishnamurthy and Peles (2007)) $C_1 = 0.0358$, $Re_f = \frac{G_{max}(1-x_e)D_h}{\mu_f}$, $X_{vv} = \left(\frac{\mu_f}{\mu_g}\right)^{0.39}\left(\frac{v_f}{v_g}\right)^{0.5}\left(\frac{1-x_e}{x_e}\right)^{0.61}$ b) $\phi_f^2 = 1 + \frac{0.24}{X_{vv}} + \frac{1}{X_{vv}^2}$ for $2 < Re_f < 1000$ (Krishnamurthy and Peles (2008))

Comparisons between experimental saturated flow boiling heat transfer coefficients and the predictions of Table 7.8 correlations, for in-line and offset pin fin surfaces tests with R113 and in-line pin fin surface tests with deionised water are presented in Figures 7.16, 7.17 and 7.18, respectively. The saturated flow boiling heat transfer coefficients were also compared with the predictions obtained from Equation (7.56), Section 7.2.3. Comparisons between experimental data and standard tube bundle methods predictions are included in the figures for each pin-fin surface. A comparison of the saturated flow boiling heat transfer data with the nucleate pool boiling correlations of Mostinski (1963) and Cooper (1984) is included in the figures as well. Figures include the root mean square, RMS, error for each correlation, obtained from Equation (7.14). Apart from RMS errors, Table 7.9 includes average error for each correlation, obtained from Equation (7.16).

As seen from Figures 7.16 and 7.17, for the in-line and off-set pin fin surface tests with R113, the predictions of the existing correlations developed for conventional tube bundles are not in a good agreement with the experimental results except for Gupta (2005) correlation, which is in a quite reasonable agreement with the in-line pin fin surface data at large mass fluxes, with an average error of 12.34%. All conventional tube bundles correlations over-predict most of the experimental data. The predictions are better at lower qualities and higher mass fluxes.

For the last two correlations in Table 7.8, Kosar and Peles (2007) and Krishnamurthy and Peles (2008) correlations, which are based on the micro-scale pin fin surfaces data, predictions of the correlation 6(a) by Kosar and Peles (2007) are reasonably in a quite good agreement with experimental data for the in-line and off-set pin fin surfaces tests with R113 at moderate and lower mass fluxes, respectively. Correlation 6(a) is a Chen-type correlation (Correlation 3 in Table 7.1) and has a similar form to the one used by Gupta et al. (1995). The second correlation of Kosar and Peles (2007), Correlation 6(b), was modified from correlations developed based on micro-channels convective boiling data. As is shown in Figures 7.16 and 7.17, the correlation 6(b) predicts very large values for both the in-line and off-set pin fin surfaces tests with R113, compared to the data.

The Krishnamurthy and Peles (2008) correlation, correlation 7, was developed based on the convective boiling heat transfer data. The frictional multiplier correlation of 7(a) was developed by Krishnamurthy and Peles (2007) at low liquid

Reynolds numbers ($Re_f < 50$), while the frictional multiplier correlation of 7(b) developed by Kawahara et al. (2002) for a $100\,\mu m$ diameter micro-channel at higher Reynolds numbers ($2 < Re_f < 1000$). As is shown in Figures 7.16 and 7.17 for both pin fin surfaces tests with R113, Krishnamurthy and Peles (2008) correlation which is based on two frictional multiplier correlations, correlations 7(a) and 7(b), predicts very small values compared to the data.

As is shown in Figure 7.18, for the in-line pin fin surface tests with deionised water, the three conventional tube bundles correlations of Hwang and Yao (1986), HSU (1987), and Dowlati et al. (1996) show a better agreement with data, in compare with the in-line pin fin surface tests with R113. The Hsu (1987) correlation shows the best agreement with an average error of 20.52%. Its predictions are quite dispersed, while the predictions of Hwang and Yao (1986) and Dowlati et al. (1996) correlations are merged and reasonably close to the experimental data at higher heat fluxes. The other two macro-scale correlations of Gupta et al. (1995) and Gupta (2005), predict very small values compared to the data.

For the last two correlations of Kosar and Peles (2007) and Krishnamurthy and Peles (2008) which are based on the flow boiling heat transfer in micro-pin fin surfaces data, predictions of the 6(a) correlation by Kosar and Peles (2007) show a worse agreement with data in compare with the tests with R113, while the 7(b) correlation by Krishnamurthy and Peles (2008) show a better agreement with experimental data in compare with the R113 tests. The other two correlations of 6(b) and 7(a) behave similar trends to those tests with R113.

As can be seen in Figures 7.16 to 7.18, predictions of the nucleate boiling correlations by Mostinski (1963) and Cooper (1984) for both surfaces tests with R113 and deionised water show reasonably good agreement with experimental data. For both surfaces tests with R113 and deionised water and for all mass fluxes, the Mostinski (1963) correlation lies slightly below the measured values and the Cooper (1984) under predicts the data for all mass fluxes at low heat fluxes and as the heat flux increases agrees reasonably well. Similar to the plate and parallel channel surfaces comparisons, the surface roughness parameter was chosen to remove the surface roughness dependency from the Cooper (1984) prediction for both pin fin surfaces. The Cooper (1984) correlation provides the best agreement

with the data among all correlations tested, with average errors of 6.16% and 10.81% for the in-line and off-set pin fin surfaces tests with R113, respectively. While for the in-line pin fin surface tests with water, the correlation of Hsu (1987) and nucleate boiling correlation of Dowlati et al. (1996) show the best agreement with the data with an average error of 20.52% and 22.01%, respectively. For water tests nucleate pool boiling correlations of Mostinski (1963) and Cooper (1984) also show a good agreement with data with an average error of 34.66% and 38.36%, respectively. Given the uncertainty in predicting nucleate boiling, this is a reasonable comparison and is further evidence that the heat-transfer process is dominated by nucleate boiling.

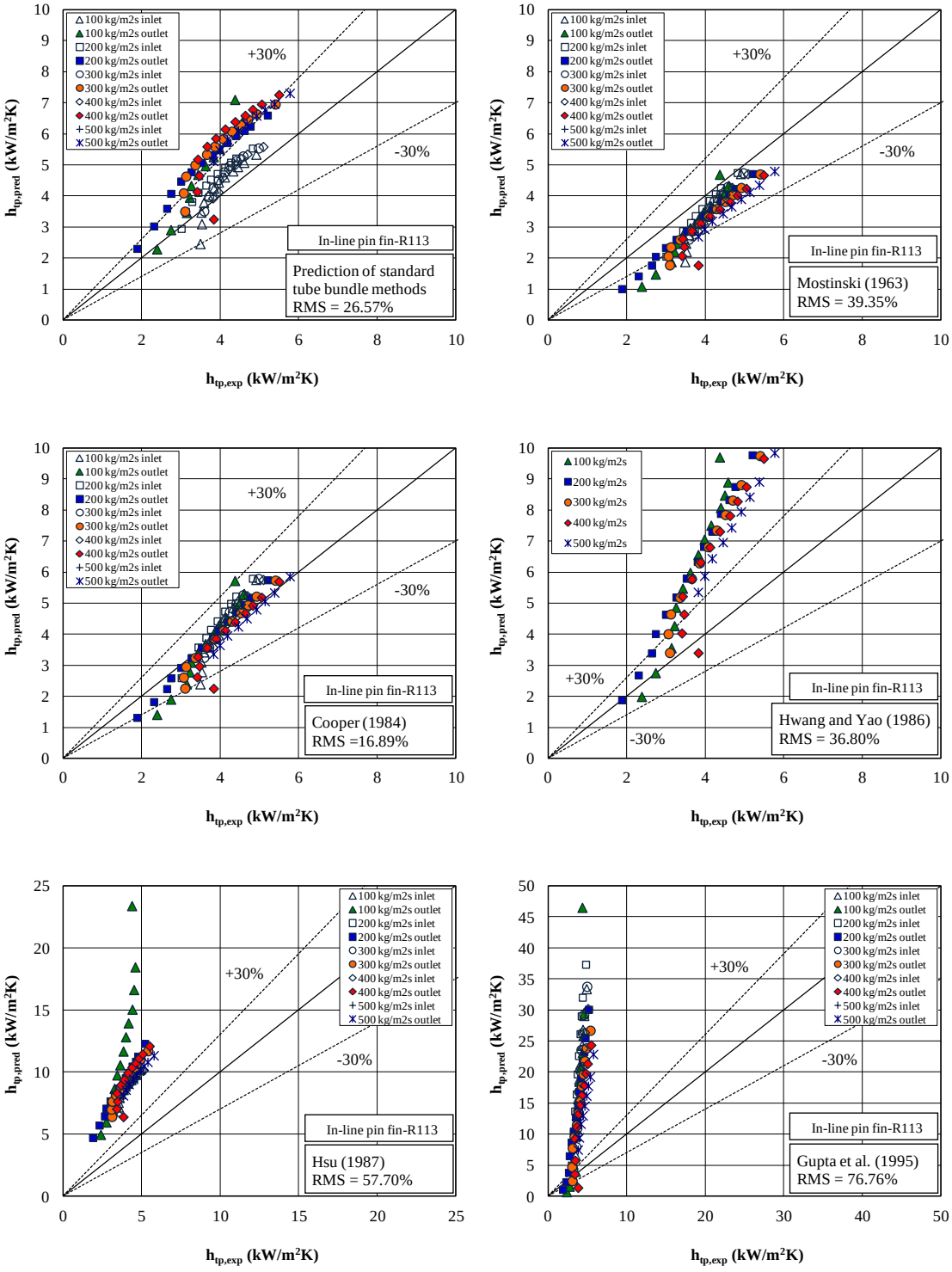

Figure 7.16 Saturated flow boiling heat transfer coefficients comparisons with existing correlations for the in-line pin fin surface tests with R113

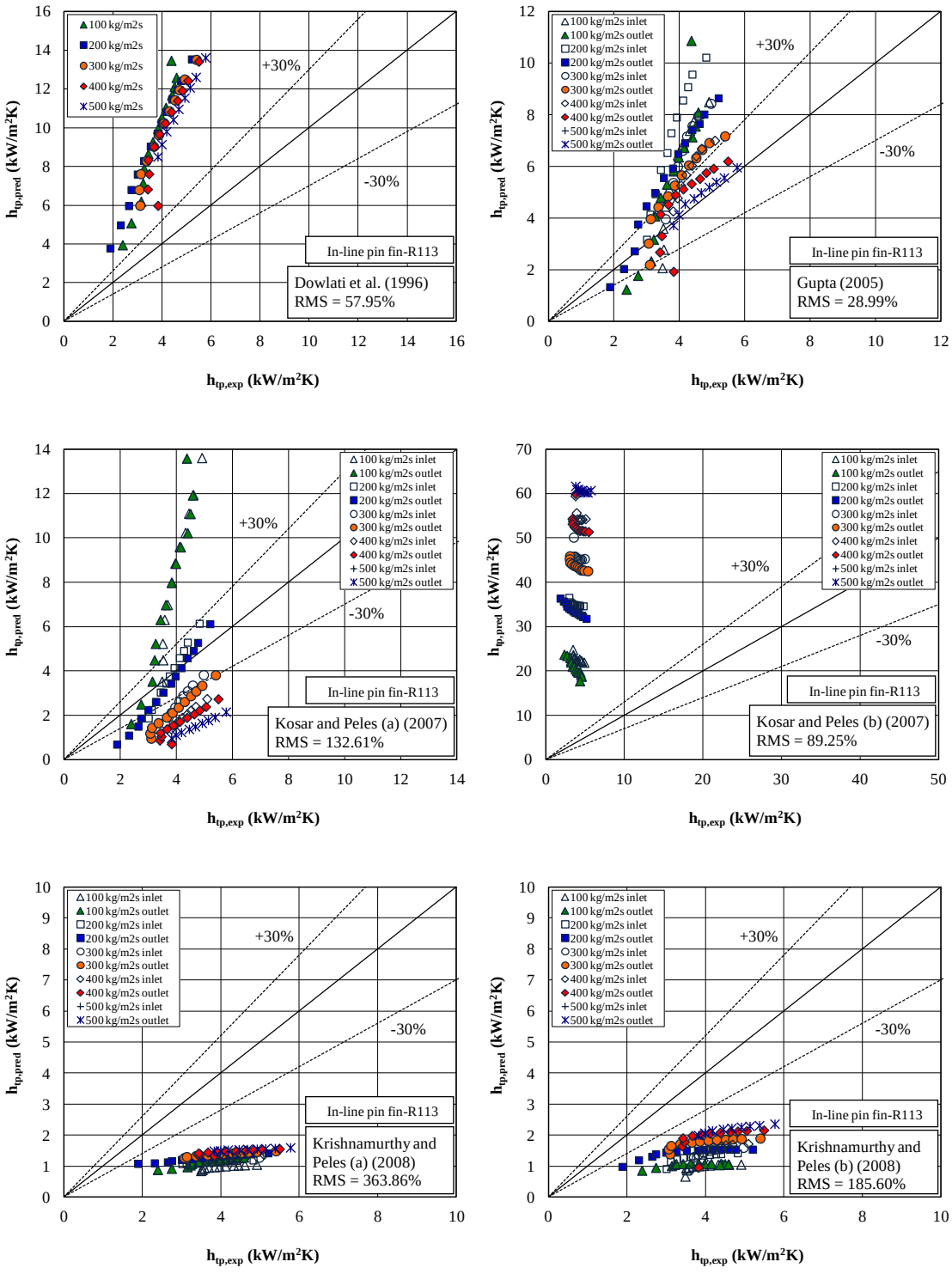

Figure 7.16 (continued) Saturated flow boiling heat transfer coefficients comparisons with existing correlations for the in-line pin fin surface tests with R113

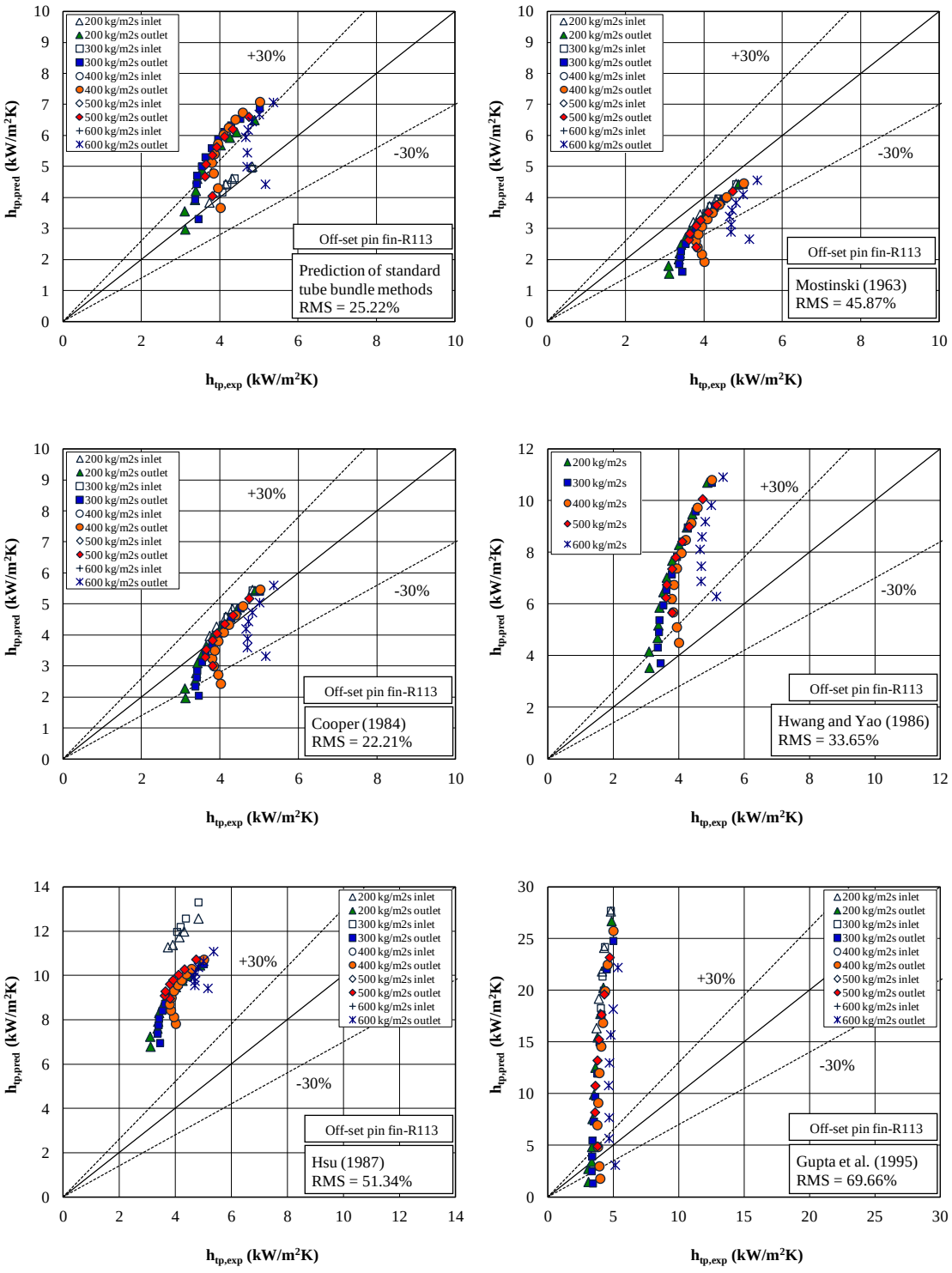

Figure 7.17 Saturated flow boiling heat transfer coefficients comparisons with existing correlations for the off-set pin fin surface tests with R113

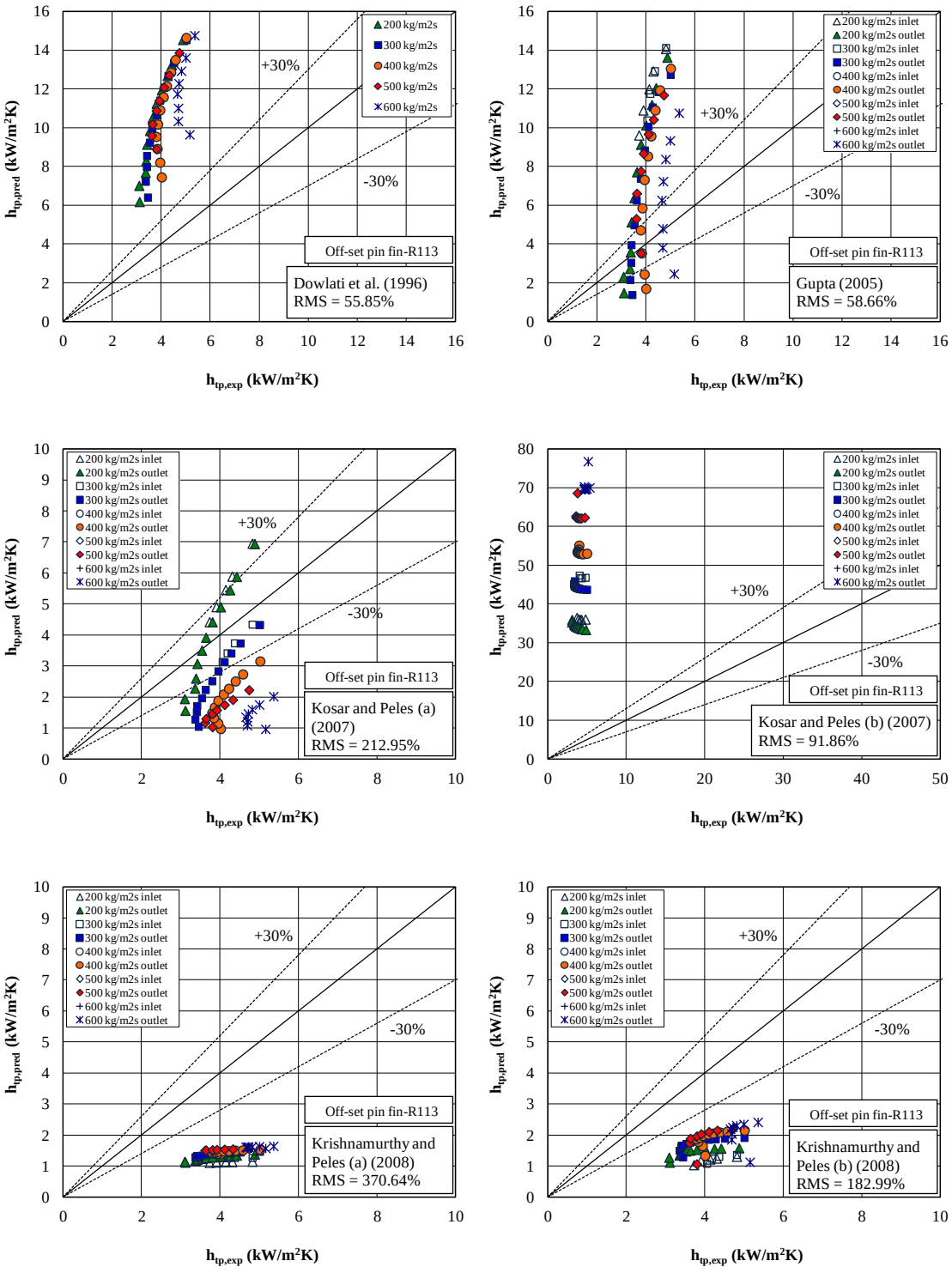

Figure 7.17 (continued) Saturated flow boiling heat transfer coefficients comparisons with existing correlations for the off-set pin fin surface tests with R113

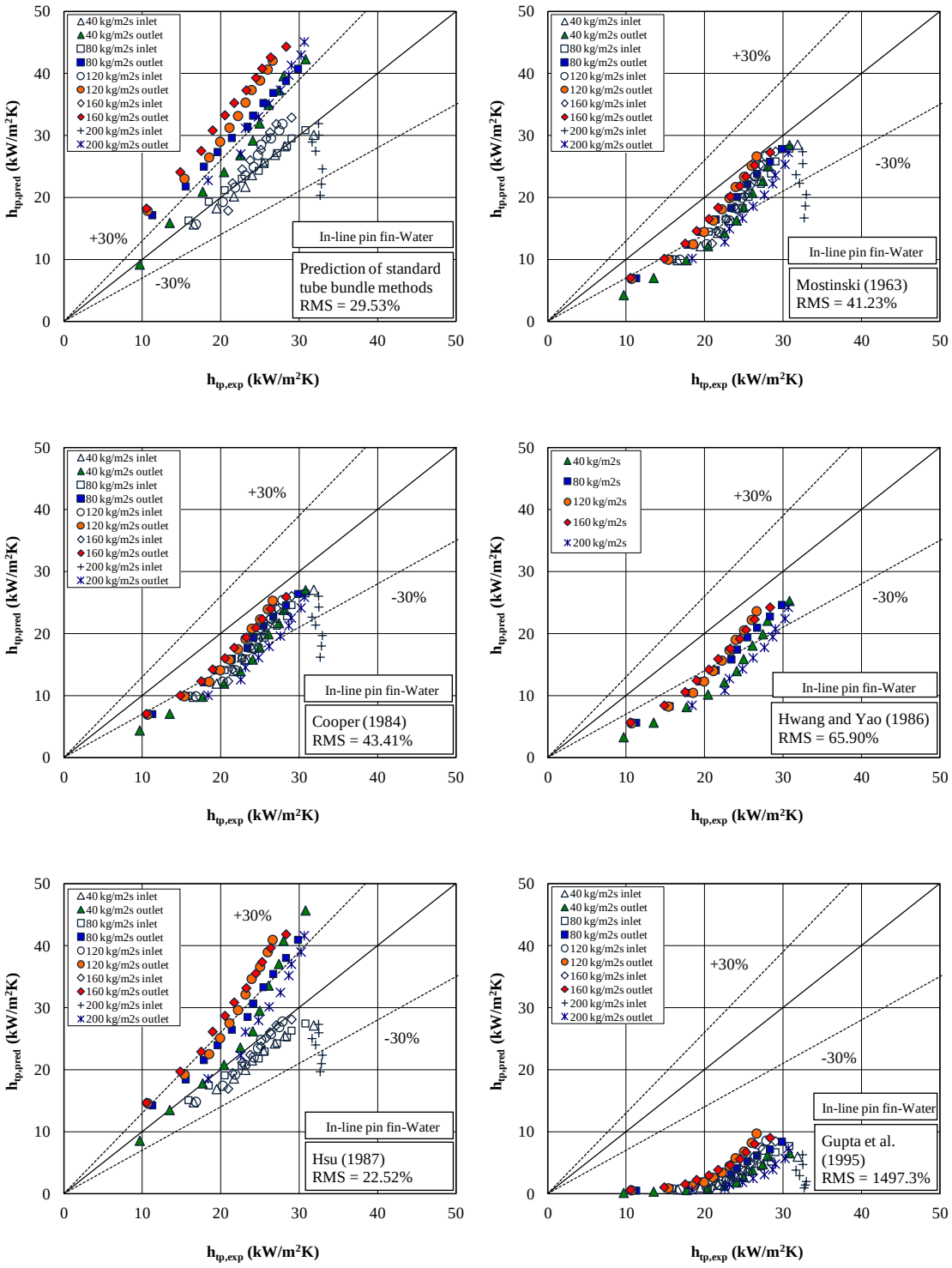

Figure 7.18 Saturated flow boiling heat transfer coefficients comparisons with existing correlations for the in-line pin fin surface tests with deionised water

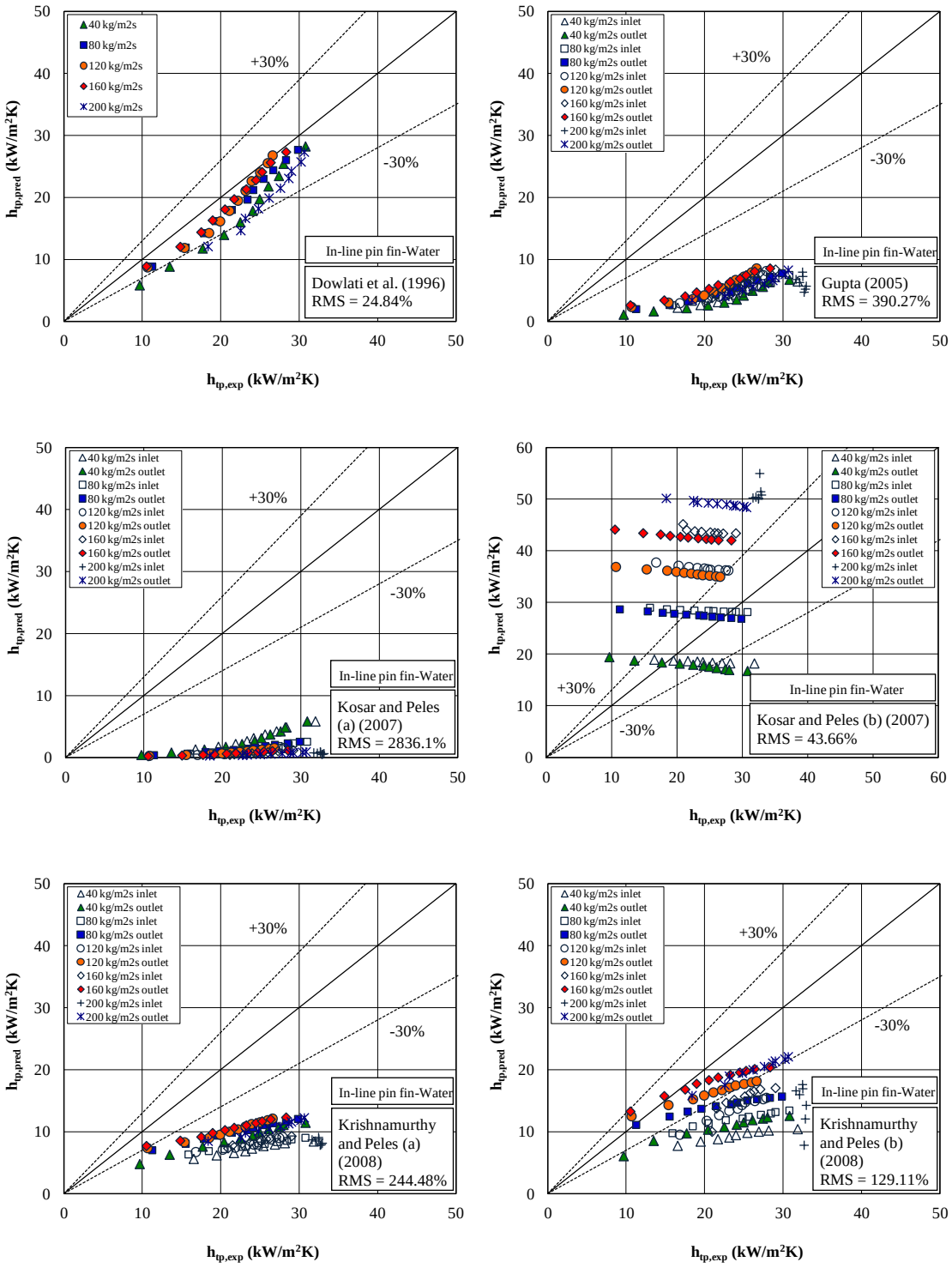

Figure 7.18 (continued) Saturated flow boiling heat transfer coefficients comparisons with existing correlations for the in-line pin fin surface tests with deionised water

Table 7.9 In-line and off-set pin fin surfaces' RMS and average errors for comparisons between the Table 7.8 correlations predictions and experimental data

Corr.	Reference	In-line pin fin – R113		Off-set pin fin – R113		In-line pin fin – water	
		RMS	Average	RMS	Average	RMS	Average
1	Hwang and Yao (1986)	36.80	34.04	33.65	30.54	65.90	57.96
2	Hsu (1987)	57.70	57.53	51.34	51.27	22.52	20.52
3	Gupta et al. (1995)	76.76	51.43	69.66	43.92	1497.3	1126.84
4	Dowlati et al. (1996)	57.95	57.73	55.85	55.51	24.84	22.01
5	Gupta (2005)	28.99	12.34	58.66	23.92	390.27	381.44
6a	Kosar and Peles (2007)	132.61	115.96	212.95	194.74	2836.1	2713.03
6b	Kosar and Peles (2007)	89.25	89.20	91.86	91.85	43.66	36.80
7a	Krishnamurthy & Peles (2008)	363.86	358.98	370.64	369.12	244.48	242.32
7b	Krishnamurthy & Peles (2008)	185.60	179.59	182.99	174.95	129.11	125.57
8	Prediction ESDU (1973)	26.57	25.12	25.22	22.48	29.53	28.98
9	Mostinski (1963)	39.35	32.19	45.87	38.21	41.23	34.66
10	Cooper (1984)	16.89	6.16	22.21	10.81	43.41	38.36

7.2.5. Two-Phase Flow Pressure Drop Predictions

As indicated in Section 7.1.4, for two-phase tests the test piece was divided into upstream single-phase and downstream two-phase regions. The total predictive test piece pressure drop can be calculated from adding the single-phase and the two-phase regions pressure drops, Equation (7.17). For the pin fin surfaces, the upstream single-phase pressure drop was evaluated from Equation (7.43), where L was substituted with the length of the upstream single-phase region, L_{sub}. Therefore upstream single-phase pressure drop is given by

$$\Delta P_{\mathrm{sp}} = \int_0^{\mathrm{L_{sub}}} \frac{dp}{dz} dz \tag{7.63}$$

The pressure gradient $\frac{dp}{dz}$ was evaluated from the single-phase pressure drop method of ESDU (1979), given by Equation (7.44).

The two-phase region pressure drop, ΔP_{tp}, was predicted from the simultaneous integration of the pressure gradient, $\left(\frac{dP}{dz}\right)_{tp}$, given by Equation (7.20), and the differential form of energy equation, Equation (7.21). This approach allows the variation of physical properties to be included. For the pin fin surfaces, the mass flux G in Equation (7.21) was based on superficial velocity U, which is the fluid flow velocity based on the unrestricted flow area, a flow area calculated ignoring the area occupied by the fins.

Similar to the plate and parallel channel surfaces, for the pin fin surfaces the two-phase acceleration pressure gradient, $\left(\frac{dP}{dz}\right)_A$, in Equation (7.20) was determined by assuming homogeneous flow, Equation (7.32). For the pin fin surfaces, the mass flux G in Equation (7.32) was based on the unrestricted flow area.

For the pin fin surfaces, the two-phase frictional pressure gradient, $\left(\frac{dP}{dz}\right)_F$, in Equation (7.20) was obtained from the two-phase multiplier method of Ishihara et al. (1980), Equation (7.59), with the liquid-only single-phase pressure gradient, $\left(\frac{dP}{dz}\right)_f$, obtained from method of ESDU (1979). Therefore $\left(\frac{dP}{dz}\right)_F$ is evaluated from

$$\left(\frac{dP}{dz}\right)_F = \left(\frac{dP}{dz}\right)_f \phi_f^2 \tag{7.64}$$

where the liquid-only single-phase pressure gradient, $\left(\frac{dP}{dz}\right)_f$, is obtained from

$$\left(\frac{dP}{dz}\right)_f = -C \frac{\frac{1}{2}(1-x_e)^2}{D_{eq}} G^2 \nu_f \tag{7.65}$$

where C is the pressure loss coefficient evaluated from Equation (7.45), based on the local liquid flow Reynolds number, Equation (7.24). As was mentioned before, for the pin fin surfaces, the mass flux G in Equation (7.24) was based on the unrestricted flow area.

The two-phase pressure drops for the in-line and off-set pin fin surfaces tests with R113 and the in-line pin fin surface tests with deionised water were predicted and the resultant predicted values are shown in Figures 7.19 to 7.21, respectively. The measured two-phase pressure drops for all pin fin surfaces tests were in a good

agreement with the predicted values indicating pressure drop methods maybe transferable, although more surfaces will need to be tested before this can be stated conclusively.

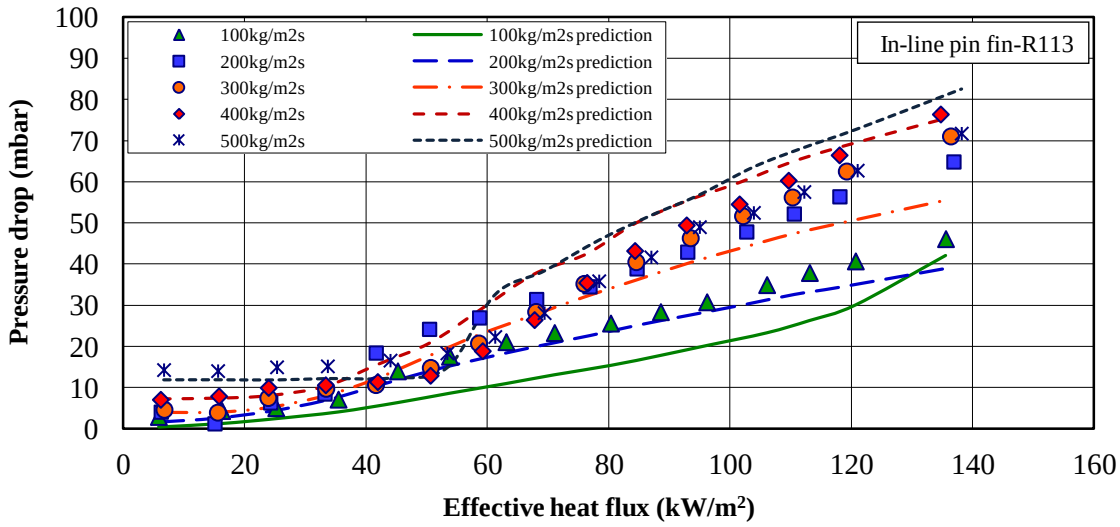

Figure 7.19 Comparison of two-phase pressure drop data with predictions for in-line pin fin surface tests with R113

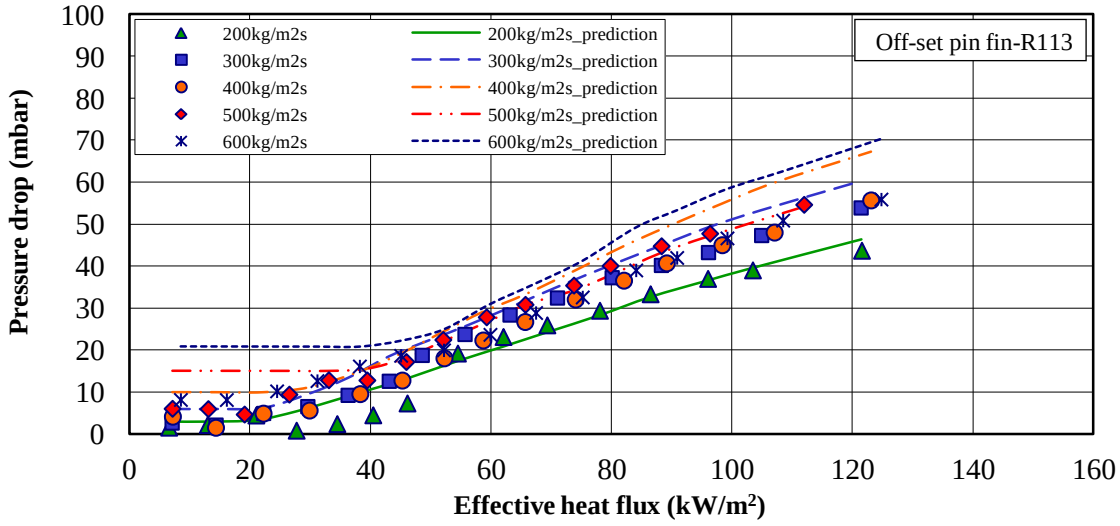

Figure 7.20 Comparison of two-phase pressure drop data with predictions for off-set pin fin surface tests with R113

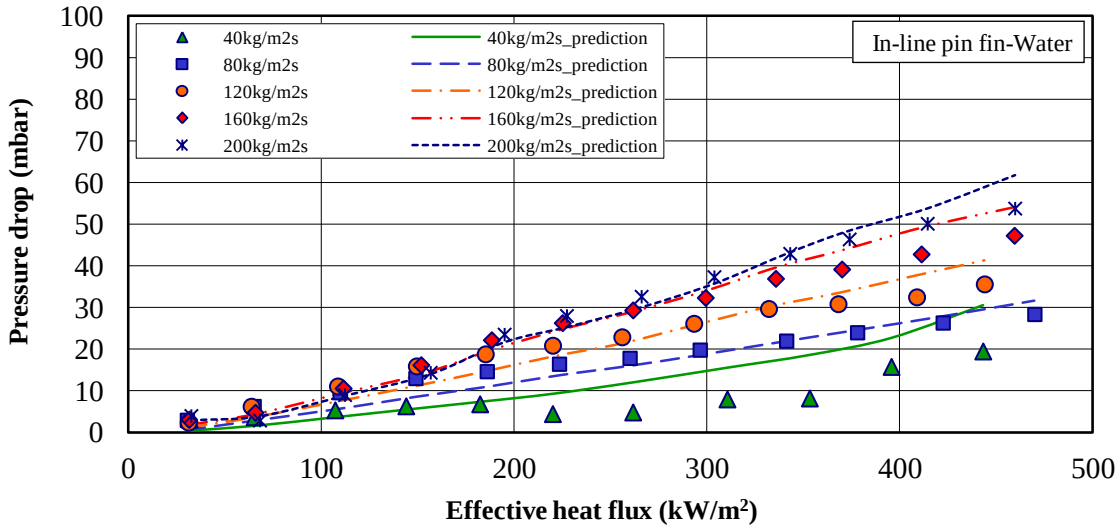

Figure 7.21 Comparison of two-phase pressure drop data with predictions for in-line pin fin surface tests with deionised water

The pin fin surfaces predicted two-phase pressure drop components for different flow rates and heat fluxes are presented in Tables F.3 to F.5, Appendix F. The Frictional pressure drop component for the in-line and off-set pin fin surfaces tests with R113 and the in-line pin fin surface tests with deionised water accounts for up to 93%, 90% and 88% of the total two-phase pressure drop, respectively, which in compare with the corresponding acceleration component is significantly higher. Thus, unlike the plate and parallel channel tests, which acceleration pressure drop component was dominated, the frictional pressure drop component was dominant for the pin fin surfaces tests.

The comparison of the in-line and off-set pin fin surfaces tests with R113 pressure drops for common mass fluxes is shown in Figure 7.22. As is shown, the off-set pin fin surface pressure drops are more than 30% smaller than the in-line pin fin surface values. It was also found that the off-set pin fin surface pressure drops are around 20% smaller for common heat and mass fluxes. This resulted from the off-set pin fins arrangement. As the fins have been staggered in the longitudinal direction, the flow follows a less tortuous path, producing a smaller pressure drop relative to the in-line pin fin array.

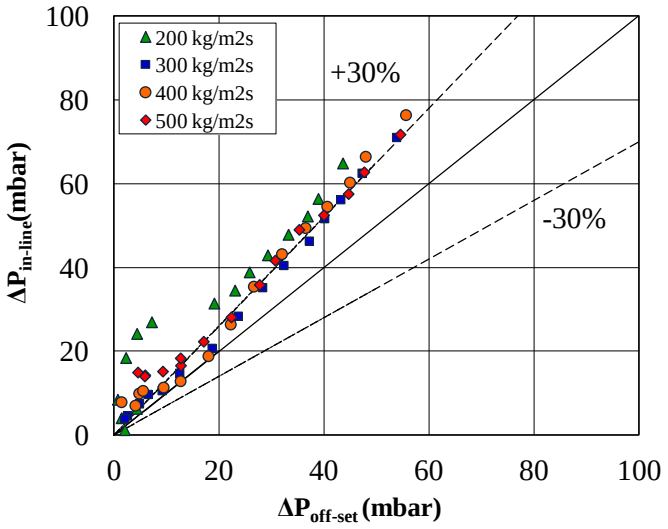

Figure 7.22 Comparison of the in-line and off-set pin fin surfaces pressure drops

The comparison of the in-line pin fin surface tests with R113 and deionised water pressure drops for common mass fluxes and same range of heat fluxes is shown in Figure 7.23.

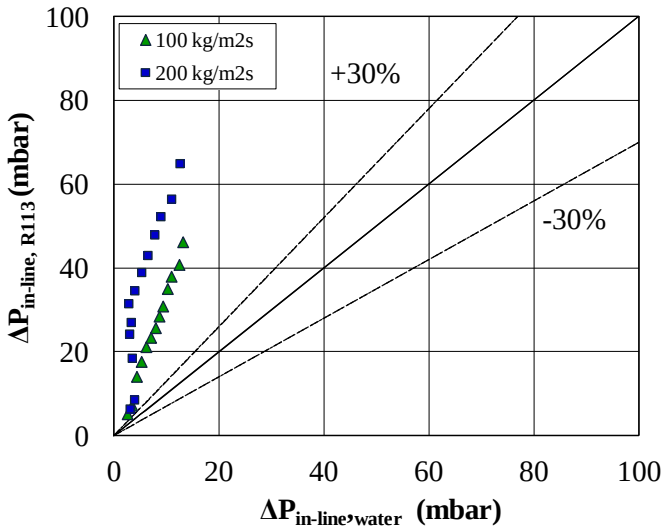

Figure 7.23 Comparison of the in-line pin fin surface pressure drops for R113 and deionised water tests

As is shown, for the same range of heat fluxes, the R113 pressure drops are much higher than the deionised water values. This was resulted from higher vapour quality of R113 than that for water.

7.3 General Conclusion

The plate and parallel channel surfaces two-phase heat transfer coefficients and pressure drop measurements were compared with several popular published macro- and micro-channel correlations. It was shown that, some of the correlations which are based on nucleate boiling heat transfer in channels with hydraulic diameters larger than $1\,mm$, such as Lazarek and Black (1982) correlation, provided reasonable agreement with the plate and parallel channel data. The plate and parallel channel surfaces tests were carried out with R113 as the working fluid. The parallel channel data were in the transition zone from macro to micro-scale channels, based on the Bond number. Lazarek and Black (1982) correlation provided the best agreement with the measured saturated boiling heat transfer coefficients among all correlations tested. Therefore the agreement between some of the macro-channel correlations predictions and saturated flow boiling heat transfer coefficients measurements indicated these correlations may be transferable for transition zone from macro to micro-scale channels, but cannot be used with confidence.

The in-line and offset pin fin surfaces data have also been compared to macro-scale design methods and several macro-scale tube bundle and micro-pin-fin correlations. It was shown that, macro-scale heat transfer may aid the selection of correlating parameters for pin-fin surfaces and that pressure drop methods may be transferable. For the pin fin surfaces, the saturated flow boiling heat transfer coefficients were predicted using a combination of nucleate boiling heat transfer coefficients obtained from method of Mostinski (1963) and single-phase convective heat transfer coefficients obtained from method of ESDU (1973). This method was novel for mini and micro pin fin surfaces. No similar approach was reported in literatures before.

For all surfaces tested, the data and the predictions suggest that heat transfer is heat flux dependent and that convective enhancement does not occur on the tested

surfaces. This shows that the heat transfer mechanism is dominated by nucleate boiling. The conclusions obtained from this chapter are stated in Chapter 8 in more details.

CHAPTER 8

CONCLUSIONS AND RECOMMENDATIONS

The objective of this work was to study and investigate the flow boiling characteristics, heat transfer coefficient, and pressure drop in small-scale multi-channel geometries with and without interconnecting passages. In order to facilitate these objectives, an experimental investigation has been carried out for different channel geometries; a single plate channel with hydraulic diameter of 1.96 mm, and multiple parallel channel and in-line and off-set pin-fin surfaces, with flow passages having hydraulic diameter of the order of 1 mm, using R-113 and deionised water as the working fluids at nominal atmospheric pressure. A summary of conclusions based on the results obtained from these tests is presented in the following sections.

8.1 Conclusion for Plate and Parallel Channel Surfaces

- The wall inlet and outlet saturated flow boiling heat transfer coefficients for both geometries were similar in magnitude, both dependent on heat flux and reasonably independent of mass flux and vapour mass fraction. This indicated that the dominant heat-transfer mechanism in the saturated boiling flow regime was nucleate boiling for both surfaces.
- The parallel channel surface saturated flow boiling heat transfer coefficients were slightly larger than the plate channel surface data. This indicated that the parallel channel surface improved heat transfer by increasing the surface area and the heat transfer coefficient.
- The correlation of Lazarek and Black (1982) which was developed based on nucleate boiling heat transfer in circular channel with diameter of 3.15 mm, provided the best agreement with the measured saturated boiling heat transfer coefficients among all correlations tested.
- For saturated flow boiling heat transfer coefficients, predictions made using the nucleate boiling correlation of Cooper (1984) provided the second best agreement with the data among all macro- mini- and micro-channel

correlations tested. This was further evidence indicating that the heat transfer mechanism in the saturated boiling flow regime was dominated by nucleate boiling.

- Lazarek and Black (1982) correlation was developed from limited data, while Cooper (1984) correlation is a general correlation, so good agreement with Cooper (1984) is more important.
- The agreement between some of the macro-channel correlations predictions and saturated flow boiling heat transfer coefficients measurements indicated these correlations may be transferable for channels with hydraulic diameter of the order of $1\ mm$, but cannot be used with confidence.
- The two-phase pressure drops for both surfaces were reasonably proportional to heat flux. The plate channel surface pressure drops were smaller than the parallel channel surface data by a factor of about 3.
- For two-phase pressure drops, the agreement between the measured and predicted values for the plate channel surface was quite good, indicated the homogeneous equilibrium flow model was reasonable for the plate channel surface.
- For the parallel channel surface, due to the presence of higher static and dynamic instabilities in parallel channel flows, the two-phase pressure drop measurements at high heat fluxes were higher than the predicted values obtained from the homogeneous equilibrium flow model, indicated the homogeneous equilibrium flow model was not suitable for predicting the parallel channel surface data.
- For both plate and parallel channel surfaces, the two-phase pressure drops were dominated by acceleration component.
- Among the several two-phase pressure drop correlations for macro-, mini- and micro-channels tested, the Qu and Mudawar (2003c) correlation which was based on the separated flow model and developed based on micro-channels data, channels with hydraulic diameter of $0.35\ mm$, yielded the most accurate predictions.

8.2 Conclusion for In-Line and Off-Set Pin-Fin Surfaces

- Similar to the plate and parallel channel surfaces, the wall inlet and outlet saturated flow boiling heat transfer coefficients for pin-fin surfaces were similar in magnitude, dependent on heat flux and almost independent of mass flux and vapour mass fraction. This indicated that the dominant heat-transfer mechanism in the saturated boiling flow regime was nucleate boiling for these surfaces as well.
- For the tests with R113, the in-line and off-set pin fin surfaces saturated flow boiling heat transfer coefficients trends were similar to the plate and parallel channel surfaces data set. The off-set pin fin surface data were slightly higher than the in-line and parallel surfaces values at lower heat fluxes, and considerably higher than the plate channel surface data at all heat fluxes. At higher heat fluxes, the off-set pin fin heat transfer coefficients values merged with the in-line and parallel surfaces data. This indicated that the parallel channel and pin-fin surfaces saturated flow boiling heat transfer coefficients were similar to within the experimental uncertainty.
- Pin-fin surfaces and parallel channel surface heat transfer areas were 75% and 50% larger than plate channel surface respectively, and their heat-transfer coefficients were considerably larger, allowing a much lower surface temperature for the same heat flux. Thus, pin-fin surfaces improved the heat transfer by increasing the heat-transfer surface area and the heat-transfer coefficient.
- The pin-fin surfaces saturated flow boiling heat transfer coefficients were predicted using a combination of standard correlations for tube bundles, ESDU (1973), and nucleate boiling correlation of Mostinski (1963). The predicted wall inlet saturated flow boiling heat transfer coefficients were in reasonable agreement with the measured values at the wall inlet and outlet, resulted from the nucleate suppression of Mostinski (1963) balancing with the convective enhancement of ESDU (1973).
- The difference between the wall inlet and outlet saturated flow boiling heat transfer coefficients predictions was due to convective enhancement. The measured data were consistent with predictions in the absence of convective enhancement. Therefore, unlike the conventionally-sized tube bundles, the

convective enhancement did not occur for the present study's mini-pin-fin surfaces, supporting the assertion that nucleate boiling is the dominant mechanism.

- The measured saturated flow boiling heat transfer coefficients were also compared with nucleate pool boiling correlations of Cooper (1984) and Mostinski (1963) and several conventional tube bundles and mini- and micro-pin-fin surfaces correlations. The Cooper (1984) correlation provided the best agreement with the data for the pin fin surfaces tests with R113 among all correlations tested. For the in-line pin fin surface tests with water, the correlation of Hsu (1987) and nucleate boiling correlation of Dowlati et al. (1996) showed the best agreement with the data. Nucleate pool boiling correlations of Mostinski (1963) and Cooper (1984) also showed a good agreement with the water tests data.
- A comparison between saturated flow boiling heat transfer coefficients obtained from tests with R113 and deionised water indicated that, for similar heat fluxes the heat transfer coefficients for tests with water were much bigger in magnitude than those with R113.
- For the tests with R113, the off-set pin fin two-phase pressure drops were more than 20% smaller than the in-line pin fin data, for common heat and mass fluxes. This resulted from the off-set pin fins arrangement. As the fins have been staggered in the longitudinal direction, the flow follows a less tortuous path, producing a smaller pressure drop relative to the in-line pin fin array.
- Unlike the plate and parallel channel tests, which acceleration pressure drop component was dominated, the frictional pressure drop component was dominant for the pin fin surfaces tests.
- The two-phase pressure drops in the in-line and off-set pin-fin surfaces were about 7 and 6 times larger than that for the plate, and 2 and 1.7 times larger than that for the parallel channel surfaces, respectively. Thus, the reduction in wall temperature is achieved by a significant pressure drop penalty.
- The measured two-phase pressure drops were also compared to macro-scale design methods. The measured two-phase pressure drops for both pin fin surfaces tests with R113 and deionised water were in a good agreement with the predicted values indicating pressure drop methods maybe transferable,

although more surfaces will need to be tested before this can be stated conclusively.

- For the in-line pin fin surface, two-phase pressure drops obtained from tests with R113 were compared with deionised water data, for common mass fluxes and same range of heat fluxes. It was found that, the R113 pressure drops were much higher than the deionised water values. This resulted from the higher vapour quality and higher two-phase multiplier of R113 compare with deionised water at saturation temperature.
- In terms of heat transfer coefficient, it was found that, the parallel channel and pin-fin surfaces saturated flow boiling heat transfer coefficients were similar to within the experimental uncertainty. In terms of pressure drop, on one hand, the two-phase pressure drops in the in-line and off-set pin-fin surfaces were about 2 and 1.7 times larger than that for the parallel channel surface, respectively. On the other hand, rapid bubble growth and no interconnecting flow passages caused back flows and high boiling flow oscillations in the parallel channel surface. To suppress these instabilities, mini-fabricated inlet orifices can be used at each mini-channel. But the reduction in boiling flow instabilities in parallel channel surface is achieved by a significant pressure drop penalty. Therefore, using the mini- and micro-pin fin surfaces in enhanced boiling heat transfer is more efficient.

8.3 Future Work and Recommendations

The research work presented in this study investigated flow boiling heat transfer characteristics and two-phase pressure drops in small scale complex geometries. In order to seek a better understanding of the mechanisms responsible for the flow boiling enhancement more work needs to be done in the future. Therefore, the following tasks are recommended:

- Prior to performing future test series running at atmospheric pressure, a new test section needs to be designed. The housing needs to be made from a material with low thermal conductivity such as PTFE to decrease the heat distribution inside the housing and minimize the heat losses to the ambient. The wall between the heater and the test piece needs to be removed and replaced with a

high thermal conductivity material such as copper to maximize the heat flux from the heater to the test piece. Preparing new test section is in progress.

- More experiments with different surfaces containing flow passages with hydraulic diameter of the order of 1 mm are recommended to investigate the extensibility and reliability of the macro-scale tubes and conventional tube bundles correlations for mini-scale geometries.
- Flow boiling heat transfer coefficients and pressure drops in mini- and micro-scale flow passages are strongly dependent on two-phase flow patterns. Therefore, flow pattern studies have to be given more attention in future work.
- In order to further study on two-phase flow patterns in these small-scale flow passages, a high speed camera with a higher quality and ability in capturing the flow boiling phenomena in mini flow passages is recommended.
- The void fraction approach needs further study as it is one of the most important parameters used to characterize two-phase flows. It has a fundamental importance in models for predicting flow pattern transitions, heat transfer and pressure drop.
- Flow static and dynamic instabilities and fluctuations need to be better investigated and understood. As their intensity is higher in mini- and micro-channels due to the higher rate of vapour generation which persuades considerable pressure drops.
- A numerical simulation based on flow boiling model should be developed to predict the heat transfer coefficient, void fraction and pressure drop along the test pieces. With this numerical model more information about local flow properties can be obtained than usually possible in experiments.

REFERENCES

Adom E., Islam S.Z., Kew P.A., 2010, *Boiling Heat Transfer on the Outside of A Miniature Diameter Compact Tube Bundle*, Proceedings of the World Congress on Engineering, Vol. 3, WCE 2010, June 30 - July 2, 2010, London, U.K.

Agostini B., Revellin R., Thome J.R., Fabbri M., Michel B., Calmi D., Kloter U., 2008, *High heat flux flow boiling in silicon multi-micro-channels – Part III: Saturated critical heat flux of R236fa and two-phase pressure drops*, Int. J. Heat and Mass Transfer, Vol. 51, pp. 5426-5442.

Alves G.E., 1954, *Co-current liquid-gas flow in a pipeline contactor*, Chem. Process. Engineering, Vol. 50 (9), pp. 449-456.

Arcanjo A.A. , Tibiriçá C.B., Ribatski G., 2010, *Evaluation of flow patterns and elongated bubble characteristics during the flow boiling of halocarbon refrigerants in a micro-scale channel*, J. Experimental Thermal and Fluid Science, Vol. 34, pp. 766-775.

Baker D., 1954, *Simultaneous Flow of Oil and Gas*, Oil and Gas J., Vol. 53, pp. 183-195.

Balasubramanian K., Lee P.S., Jin L.W., Chou S.K., Teo C.J., Gao S., 2011, *Experimental investigations of flow boiling heat transfer and pressure drop in straight and expanding micro-channels - A comparative study*, Int. J. Thermal Sciences, Vol. 50, pp. 2413-2421.

Bao Z.Y., Fletcher D.F., Haynes B.S., 2000, *Flow boiling heat transfer of Freon R11 and HCFC123 in narrow passages*, Int. J. Heat and Mass Transfer, Vol. 43, pp. 3347-3358.

Barajas A.M., Panton R.L., 1993, *The effects of contact angle on two-phase flow in capillary tubes*, Int. J. Multiphase Flow, Vol. 19, pp. 337–346.

Barnea B., Luninski Y., Taitel Y., 1983, *Flow pattern in horizontal and vertical two-phase flow in small diameter pipes*, The Canadian Journal of Chemical Engineering, Vol. 61, pp.617-620.

Basu S., Ndao S., Michna G.J., Peles y., Jensen M.K., 2011, *Flow Boiling of R134a in Circular Microtubes—Part I: Study of Heat Transfer Characteristics*, J. Heat Transfer, Vol. 133, pp. 051502.

Bennett D.L., Davis M.W., Hertzler B.L., 1980, *The suppression of saturated nucleate boiling by forced convective flow*, AIChE Symp. Ser. 26, pp. 91-103.

Bergles, A.E., 1964, *Burnout in tubes of small diameter*, ASME paper No. 63-WA-182, pp.1-9.

Bertsch S.S., Groll E.A., Garimella S.V., 2009, *A composite heat transfer correlation for saturated flow boiling in small channels*, Int. J. of Heat and Mass Transfer, Vol. 52, pp. 2110–2118.

Brauner N., Moalem Maron D., 1992, *Flow pattern transitions in two-phase liquid-liquid flow in horizontal tubes*, International Journal of Multiphase Flow. Vol. 18, pp. 123-140.

Burnside B.M., Shire N.F., 2005, H*eat transfer in flow boiling over a bundle of horizontal tubes*, Trans. IChemE Part A Chem. Eng. Res. Des., Vol. 83, pp. 527–538.

Celata G.P., Cumo M., Zummo G., 2004, *Thermal-hydraulic characteristics of single-phase flow in capillary pipes*, Experimental Thermal and Fluid Science, Vol. 28, pp. 87-95.

Chang W.R., Chen C.A., Ke J.H., Lin T.F., 2010, *Subcooled flow boiling heat transfer and associated bubble characteristics of FC-72 on a heated micro-pin-finned silicon chip*, Int. J. Heat and Mass Transfer, Vol. 53, pp. 5605-5621.

Chen J.C., 1966, *Correlation for boiling heat transfer to saturated fluids in convective flow*, I & EC Process Design Develop, Vol. 5, pp. 322-329.

Cheng L., Mewes D., 2006, *Review of two-phase flow and flow boiling of mixtures in small and mini channels,* J. Multiphase flow, Vol. 32, pp. 183-207.

Chisholm D., 1973, *Pressure gradients due to friction during the flow of evaporation two-phase mixtures in smooth tubes and channels*, Int. J. Heat Mass Transfer, Vol. 16, pp. 347–358.

Chisholm D., 1983, *Two-Phase flow in pipelines and heat exchangers*, George Goodwin, London and New York, Longman, New York.

Collier J.G., Thome J.R., 1994, *Convective boiling and condensation*, Third ed., Oxford University Press, Oxford.

Cooper M.G., 1984, *Heat flow rates in saturated nucleate pool boiling e - A wide ranging examination using reduced properties*, Advances in Heat Transfer, Academic Press, Orlando, Vol. 16, pp. 157-239.

Cornwell K., 1990, *The influence of bubbly flow on boiling from a tube in a bundle*, Int. J. Heat Mass Transfer, Vol. 33, pp. 2579–2584.

Cornwell K., Kew P.A., 1993, *Boiling in small parallel channels*. In: Pilavachi, P.A. (Ed.), Energy Efficiency in Process Technology. Elsevier, New York, pp. 624-638.

Cornwell K., Kew P.A., 1995, *Evaporation in micro-channel heat exchangers*, Proceedings of 4th UK National Conference on Heat Transfer, pp. 289-293.

Cornwell K., 2011, *Tubes and tube banks, boiling heat transfer on* [online]. Article added 02 Feb 2011, Available at: http://www.thermopedia.com/content/1213/ [Accessed 19 March 2011].

Damianides C.A., Westwater J.W., 1988, *Two-phase flow patterns in a compact heat exchanger and in small tubes*, Proceeding 2nd UK National Heat Transfer Conference, Glasgow, Scotland, Vol. 2, pp. 1257-1268.

Ding L.S., Jiang M.J., Sun H., 1996, *Measurement of heat transfer characteristics and friction factors for the flow boiling of CFC-12 through triangular micro-channels used*

for the refrigerating evaporators, B.X. Wang, Editor, Heat Transfer Science and Technology 1996, Higher Education Press, Beijing, pp. 360–365.

Dowlati R., Chan A.M.C., Kawaji M., 1992, *Hydrodynamics of two-phase flow across horizontal in-line and staggered rod bundles*, J. Fluids Eng., Trans. ASME 114, pp. 450-456.

Dowlati R., Kawaji M., Chan A.M.C., 1990, *Pitch-to-diameter effect on two-phase flow across an in-line tube bundle*, AIChE. J., Vol. 36, pp. 765-772.

Dowlati R., Kawaji M., Chan A.M.C., 1996, *Two-Phase cross-flow and boiling heat transfer in horizontal tube bundles*, J. Heat Transfer, Vol. 118, pp. 124-131.

Edelstein S., Perez A.J., Chen J.C., 1984, *Analytic representation of convective boiling functions*, AIChE J., Vol. 30, pp. 840–841.

ESDU, 1973, *Convective Heat Transfer during Crossflow of Fluids over Plain Tube Banks*, Engineering Sciences Data Unit, Vol. 73031.

ESDU, 1979, *Crossflow Pressure Loss over Banks of Plain Tubes in Square and Triangular Arrays Including Effects of Flow Direction*, Engineering Sciences Data Unit, Vol. 79034.

Feenstra A., Weaver D.S., Judd R.L., 2000, *Improved void fraction model for two-phase cross-flow in horizontal tube bundles*, Int. J. Multiphase Flow, Vol. 26, pp. 1851-1873.

Felcar H.O.M., Ribatski G., Saiz-Jabardo J.M., 2007, *A gas–liquid flow pattern predictive method for macro- and mini-scale round channels*, in: Proceedings of the 10th UK Heat Transfer Conference, Edinburgh, Scotland.

Feng Z., Serizawa A., 2000, *Two-phase flow patterns in ultra small channels*, in: Second Japanese-European Two-Phase Flow Group Meeting, Tsukuba, Japan.

Friedel L., 1979, *Improved friction pressure drop correlations for horizontal and vertical two-phase pipe flow*, European Two-phase Flow Group Meeting, Ispra, Italy, Paper E2, June.

Fukano T., Kariyasaki A., Kagawa M., 1989, *Flow patterns and pressure drop in isothermal gas–liquid flow in a horizontal capillary tube*, ANS Proceedings, National Heat Transfer Conference, ISBN 0-89448-149-5, ANS, Vol. 4, pp. 153-161.

Gouse S.W.J, 1964, *An introduction to two-phase gas-liquid flow*, report 8734-3 Engineering Projects Lab, MIT.

Grant I.D.R., Chisholm D., 1979, *Two-Phase Flow on the Shell-Side of a Segmentally Baffled Shell-and-Tube Heat Exchanger*, J. Heat Transfer, Vol. 101, pp. 38-43.

Gungor K.E., Winterton R.H.S., 1986, *A general correlation for flow boiling in tubes and annuli*, Int. J. Heat Mass Transfer, Vol. 29, pp. 351–358.

Gupta A., 2005, *Enhancement of boiling heat transfer in a 5×3 tube bundle*, Int. J. Heat Mass Transfer, Vol. 48, pp. 3763-3772.

Gupta A., Saini J.S., Varma H.K., 1995, *Boiling heat transfer in small horizontal tube bundles at low cross-flow velocities*, Int. J. Heat Mass Transfer, Vol. 38, pp. 599-605.

Hetsroni G., Mosyak A., Pogrebnyak E., Segal Z., 2005, *Explosive boiling of water in parallel micro-channels*, Int. J. Multiphase Flow, Vol. 31, pp. 371-392.

Hewitt G.F., Robert D.N., 1969, *Studies of two phase flow patterns by simultaneous X-ray and flash photography*, UK AEA Report ASRE-M-2159 HMSO.

Honda H., Takamastu H., Wei J.J., 2002, *Enhanced boiling of FC-72 on silicon chips with micro-pin-fins and submicron-scale roughness*, ASME J. Heat Transfer, Vol. 124, pp. 383-390.

Honda H., Wei J.J., 2004, *Enhanced boiling heat transfer from electronic components by use of surface microstructures*, Exp. Therm. Fluid Sci., Vol. 28, pp. 159-169.

Honkanen M., Jung J., Kuo C.-J., Peles Y., Amitay M., 2010, *Two-phase PIV/PTV measurement of bubbly flow across pin fins in a micro-channel,* 7th International Conference on Multiphase Flow, Tampa, FL USA, May 30-June 4.

Hosler E. R., 1967, *Flow patterns in high pressure two-phase (steam-water) flow with heat addition*, AIChE Symp, Ser. 64, pp. 54-66.

Houston S.D., Cornwell K., 1996, *Heat transfer to sliding bubbles on a tube under evaporating and non-evaporating conditions*, Int. J. Heat Mass Transfer, Vol. 39, pp. 211–214.

Hsu J.T., 1987, *A parametric study of boiling heat transfer in a horizontal tube bundle,* Ph.D. Dissertation, University of Wisconsin-Milwaukee, Milwaukee, WI.

Hu X., Lin G., Cai Y., Wen D., 2011, *Experimental study of flow boiling of FC-72 in parallel mini-channels under sub-atmospheric pressure,* J. Applied Thermal Engineering, Vol. 31, pp. 3839-3853.

Huang L.D., Witte L.C., 2001, *Highly sub-cooled boiling in cross-flow,* J. Heat Transfer, Vol. 123, pp. 1080-1085.

Hwang T.H., Yao S.C., 1986, *Cross flow heat transfer in tube bundles at low Reynolds numbers*, J. Heat Transfer, Vol. 108, pp. 697-700.

Hwang T.H., Yao S.C., 1986, *Forced convective boiling in horizontal tube bundles*, Int. J. Heat Mass Transfer, Vol. 29, pp. 785–795.

Ishihara K., Palen J.W., Taborek J., 1980, *Critical review of correlations for predicting two-phase flow pressure drop across tube banks*, Heat Transfer Eng. Vol. 1, pp. 23-32.

Incropera F.P., Dewitt D.P., 2002, *Fundamentals of Heat and Mass Transfer*, fifth ed., Wiley, New York.

Incropera F.P., Dewitt D.P., 2007, *Introduction to Heat Transfer*, Fifth edition, Wiley, New York.

Jacobi A.M., Thome J.R., 2002, *Heat Transfer Model for Evaporation of Elongated Bubble Flows in Micro-channels,* J. Heat Transfer, Vol. 124, pp. 1131-1136.

Jensen M.K., Hsu J.T., 1988, *A parametric study of boiling heat transfer in a horizontal tube bundle,* ASME J. Heat Transfer, Vol. 110, pp. 976–981.

Kandlikar S.G., 1983, *An improved correlation for predicting two-phase flow boiling heat transfer coefficient in horizontal and vertical tubes*, National Heat Transfer Conference, pp. 3-10.

Kandlikar S.G., 1990, *A general correlation for saturated two-phase flow boiling heat transfer inside horizontal and vertical tubes*, J. Heat Transfer, Vol. 112, pp. 219–228.

Kandlikar S.G., 1999, ed. *Hand book of phase change: Boiling and Condensation*, Taylor and Francis.

Kandlikar S.G., 2001, *Two-phase flow patterns, pressure drop and heat transfer during boiling in mini-channel and micro-channel flow passages of compact evaporators,* in: Proc. of the Third International Conference on Compact Heat Exchangers and Enhancement Technology for the Process Industries. Begell House Inc., New York, pp. 319-334.

Kandlikar S.G., 2002, *Fundamental issues related to flow boiling in mini-channels and micro-channels*, Experimental Thermal and Fluid Science, Vol. 26, pp. 389-407.

Kandlikar S.G., Balasubramanian P., 2003, *Extending the Applicability of the Flow Boiling Correlation to Low Reynolds Number Flows in Micro-channels*, Proceedings of 1st International Conference on Micro-channels and Mini-channels, ASME, New York.

Kandlikar S.G., Garimella S., Li D., Colin S. King M.R., 2006, *Heat transfer and fluid flow in mini-channels and micro-channels*, Elsevier, Oxford, UK.

Kandlikar S.G., Grande W.J., 2004, *Evaluation of single phase flow in microchannels for high heat flux chip cooling—thermo-hydraulic performance enhancement and fabrication technology*, Heat Transfer Engineering, Vol. 25, pp. 5-16.

Kandlikar S.G., Steinke M.E., 2003, *Predicting Heat Transfer During Flow Boiling In Mini-channels and Micro-channels*, ASHRAE Trans., Vol. 109, pp. 1-9.

Kandlikar S.G., Steinke M.E., 2004, *An Experimental Investigation of Flow Boiling Characteristics of Water in Parallel Micro-channels*, Int. J. Heat Transfer, Vol. 126, pp. 518-526.

Kandlikar S.G., Steinke M.E., Tian S., Campbell L.A., 2001, *High Speed Photographic Observation of Flow Boiling of Water in Parallel Mini-channels*, 35th Proceedings of National Heat Transfer Conference, ASME, New York.

Kandlikar S.G., 2010, History, *Advances, and Challenges in Liquid Flow and Flow Boiling Heat Transfer in Micro-channels: A Critical Review*, Int. Heat Transfer Conference, Washington DC, USA.

Kasza K.E., Didascalou T., Wambsganss M.W., 1997, *Micro-scale flow visualization of nucleate boiling in small channels: mechanisms influencing heat transfer*, Proceeding of International Conference on Compact Heat Exchangers or the Process Industries, Ed. R.K. Shah, New York, Eegell, House, Inc., pp. 343-352.

Kawahara A., Chung P.M.Y., Kawaji M., 2002, *Investigation of two-phase flow pattern, void fraction and pressure drop in a micro-channel*, Int. J. Multiphase Flow, Vol. 28, pp. 1411.

Kew P.A., Cornwell K., 1995, *Confined bubble flow and boiling in narrow spaces*, 10th International Heat Transfer Conference, pp. 473-478.

Kew P.A., Cornwell K., 1997, *Correlations for the Prediction of Boiling Heat Transfer in Small-Diameter Channels*, Appl. Therm. Eng., Vol. 17(8-10), pp. 705-715.

Kew P.A., Adom E., Cornwell K., 2006, *Heat flux controlled boiling in confined spaces*, in: 13th International Heat Transfer Conference, Sydney.

Kim N.H., Cho J.P., Youn B., 2002, *Forced convective boiling of pure refrigerants in a bundle of enhanced tubes having pores and connecting gaps*, Int. J. Heat Mass Transfer, Vol 45, pp. 2449-2463.

Klimenko V.V., 1982, *Heat transfer intensity at forced flow boiling of cryogenics liquids in tubes*, Cryogenics, Vol. 22, pp. 569-576.

Kosar A., 2008, *Two-phase pressure drop across a hydrofoil-based micro pin device using R-123*, Exp. Therm. Fluid Science, Vol. 32, pp. 1213-1221.

Kosar A., Kuo C.J., Peles Y., 2005a, *Boiling heat transfer in rectangular micro-channels with re-entrant cavities*, International Journal of Heat and Mass Transfer, Vol. 48, pp. 4867-4886.

Kosar A., Kuo C.J., Peles Y., 2005b, *Reduced pressure boiling heat transfer in rectangular micro-channels with interconnected re-entrant cavities*, Journal of Heat Transfer, Vol. 127, pp. 1106-1114.

Kosar A., Özdemir M.R., Keskinoz M., 2010, *Pressure drop across micro-pin heat sinks under unstable boiling conditions*, Int. J. Thermal Sciences, Vol. 49, pp. 1253-1263.

Kosar A., Peles Y., 2007, *Boiling heat transfer in a hydrofoil-based micro pin fin heat sink*, Int. J. Heat Mass Transfer, Vol. 50, pp. 1018-1034.

Krishnamurthy S., Peles Y., 2007, *Gas-liquid two-phase flow across a bank of micro pillars*, Phys. Fluids, Vol. 19, pp. 43302-43314.

Krishnamurthy S., Peles Y., 2008, *Flow boiling of water in a circular staggered micro-pin fin heat sink*, Int. J. Heat Mass Transfer, Vol. 51, pp. 1349-1364.

Krishnamurthy S., Peles Y. 2010a, *Flow Boiling Heat Transfer on Micro Pin Fins Entrenched in a Micro-channel*,J. Heat Transfer, Vol. 132, pp. 041007-1-10.

Krishnamurthy S., Peles Y. 2010b, *Flow Boiling on Micro-pin Fins Entrenched inside a Micro-channel-Flow patterns and bubble departure diameter and bubble frequency,* J. Heat Transfer, Vol. 132, pp. 041002-1-9.

Kuwahara K., Koyama S., Yu J., Watanabe C., Osa N., 2000, *Flow pattern of pure refrigerant HFC134a evaporating in a horizontal capillary tube*, in: Proceedings of Symposium on Energy Engineering in the 21st Century, Hong Kong, Vol. 2, pp. 445–450.

Lazarek G.M., Black S.H., 1982, *Evaporative heat transfer, pressure drop and critical heat flux in a small vertical tube with R-113*, International Journal of Heat and Mass Transfer, Vol. 25, pp. 945-960.

Lee H.J., Lee S.Y., 2001, *Heat transfer correlation for boiling flows in small rectangular horizontal channels with low aspect ratios*, Int. J. Multiphase Flow, Vol. 27, pp. 2043–2062.

Lee J., Mudawar I., 2005a, *Two-phase flow in high-heat-flux micro-channel heat sink for refrigeration cooling applications: Part I-pressure drop characteristics*, International Journal of Heat and Mass Transfer, Vol. 48, pp. 928-940.

Lee J., Mudawar I., 2005b, *Two-phase flow in high-heat-flux micro-channel heat sink for refrigeration cooling applications: Part II-heat transfer characteristics*, International Journal of Heat and Mass Transfer, Vol. 48, pp. 941-955.

Lee P.S., Garimella S.V., 2005, *Investigation of heat transfer in rectangular microchannels*, International Journal of Heat and Mass Transfer, Vol. 48, pp. 1688-1704.

Li J., Peterson G. P., Cheng P., 2004, *Three-dimensional analysis of heat transfer in a micro-heat sink with single phase flow*, International Journal of Heat and Mass Transfer, Vol. 47, pp. 4215-4231.

Lie Y.M., Ke J.H., Chang W.R., Cheng T.C., Lin T.F., 2007, *Saturated flow boiling heat transfer and associated bubble characteristics of FC-72 on a heated micro-pin finned silicon chip*, Int. J. Heat Mass Transfer, Vol. 50, pp. 3862-3876.

Lin L., Udell K.S., Pisano A.P., 1994, *Liquid-vapour phase transition and bubble formation in micro structures*, Thermal Science and Engineering, Vol. 2, pp. 52–59.

Lin S., Kew P.A., Cornwell K., 1998, *Two-phase flow regimes and heat transfer in small tubes and channels*, Proceedings of 11th International Heat Transfer Conference, Kyongju, Korea, Vol. 2, pp. 45-50.

Liu Z., Winterton R.H.S., 1991, *A general correlation for saturated and subcooled flow boiling in tubes and annuli, based on a nucleate pool boiling equation*, Int. J. Heat Mass Transfer, Vol. 34, pp. 2759–2766.

Lockhart R.W., Martinelli R.C., 1949, *Proposed correlation of data for isothermal two-phase, two-component flow in pipes*, Chem. Eng. Prog., Vol. 45, pp. 39–48.

Ma A., Wei J., Yuan M., Fang J., 2009, *Enhanced flow boiling heat transfer of FC-72 on micro-pin-finned surfaces*, Int. J. Heat Mass Transfer, Vol. 52, pp. 2925-2931.

Martinelli R.C., Nelson D.B., 1948, *Prediction of pressure drop during forced-circulation boiling of water*, Trans. ASME, Vol. 70, pp. 695–702.

Massey B.S., 2006, *Mechanics of Fluids*, Eighth Edition, Taylor and Francis, New York, 2006.

Mehendal S.S., Jacobi A.M., Shah R.K., 2000, *Fluid flow and heat transfer at micro and meso-scales with application to heat exchanger design*, Appl. Mech. Rev. Vol. 53, pp. 175-193.

Mertz R., Wien A., Groll M., 1996, *Experimental investigation of flow boiling heat transfer in narrow channels*, 2nd Europe Therman Science and 14th UIT National Heat Transfer Conference, pp. 219-226.

Mishima K., Hibiki T., 1996, *Some characteristics of air–water two-phase flow in small diameter vertical tubes*, Int. J. Multiphase Flow, Vol. 22, pp. 703–712.

Morshed A.K.M.M., Yang F., Yakut Ali M., Khan J.A., Li C., 2012, *Enhanced flow boiling in a microchannel with integration of nanowires*, J. Applied Thermal Engineering, Vol. 32, pp. 68-75.

Mostinski I.L., 1963, *Calculation of heat transfer and critical heat flux in boiling liquids based on law of corresponding states*, Vol. 10, Teploenergetika, pp. 66-71.

Ong Ch.L., Thome J.R., 2009, *Flow boiling heat transfer of R134a, R236fa and R245fa in a horizontal 1.030 mm circular channel*, J. Experimental Thermal and Fluid Science, Vol. 33, pp. 651-663.

Peng X.F., Hu H.Y., Wang B.X., 1998, *Boiling nucleation during liquid flow in micro-channels*, Int. J. Heat and Mass Transfer, Vol. 41, pp. 101-106.

Peng X.F., Peterson G.P., Wang B.X., 1996, *Flow boiling of binary mixtures in micro-channeled plates*, International Journal of Heat and Mass Transfer, Vol. 39, pp. 1257–1264.

Peng X.F., Wang B.X., 1993, *Experimental investigation on flow boiling of subcooled liquid through micro-channels*, Journal of Engineering Thermophysics, Vol. 14, pp. 281–286.

Peng X.F., Wang B.X., 1993, *Forced-convection and flow boiling heat transfer for liquid flowing through micro-channels*, International Journal of Heat and Mass Transfer, Vol. 36, pp. 3421–3427.

Peng X.F., Wang B.X., 1994, *Cooling characteristics with micro-channeled structures*. Journal of Enhanced Heat Transfer, Vol. 1, pp. 315–326.

Peng X.F., Wang B.X., 1994, *Evaporating space and fictitious boiling for internal evaporation of liquid*, Science Foundation in China, Vol. 2, pp. 55–59.

Peng X.F., Wang B.X., 1994, *Liquid flow and heat transfer in micro-channels with/without phase change*, special keynote lecture, Heat Transfer 1994, Vol. 1, 10th International Heat Transfer Conference, Brighton, England, 1994 (1st edn.), Taylor and Francis, London, pp. 159–178.

Peng X.F., Wang B.X., Peterson G.P., Ma H.B., 1994, *Experimental investigation of heat transfer in flat plates with rectangular micro-channels*, International Journal of Heat and Mass Transfer, Vol. 37, pp. 127–137.

Qi S.L., Zhang P., Wang R.Z., Xu L.X., 2007a, *Flow boiling of liquid nitrogen in micro-tubes: Part I* – The onset of nucleate boiling, two-phase flow instability and two-phase flow pressure drop, Int. J. Heat and Mass Transfer, Vol. 50, pp. 4999-5016.

Qi S.L., Zhang P., Wang R.Z., Xu L.X., 2007b, *Flow boiling of liquid nitrogen in micro-tubes: Part II – Heat transfer characteristics and critical heat flux*, Int. J. Heat and Mass Transfer, Vol. 50, pp. 5017-5030.

Qu W., Mudawar I., 2002, *Prediction and measurement of incipient boiling heat flux in micro-channel heat sinks*, Int. J. Heat and Mass Transfer, Vol. 45, pp. 3933-3945.

Qu W., Mudawar I., 2003a, *Flow boiling heat transfer in two-phase micro-channel heat sinks-I. Experimental investigation and assessment of correlation methods*, International Journal of Heat and Mass Transfer , Vol. 46, pp. 2755-2771.

Qu W., Mudawar I., 2003b, *Flow boiling heat transfer in two-phase micro-channel heat sinks-II. Annular two-phase flow model*, International Journal of Heat and Mass Transfer , Vol. 46, pp. 2773-2784.

Qu W., Mudawar I., 2003c, *Measurement and prediction of pressure drop in two-phase micro-channel heat sinks*, International Journal of Heat and Mass Transfer, Vol. 46, pp. 2737-2753.

Qu W., Siu-Ho A., 2009a, *Experimental study of saturated boiling heat transfer in an array of staggered micro-pin-fins*, Int. J. Heat and Mass Transfer, Vol. 52, pp. 1853-1863.

Qu W., Siu-Ho A., 2009b, *Measurement and prediction of pressure drop in a two-phase micro-pin-fin heat sink*, Int. J. Heat and Mass Transfer, Vol. 52, pp. 5173-5184.

Rahman F.H., Gebbie J.G., Jensen M.K., 1996, *Interfacial friction correlation for shell-side vertical two-phase cross-flow past horizontal in-line and staggered tube bundles*, Int. J. Multiphase Flow, Vol. 22, pp. 753-766.

Revellin R., Thome J.R., 2007, *A new type of diabatic flow pattern map for boiling heat transfer in micro-channels*, J. Micromech. Microeng., Vol. 17, pp. 788–796.

Ribatski G., Thome J.R., 2007, *Two-Phase Flow and Heat Transfer across Horizontal Tube Bundles-A Review,* Heat Transfer Engineering, Vol. 28, pp. 508-524.

Richardson B. L., 1958, *Some problems in horizontal two-phase two-component flow,* Argonne National Lab, Report ANL-5949.

Rotameter manufacturing company limited, *Calibrating Data for Metric Series Rotameters handbook*, Rotameter manufacturing company limited, Surry, UK.

Sattelmayer T., 2011, *Influence of Turbulence and Secondary Flow on the Subcooled Flow Boiling in characteristical Reactor Configurations,* [Online]: http://www.td.mw.tum.de/tum-td/de/forschung/themen/subcooled_flow_boiling.

Schrage D.S., Hsu J.T., Jensen M.K., 1988, *Two-phase pressure drop in vertical cross-flow across a horizontal tube bundle,* AIChE J., Vol. 34, pp. 107-115.

Serizawa A., Feng Z., Kawara Z., 2002, *Two-phase flow in micro-channels*, Experimental Thermal and Fluid Science, Vol. 26, pp.703-714.

Shah M.M., 1976, *A new correlation for heat transfer during boiling flow through pipes,* ASHRAE Trans., Vol. 82, pp. 66–86.

Shah M.M., 1982, *Chart correlation for saturated boiling heat transfer: equations and further study,* ASHRAE Trans., Vol. 88, pp. 185–196.

Shah M.M., 1984, Prediction of heat transfer during boiling of cryogenics fluids flowing in tubes, Cryogenics, Vol. 24, pp. 231-236.

Shah R.K., London A.L., 1978, *Laminar flow forced convection in ducts: a source book for compact heat exchanger analytical data,* Advances in Heat Transfer, Academic Press, New York, Supplement 1.

Shah R.K., 1986, *Classification of heat exchangers*. In: Kakac S., Bergles A.E., Mayinger F., Heat Exchangers: Thermal Hydraulic Fundamentals and Design. Hemisphere Publishing Corp., Washington DC, pp. 9-46.

Sheng C.H., Palm B., 2001, *The visualization of boiling in small-diameter tubes*, Heat Transport and Transport Phenomena in Microsystems.

Sonntag R.E., Borgnakke C., Van Wylen G.J., 2008, *Fundamentals of thermodynamics*, Eighth edition, Wiley.

Steiner D., Taborek J., 1992, *Flow boiling heat transfer in vertical tubes correlated by an asymptotic model*, Heat Transfer Eng., Vol. 13, pp. 43–69.

Steinke M.E., Kandlikar S.G., 2003, *Flow boiling and pressure drop in parallel flow microchannels*, 1st International Conference on Microchannels and Minichannels, New York, USA.

Suo M., Griffith P., 1964, *Two-phase flow in capillary tubes*, J. Basic Eng, Vol. 86, pp. 576-582.

Tadrist L., 2007, *Review on two-phase flow instabilities in narrow spaces*, Int. J. Heat and Fluid Flow, Vol. 28, pp.54-62.

Taitel Y., Dukler A.E., 1976, *A model for predicting flow regime transitions in horizontal and near horizontal gas-liquid flow*, AICHE J., Vol. 22, pp. 47-55.

Thome J.R., 2003, *Boiling (chapter 9)*, Laboratory of Heat and Mass Transfer, Swiss Federal Institute of Technology Lausanne, Switzerland, pp. 635-717, (Bejan A., Kraus A.D., 2003, Heat transfer handbook).

Thome J.R., 2004a, *Boiling in micro-channels: a review of experiment and theory*, Int. J. Heat and Fluid Flow, Vol. 25, pp. 128-139.

Thome J.R., 2004b, Engineering Data Book III, Wolverine Tube, Inc.

Tong L.S., Tang Y.S., 1997, *Boiling heat transfer and two-phase flow*, second edition.

Tong W., Bergles A.E., Jensen M.K., 1997, *Pressure drop with highly subcooled flow boiling in small-diameter tubes*, Experimental Thermal and Fluid Science, Vol. 15, pp. 202-212.

Tran T.N., Wambsganss M.W., France D.M., Jendrzejczyk J.A., 1993, *Boiling Heat Transfer in a Small, Rectangular Channel,* AIChE Symposium Series, Ser. 89 (295), Heat Transfer, Atlanta, pp. 253-26l.

Tran T.N., Wambsganss M.W., France D.M., 1995, *Boiling heat transfer with three fluids in small circular and rectangular channels,* Argon National Laboratory, Report ANL-95-9, NTIS, Springfield, VA.

Tran T.N., Wambsganss M.W., France D.M., 1996, *Small circular- and rectangular-channel boiling with two refrigerants,* International Journal of Multiphase Flow, Vol. 22, pp. 485-498.

Tran T.N., Chyu M.C., Wambsganss M.W., France D.M., 2000, *Two-phase pressure drop of refrigerants during flow boiling in small channels: an experimental investigation and correlation development*, Int. J. Multiphase Flow, Vol. 26, pp. 1739–1754.

Triplett K.A., Ghiaasiaan S.M., Abdel-Khalik S.I., Sadowski D.L., 1999a, *Gas-liquid two-phase flow in micro-channels, Part I: Two-phase flow patterns*. Int. J. Multiphase Flow, Vol. 25, pp. 377-394.

Triplett K.A., Ghiaasiaan S.M., Abdel-Khalik S.I., LeMouel A., McCord B.N., 1999b, *Gas-liquid two-phase flow in micro-channels, Part II: void fraction and pressure drop*. Int. J. Multiphase Flow, Vol. 25, pp. 395-410.

Troniewski L., Ulbrich R., 1984, *Two-phase gas-liquid flow in rectangular channels*, Chem. Eng Sci., Vol. 39, pp. 751-765.

Tuckerman D.B., Pease R.F.W., 1981, *High-performance heat sinking for VLSI*, Electron Device Letters, IEEE, Vol. 2, pp. 126-129.

Wambsganss M.W., Jendrazejczyk J.A., France D.M., 1991, *Two-phase flow patterns and transitions in a small, horizontal, rectangular channel*, Int. J. Multiphase Flow, Vol. 17 (3), pp. 327-342.

Wambsganss M.W., France D.M., Jendrzejczyk J.A., Tran T.N., 1993, *Boiling heat transfer in a small-diameter tube*, ASME J. Heat Transfer, Vol. 115, pp. 963-972.

Wanga Y., Sefiane K., Harmand S., 2011, *Flow boiling in high-aspect ratio mini- and micro-channels with FC-72 and ethanol: Experimental results and heat transfer correlation assessments,* J. Experimental Thermal and Fluid Science.

Warrier G.R., Dhir V.K., Momoda L.A., 2002, *Heat transfer and pressure drop in narrow rectangular channels*, Exp. Therm. Fluid Science, Vol. 26, pp. 53–64.

Wen D.S., Kenning D.B.R., 2004, *Two-phase pressure drop of water during flow boiling in a vertical narrow channel*, Experimental Thermal and Fluid Science, Vol. 28, pp. 131-138.

Wilmarth T., Ishii M., 1994, *Two-phase flow regimes in narrow rectangular vertical and horizontal channels,* Int. J. Heat Mass Transfer, Vol. 37, pp.1749-1758.

Wolk G., Dreyer M., Rath H.J., 2000, *Flow patterns in small diameter vertical non-circular channels*, Int. J. Multiphase Flow, Vol. 26, pp. 1037-1061.

Wongwises S., Disawas S., Kaewon J., Onurai C., 2000, *Two-phase evaporative heat transfer coefficients of refrigerant HFC-134a under forced flow conditions in a small horizontal tube*, Int. Commun. Heat Mass Transfer, Vol. 27, pp. 35-48.

Wu H.Y., Cheng P., 2003, *Liquid/two-phase/vapor alternating flow during boiling in micro-channels at high heat flux*, Int. J. Heat and Mass Transfer, Vol. 30, pp. 295-302.

Xue Y., Yuan M., Ma A., Wei J., 2011, *Enhanced Boiling Heat Transfer by Using Micro-Pin-Finned Surface in Three Different Test Systems,* J. Heat Transfer Engineering, Vol. 32, pp. 1-8.

Yang C., Shieh C., 2001, *Flow pattern of air–water and two-phase R134a in small circular tubes*. Int. J. Multiphase Flow, Vol. 27, pp. 1163–1177.

Yuan M., Wei J., Xue Y., Fang J., 2009, *Subcooled flow boiling heat transfer of FC-72 from silicon chips fabricated with micro-pin-fins*, Int. J. Thermal Sciences, Vol. 48, pp. 1416-1422.

Yu W., France D.M., Wambsganss M.W., Hull J.R., 2002, *Two-phase pressure drop, boiling heat transfer, and critical heat flux to water in a small-diameter horizontal tube*, Int. J. Multiphase Flow, Vol. 28, pp. 927–941.

Zivi S.M., 1964, *Estimation of steady state steam void-fraction by means of the principle of minimum entropy production*, J. Heat Transfer, Vol. 86, pp. 247-252.